

MOTOR DESIGN FOR A SUB-ORBITAL HYBRID ROCKET

Kai Mitchell Broughton

Submitted in fulfilment of the academic requirements for the degree of Master of Science in
Mechanical Engineering, College of Agriculture, Engineering and Science, University of
KwaZulu-Natal.

Durban, South Africa

November 2018

Supervisor: Dr Michael J. Brooks

Co-Supervisor: Mr Jean-Francois Pitot de la Beaujardiere

DECLARATION 1 – PLAGIARISM

I, Kai Mitchell Broughton, declare that

1. The research reported in this thesis, except where otherwise indicated, is my original research.
2. This thesis has not been submitted for any degree or examination at any other university.
3. This thesis does not contain other persons' data, pictures, graphs or other information, unless specifically acknowledged as being sourced from other persons.
4. This thesis does not contain other persons' writing, unless specifically acknowledged as being sourced from other researchers. Where other written sources have been quoted, then:
 - a. Their words have been re-written but the general information attributed to them has been referenced
 - b. Where their exact words have been used, then their writing has been placed in italics and inside quotation marks, and referenced.
5. This thesis does not contain text, graphics or tables copied and pasted from the Internet, unless specifically acknowledged, and the source being detailed in the thesis and in the References sections.

Signed:..... Date:.....

Mr Kai Mitchell Broughton

As the candidate's supervisor I agree/do not agree to the submission of this thesis.

Signed:..... Date:.....

Dr Michael J. Brooks

As the candidate's co-supervisor I agree/do not agree to the submission of this thesis.

Signed:..... Date:.....

Mr Jean-Francois Pitot de la Beaujardiere

DECLARATION 2 - PUBLICATIONS

Broughton, K. M., Williams, D. R., Brooks, M. J., Pitot de la Beaujardiere, J., 2018. Development of the Phoenix-1B Mk II 35 km Apogee Hybrid Rocket. *2018 Joint Propulsion Conference, AIAA Propulsion and Energy Forum*. Cincinnati, OH.

Velthuysen, T., Broughton, K. M., Brooks, M. J., Pitot de la Beaujardiere, J., Lineberry, D. M., Tingley, E., 2018. Safety Aspects of Nitrous Oxide Use in Hybrid Rocket Motor Design and Testing. *2018 Joint Propulsion Conference, AIAA Propulsion and Energy Forum*. Cincinnati, OH.

Signed:..... Date:.....

Mr Kai Mitchell Broughton

ACKNOWLEDGEMENTS

My sincere thanks and appreciation go to the following:

- My supervisor, Dr Mike Brooks, and my co-supervisor, Mr Jean Pitot, for their consistent support, motivation and guidance throughout the project. I am truly grateful for the opportunity to take on such a project, which would never have been possible without them.
- Mr Dylan Williams, my project colleague and friend, for his reassuring support and companionship throughout the project.
- Mr Udit Balmogim for his astute guidance and endless support, whose incredible work set the foundation for this project.
- Mr Bernard Genevieve for his assistance with MATLAB™, HYROPS and LabVIEW™ programming.
- Mr Chikhar Maharaj for his advice on fuel grain casting techniques.
- My colleagues and friends in the Aerospace Systems Research Group (ASReG): Mr Tim Velthuysen, Mr Nino Wunderlin and Mr Duran Martin, for their daily companionship and assistance with testing operations.
- Mr Mathew Jo Mathew, Mr Calvin Van Wierengen, Mr Ryan Cooper and Mr Phillip Gyasi-Ageyi for their assistance as safety marshals during tests.
- The UKZN mechanical engineering workshop technicians: Mr Strini Govender, Mr Danesh Singh and Mr Yushen Reddy, for their work done and practical advice given.
- Rheinmetall Denel Munition for sponsoring the manufacturing of the nozzles and Mr Kelly Scholtz for his assistance.
- Mr Jeremy Williams for the use of his workshop.
- The South African National Space Agency (SANSA) for their financial assistance.
- The National Research Foundation (NRF) for funding the project with their Thuthuka grant.
- Denel Overberg Test Range (OTR) for their assistance with launch preparations.
- My family, friends and fiancée for their endless understanding, encouragement and loving support.

In dedication to Bianca-Anne Adlam, whose sacrifice made this possible

ABSTRACT

The Phoenix Hybrid Sounding Rocket Programme (HSRP) was started in 2010 with the primary aim of developing an indigenous sounding rocket service for South Africa. Two vehicles have been developed to date, with nominal design apogees of 10 km and 16 km respectively. This study describes the development of the hybrid propulsion system for the Phoenix-1B Mk II demonstrator rocket, with the primary mission of achieving a 35 km apogee. A particular emphasis of the project work was refining the motor from the baseline Phoenix-1B Mk I vehicle so as to double its apogee.

Initial design requirements specified to achieve this target apogee included the use of energetic metal fuel additives, improving motor performance and improving vehicle propellant mass fraction. The in-house developed Hybrid Rocket Performance Simulator (HYROPS) and NASA CEA™ were used extensively in an iterative manner to design the motor and vehicle. The motor utilises a propellant combination of nitrous oxide and paraffin wax with aluminium additive at 20% by mass. Magnesium additive was also considered for its relative ease of ignition and thus postulated higher combustion efficiency, but was abandoned due to lack of empirical regression data. The addition of aluminium into the fuel improves the density specific impulse and reduces the nominal oxidiser-to-fuel ratio from 6.8 to 5.4. This was found to effectively reduce the vehicle inert mass by 3.1% with an apogee increase of 1.7%. An associated decrease in combustion efficiency and increase in nozzle erosion and flame temperature were noted. A nominal thrust of 7250 N, or average of 5280 N, with a chamber pressure of 40 bar for a burn time of 14.2 s, or an average total impulse of 76.5 kNs, was found to propel a 76 kg vehicle to a 35 km apogee. Due to the motor calibre constraint, it proved challenging to arrive at an adequate motor design whilst remaining below the stable oxidiser mass flux limit set at $700 \text{ kg/m}^2\text{-s}$.

Analytical and numerical methods were employed to design each of the motor components, ensuring a safety factor of 1.5, focusing on the injector and nozzle designs. Analytical models and CFD analyses were used to predict the mass flow rate through the axial injector, which is non-trivial due to the two-phase flow nature of nitrous oxide. Cold flow testing showed that these modelling techniques under-predict the required injector flow area, necessitating a subsequent injector design revision, to increase the flow area by 44%. The composite ablatively-cooled nozzle was adapted from the Phoenix-1B Mk I nozzle and verified with a coupled thermal-structural analysis, with the Bartz equation used to obtain the temporal and spatial thermal loading. A hot-fire test confirmed that the motor slightly under-performed with an average thrust and chamber pressure of 4920 N and 27.9 bar, respectively. A total impulse of 63.3 kNs was achieved, 17% below nominal. Combustion and specific impulse efficiencies of 79.4% and 77.6% were recorded. The motor was deemed qualified for flight and integrated with the Phoenix-1B Mk II for launch.

TABLE OF CONTENTS

| | |
|--------------------------------------------------------------|-------|
| DECLARATION 1 – PLAGIARISM | i |
| DECLARATION 2 - PUBLICATIONS | ii |
| ACKNOWLEDGEMENTS | iii |
| ABSTRACT..... | v |
| LIST OF FIGURES | xi |
| LIST OF TABLES..... | xvi |
| NOMENCLATURE..... | xviii |
| 1. INTRODUCTION..... | 1 |
| 1.1. Rocket Propulsion | 1 |
| 1.2. Sounding Rockets | 3 |
| 1.3. Phoenix Hybrid Sounding Rocket Programme Overview | 3 |
| 1.4. Problem Statement and Research Objectives..... | 5 |
| 1.5. Dissertation Outline | 6 |
| 2. HYBRID ROCKET PROPULSION | 7 |
| 2.1. Introduction..... | 7 |
| 2.2. State of the Art..... | 8 |
| 2.3. Configuration and Operation..... | 9 |
| 2.4. Fundamental Theory and Performance Characteristics..... | 10 |
| 2.5. Hybrid Combustion Model and Internal Ballistics | 11 |
| 2.5.1. Classical Regression Rate Theory..... | 12 |
| 2.5.2. Non-classical Regression Rate Theory | 14 |
| 2.6. Combustion Instabilities..... | 16 |
| 2.7. Hybrid Propellants | 18 |
| 2.7.1. Nitrous Oxide | 19 |
| 2.7.2. Paraffin Wax | 19 |
| 2.8. Energetic Metal Additives..... | 20 |
| 2.8.1. Types of Additives | 21 |

| | |
|-------------------------------------------------------|-----------|
| 2.8.2. Additive Geometry and Concentration | 22 |
| 2.8.3. Combustion Efficiency..... | 23 |
| 2.8.4. Two-Phase Flow Losses and Nozzle Erosion | 23 |
| 2.9. Summary | 24 |
| 3. DESIGN CRITERIA AND METHODOLOGY | 25 |
| 3.1. Introduction..... | 25 |
| 3.2. Phoenix Rockets..... | 25 |
| 3.2.1. Phoenix-1A | 26 |
| 3.2.2. Phoenix-1B Mk I..... | 27 |
| 3.3. Phoenix-1B Mk II Design Requirements | 29 |
| 3.4. Methodology | 30 |
| 3.5. Hybrid Rocket Performance Simulator | 32 |
| 3.5.1. Hybrid Rocket Performance Code | 32 |
| 3.5.2. 6 DOF Flight Dynamics Simulator | 33 |
| 3.6. Summary | 34 |
| 4. PRELIMINARY SYSTEM DESIGN | 35 |
| 4.1. Introduction..... | 35 |
| 4.2. Metal Additive Study | 35 |
| 4.2.1. Thermochemical Analysis..... | 35 |
| 4.2.2. Effect on Motor and Vehicle Performance | 39 |
| 4.3. Propulsion System Design | 43 |
| 4.3.1. Design Requirements and Constraints | 43 |
| 4.3.2. Propellant Performance Analysis | 44 |
| 4.3.3. PV-3 Motor Design and Methodology | 44 |
| 4.3.4. Final Propulsion System Specifications | 46 |
| 4.4. Summary | 49 |
| 5. PV-3 MOTOR COMPONENT DESIGN..... | 50 |
| 5.1. Introduction..... | 50 |
| 5.2. PV-3 Motor Overview..... | 50 |

| | | |
|--------|-------------------------------------------------------|----|
| 5.3. | Combustion Chamber Casing | 50 |
| 5.3.1. | Pressure Vessel Design | 51 |
| 5.3.2. | Bulkhead Retention..... | 53 |
| 5.3.3. | Manufacture and Pressure Testing | 56 |
| 5.4. | Injector Bulkhead Assembly | 58 |
| 5.4.1. | Bulkhead Design | 58 |
| 5.4.2. | Injector Plate Design | 60 |
| 5.4.3. | Manufacture and Pressure Testing | 67 |
| 5.5. | Feed System Design..... | 68 |
| 5.5.1. | Oxidiser Valve and Feedline Sizing..... | 68 |
| 5.5.2. | Feedline Losses | 69 |
| 5.5.3. | Oxidiser Valve Actuation..... | 69 |
| 5.6. | Injector Design | 70 |
| 5.6.1. | Injector Configuration | 70 |
| 5.6.2. | Hydraulic Characteristics and Injector Geometry | 71 |
| 5.6.3. | Mass Flow Rate Modelling | 75 |
| 5.6.4. | Axisymmetric Orifice CFD Analysis | 78 |
| 5.6.5. | 3D Injector CFD Analysis..... | 79 |
| 5.6.6. | Final Injector Design..... | 83 |
| 5.7. | Fuel Grain Cartridge | 84 |
| 5.7.1. | Fuel Grain | 84 |
| 5.7.2. | Thermal Insulation | 85 |
| 5.8. | Summary | 86 |
| 6. | NOZZLE DESIGN..... | 87 |
| 6.1. | Introduction..... | 87 |
| 6.2. | Nozzle Design Considerations | 87 |
| 6.2.1. | Design and Construction | 87 |
| 6.2.2. | Ablation..... | 88 |
| 6.2.3. | Multiphase Flow and Nozzle Erosion | 88 |

| | | |
|--------|-------------------------------------------|-----|
| 6.3. | Design Methodology | 89 |
| 6.4. | Design Requirements and Constraints | 90 |
| 6.5. | Aerodynamic Contour Design..... | 90 |
| 6.5.1. | Converging Section..... | 90 |
| 6.5.2. | Throat Section | 91 |
| 6.5.3. | Diverging Section..... | 91 |
| 6.6. | Nozzle Loading | 91 |
| 6.6.1. | Thermal Loading..... | 92 |
| 6.6.2. | Structural Loading..... | 93 |
| 6.6.3. | Spatial and Temporal Modelling..... | 93 |
| 6.7. | Thermal and Structural Design | 94 |
| 6.7.1. | Throat Insert | 95 |
| 6.7.2. | Fore and Aft Insulation | 96 |
| 6.7.3. | Nozzle Structure..... | 97 |
| 6.8. | Axisymmetric Thermal Analysis | 98 |
| 6.8.1. | Solver | 98 |
| 6.8.2. | Model and Mesh..... | 98 |
| 6.8.3. | Constraints and Loading Conditions | 99 |
| 6.8.4. | Results..... | 100 |
| 6.9. | 3D Thermal-Structural Analysis | 102 |
| 6.9.1. | Solver | 102 |
| 6.9.2. | Model and Mesh..... | 103 |
| 6.9.3. | Constraints and Loading Conditions | 104 |
| 6.9.4. | Results..... | 104 |
| 6.10. | Nozzle Manufacture | 106 |
| 6.11. | Summary | 107 |
| 7. | STATIC TESTING | 108 |
| 7.1. | Introduction..... | 108 |
| 7.2. | Mobile Rocket Launch Platform..... | 108 |

| | |
|----------------------------------------------------------------------------|-----|
| 7.3. Igniter Test | 109 |
| 7.4. Cold Flow Test..... | 109 |
| 7.4.1. Test Setup..... | 110 |
| 7.4.2. Results and Discussion..... | 110 |
| 7.4.3. Injector Plate Revision | 113 |
| 7.5. Hot-fire Test..... | 114 |
| 7.5.1. Test Setup..... | 114 |
| 7.5.2. Results and Discussion..... | 115 |
| 7.5.3. Post-inspection | 120 |
| 7.6. Summary | 122 |
| 8. CONCLUSION AND RECOMMENDATIONS | 123 |
| 8.1. Overview | 123 |
| 8.2. Conclusions..... | 123 |
| 8.3. Discussion of Problems..... | 125 |
| 8.4. Recommendations and Future Work..... | 126 |
| REFERENCES..... | 128 |
| Appendix A: P-1A and P-1B Mk I Design Specifications and Performance | 135 |
| Appendix B: Metal Additive Study..... | 137 |
| Appendix C: Composite Oxidiser Tank Specific Heat Variation | 140 |
| Appendix D: PV-3 Motor Specifications and Theoretical Performance..... | 141 |
| Appendix E: Recommended Motor Design and Performance Constraints..... | 144 |
| Appendix F: Injector Bulkhead Aluminium 7075-T6..... | 146 |
| Appendix G: Heli-Coil™ Chart | 147 |
| Appendix H: Oxidiser Valve Control Schematic | 148 |
| Appendix I: Nozzle Design Charts | 149 |
| Appendix J: Nozzle Material Properties | 150 |
| Appendix K: Manufacturing Drawings..... | 151 |
| Appendix L: Videos | 156 |

LIST OF FIGURES

| | |
|--------------------------------------------------------------------------------------------------------------------------------------------------------|----|
| Figure 1-1: Comparison between liquid, solid and hybrid rockets (Altman and Holzman, 2007). | 1 |
| Figure 1-2: Flight profile of a sounding rocket (Marconi, 2004). | 3 |
| Figure 2-1: Typical hybrid rocket motor schematic (Cantwell et al., 2010). | 9 |
| Figure 2-2: A multi-port, wagon wheel fuel grain and a single port fuel grain (Cantwell et al., 2010). | 10 |
| Figure 2-3: Schematic of turbulent boundary layer formation in a hybrid motor (Altman and Holzman, 2007). | 11 |
| Figure 2-4: Schematic of diffusion-controlled combustion zone in a hybrid motor (Humble et al., 1995). | 12 |
| Figure 2-5: Effect of pressure on regression rate (Humble et al., 1995). | 13 |
| Figure 2-6: Liquid layer instability and droplet entrainment mechanism (Karabeyoglu, 2012). | 14 |
| Figure 2-7: Regression rate data of paraffin wax (SP-1A) and HTPB with gaseous oxygen over a range of oxidiser mass fluxes (Karabeyoglu et al., 2003). | 16 |
| Figure 2-8: (a) Specific impulse in units of m/s and (b) density impulse versus O/F ratio for different propellant combinations (Dyer et al., 2007). | 18 |
| Figure 2-9: Comparison of heats of combustion with oxygen for various metals (Risha et al., 2007). | 21 |
| Figure 2-10: (a) Slag accumulation and (b) throat erosion on a laboratory-scale copper nozzle (Maharaj, 2018). | 24 |
| Figure 3-1: The Phoenix rocket series. | 25 |
| Figure 3-2: (a) Mass analysis and (b) apogees of Phoenix rockets (Broughton et al., 2018). | 25 |
| Figure 3-3: Cross-section Phoenix-1A. | 26 |
| Figure 3-4: (a) Hot-fire test of P-1A on the MRLP (Balmogim, 2016) and (b) launch of P-1A (Genevi  e et al., 2015). | 27 |
| Figure 3-5: Cross-section of the Phoenix-1B Mk I. | 27 |
| Figure 3-6: (a) Cross-section of PV-2 nozzle design and (b) assembled PV-2 nozzle (Balmogim, 2016). | 28 |
| Figure 3-7: (a) Injector oxidiser plume of P-1B Mk I (Balmogim, 2016) and (b) P-1B Mk I hot-fire test. | 29 |
| Figure 3-8: (a) PV-2 nozzle insulation ablation and (b) PV-2 thermal liner after hot-fire test. | 29 |
| Figure 3-9: Project methodology. | 31 |
| Figure 3-10: Hierarchy model of HYROPS with dashed lines representing manual coupling (Leverone, 2013). | 32 |
| Figure 3-11: HRPC Motor Design Model (Balmogim, 2016). | 33 |

| | |
|------------------------------------------------------------------------------------------------------------------------------------------------------------------------------------------------------------------------------------------------------------------------------------|----|
| Figure 3-12: HRPC Performance Model (Balmogim, 2016)..... | 33 |
| Figure 3-13: Flow structure of the HYROPS flight dynamics simulator (Chowdhury et al., 2011). | 34 |
| Figure 4-1: Characteristic velocity curves for various aluminium additive concentrations over a range of O/F ratios at 40 bar chamber pressure. | 36 |
| Figure 4-2: Performance metric comparison of aluminium and magnesium additives at various concentrations: (a) characteristic velocity, (b) optimum O/F ratio, (d) specific impulse, (d) density specific impulse, (e) adiabatic flame temperature, and (f) thrust coefficient..... | 37 |
| Figure 4-3: (a) Molar fraction of condensed phase species at the nozzle throat and (b) molar fraction of oxidising species at the nozzle throat. | 38 |
| Figure 4-4: Metal additive study methodology considering effects on motor and vehicle performance. | 39 |
| Figure 4-5: Altitude vs. range for various aluminium concentrations (Broughton et al., 2018). 43 | |
| Figure 4-6: Characteristic velocity and specific impulse for various O/F ratios for nitrous oxide/paraffin wax with 20% aluminium additive by mass for 40 bar chamber pressure and 85% combustion efficiency. | 44 |
| Figure 4-7: Design methodology flow chart based on HYROPS for Phoenix-1B Mk II propulsion system. | 45 |
| Figure 4-8: PV-3 motor theoretical pressure and thrust curves..... | 46 |
| Figure 4-9: Nozzle exit pressure and atmospheric pressure comparison over burn time..... | 47 |
| Figure 4-10: CAD model of the Phoenix-1B Mk II. | 49 |
| Figure 5-1: Cross-section of PV-3 motor..... | 50 |
| Figure 5-2: Revolved axisymmetric FEM analysis of chamber casing showing Von-Mises stress. | 52 |
| Figure 5-3: 3D cyclic-symmetry assembly of casing, injector bulkhead, interstage coupler, and simplified bolts..... | 55 |
| Figure 5-4: Von-Mises stress on casing wall for (a) internal wall (no preload), (b) external wall (no preload), (c) internal wall (6 kN preload), and (d) external wall (6 kN preload) (capped at 276 MPa). | 56 |
| Figure 5-5: (a) Combustion chamber casing and (b) motor assembly with injector bulkhead and nozzle. | 57 |
| Figure 5-6: Hydrostatic pressure test setup of combustion chamber with bulkheads attached... 57 | |
| Figure 5-7: Injector bulkhead CAD model (a) isometric and (b) cross-section. | 59 |
| Figure 5-8: Von-Mises stress of the injector bulkhead (a) top view and (b) bottom view (capped at 478.32 MPa). | 60 |
| Figure 5-9: Sectioned view of injector bulkhead assembly. | 63 |
| Figure 5-10: Injector plate..... | 63 |

| | |
|-------------------------------------------------------------------------------------------------------------------------------------------------------------------------------------------------------------------------------------------------------------------------------------|----|
| Figure 5-11: Assembly model of injector plate and injector bulkhead. | 64 |
| Figure 5-12: Displacement (10% of model) of injector bulkhead assembly FEA for (a) cold-flow condition and (b) hot-fire condition, with a 60% preload. | 65 |
| Figure 5-13: Von-Mises stress (capped at yield stress) of injector plate for (a) cold-flow condition and (b) hot-fire condition, with a 60% preload. | 65 |
| Figure 5-14: (a) Injector bulkhead assembly and (b) Injector plate. | 67 |
| Figure 5-15: Hydrostatic pressure test setup of (a) injector bulkhead and (b) injector bulkhead. | 67 |
| Figure 5-16: Propagation threshold for nitrous oxide in various pipe sizes (Gas Industries Association, 2014). | 69 |
| Figure 5-17: Feedline and ball valve actuation mechanism assembly. | 70 |
| Figure 5-18: (a) Axial injector (Sutton and Biblarz, 2001), (b) pressure trace from hot-fire with axial injector (Waxman et al., 2010), (c) impinging injector (Sutton and Biblarz, 2001), and (d) pressure trace from hot-fire with impinging injector (Waxman et al., 2010). | 71 |
| Figure 5-19: Atomisation regimes dependent on Reynolds and Ohnesorge numbers (Van Romunde, 2011). | 73 |
| Figure 5-20: Theoretical transient injector pressure drop ($\Delta P/P_c$) and chamber pressure compared to oxidiser vapour pressure (P_c/P_v). | 74 |
| Figure 5-21: Injector plate orifice pattern. | 75 |
| Figure 5-22: Injector pressure history for (a) low vapour pressure propellant and (b) high vapour pressure propellant (Waxman et al., 2013). | 76 |
| Figure 5-23: (a) Meshed computational domain and (b) nitrous oxide vapour volume fraction. | 79 |
| Figure 5-24: (a) Quarter-symmetry computational domain of 3D injector CFD analysis, (b) polyhedral mesh close-up on orifice. | 80 |
| Figure 5-25: (a) Volume fraction of nitrous oxide vapour, (b) velocity vector field, and (c) static pressure distribution. | 82 |
| Figure 5-26: Vector field distribution in injector manifold and chamber. | 83 |
| Figure 5-27: Velocity streamlines of nitrous oxide flow through injector. | 83 |
| Figure 5-28: (a) Fuel grain half, (b) fuel grain assembly, (c) wrapped fuel grain, (d) post-cured fuel grain being machined, and (e) final fuel grain cartridge. | 86 |
| Figure 6-1: Typical external nozzle configuration (NASA, 1975). | 88 |
| Figure 6-2: Nozzle design flow chart (NASA, 1975). | 89 |
| Figure 6-3: Adiabatic flame temperature over burn time of PV-3 motor. | 90 |
| Figure 6-4: Nozzle contour comparison between PV-2 and PV-3 nozzles. | 91 |
| Figure 6-5: Convective heat transfer coefficient spatial variation and nozzle contour for 20% aluminised fuel grain at instantaneous 40 bar chamber pressure. | 94 |

| | |
|-------------------------------------------------------------------------------------------------------------------------------------------------------------------------------------------------|-----|
| Figure 6-6: Temperature and pressure spatial variation for 20% aluminised fuel grain at instantaneous 40 bar chamber pressure..... | 94 |
| Figure 6-7: PV-3 nozzle cross-section | 95 |
| Figure 6-8: Mesh of axisymmetric nozzle model..... | 99 |
| Figure 6-9: Temporal-spatial graphs of (a) heat transfer coefficient and (b) temperature for 20% aluminium concentration imported into Siemens NX TM 11..... | 100 |
| Figure 6-10: (a) Temperature distribution of nozzle after 18 s and (b) temperature response of the nozzle structure after 250 s. | 101 |
| Figure 6-11: Soak-through temperature response of the nozzle structure at the exit plane. | 102 |
| Figure 6-12: One-way coupled thermal-structural FEM analysis methodology..... | 103 |
| Figure 6-13: Cyclic-symmetric model thermal solution mesh for the thermal-structural analysis. | 103 |
| Figure 6-14: (a) Temperature distribution, (b) Von-Mises stress distribution, and (c) displacement of the cyclic-symmetric nozzle after 15 s..... | 105 |
| Figure 6-15: Von-Mises stress of nozzle structure after 15 s..... | 106 |
| Figure 6-16: Transient (a) Von-Mises stress and (b) displacement response on a point on the nozzle exit plane..... | 106 |
| Figure 6-17: (a) Compression moulded silica/phenolic, (b) tape-wrapped silica/phenolic, (c) final nozzle top view, and (d) final nozzle bottom view. | 107 |
| Figure 7-1: Mobile Rocket Launch Platform in static test configuration..... | 109 |
| Figure 7-2: Still image of igniter test 2 | 109 |
| Figure 7-3: Cold flow test setup with propulsion system on the MRLP..... | 110 |
| Figure 7-4: Injector plume after 1 s..... | 111 |
| Figure 7-5: Cold flow test pressure and mass traces during filling process..... | 111 |
| Figure 7-6: Cold flow test pressure traces..... | 112 |
| Figure 7-7: Infrared camera image of oxidiser tank after filling process..... | 113 |
| Figure 7-8: (a) P-1B Mk II assembled in static test configuration and (b) feedline assembly.. | 114 |
| Figure 7-9: Hot-fire test setup with propulsion system on the MRLP. | 115 |
| Figure 7-10: Thrust and pressure traces from the hot-fire test..... | 117 |
| Figure 7-11: Comparison of hot-fire test results to nominal simulated results from HRPC (thrust and chamber pressure traces smoothed)..... | 118 |
| Figure 7-12: Hot-fire test (a) still image 1, (b) still image 2, and (c) MRLP after hot-fire test.119 | 119 |
| Figure 7-13: Hot-fire test and thermal FEA soak-through nozzle temperatures..... | 120 |
| Figure 7-14: (a) Nozzle Converging section, (b) nozzle throat, (c) nozzle diverging section, (d) injector plate, and (e) thermal liner..... | 121 |
| Figure B-1: Characteristic velocity for various O/F ratios for 40% magnesium concentration at 40 bar chamber pressure, with and without MgO and MgO (L) omitted in NASA CEA TM | 137 |

| | |
|-----------------------------------------------------------------------------------------------------------------------------------------------------------------------------------------------------------------------------------------------------------------------------------------------------------------------------------------|-----|
| Figure B-2: Combustion temperature for various magnesium additive concentrations at 40 bar chamber pressure with and without MgO and MgO (L) omitted in NASA CEA™..... | 138 |
| Figure C-1: Specific heat capacity as a function of temperature for aluminium and carbon fibre/epoxy in the pre-glass transition stage..... | 140 |
| Figure E-1: Fuel grain stress distribution due to pressure loading for a 34.5 bar chamber pressure paraffin-based fuel grain (Karabeyoglu, 2012)..... | 145 |
| Figure F-1: Aluminium 7075-T6 material test certificate (Metal and Tool Trade, 2015). | 146 |
| Figure F-2: Rockwell Hardness A (HRA) over the cross-section of the aluminium 7075-T6 billet (average from two tests)..... | 146 |
| Figure G-1: Heli-Coil™ chart of tensile strength versus shear strength of parent material (Stanley, 2018). | 147 |
| Figure H-1: Oxidiser valve control schematic. | 148 |
| Figure I-1: (a) Nozzle geometric nomenclature for different nozzle types at an area ratio of 25, (b) nozzle losses in terms of a correction factor for conical and bell-shaped nozzles, and (c) nozzle initial and final parabola angles as functions of the nozzle percent length and expansion ratio (Sutton and Biblarz, 2001). | 149 |

LIST OF TABLES

| | |
|--------------------------------------------------------------------------------------------------------------------------------------------------------------------------------|----|
| Table 2-1: Typical regression rate coefficients and exponents for various hybrid fuels with nitrous oxide. [r] = mm/s and [Go] = kg/m ² -s. | 15 |
| Table 2-2: Properties of SASOL 0907 paraffin wax (Grosse, 2009; Geneviève, 2013). | 20 |
| Table 2-3: Properties of aluminium and magnesium (Risha et al., 2007). | 21 |
| Table 2-4: Combustion efficiencies from various tests with and without aluminium additive... | 23 |
| Table 4-1: Common input conditions for thermochemical analysis. | 35 |
| Table 4-2: Common input conditions used in HRPC..... | 40 |
| Table 4-3: Interpolated regression rate coefficient and theoretical fuel densities for various aluminium additive concentrations. | 41 |
| Table 4-4: Effect of aluminium concentration on motor geometry and steady state performance. | 41 |
| Table 4-5: Effect of aluminium concentration on vehicle mass and geometry..... | 42 |
| Table 4-6: Effect of aluminium concentration on vehicle performance. | 42 |
| Table 4-7: Phoenix-1B Mk II theoretical flight performance. | 47 |
| Table 4-8: Phoenix-1B Mk II propulsion system design specifications. | 48 |
| Table 5-1: Aluminium 6061-T6 properties (Aerospace Specification Metals, 2018)..... | 51 |
| Table 5-2: Analytical and FEM results of chamber casing analysis. | 53 |
| Table 5-3: Safety factors for failure modes present on bolted joints of injector bulkhead, nozzle and interstage coupler. | 54 |
| Table 5-4: Aluminium 7075-T6 properties (Aerospace Specification Metals, 2018), specifications in parenthesis from material test certificate (Metal and Tool Trade, 2015)..... | 58 |
| Table 5-5: Copper CDA 110 (ETP) H02 properties (Non-Ferrous Metals, 2018), specifications in parenthesis from material test certificate (Non-Ferrous Metals, 2017)..... | 61 |
| Table 5-6: Injector plate joint design per screw..... | 63 |
| Table 5-7: Results of the injector bulkhead assembly FEA with a 60% preload. | 66 |
| Table 5-8: Results from the preload study. | 66 |
| Table 5-9: Feedline pressure drop for a ¾" feedline at start-up and average flow conditions.... | 69 |
| Table 5-10: Non-dimensional atomisation and cavitation numbers for the PV-3 motor injector with a 1 mm orifice diameter at nominal flow conditions. | 74 |
| Table 5-11: Properties of nitrous oxide used for mass flow rate models for upstream and downstream state points. Properties obtained from REFPROP™. | 77 |
| Table 5-12: Properties of liquid and gaseous nitrous oxide at equilibrium. Properties taken from REFPROP™. | 78 |
| Table 5-13: Mass flow rate per orifice (1 mm diameter) and number of orifices required for both analytical and numerical modelling techniques. | 84 |

| | |
|-------------------------------------------------------------------------------------------------------------------------------------------------|-----|
| Table 6-1: Properties of ATJ graphite (GRAFTech, 2009)..... | 96 |
| Table 6-2: Material properties for tape-wrapped and compression moulded Silica/phenolic (Park Electrochemical Corp, 2018). | 97 |
| Table 6-3: EN19T alloy steel material properties (Macsteel, 2018; Voestalpine High Performance Metals (Australia), 2018). | 98 |
| Table 6-4: Peak temperatures of nozzle components from axisymmetric thermal FEA for burn time and soak-through analyses. | 102 |
| Table 7-1: Cold flow test results for liquid feed time only. | 113 |
| Table 7-2: PV-3 motor hot-fire test results for liquid burn only. Nominal design values for liquid burn only given for comparison. | 116 |
| Table 7-3: Hot-fire test averaged efficiencies for liquid burn only..... | 116 |
| Table A-1: Design specifications of the P-1A and P-1B Mk I rockets. | 135 |
| Table A-2: Theoretical flight performance of the P-1A and P-1B Mk I rockets. | 136 |
| Table B-1: Effect of aluminium additive concentration on motor performance..... | 138 |
| Table B-2: Effect of magnesium additive concentration on motor performance..... | 138 |
| Table B-3: Condensed phase species and oxidising species molar fractions for aluminium additive..... | 139 |
| Table B-4: Condensed phase species and oxidising species molar fractions for magnesium additive..... | 139 |
| Table E-1: Motor design and performance constraints. | 144 |
| Table J-1: Thermal conductivity of ATJ graphite (taken as the average between the perpendicular and parallel directions) (Ho et al., 1968)..... | 150 |
| Table J-2: Specific heat capacity of ATJ graphite (Haines, 2000)..... | 150 |
| Table J-3: Thermal conductivity of EN19T alloy steel (eFunda, 2017). | 150 |
| Table J-4: Specific heat capacity of EN19T alloy steel (eFunda, 2017)..... | 150 |

NOMENCLATURE

Symbols

| Symbol | Description | Unit |
|---------------|-------------------------------------------------------------------------|-------------------------------------|
| A | Area | m^2 |
| a | Ballistic coefficient | - |
| B | Blowing parameter | - |
| B_g | Evaporative blowing parameter | - |
| b | Port radius | m |
| C | Coefficient | - |
| C_a | Cavitation number | - |
| C_d | Coefficient of discharge | - |
| C_f | Coefficient of thrust | - |
| C_p | Specific heat | $\text{J/kg}\cdot\text{s}$ |
| c | Effective exhaust velocity | m/s |
| c^* | Characteristic velocity | m/s |
| D | Diameter | m |
| E | Joint efficiency | - |
| \dot{e} | Erosion rate | m/s |
| F | Force or Thrust | N |
| G | Mass flux | $\text{kg}/\text{m}^2\cdot\text{s}$ |
| g | Gravitational constant | m/s^2 |
| h | Enthalpy | J/kg |
| h_f | Enthalpy of formation | J/kg |
| h_g | Gas side heat transfer coefficient | $\text{W}/\text{m}^2\cdot\text{K}$ |
| I_{sp} | Specific impulse | s |
| I_{tot} | Total impulse | Ns |
| I_v | Density specific impulse | $\text{kg}\cdot\text{s}/\text{m}^3$ |
| L | Length | m |
| L^* | Characteristic length | m |
| M | Mach number | - |
| m | Mass or ballistic exponent related to port length | kg |
| \dot{m} | Mass flow rate | kg/s |
| N | Number | - |
| n | Number of atoms or ballistic exponent related to propellant combination | - |

| | | |
|-----------|------------------------------------------------------------------------------------------|--------|
| Oh | Ohnesorge number | - |
| P | Thread pitch | m |
| Pr | Prandtl number | - |
| p | Pressure | Pa |
| \dot{Q} | Rate of heat transfer | J/s |
| \dot{q} | Specific rate of heat transfer | J/kg·s |
| R | Radius | m |
| Re | Reynolds number | - |
| r | Ratio of frictional temperature increase to the increase caused by adiabatic compression | - |
| \dot{r} | Regression rate | m/s |
| S | Strength | Pa |
| SF | Safety factor | - |
| T | Temperature | K |
| t | Thickness | m |
| v | Velocity | m/s |
| We | Weber number | - |
| x | Axial length or position | m |
| Y | Compressibility correction factor | - |
| y | Radial length | m |

Greek

| Symbol | Description | Unit |
|----------------|------------------------------------------------|------------------------|
| α | Thermal diffusivity | m^2/s |
| $\hat{\alpha}$ | Dynamic pressure exponent | - |
| β | Blowing/blocking coefficient | - |
| $\hat{\beta}$ | Thickness exponent | - |
| γ | Ratio of specific heats | - |
| Δ | Difference | - |
| ε | Emissivity or expansion ratio | - |
| η | Efficiency | - |
| κ | Non-equilibrium factor | - |
| μ | Viscosity | Pa·s |
| ν | Poisson's Ratio | - |
| ρ | Density | kg/m^3 |
| σ | Stress or correction factor or surface tension | Pa or N/m |

| | | |
|--------|------|---|
| τ | Time | s |
|--------|------|---|

Subscripts

| Symbol | Description |
|---------------|------------------------|
| <i>a</i> | Ambient |
| <i>aw</i> | Adiabatic wall |
| <i>b</i> | Bolt or bubble growth |
| <i>boil</i> | Boiling |
| <i>c</i> | Convective or chamber |
| <i>com</i> | Compressible |
| <i>e</i> | Exit |
| <i>ent</i> | Entrainment |
| <i>exp</i> | Experimental |
| <i>f</i> | Fuel or final |
| <i>g</i> | Gas |
| <i>gr</i> | Grain |
| <i>hoop</i> | Hoop |
| <i>inj</i> | Injector |
| <i>l</i> | Liquid |
| <i>long</i> | Longitudinal |
| <i>m</i> | Motor |
| <i>max</i> | Maximum |
| <i>min</i> | Minimum |
| <i>mix</i> | Mixture |
| <i>melt</i> | Melting |
| <i>n</i> | Nut |
| <i>o</i> | Oxidiser |
| <i>p</i> | Port |
| <i>pipe</i> | Pipe |
| <i>prop</i> | Propellant |
| <i>r</i> | Residence or radiative |
| <i>sat</i> | Saturation |
| <i>t</i> | Throat |
| <i>T</i> | Tank |
| <i>theo</i> | Theoretical |
| <i>tot</i> | Total |

| | |
|----------|-----------------------|
| v | Vapour or evaporative |
| w_g | Gas side wall |
| y | Yield |
| θ | Stagnation or total |

Abbreviations

| Acronym | Description |
|------------------|-----------------------------------------------|
| 1D | One Dimensional |
| 2D | Two Dimensional |
| 3D | Three Dimensional |
| AMROC | American Rocket Company |
| ASReG | Aerospace Systems Research Group |
| CDR | Critical Design Review |
| CEA | Chemical Equilibrium with Applications |
| CFD | Computational Fluid Dynamics |
| DOF | Degree of Freedom |
| EDM | Electrical Discharge Machined |
| ETP | Electrolytic Tough Pitch |
| FEA | Finite Element Analysis |
| FEM | Finite Element Method |
| FRR | Flight Readiness Review |
| GOX | Gaseous Oxygen |
| GSE | Ground Support Equipment |
| HEM | Homogenous Equilibrium Model |
| HDPE | High Density Polyethylene |
| HRA | Hardness Rockwell A |
| HRPC | Hybrid Rocket Performance Code |
| HSRP | Hybrid Sounding Rocket Programme |
| HTPB | Hydroxyl-terminated Polybutadiene |
| HYROPS | Hybrid Rocket Performance Simulator |
| LOX | Liquid Oxygen |
| MEOP | Maximum Expected Operating Pressure |
| MRLP | Mobile Rocket Launch Platform |
| N ₂ O | Nitrous Oxide |
| NASA | National Aeronautics and Space Administration |
| NHNE | Non-homogeneous Non-equilibrium |

| | |
|-------|-------------------------------------|
| NPT | National Pipe Thread |
| O/F | Oxidiser-to-fuel Ratio |
| OTR | Overberg Test Range |
| P-1A | Phoenix-1A |
| P-1B | Phoenix-1B |
| P-2A | Phoenix-2A |
| PCD | Pitch Circle Diameter |
| PDR | Preliminary Design Review |
| PE | Polyethylene |
| PFS | Propellant Feed System |
| PMMA | Polymethyl-methacrylate |
| PV-1 | Phoenix vehicle motor 1 |
| PV-2 | Phoenix vehicle motor 2 |
| PV-3 | Phoenix vehicle motor 3 |
| TIS | Tank Inverting System |
| UKZN | University of KwaZulu-Natal |
| RBE | Rigid Body Element |
| RTV | Room Temperature Vulcanising |
| SANSA | South African National Space Agency |
| SPG | Space Propulsion Group |
| VOF | Volume of Fluid |

1. INTRODUCTION

1.1. Rocket Propulsion

Propulsion is the act of changing the motion of a body and is used to provide a force to move a body initially at rest, overcome retarding forces as it is propelled through a medium, or change its velocity. The means of propulsion in which a reaction force is imparted on a body by the momentum of ejected matter is known as jet propulsion, of which rocket propulsion is a sub-class. The energy sources available to rocket propulsion are chemical combustion, nuclear reaction and solar radiation, with chemical propulsion being the most popular. Thrust is produced by the thermo-dynamic expansion of gas, with the gas exerting pressure on exposed surfaces (Sutton and Biblarz, 2001).

Chemical rocket propulsion uses the energy from high pressure combustion of a fuel and an oxidiser to heat the reaction product gases to high temperatures which are subsequently expanded and accelerated in a nozzle. There are three classes depending on the physical state of the propellant, namely liquid, solid and hybrid rocket propulsion, as shown in Figure 1-1.

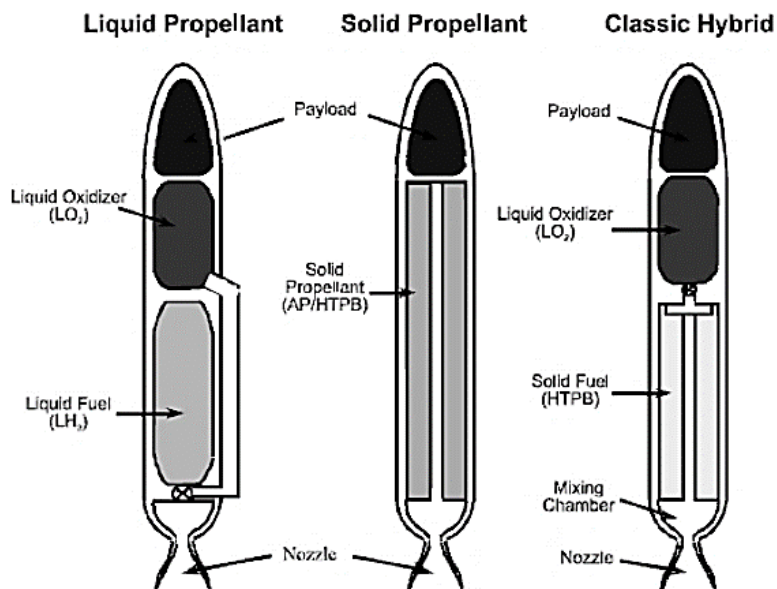


Figure 1-1: Comparison between liquid, solid and hybrid rockets (Altman and Holzman, 2007).

In a liquid propellant rocket, the fuel and oxidiser are fed into a thrust chamber through an injector, by either a pressure or pump feed system, where they are mixed in the thrust chamber to form a combustible mixture. Liquid systems are highly efficient but are mechanically complex and costly compared to the other systems.

Solid propellant rockets store the propellant in the combustion chamber as a cast grain, consisting of both the fuel and oxidiser intimately mixed in the solid phase. Combustion occurs in the grain

ports once ignition temperature is reached. While simple in construction with dense propellant storage, they are inherently dangerous and cannot be shut down once ignited (Sutton and Biblarz, 2001).

Hybrid propellant rockets, being the focus of this work, store the propellants in two different physical phases with the general configuration being a liquid or gaseous oxidiser and a solid fuel. Typically, the oxidiser is fed into the combustion chamber through an injector, by means of either a pressure or pump feed system. The fuel grain, housed within the combustion chamber, contains one or more axial combustion ports that generate fuel vapour to combust with the oxidiser in a turbulent diffusion flame. A more detailed description of hybrid rocket propulsion is given in Chapter 2. The advantages of hybrid rocket propulsion systems are:

1. Safety: the fuel grain is inert, and the system is non-explosive due to the separation of fuel and oxidiser
2. Simplicity: they are not as mechanically complex as liquid systems
3. Throttling and shut down: the motor can be throttled and shut down by modulating the oxidiser mass flow rate
4. Grain robustness: fuel grain cracks are not catastrophic such as in solid rockets
5. Propellant versatility: the range of propellants is broader than for solid and liquid systems
6. Chamber pressure sensitivity: the regression rate has weak dependence on chamber pressure allowing optimisation of operating pressure
7. Temperature tolerance: ambient launch temperature variations have little effect on operating chamber pressure since the temperature effect on burn rate is small
8. Low cost: lower system cost due to less plumbing and inert propellant
9. Performance: typically better performance compared to solids and specific impulses close to liquids. Energetic metal additives may also be added to the fuel grain

Due to the propellant versatility, inherent safety, throttling, and shut down/restart capability, hybrid propulsion systems can be used in many applications, including sounding rockets, tactical and target missiles, launch vehicle boosters, upper stage engines, and satellite propulsion. There are also disadvantages with the use of hybrid rocket propulsion systems, including:

1. Low regression rate: the fuel burn rate is characteristically low for classical fuels, therefore, multiple ports are needed to increase the burning surface area
2. Low bulk density: multiple ports lead to relatively low volumetric fuel loading or bulk density. A fuel sliver is also retained in the combustion chamber at the end of the burn
3. Combustion efficiency: the nature of the diffusion flame typically results in a lower degree of mixing and hence lower impulse efficiency

4. O/F ratio shift: during the burning process the port diameter increases causing an O/F ratio shift which can lower motor performance
5. Slower transients: the ignition transient and throttling thrust response are slower

1.2. Sounding Rockets

A sounding rocket is a vehicle specifically designed to carry scientific instruments into the upper atmosphere for the purpose of conducting research. Sounding rockets are launched on parabolic sub-orbital trajectories, and can provide direct access to the atmospheric region that cannot be reached by air balloons, with a maximum altitude of 40 km, or satellites with a minimum altitude of 200 km (Seibert, 2007). Along with enabling upper atmospheric research, they are also used for testing of rocket prototypes, sub-systems, and instruments prior to use on satellites. With substantially reduced mission costs and turn-around times compared to orbital missions, they provide cost effective access to the upper atmosphere and space.

The typical mission sequence, shown in Figure 1-2, involves the launch of the rocket followed by separation of the booster from the payload which falls back to Earth. The payload follows a sub-orbital parabolic trajectory with a long apogee duration during which the experiment is performed. The payload then falls back to Earth via a parachute and is recovered.

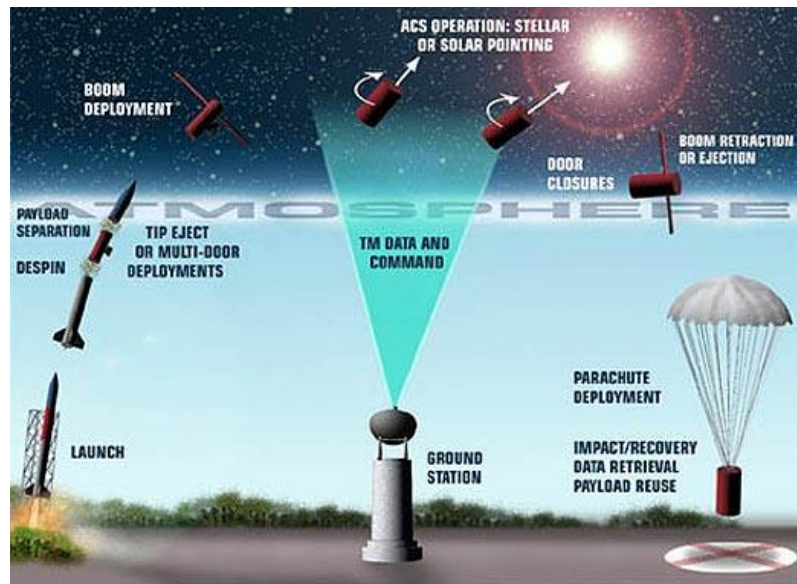


Figure 1-2: Flight profile of a sounding rocket (Marconi, 2004).

1.3. Phoenix Hybrid Sounding Rocket Programme Overview

The Phoenix Hybrid Sounding Rocket Programme (HSRP) was initiated by the University of KwaZulu-Natal (UKZN) in 2010 within Mechanical Engineering's Aerospace Systems Research Group (ASReG) (Brooks et al., 2010). It started against the backdrop of the South African government's prioritisation of skills and resource development in space research, which has also

seen the establishment of a centralised South African National Space Agency (SANSA) and the deployment of several small satellites.

South Africa does not offer a sounding rocket launch service to support the African continent's scientific endeavours. The primary aim of the HSRP is to produce a series of indigenous civilian rockets, with incrementally improved apogees, the eventual outcome of which will be a 100 km sounding rocket capability. Secondary objectives of the programme include advancing hybrid propulsion technology and promoting human capital development in South Africa (Brooks et al., 2010). Eventually, the HSRP aims to provide the capability for weather and physics related research in the upper atmosphere, to test satellite systems in a micro-gravity environment, and to test rocket technologies in flight prior to deployment.

Four graduate students have contributed to the HSRP to date, namely Geneviève (2013), Chowdhury (2012), Leverone (2013) and Balmogim (2016). Geneviève and Chowdhury developed the programme's first hybrid rocket, called the Phoenix-1A (P-1A), as a technical demonstrator. Geneviève (2013) developed a Hybrid Rocket Performance Code (HRPC) for motor design and performance analysis. Chowdhury (2012) developed a six degree-of-freedom flight dynamics simulator known as the Hybrid Rocket Performance Simulator (HYROPS). These two codes can be used together to design and optimise a hybrid rocket. Leverone (2013) designed a 100 km apogee hybrid sounding rocket, called the Phoenix-2A (P-2A), although it remained a theoretical investigation. Balmogim (2016) developed the Phoenix-1B Mk I (P-1B Mk I) hybrid rocket with the intent of improving the design and performance of the P-1A. This would become the workhorse vehicle to serve as a reliable platform for future development.

Undergraduate students have also contributed to the programme through capstone design and research projects. A Mobile Rocket Launch Platform (MRLP) was designed and manufactured in 2011 to perform static testing and launching of rockets. It consists of all the required Ground Support Equipment (GSE), a launch gantry, stabilising arms and a propellant tank inverting system. A laboratory-scale test facility was developed in 2010, recently upgraded in 2017, to support the development of the P-1A and has since enabled research into metal fuel additives and motor throttling (Maharaj, 2018; Velthuysen, 2018).

The HSRP has developed and tested two hybrid sounding rockets to date with the development of third rocket, designated as the Phoenix-1B Mark II (P-1B Mk II), the focus of this work. The Mk II of the P-1B workhorse vehicle thus builds upon its Mk I predecessor in several ways whilst maintaining the same configuration and similar fabrication methods to ensure modularity between them. This vehicle forms an iterative step in the progress towards an eventual 100 km apogee hybrid sounding rocket.

1.4. Problem Statement and Research Objectives

As the next step in the HSRP, the P-1B Mk II was required to achieve a higher apogee target while also improving on the previous vehicle performance and technology. The primary aim of this work is to design the hybrid propulsion system of the P-1B Mk II rocket to achieve a 35 km apogee, using the P-1B Mk I as a baseline vehicle, and test and launch the vehicle to validate its performance. The research is therefore intended to improve the apogee performance of the P-1B Mk I through refinements to the motor, designated as the PV-3, while using similar fabrication techniques and the same motor calibre. The project workload was split into two, with the current work focusing on the propulsion system and hybrid rocket motor, whilst the oxidiser tank development, vehicle aerodynamics and airframe structure were undertaken by Williams (2018).

In light of the above, the proposed methods of improving the apogee performance include the use of energetic metal additives in the fuel grain, improving the performance of the motor, and improving the vehicle propellant mass fraction. The addition of energetic metal additives to the fuel grain has the potential to increase the performance of the motor and reduce the optimal oxidiser-to-fuel (O/F) ratio, resulting in a lower liquid oxidiser mass fraction, and thus lower inert vehicle mass, improving flight performance. Motor performance must be improved significantly to achieve the apogee requirement, with the delivered total impulse of the motor a critical parameter given the fixed motor calibre. The vehicle inert mass must be reduced by optimising airframe components with respect to mass and the development of a composite oxidiser tank, designed by Williams (2018). The primary research objectives of this study are therefore as follows:

1. Investigate the effects and feasibility of energetic metal additives on motor design and performance
2. Specify the Phoenix-1B Mk II propulsion system design to meet the apogee requirement of 35 km
3. Design and manufacture the PV-3 hybrid rocket motor
4. Static test the PV-3 hybrid rocket motor to validate performance

For reasons of cost and modularity, the PV-3 motor calibre was fixed by the availability of extruded aluminium tubing. Motor throttling was preliminarily found to provide a negligible apogee improvement and was not pursued. The use of energetic metal additives was considered in the development of the P-1B Mk I, but was abandoned due to lack of empirical regression rate data. Their use is investigated further in this work, implemented and tested. The significance of this work lies in quantifying the effect of energetic metal additives on vehicle performance, and in articulating a methodology for designing a hybrid rocket motor with a fixed diametrical constraint.

1.5. Dissertation Outline

A detailed description of hybrid rocket propulsion systems is given in Chapter 2. It includes a brief historical perspective and recent developments in the field. The basic configurations, operation and combustion models of a hybrid propulsion system are described followed by the relevant theory and critical performance metrics. Hybrid propellants are discussed including a review of energetic metal additives.

Chapter 3 briefly summarises the work done on the previous Phoenix rockets. The design requirements and constraints for the P-1B Mk II are given, derived from the mission statement and the performance of previous rockets. The overall project methodology is presented which shows the sequential steps taken to arrive at the final motor and vehicle design. Use of the Hybrid Rocket Performance Simulator (HYROPS) is briefly described, which was the primary tool used for iterative system design.

Chapter 4 describes the preliminary system design of the P-1B Mk II. The effects of energetic metal additives on motor and vehicle design and performance are presented, concluding with the selected propellant composition. The propulsion system design follows, including final specifications.

Chapter 5 addresses the motor component design and manufacture. The analytical and numerical methods used to design the combustion chamber, injector bulkhead, injector, and feed system are described. The chapter focuses on the design of the injector since it is critical to achieving desired motor performance. The fuel grain cartridge development with aluminium additive is also given.

Chapter 6 describes the design of the nozzle which was adapted from the PV-2 motor nozzle, with an updated geometry and loading conditions. A thermal-structural numerical analysis was performed to verify the nozzle design.

Chapter 7 describes the static testing performed on the PV-3 hybrid rocket motor. An igniter test, cold flow test, and hot-fire test were performed. The test setup, procedure and equipment are described along with results. The cold flow test indicated the need to revise the injector design, with the revision methodology included.

The dissertation is concluded in Chapter 8 with a discussion of problems and recommendations for future work.

2. HYBRID ROCKET PROPULSION

2.1. Introduction

The initial development of hybrid rocket propulsion was slow compared to the rapid advancement of solid and liquid systems in the past century. This was primarily due to technological barriers unique to hybrids, however, after recent advances numerous hybrid propulsion projects have started in the past decade, with a variety of potential applications.

Hybrid rocket motors were first developed in Russia and Germany in the 1930s, and subsequently in the United States in the 1940s. The first hybrid sounding rockets were developed in France and Sweden in the 1960s, while target drones for military applications were also explored in the United States. Several companies developed larger scale hybrid motors in the United States during the 1980s and 1990s, primarily using liquid oxygen (LOX) and Hydroxyl Terminated Polybutadiene (HTPB) as propellants. The American Rocket Company (AMROC) has developed the largest hybrid rocket motors to date, recording thrusts up to 1 MN, with the original goal of replacing the solid boosters of the Space Shuttle (Sutton and Biblarz, 2001). Lockheed Martin and the National Aeronautics and Space Administration (NASA) worked on a hybrid sounding rocket project together, culminating in the launch of a LOX/HTPB rocket to 70 km (Arves et al., 2003). The most successful demonstration of a hybrid rocket motor to date was the launch of SpaceShipOne to 100 km in 2004 by Virgin Galactic, utilising HTPB and nitrous oxide (Virgin Galactic, 2018).

Although various oxidiser and fuel combinations were tried, hybrids were unable to compete with the well-established systems of solids and liquids due to the recurring problems of low regression rates, low thrust levels attainable, oxidiser valve freezing, combustion instabilities, and fuel grain complexity.

The primary problem for classical hybrid rocket motors was the low fuel regression rates, typically less than one-third that of solid rocket motors, due to the diffusion-limited combustion process. This has led to various attempts at increasing the regression rate which have consequently compromised the inherent safety and simplicity of hybrid motors. A common solution was the use of complex multi-port fuel grain designs to increase the burning surface area, which resulted in reduced volumetric loading, reduced performance, and compromised structural integrity. Fuel additives such as energetic metal particles and oxidising agents have also been tried, although they can introduce toxicity and explosion risks (Pastrone, 2012).

Other methods of improving hybrid motor performance include vortex injectors, turbulence generators in the form of annular discs or diaphragms, and non-conventional fuel grain geometries. These methods aim to improve the regression rate by modifying the internal flow

structure and increasing combustion efficiency to improve fuel surface heat transfer (Pastrone, 2012). However, the increase in fuel heat transfer increases the fuel mass flux which tends to reduce the temperature gradient at the surface. Known as the blocking effect, this constrains the heat transfer rate, limiting the effectiveness of the approach to maximum regression rate increases of 30% to 50% (Karabeyoglu et al., 2001).

2.2. State of the Art

A major breakthrough in overcoming low regression rates problem was made by researchers at Stanford University. Karabeyoglu et al. (2001) postulated that the best approach was to formulate a fuel that would generate mass transfer by mechanical means in addition to direct gasification. They discovered high regression rate liquefying fuels with low viscosity and surface tension melt layers that allow the entrainment of liquid droplets into the gas stream due to the instability of the liquid layer. This leads to higher fuel regression rates and thus higher fuel mass flow rates (Cantwell et al., 2010). These fuels therefore avoid the need for regression rate enhancement methods which compromise the inherent safety, simplicity and cost-effectiveness of hybrids.

Karabeyoglu et al. (2001) found that paraffin waxes and polyethylene waxes had higher predicted regression rates than other classical hybrid fuels. During laboratory-scale testing in 1998, regression rates of 3 to 4 times the classical rate were observed. Further testing was performed by NASA, Stanford University, and the Space Propulsion Group (SPG) to establish design guidelines for stable and efficient single-port hybrid motors, conducting over 500 tests of paraffin-based fuels with different oxidiser and scale combinations. They concluded that the regression rate behaviour successfully scaled up to chamber pressures and mass fluxes of operational systems with a weak dependence of regression rate on grain length. The paraffin-based fuels were found to reliably ignite and exhibit stable combustion over a range of mass fluxes and oxidisers (Cantwell et al., 2010).

The development of high regression rate, liquefying fuels by Stanford researchers in the 1990s made the use of simple single-port fuel grain configurations a feasible option, as they could provide the required thrust levels required for a range of applications. This development was the catalyst behind the revitalisation in hybrid rocket motor research and development. Numerous universities worldwide have since started hybrid rocket research programmes, primarily due to the inherent safety and simplicity of hybrid motors, contributing to the advancement of hybrid motor technology. This has resulted in several hybrid sounding rocket launches such as the Stratos I, II and III by Delft University of Technology (Delft University of Technology, 2018) and the HEROS 3 by the University of Stuttgart, reaching a record apogee of 32.3 km (University of Stuttgart, 2018).

Commercial companies have also seen the potential of hybrid propulsion for sub-orbital and orbital launch vehicles, and space tourism. Examples include, the Peregrine hybrid sounding rocket by NASA (Dyer et al., 2007), and orbital launch vehicle developments such as the ERIS by Gilmour Space Technologies (Gilmour Space Technologies, 2018) and Intrepid-1™ by Rocket Crafters (Rocket Crafters, 2018). Virgin Galactic is continuing its development of sub-orbital space planes for tourism with the SpaceShipTwo (Virgin Galactic, 2018). Hybrid propulsion is also now being considered for solar system exploration missions such as orbit insertion motors, Mars ascent vehicles and satellite attitude control (Karp et al., 2018).

2.3. Configuration and Operation

Hybrid rockets are inherently safer than liquid and solid rockets since their propellants are stored in different phases. In a classical hybrid rocket, the oxidiser is in the liquid phase and the fuel is in the solid phase, which makes the rocket less susceptible to a chemical explosion. The typical hybrid rocket motor, shown in Figure 2-1, consists of a gas pressurisation system, propellant tank, oxidiser feed system with control valve, injector, igniter, combustion chamber with a solid fuel grain, and a nozzle. The basic operation of the motor starts with the injection of the oxidiser into the combustion chamber via the feed system. The oxidiser is atomised by the injector, mixes with the fuel vapour from the fuel grain and is ignited by an igniter. Combustion occurs along the ports in the fuel grain and the exhaust gases are expanded through the nozzle to generate thrust.

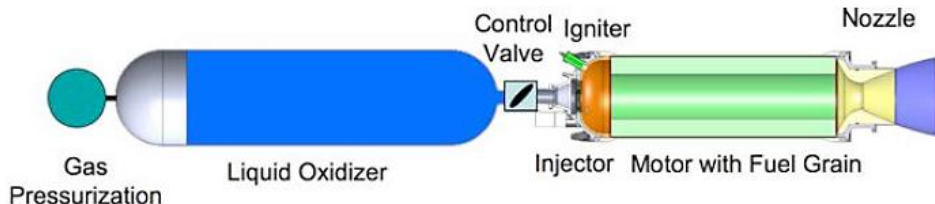


Figure 2-1: Typical hybrid rocket motor schematic (Cantwell et al., 2010).

The propellant tank stores the oxidiser as either a gas or a liquid. The oxidiser is fed to the combustion chamber by means of either a gas pressurisation system, a pump feed system or under its own pressure. The gas pressurisation system, consisting of a pressurant tank, maintains the propellant tank pressure with helium or nitrogen. A pump feed system is used to directly pump the oxidiser from the propellant tank to the combustion chamber but is a more complex system used on larger rockets. A self-pressurising oxidiser, such as nitrous oxide, is able to maintain the propellant tank pressure due to its high vapour pressure at room temperature. This is referred to as a blowdown process and is the simplest and most cost-effective of the systems.

The oxidiser feed system transfers the oxidiser to the combustion chamber and includes a control valve that allows the motor to be shut down and restarted, and that can throttle the motor by

modulating the oxidiser flow rate. The oxidiser passes through an injector prior to the combustion chamber that atomises the oxidiser. The pre-combustion chamber is located upstream of the fuel grain and enhances oxidiser vaporisation. The cylindrical fuel grain is housed within the combustion chamber and may include one or more combustion ports, as shown in Figure 2-2. The oxidiser and fuel combust along the length of the fuel grain ports. The fuel grain is surrounded by a thermal liner to minimise the heat transferred to the outer chamber casing. Aft of the fuel grain is the post-combustion chamber which assists in mixing of the oxidiser and fuel to ensure complete combustion. The nozzle then expands the exhaust products to ambient pressure.

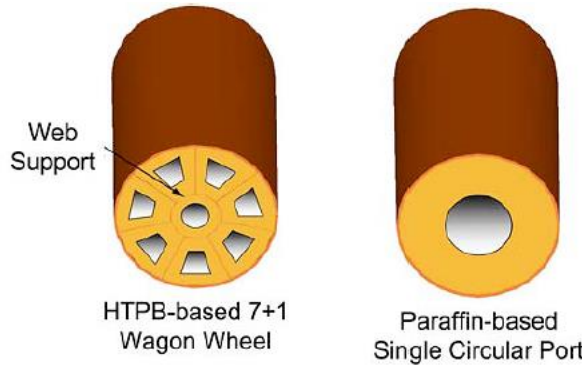


Figure 2-2: A multi-port, wagon wheel fuel grain and a single port fuel grain (Cantwell et al., 2010).

2.4. Fundamental Theory and Performance Characteristics

The typical performance parameters associated with a rocket motor are the thrust (F), thrust coefficient (C_f), effective exhaust velocity (c), characteristic velocity (c^*), and specific impulse (I_{sp}). Thrust is a reaction force experienced by the vehicle structure due to the ejection of matter at high velocity. The thrust force, found using Equation 2-1, can be divided into both the momentum thrust from the ejected propellant and the pressure thrust due to the difference between nozzle exit pressure (p_e) and ambient pressure (p_a). The pressure thrust varies due to the change in ambient pressure with increasing altitude. The thrust coefficient, found with Equation 2-2, depends on the nozzle characteristics and is independent of the rest of the rocket.

$$F = \dot{m}v_e + (p_e - p_a)A_e \quad (2-1)$$

$$C_f = \frac{F}{p_c A_t} \quad (2-2)$$

where \dot{m} is the propellant mass flow rate, v_e is the exit velocity, A_e is the nozzle exit area, A_t is the nozzle throat area, and p_c is the chamber pressure. The effective exhaust gas velocity is defined as the average equivalent velocity at which the propellant is ejected, given in Equation 2-3. The characteristic velocity, given in Equation 2-4, relates to the combustion efficiency and is

commonly used for comparing the relative performance of different chemical propulsion system designs. It focuses on propellant and chamber performance and is independent of the nozzle. Typical values of combustion efficiency range from 96% to 98% (Humble et al., 1995).

$$c = v_e + \frac{(p_e - p_a)A_e}{\dot{m}} \quad (2-3)$$

$$c^* = \frac{p_c A_t}{\dot{m}} \quad (2-4)$$

The specific impulse (I_{sp}) is the total impulse (I_{tot}) per unit weight of the propellant flow (m_{prop}), or the thrust as a function of the propellant mass flow rate (\dot{m}). It is commonly used in propulsion system design as a measure of performance. It is given in seconds and describes the time that the rocket can deliver thrust equal to the weight of the total propellant mass under Earth's gravitational acceleration. Specific impulse values for hybrid rockets typically lie between 290 s and 350 s (Humble et al., 1995). Equation 2-5 gives the specific impulse for constant propellant mass flow rate and constant thrust:

$$I_{sp} = \frac{I_{tot}}{m_{prop}g} = \frac{F}{\dot{m}g} \quad (2-5)$$

2.5. Hybrid Combustion Model and Internal Ballistics

The combustion process of a hybrid rocket motor, depicted in Figure 2-3 and Figure 2-4, starts with the firing of the igniters in the pre-combustion chamber. The generated heat vaporises the exposed surface of the solid fuel after which the oxidiser is passed through an injector into the pre-combustion chamber. The injector atomises the oxidiser flow which is decomposed by the heat of the igniters. After the vaporised fuel and atomised oxidiser combust, a turbulent diffusion flame is set up within the boundary layer along the combustion port. Combustion is sustained by diffusion of the vaporised oxidiser flowing through the port and vaporised fuel from the solid fuel surface into the flame zone, as shown in Figure 2-3. The fuel is vaporised by the heat generated from the flame zone. Combustion is maintained until either the oxidiser or fuel is depleted (Humble et al., 1995).

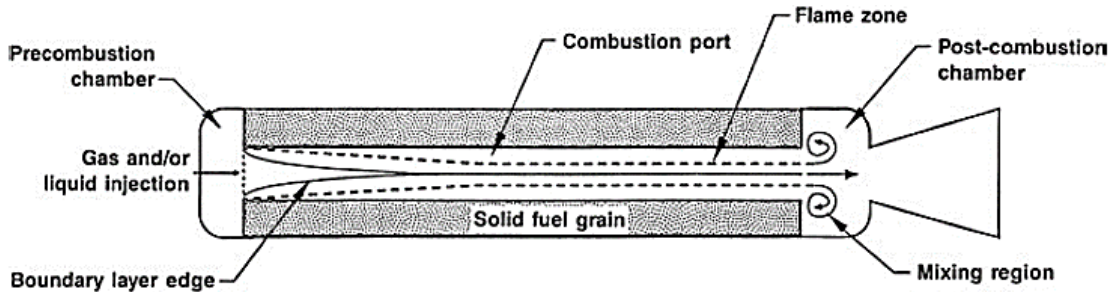


Figure 2-3: Schematic of turbulent boundary layer formation in a hybrid motor (Altman and Holzman, 2007).

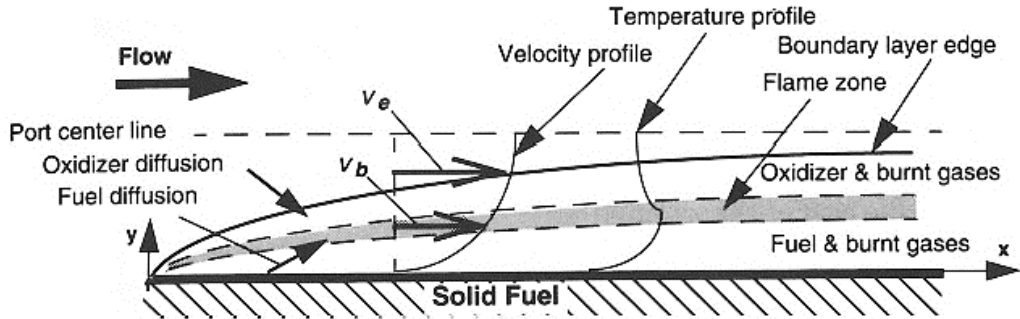


Figure 2-4: Schematic of diffusion-controlled combustion zone in a hybrid motor (Humble et al., 1995).

The fundamental characteristic of the hybrid combustion model is the fuel regression rate, which has a direct impact on the configuration and performance of the motor. Accurate regression rate data is necessary to compare propellants, fuel grain sizes, predict performance, and to prevent burn-throughs. Most of the theories developed to analyse hybrid fuel combustion are based on a regression rate law that relates the local instantaneous fuel burning rate to the local instantaneous mass flux through the fuel port via an empirically-derived power law (Zilliac and Karabeyoglu, 2006). The two main regression rate theories are: the classical diffusion-limited theory and the non-classical liquefying droplet entrainment theory.

2.5.1. Classical Regression Rate Theory

The first comprehensive theory to describe the hybrid combustion mechanism was developed by Marxman and Gilbert (1963). They described the hybrid combustion model as a turbulent diffusion flame within a boundary layer, depicted in Figure 2-4. The fuel enters the boundary layer as a result of sublimation at the wall surface and oxidiser enters from the free stream flow. Marxman et al. (1963) derived a hybrid regression rate law based on this model by assuming that the regression rate is controlled by heat transfer from the diffusion-limited flame to the fuel surface.

For a non-metallised fuel, hybrid motors typically operate in the diffusion region, depicted in Figure 2-5, where convective heat transfer dominates. Here the regression rate depends on the total mass flux and is independent of chamber pressure. However, the regression rate can be affected by chamber pressure over a range of mass fluxes from the effects of kinetics and radiation. When the mass flux is high, the combustion is dominated by chemical kinetics, and when it is low, radiative heat transfer dominates convection (Humble et al., 1995).

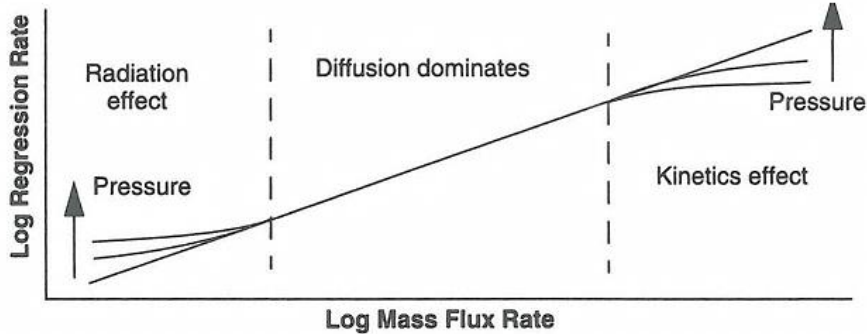


Figure 2-5: Effect of pressure on regression rate (Humble et al., 1995).

From an energy balance at the fuel grain surface, the local instantaneous fuel regression rate of a hybrid motor with negligible radiative heat transfer is expressed as follows:

$$\dot{r} = 0.036 \frac{G^{0.8}}{\rho_f} \left(\frac{\mu}{x} \right)^{0.2} \beta^{0.23} \quad (2-6)$$

where G is the total propellant mass flux, ρ_f is the solid fuel density, μ is the combustion gas viscosity, x is the axial location along the port, and β is the blowing coefficient. The radiative heat transfer term is excluded for fuels with no metal additives. Equation 2-6 indicates that the regression rate is strongly dependent on G and weakly dependent on x and β for a non-metallised system. The regression rate is not explicitly dependant on chamber pressure while metallised fuels exhibit a strong pressure dependence (Sutton and Biblarz, 2001).

Equation 2-6 is not accurate for rocket design purposes as the expression was developed for a slab motor. Hence, it is standard practice today to use the simplified regression rate law given in Equation 2-7, and consisting of an empirically derived coefficient and exponents:

$$\dot{r} = a G^n x^m \quad (2-7)$$

where the coefficient a and the exponents n and m are dependent on specific propellant combinations and are determined experimentally. The effects of β , ρ_f and μ are lumped into the coefficient a . Equation 2-7 can be further simplified into the more commonly used Equation 2-8 for a motor of a given grain length. The exponent m is neglected as the regression rate has a weak dependence on x (Sutton and Biblarz, 2001). Conveniently, the oxidiser mass flux (G_o) is used instead of the total mass flux since it is much larger than the fuel mass flux. The regression rate is therefore solely dependent on the oxidiser mass flow rate which can be determined by dividing the oxidiser mass flow rate (\dot{m}_o) by the port area (A_p):

$$\dot{r} = a G_o^n = a \left(\frac{\dot{m}_o}{A_p} \right)^n \quad (2-8)$$

2.5.2. Non-classical Regression Rate Theory

Karabeyoglu et al. (2002) extended the classical hybrid combustion theory to solid fuels that form a liquid layer on their burning surface, as illustrated in Figure 2-6. This includes cryogenic fuels such as solid pentane and non-cryogenic fuels such as paraffin wax. These fuels form a hydrodynamically unstable liquid layer over the burning surface during combustion, from which liquid droplets are entrained from the liquid layer into the gas stream. The droplets are formed due to the liquid layer instability and high velocity gas stream through the port. The degree of instability increases with decreasing viscosity and surface tension of the liquid layer (Karabeyoglu et al., 2001). Since droplet entrainment is not limited by diffusive heat transfer to the fuel, this mechanism is not limited by the blocking effect.

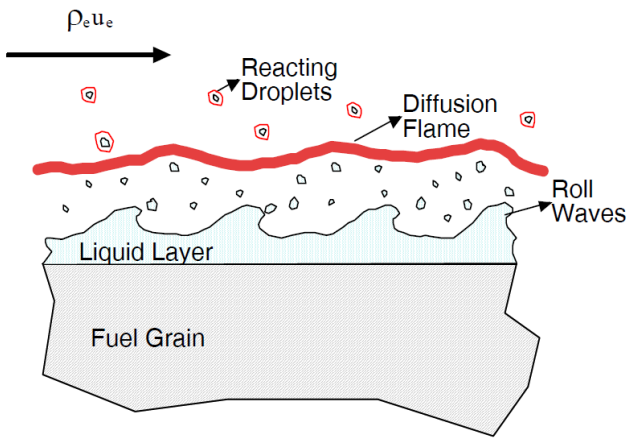


Figure 2-6: Liquid layer instability and droplet entrainment mechanism (Karabeyoglu, 2012).

The higher regression rates of these fuels are due to the mass transfer of the droplet entrainment mechanism in addition to the classical fuel vaporisation mechanism. Therefore, the total regression rate is the sum of the evaporative regression rate (\dot{r}_v) due to fuel vaporisation mechanism and the entrainment regression rate (\dot{r}_{ent}) due to the droplet entrainment mechanism:

$$\dot{r} = \dot{r}_v + \dot{r}_{ent} \quad (2-9)$$

The following modifications are required in order to apply the classical hybrid combustion theory to include the formation of liquid layer instabilities and entrainment of liquid droplets (Karabeyoglu et al., 2001):

1. The effective heat of gasification is reduced since the energy required for evaporation of the fuel at the surface is decreased due to droplet entrainment from the liquid layer
2. The blocking factor is altered to consider two-phase flow. The effect of the liquid droplets on the momentum and energy transfer is ignored and it is assumed that the evaporation of the droplets only occurs above the flame sheet

3. There is an increase in the heat transfer from the flame to the surface due to the increase in surface roughness from ripples on the liquid layer

A detailed derivation of the energy balance at the liquid-gas interface is provided by Karabeyoglu et al. (2001), but is beyond the scope of this work. The simplified entrainment regression rate, given in Equation 2-10, can be restated in terms of the total mass flux and the total regression rate:

$$\dot{r}_{ent} = a_{ent} \frac{G^{2\hat{\alpha}}}{\dot{r}^{\hat{\beta}}} \quad (2-10)$$

where a_{ent} is the entrainment parameter which is a function of the properties of the selected propellant and the average gas density in the chamber, and $\hat{\alpha}$ and $\hat{\beta}$ are the dynamic pressure and thickness exponents, respectively. Equations 2-9 and 2-10 form part of a set of non-linear algebraic equations that can be solved for a given propellant combination. This provides the total regression rate as a function of axial location and total mass flux.

Table 2-1 gives the regression rate constants for various fuels with nitrous oxide. Figure 2-7 plots the average regression rate for HTPB and SP-1A paraffin wax, Stanford's proprietary formulation, with gaseous oxygen over a range of oxidiser mass fluxes, illustrating the difference in regression rate between classical and liquefying fuels.

Table 2-1: Typical regression rate coefficients and exponents for various hybrid fuels with nitrous oxide. $[\dot{r}]$ = mm/s and $[G_o]$ = kg/m²-s.

| Fuel | <i>a</i> | <i>n</i> | Reference |
|---------------------|----------|----------|--------------------------|
| Paraffin wax | 0.155 | 0.5 | (McCormick et al., 2005) |
| HTPB | 0.198 | 0.33 | (Lohner et al., 2006) |
| HDPE | 0.104 | 0.35 | (Lohner et al., 2006) |
| PMMA | 0.111 | 0.38 | (Lohner et al., 2006) |
| Sorbitol | 0.286 | 0.31 | (Lohner et al., 2006) |

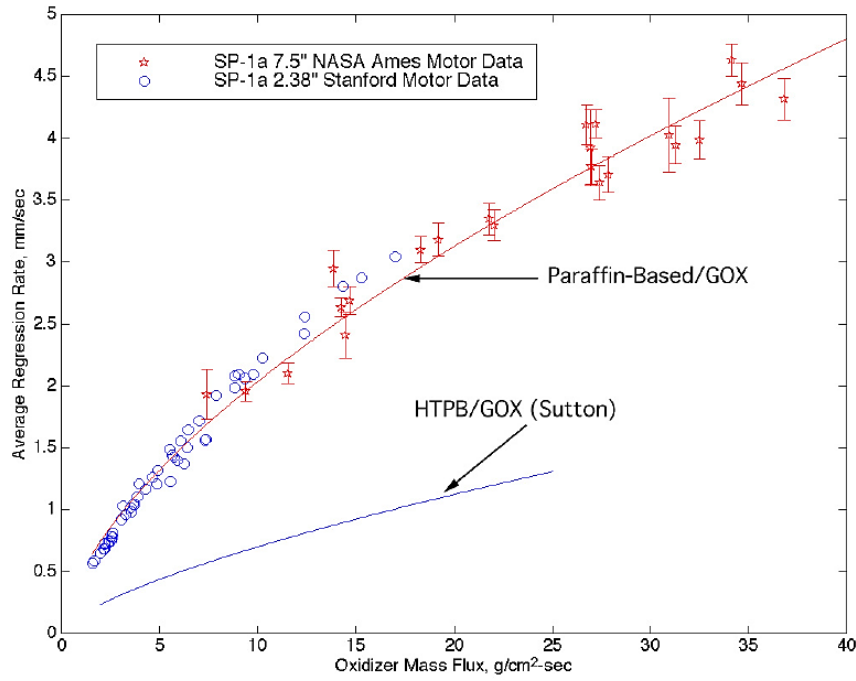


Figure 2-7: Regression rate data of paraffin wax (SP-1A) and HTPB with gaseous oxygen over a range of oxidiser mass fluxes (Karabeyoglu et al., 2003).

2.6. Combustion Instabilities

Combustion instabilities occur when fluctuations in pressure, temperature and velocity interact with the natural frequencies of the oxidiser feed system, or chamber acoustics, resulting in periodic superimposed oscillations. If not controlled, they can cause large pressure spikes and thrust oscillations, resulting in vibrational and thermal loads on the rocket. Instability is characterised by organised pressure oscillations at well-defined intervals that exceed 5% of the mean chamber pressure during steady operation (Sutton and Biblarz, 2001). The mechanisms that have been postulated to cause hybrid combustion instabilities include (Greiner and Frederick Jr, 1993):

1. Time lag of vaporisation and combustion of the injected oxidiser
2. Fuel grain chuffing
3. Pressure coupled combustion in high or low total mass flux regimes
4. Vortex shedding
5. Shear layer/acoustic interactions in the aft mixing chamber
6. Time dependent nature of boundary layer leading edge
7. Hydrodynamic feed system coupling

The two general types of combustion instabilities experienced by hybrid motors are low frequency (non-acoustic) and high frequency (acoustic) instabilities. Low frequency instabilities are commonly experienced by hybrid motors whose pressure fluctuations are in the range of 10 to 50

Hz. They are broadly classified into two types: Interactions between the turbulent boundary layer combustion and chamber fluid dynamic behaviour, and feed system coupled instability (Waxman, 2014). The cause of the first type is based on the complex coupling of the thermal transients in the solid fuel, the wall heat transfer blocking due to the fuel regression rate, and the transients in the boundary layer. The mechanism which generates the low frequency pressure oscillations is due to the coupling of the thermal lags, gas phase combustion, and gas dynamics subsystems (Karabeyoglu et al., 2007).

Feed system coupled instabilities are due to the hydrodynamic interaction between the feed system and the combustion chamber. The driving mechanisms include oxidiser flow rate dependency on chamber pressure, oxidiser and fuel vaporisation delays, and compressibility of fluid in the feed line (Karabeyoglu et al., 2007). Methods of limiting these instabilities include (Karabeyoglu et al., 2007; Waxman, 2014):

1. Minimising vaporisation time of the oxidiser
2. Avoiding a “hydraulic flip” in the injector in which the flow never reattaches
3. Ensuring a high injector pressure drop (15% to 20% of chamber pressure)
4. Using an isolating element on the feed line
5. Decreasing compressibility in the feed line

High frequency acoustic instabilities occur when the flame in the boundary layer becomes unstable, causing resonance between the combustion process forces and the acoustic modes of the combustion chamber. There are three acoustic modes: longitudinal, tangential and radial, with only the longitudinal mode observed in hybrids (Sutton and Biblarz, 2001). These instabilities can be removed by stabilising the combustion in the boundary layer through ensuring that the injector flow field forms a sufficiently large hot-gas recirculation zone in the pre-combustion chamber. This can be achieved using an axial injector.

Combustion instabilities have also been observed on motors with high initial oxidiser mass fluxes, associated with inadequate flame-holding in the fuel grain port. Combustion is then dominated by chemical kinetics rather than convective heat transfer, and the regression rate increases its dependency on chamber pressure. This can result in structural failures due to over-pressurisation, burn-through due to higher heat fluxes, and lower combustion efficiencies. Although there is no known theoretical oxidiser mass flux limit for combustion stability, no single-port N₂O/paraffin wax laboratory-scale motors have shown stable combustion for oxidiser mass fluxes greater than 650 kg/m²-s (Zilliac et al., 2012; Werner et al., 2016).

2.7. Hybrid Propellants

The number of oxidisers and fuels that have been tested for hybrid propulsion systems far exceeds that of solid and liquid systems due to the two-phase nature of the propellant combination. The most common combination is a liquid oxidiser and a solid fuel, with the reverse also tried. Common oxidisers include liquid or gaseous oxygen (LOX or GOX), nitrous oxide (N_2O), hydrogen peroxide (H_2O_2) and nitrogen tetroxide (N_2O_4). Fuels are classified as either classical or liquefying. Classical fuels include hydroxyl-terminated polybutadiene (HTPB), polymethyl-methacrylate (PMMA), polyethylene (PE), and sorbitol. Liquefying fuels include paraffin wax, solid pentane, and solid methane. HTPB, paraffin waxes, and sorbitol are cast fuels and thus offer the advantage of allowing performance enhancing additives.

In choosing a propellant combination, one must consider both quantitative performance metrics such as specific impulse delivered and qualitative factors such as ease of handling, toxicity, and ignition. Figure 2-8 shows the specific impulse and density impulse over a range of O/F ratios for several propellant combinations. The LOX/paraffin wax combination provides the highest specific impulse performance at a low optimal O/F ratio. However, it has a steep curve and thus O/F ratio shift is limited. The N_2O /paraffin wax combination has a relatively lower specific impulse but a weaker dependence on O/F ratio. This allows near optimal performance during motor burn for blowdown systems with large O/F ratio shifts. It has a high optimal O/F ratio of 8, however, resulting in a large liquid propellant fraction.

The P-1B Mk II was specified to utilise nitrous oxide and paraffin wax as the oxidiser and fuel respectively, with energetic metal additives, as described in the following sections.

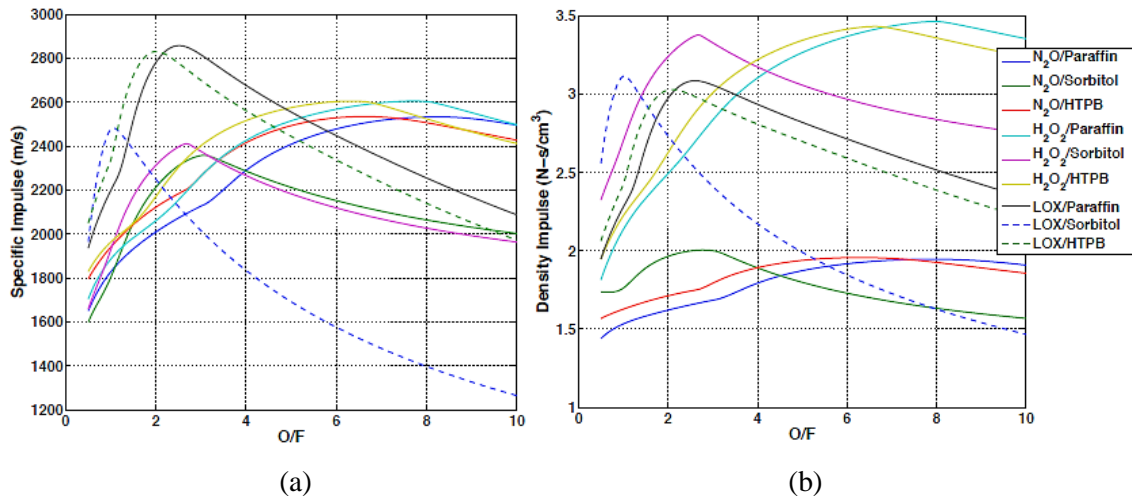


Figure 2-8: (a) Specific impulse in units of m/s and (b) density impulse versus O/F ratio for different propellant combinations (Dyer et al., 2007).

2.7.1. Nitrous Oxide

Nitrous oxide (N_2O) is a chemical compound consisting of a nitrogen molecule and an oxygen atom which decomposes exothermically to form gaseous nitrogen and oxygen as products, from which the oxygen is used to support combustion. Pressurised nitrous oxide is a subcritical fluid at room temperature resulting in both gas and liquid phases. Its high vapour pressure at room temperature (52.4 bar at 20 °C) makes it self-pressurising, allowing a simple blow down oxidiser delivery system that eliminates the additional weight, complexity and cost of a pressurisation or pump feed system. It is inexpensive, commonly available, non-toxic, easy to handle, and storable at room temperature.

Disadvantages with the use of nitrous oxide include its relatively low specific impulse and density impulse performance, its high operating O/F ratio, its high dependency of density and pressure on temperature, and its risk of self-decomposition. This risk of decomposition can be mitigated by supercharging the tank ullage with an inert gas such as helium or nitrogen (Karabeyoglu et al., 2008). This also helps to prevent cavitation in the feed system and improves motor performance by allowing higher chamber pressures. The inherent advantages of nitrous oxide generally dominate the disadvantages for small hybrid propulsion systems, which makes the oxidiser desirable despite having inferior performance compared to other oxidisers. It is therefore the most popular oxidiser used in amateur rocketry and sounding rocket programmes, where operational simplicity and safety are critical.

2.7.2. Paraffin Wax

Paraffins, or alkanes, are part of a family of homologous straight-chain, saturated hydrocarbons with the general formula $C_n\text{H}_{2n+2}$. Paraffin waxes are mixtures of mainly normal alkanes, usually greater than 75%, with the rest consisting of iso-alkanes, cycloalkanes and alkyl-benzene (Himran et al., 1994). Depending on the number of carbon atoms, they are either liquid or waxy solids at room temperature. Paraffin waxes are relatively inexpensive, commonly available, non-toxic, and non-hazardous, making fuel grain manufacturing, handling, and storage safe. This, along with their higher regression rates, makes them attractive fuels for hybrid rocket motors.

SASOL 0907 paraffin wax was used as the fuel for the P-1B Mk II due to available stock in ASReG. It is classified as a microcrystalline paraffin type with a chain length of 50 carbon atoms. The properties of SASOL 0907 paraffin wax are given in Table 2-2. The enthalpy of formation of SASOL 0907 was found using Equation 2-11 provided by Karabeyoglu et al. (2005).

$$\Delta H_{f,25^\circ\text{C}}^s = -6.713 \times n - 7.846 \quad (2-11)$$

Table 2-2: Properties of SASOL 0907 paraffin wax (Grosse, 2009; Genevi  e, 2013).

| Property | Value | Unit |
|------------------------------------------------|----------------------------------|--------------------|
| Chemical formula | C ₅₀ H ₁₀₂ | - |
| Composition | 14.7% H, 85.3% C | - |
| Molecular weight | 703.4 | g/mol |
| Melting point | 107.85 |   C |
| Boiling point | 270.85 |   C |
| Congealing point | 84.5 |   C |
| Flash point | > 200 |   C |
| Density (solid) | 900 | kg/m ³ |
| Density (liquid) (200   C) | 720 | kg/m ³ |
| Dynamic viscosity (200   C) | 0.0047 | Pa.s |
| Kinematic viscosity (100   C) | 14.5 | mm ² /s |
| Heat of fusion | 221000 | J/kg |
| Enthalpy of formation | -1438200* | J/mol |
| Specific heat (solid) | 2000 | J/kg-K |
| Specific heat (liquid) | 3000 | J/kg-K |
| Thermal conductivity (liquid) (170   C) | 0.246 | W/m-K |

*Found using Equation 2-11.

2.8. Energetic Metal Additives

As discussed above, classical hybrid rocket motors have been hindered by low solid fuel regression rates, which led to the exploration of many performance enhancing techniques. A commonly used method is the introduction of energetic metal particles into the fuel grain. Generally, the addition of metal additives improves the heat of combustion and the adiabatic flame temperature, thus accelerating the pyrolysis process of solid fuels. This improves the fuel regression rate and thus fuel mass flow rate, reducing the O/F ratio, and improves the specific impulse and density specific impulse of the motor.

Since a high regression rate liquefying fuel was specified for use in the PV-3 motor, the primary incentive for the inclusion of metal additives is the reduction in the O/F ratio. A lower O/F ratio increases the proportion of the denser solid fuel for the same total propellant mass. With less liquid oxidiser, a smaller tank can be used which reduces the size and inert mass of the vehicle, therefore improving flight performance. However, the introduction of metal additives into the fuel grain is expected to result in reduced combustion efficiency due to incomplete particle combustion, and reduced nozzle efficiency due to two-phase losses and erosion.

2.8.1. Types of Additives

Metal additives used in hybrid motors include aluminium (Al), magnesium (Mg), boron (B), and beryllium (Be), and metal hydrides such as lithium aluminium hydride (LiAlH_4), aluminium hydride (AlH_3), magnesium hydride (MgH_2), and lithium boron hydride (LiBH_4). Metal alloys such as magnesium boron (MgB_3) and strained hydrocarbons have also been used (Karabeyoglu and Arkun, 2014). Figure 2-9 shows the relative gravimetric and volumetric heats of oxidisation for various metals. Compared to HTPB, most of the metals have a higher volumetric heat of combustion and thus their inclusion provides a higher energy release and therefore improved flame temperature and specific impulse. A comprehensive investigation of metal additives is provided by Risha et al. (2007) and Karabeyoglu and Arkun (2014).

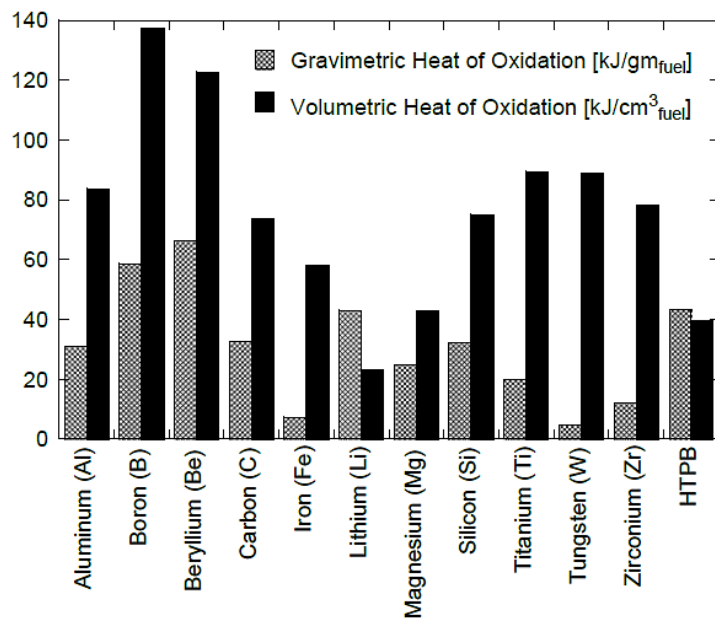


Figure 2-9: Comparison of heats of combustion with oxygen for various metals (Risha et al., 2007).

Many metal additives are however not locally available or are very expensive, ruling them out for this study. Only aluminium and magnesium were considered as candidate additives for the PV-3 motor with their properties given in Table 2-3.

Table 2-3: Properties of aluminium and magnesium (Risha et al., 2007).

| Fuel | Virgin material properties | | | Gravimetric heat of oxidisation (kJ/gm _{fuel}) | Volumetric heat of oxidisation (kJ/cm ³ _{fuel}) | Final oxide | Final oxide properties | | | | | | |
|------|---------------------------------|--------------------|--------------------|-------------------------------------------------------------|-------------------------------------------------------------------------|-----------------------------------|-----------------------------------|--------------------|--------------------|--------------------------------|--|--|--|
| | Density (kg/m ³) | T_{melt} (°C) | T_{boil} (°C) | | | | $Density$ (kg/m ³) | T_{melt} (°C) | T_{boil} (°C) | ΔH_f° (kJ/mol) | | | |
| | | | | | | | | | | | | | |
| Al | 2700 | 660 | 2467 | 31.1 | 83.9 | $\text{Al}_2\text{O}_3(\text{s})$ | 3970 | 2054 | 3800 | -1676 | | | |
| Mg | 1740 | 649 | 1107 | 24.7 | 43.0 | $\text{MgO}(\text{s})$ | 3580 | 2832 | 3260 | -601 | | | |

Aluminium

Aluminium additive is commonly used in hybrid and solid rockets and is the most researched additive to date. It is widely available in various shapes and sizes, cost effective, and relatively non-toxic, making it a practical additive. It provides a good performance improvement, especially with low energy oxidisers such as nitrous oxide, and has a high heat of oxidation and high density compared to magnesium. Risha et al. (2007) found a 12% increase in regression rate is achieved with the addition of 20% micrometre-sized aluminium powder in a GOX/HTPB slab motor.

Magnesium

Magnesium additive is less commonly used than aluminium as it has a lower heat of oxidation, lower density and is more expensive. Franz et al. (2013) found that specific impulse increased by 15 s with 10% magnesium from experimental results. The incentive to use magnesium was, for this study, its ease of ignition and faster reaction rate compared to aluminium. Aluminium particles develop an inert oxide layer that makes ignition difficult and thus reduces combustion efficiency. Therefore, the use of magnesium potentially provides a higher combustion efficiency and thus better performance, despite the reduced energy content and density.

2.8.2. Additive Geometry and Concentration

The variables to consider when selecting an additive include particle type, particle size, and concentration level in the fuel grain. Particle types are either round or flake powders, depending on the manufacturing process. Particles in the micrometre range are commonly used as they are readily available. Particles in the nanometre range have reduced ignition and burning times and thus greater combustion efficiency, but are expensive and complicate fuel grain production with particle settling problems (Pastrone, 2012). However, for both aluminium and magnesium, varying particle size on the micrometre level has no effect on regression rate, but a decrease in characteristic velocity and specific impulse was found with increasing particle size (Risha et al., 2007).

Various concentrations of additives in fuels have been tried with typical concentrations between 20% and 60%. Lips (1977) showed that there is a significant increase in regression rate with aluminium concentrations up to 60%, but further increases produce negligible effects on regression rate. This is believed to be related to the agglomeration of aluminium particles on the fuel grain surface (Karabeyoglu and Arkun, 2014).

2.8.3. Combustion Efficiency

Combustion efficiency is defined as the ratio of the experimental to theoretical characteristic velocity, given in Equation 2-12. A sample of combustion efficiencies collected from various tests is shown in Table 2-4. Laboratory-scale tests performed by Maharaj (2018) found that the combustion efficiency dropped by 11% with the addition of 40% aluminium powder (75 micrometre average particle size). Doran et al. (2007) described a drop of 4% with 20% aluminium powder. The primary cause for this decrease in efficiency is the increased residence time required to completely combust the particles since they are covered in an inert aluminium oxide layer. Methods for improving the combustion efficiency include treating the metal powder by either removing the oxide layer or sourcing coated powder, and increasing the particle residence time by increasing the volume of the post-combustion chamber, or adding a mixing plate.

$$\eta_{c^*} = \frac{c_{exp}^*}{c_{theo}^*} \quad (2-12)$$

Table 2-4: Combustion efficiencies from various tests with and without aluminium additive.

| Fuel | Oxidiser | Additive | Combustion efficiency (%) | Reference |
|----------------------------------|------------------|----------|---------------------------|----------------------|
| Paraffin wax (SASOL 0907) | N ₂ O | None | 95* | (Maharaj, 2018) |
| Paraffin wax (SASOL 0907) | N ₂ O | None | 87 | (Grosse, 2009) |
| Paraffin wax (SASOL 0907) | N ₂ O | 40% Al | 84* | (Maharaj, 2018) |
| Paraffin wax (SP-1A) | N ₂ O | None | 91** | (Doran et al., 2007) |
| Paraffin wax (SP-1A) | N ₂ O | 20% Al | 87* | (Doran et al., 2007) |

*Average over 3 tests, **Average over 6 tests.

2.8.4. Two-Phase Flow Losses and Nozzle Erosion

During combustion, a fraction of the metal particles may not react but rather agglomerate and thus burn slower. The vaporised aluminium reacts to form aluminium oxide (Al₂O₃) smoke. Some of the smoke condenses on to the aluminium droplets, resulting in a slower reaction rate. The presence of both aluminium and aluminium oxide coated particles or droplets results in two-phase flow losses as they pass through the nozzle, reducing the specific impulse, which is normally expected to increase with increasing additive concentration (Thakre et al., 2013).

Nozzle erosion is caused by mechanical impingement of the metal particles, chemical erosion by aggressive oxidising species, and vaporisation, melting, and charring of the ablative nozzle surface. These effects are expected to increase as the metal additive concentration increases,

receding the nozzle surface and increasing the throat area, subsequently decreasing the motor performance over time.

Laboratory-scale testing performed by Maharaj (2018) with 40% aluminium additive in paraffin wax showed substantial slag accumulation on the nozzle converging section, indicating a lack of combustion residence time and thus a lower combustion efficiency, as indicated in Table 2-4. The copper nozzle throat also melted and eroded away due to the increased adiabatic flame temperature and particle impingement, shown in Figure 2-10.

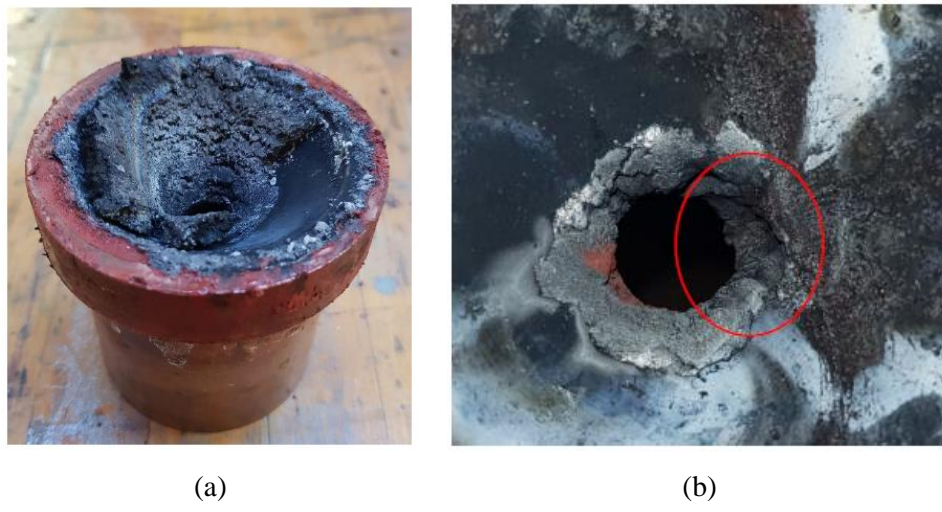


Figure 2-10: (a) Slag accumulation and (b) throat erosion on a laboratory-scale copper nozzle (Maharaj, 2018).

2.9. Summary

The recent discovery of high regression rate liquefying fuels has advanced hybrid propulsion technology past its historical limitations. Single-port fuel configurations now provide adequate thrust levels, opening up applications for hybrids. Metal additives have been shown to improve motor specific and density specific impulse and increase the fuel regression rate with a decrease in the optimal O/F ratio. However, an associated decrease in combustion efficiency and other undesirable implications follow. Aluminium and magnesium are the two candidate additives considered for the PV-3 motor, with magnesium preferred because of its postulated higher combustion efficiency.

3. DESIGN CRITERIA AND METHODOLOGY

3.1. Introduction

This chapter briefly describes the previous hybrid rockets in the Phoenix series, after which the design criteria for the present vehicle are introduced. The project methodology is given along with a brief description of the Hybrid Rocket Performance Simulator (HYROPS) software tool with which the P-1B Mk II system design was undertaken.

3.2. Phoenix Rockets

The three rockets of the Phoenix series are shown in Figure 3-1, with the P-1B Mk II the focus of the current work. Figure 3-2 (a) compares the inert and propellant mass totals, illustrating a decreasing trend in vehicle inert mass. The propellant mass fraction, defined as the ratio between the propellant mass and vehicle initial mass, increases from 0.4 for the P-1A to 0.47 for the P-1B Mk I, with the P-1B Mk II predicted to be 0.54. Figure 3-2 (b) shows the increasing target and achieved apogees of the vehicles. Design and performance data for the P-1A and P-1B Mk I are given in Appendix A.

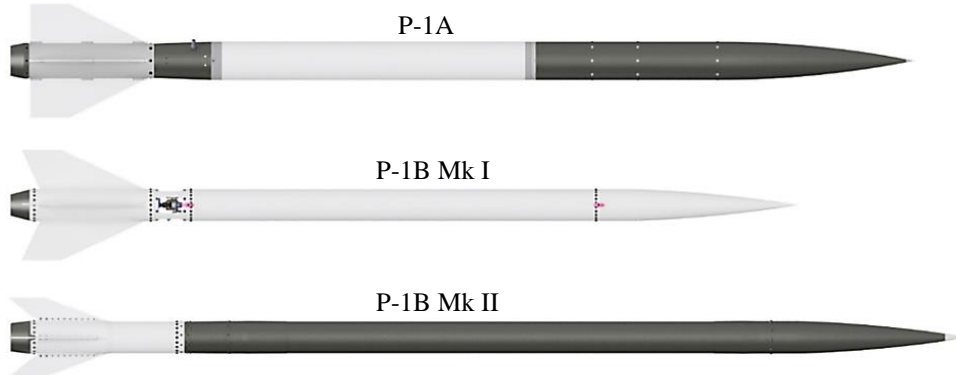


Figure 3-1: The Phoenix rocket series.

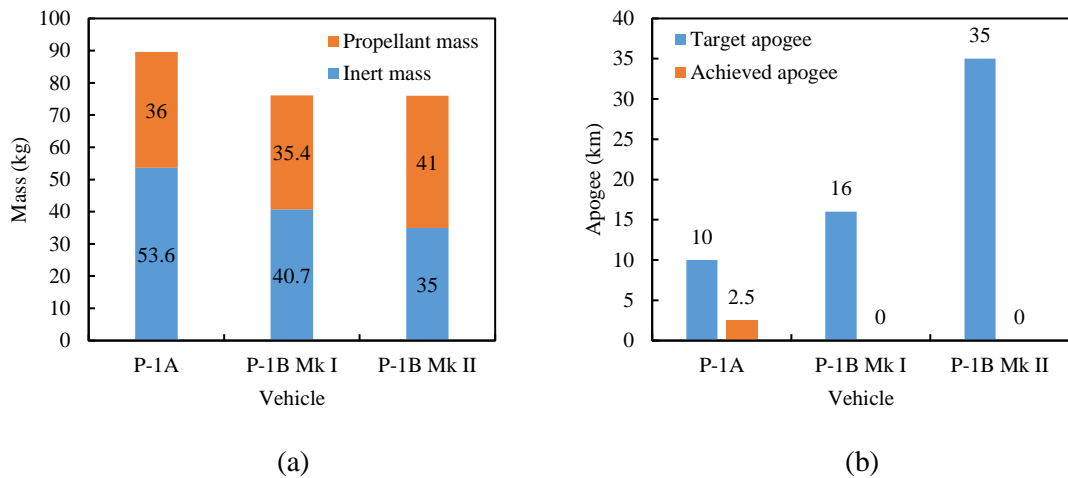


Figure 3-2: (a) Mass analysis and (b) apogees of Phoenix rockets (Broughton et al., 2018).

3.2.1. Phoenix-1A

The P-1A was the first hybrid rocket developed at UKZN. It was designed by Geneviève (2013), who developed the hybrid propulsion system, and Chowdhury (2012), who worked on the vehicle aerodynamics and structure. The vehicle was intended as a technology demonstrator to test the functionality and feasibility of hybrid rockets at UKZN.

Vehicle Design

The P-1A was designed to reach a target apogee of 10 km with a 1 kg payload. Its PV-1 hybrid motor used nitrous oxide and paraffin wax as the oxidiser and fuel, respectively. It had a nominal thrust of 4250 N with a 20 s burn time, and a design total impulse of 75 000 Ns. A blow-down feed system was used. A primary concern was the expense of manufacturing, since the combustion chamber and oxidiser tank were machined from solid aluminium 6082-T6 round bar. The tank bulkheads were also welded on to the ends of the tank causing bulging near the seams. A cross-section of the P-1A vehicle is shown in Figure 3-3.



Figure 3-3: Cross-section Phoenix-1A.

Testing

The P-1A was successfully hot-fire tested in August 2013, shown in Figure 3-4 (a), with a peak thrust of 3250 N measured with a burn time of only 11 s due to oxidiser under-loading. The reduced peak thrust was attributed to reduced oxidiser flow rate and lower combustion efficiency. High-frequency acoustic combustion instabilities were audible and attributed to the use of a conical injector, which limits the hot-gas recirculation, as discussed in Chapter 5 (Geneviève, 2013). An axial injector was used for the flight test.

The P-1A was launched in August 2014 from Denel Overberg Test Range (OTR) in the Western Cape, shown in Figure 3-4 (b). Only 18.5 kg of oxidiser was loaded into the tank for safety reasons which limited the theoretical apogee to 6 km. The motor successfully ignited however an apogee of only 2.5 km was reached due to the under-loading of the oxidiser and a nozzle structural failure at lift-off (Geneviève et al., 2015). The cause of the nozzle failure is unknown but was most likely due to a hard-start or a high stress concentration between the graphite nozzle and nozzle retainer (Balmogim et al., 2015).

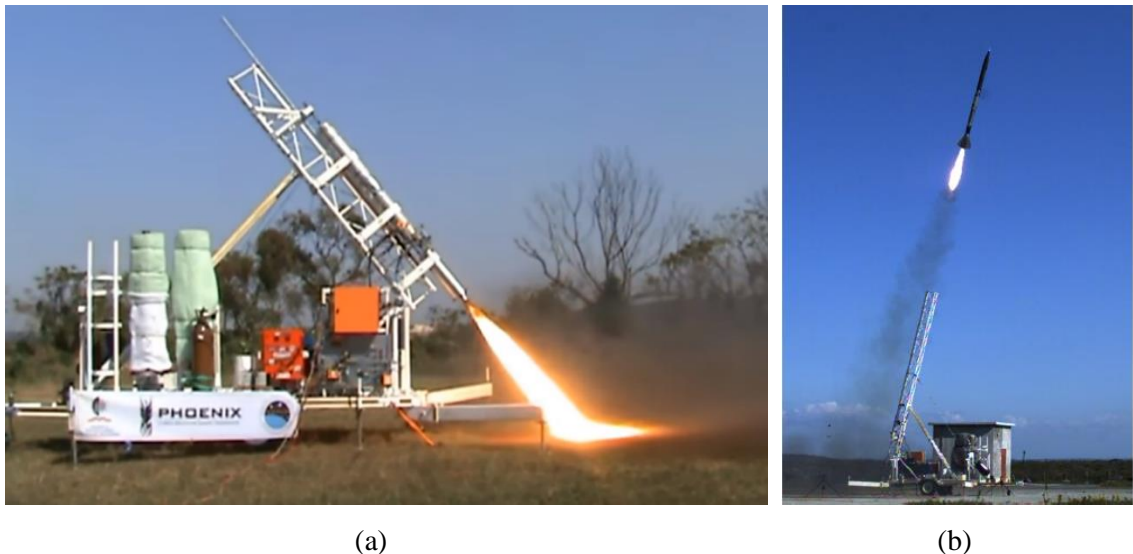


Figure 3-4: (a) Hot-fire test of P-1A on the MRLP (Balmogim, 2016) and (b) launch of P-1A (Geneviève et al., 2015).

3.2.2. Phoenix-1B Mk I

The P-1B Mk I hybrid rocket was designed by Balmogim (2016) as a modular workhorse for ongoing testing. The main objectives were to improve the target apogee and reduce the mass and cost of the P-1A, and to solve design problems identified in the P-1A, particularly the nozzle design.

Vehicle Design

The P-1B Mk I was designed to reach an apogee of 16 km. Its propulsion system utilised nitrous oxide and paraffin wax with a peak design thrust of 5000 N, an 18 s burn time, and a 69 000 Ns design total impulse. An aluminised fuel grain was initially considered but abandoned due to lack of motor performance data. It had a lift off mass of 76.1 kg, a reduction of 13.5 kg from the P-1A. A cross-section of the P-1B Mk I is shown in Figure 3-5.

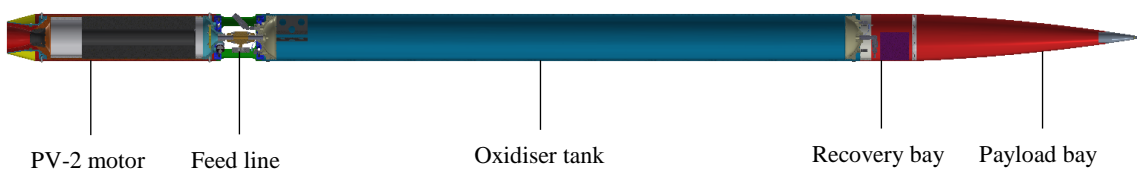


Figure 3-5: Cross-section of the Phoenix-1B Mk I.

Both the oxidiser tank and combustion chamber used a commercially extruded aluminium tube, avoiding the manufacturing problems experienced with the P-1A. The structural failure of the P-1A nozzle prompted the development of a more robust nozzle for the P-1B Mk I, which was

designed for up to 40% aluminium additive to the fuel by mass. Since an aluminised fuel grain was abandoned for the P-1B Mk I, the nozzle contour was adjusted for use with pure paraffin wax. The new design comprised silica/phenolic convergent and divergent sections, a graphite throat, and a steel retaining structure, as shown in Figure 3-6. Since the P-1B Mk I nozzle was designed for modularity, it was adapted for the PV-3 motor of this study.

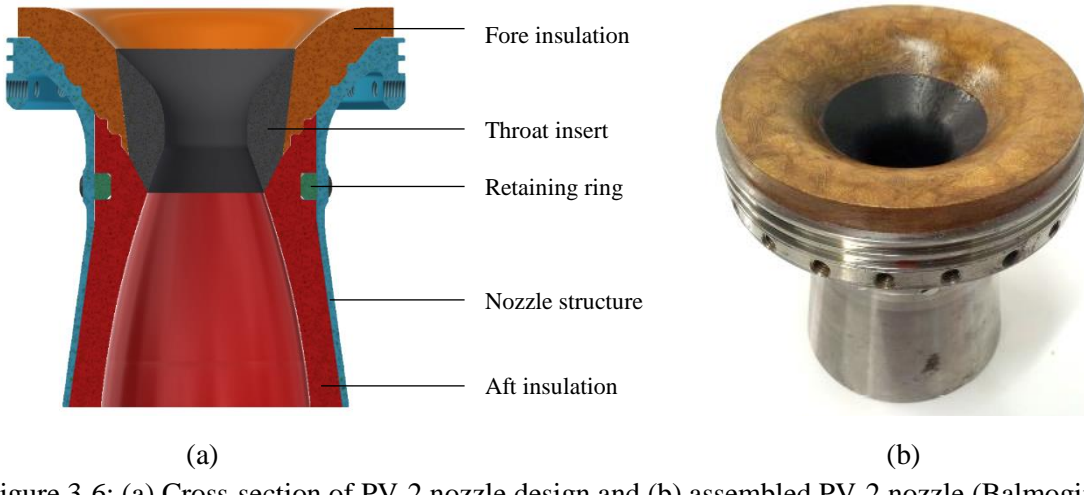


Figure 3-6: (a) Cross-section of PV-2 nozzle design and (b) assembled PV-2 nozzle (Balmogim, 2016).

Testing

The P-1B Mk I was successfully cold flow and hot-fire tested in 2018, as shown in Figure 3-7 (a) and (b). High-frequency acoustic instabilities were noted after ignition, possibly due to flame-holding instabilities caused by a high initial oxidiser mass flux. Instabilities were also present at the end of the burn due to sloughing of the fuel grain. An additional 8 kg of oxidiser over the nominal mass was loaded into the tank to account for mass loss via venting. However, this was over-estimated and resulted in the complete burn away of the thermal liner, seen in Figure 3-8 (b).



(a)

(b)

Figure 3-7: (a) Injector oxidiser plume of P-1B Mk I (Balmogim, 2016) and (b) P-1B Mk I hot-fire test.



(a)

(b)

Figure 3-8: (a) PV-2 nozzle insulation ablation and (b) PV-2 thermal liner after hot-fire test.

3.3. Phoenix-1B Mk II Design Requirements

The primary mission requirement of the P-1B Mk II is to reach a target apogee of 35 km. This was the driving condition behind the four main design requirements of the study:

1. Use energetic metal additives in the fuel to reduce the nominal O/F ratio
2. Improve total impulse of motor
3. Optimise vehicle aerodynamic performance
4. Reduce vehicle inert mass through use of a composite oxidiser tank and airframe

The addition of either aluminium or magnesium additives to the fuel grain is proposed as these have been shown to reduce the nominal O/F ratio, resulting in a lower liquid oxidiser fraction, and therefore increase vehicle performance. A large total impulse improvement and inert mass reduction is required compared to the P-1B Mk I to achieve the apogee requirement. The vehicle aerodynamic optimisation, composite oxidiser tank development, and airframe design were carried out by Williams (2018) in a parallel project.

Other requirements imposed on the vehicle include the use of nitrous oxide and paraffin wax as propellants, use of an available aluminium tube for the combustion chamber, adaption of the PV-2 nozzle design for modularity with the combustion chamber, the use of a ballistic flight trajectory with no payload recovery, and the use of the same avionics module developed for the P-1B Mk I. Nitrous oxide was specified for its self-pressurising capability in the simple blowdown system and paraffin wax was used for its high regression rate and capability to add an additive.

3.4. Methodology

Figure 3-9 shows the project methodology followed in this study, focusing on the propulsion system and motor design. A preliminary system design preceded the final propulsion system design. The HYROPS and NASA CEA™ (Chemical Equilibrium with Applications) software applications were used extensively to quantify the effect of metal additives on vehicle performance and to arrive at an adequate propulsion system design. A Preliminary Design Review (PDR) was held to verify that the design requirements had been met.

The design and manufacture of the motor components followed the specification of the propulsion system. Standard analytical design theory was often used as a starting point and verified using numerical techniques, with Siemens NX™ for Finite Element Method (FEM) analyses and Star-CCM+™ for Computational Fluid Dynamics (CFD) analyses. A Critical Design Review (CDR) was held prior to the testing phase.

The testing phase then followed to experimentally verify the motor performance. The standard hybrid rocket motor testing sequence included pressure testing, igniter testing, cold flow testing, and hot-fire testing. A Flight Readiness Review (FRR) was held to qualify the propulsion system for flight, after which the launch operations may begin. Specific design methodologies for each step are detailed further in their respective chapters. A brief description of the HYROPS software tool is given below.

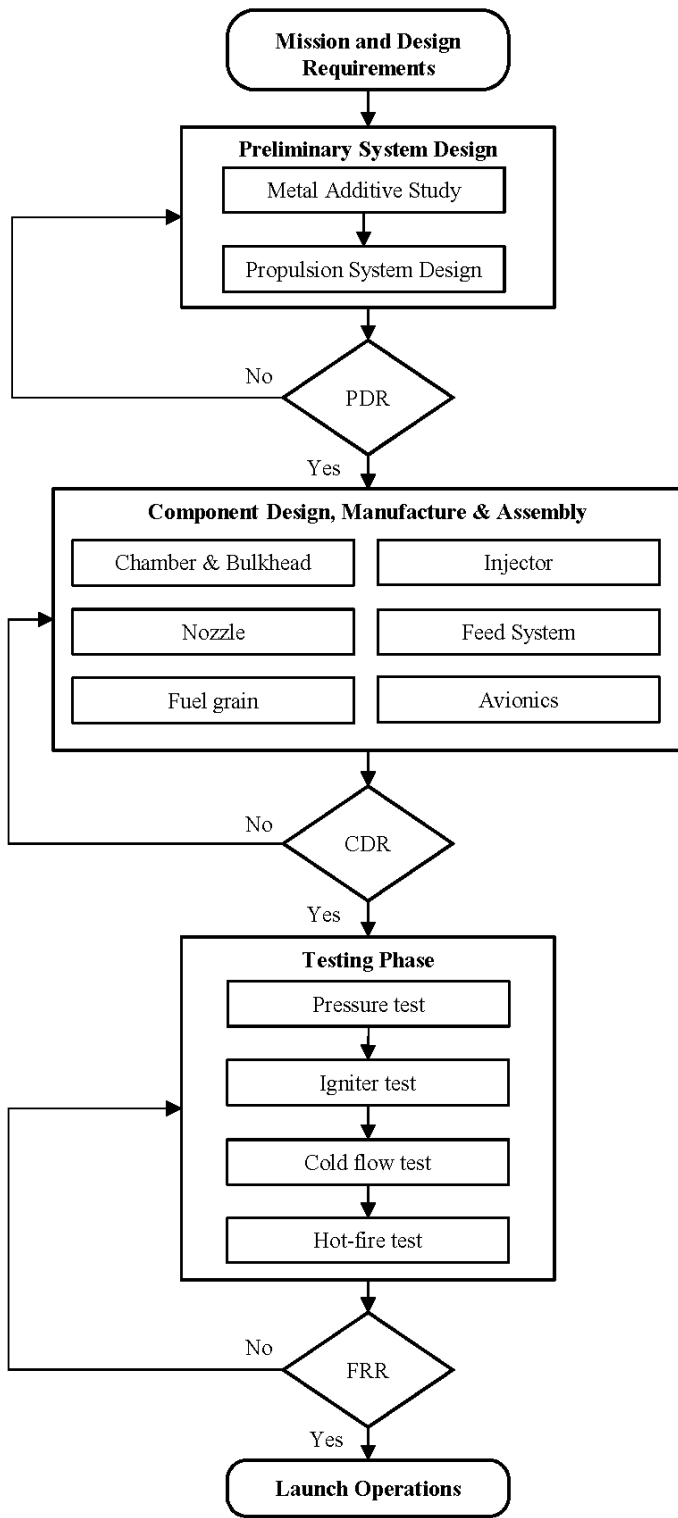


Figure 3-9: Project methodology.

3.5. Hybrid Rocket Performance Simulator

The Hybrid Rocket Performance Simulator was developed by Geneviève (2013) and Chowdhury (2012) to assist in the design of hybrid rockets for the Phoenix HSRP. It consists of the Hybrid Rocket Performance Code (HRPC) and a 6 Degree of Freedom (DOF) flight dynamics simulator, shown in the hierarchy of Figure 3-10. HRPC is used to specify motor geometry and simulate performance, and the flight dynamics simulator is used to model vehicle trajectories and flight performance.

HYROPS is used in an iterative manner to obtain the required vehicle apogee and performance. Once the motor transient performance has been simulated in HRPC, a thrust curve is exported to the flight dynamics simulator where the vehicle geometry is modelled with aerodynamic data imported from RASAero™. Simulation and launch parameters are configurable before the simulation is run. A brief description of each tool is given below with detailed descriptions provided by Geneviève (2013) and Chowdhury (2012).

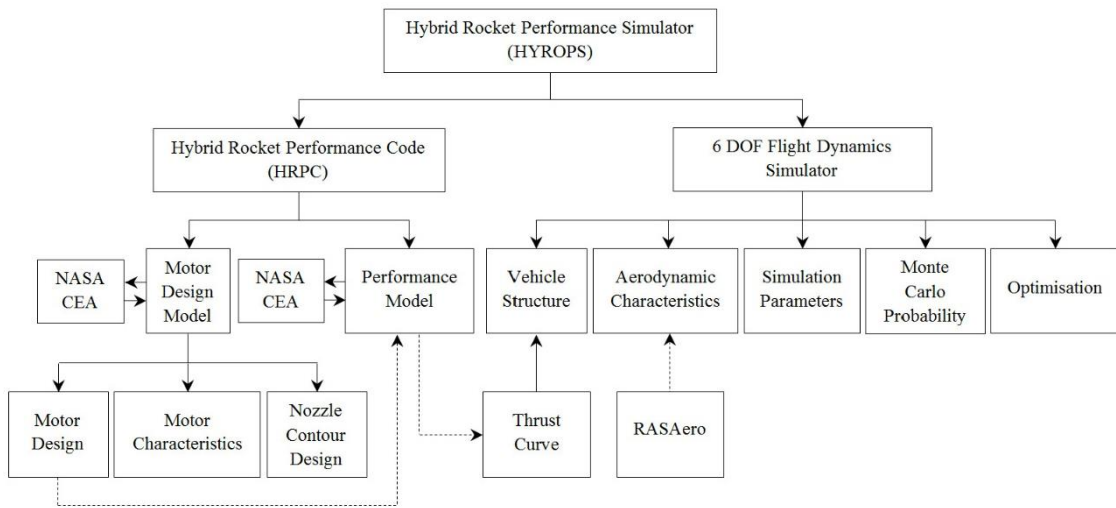


Figure 3-10: Hierarchy model of HYROPS with dashed lines representing manual coupling (Leverone, 2013).

3.5.1. Hybrid Rocket Performance Code

HRPC consists of a Motor Design Model and a Performance Model, both of which make use of NASA CEA™ (Gordon and McBride, 1994). NASA CEA™ is used to obtain the chemical equilibrium compositions of propellant mixtures with thermodynamic, transport, and rocket performance properties as outputs.

HRPC Motor Design is built on three sub-models, as depicted in Figure 3-11. The Motor Design Model determines the mass flow rates, fuel grain, and nozzle geometry for steady-state conditions. The Motor Characteristics Model generates rocket performance data over a range of O/F ratios

and chamber pressures, for the purpose of comparing and selecting motor designs. The Nozzle Contour Model generates the internal aerodynamic contour of a conical or bell-shaped nozzle. HRPC Performance Model, shown in Figure 3-12, is used to obtain the transient motor performance including thrust, pressures, temperatures, and mass flow rates. It uses a 4th order Runge-Kutta numerical solver and refers to thermochemical look-up tables generated by NASA CEATM.

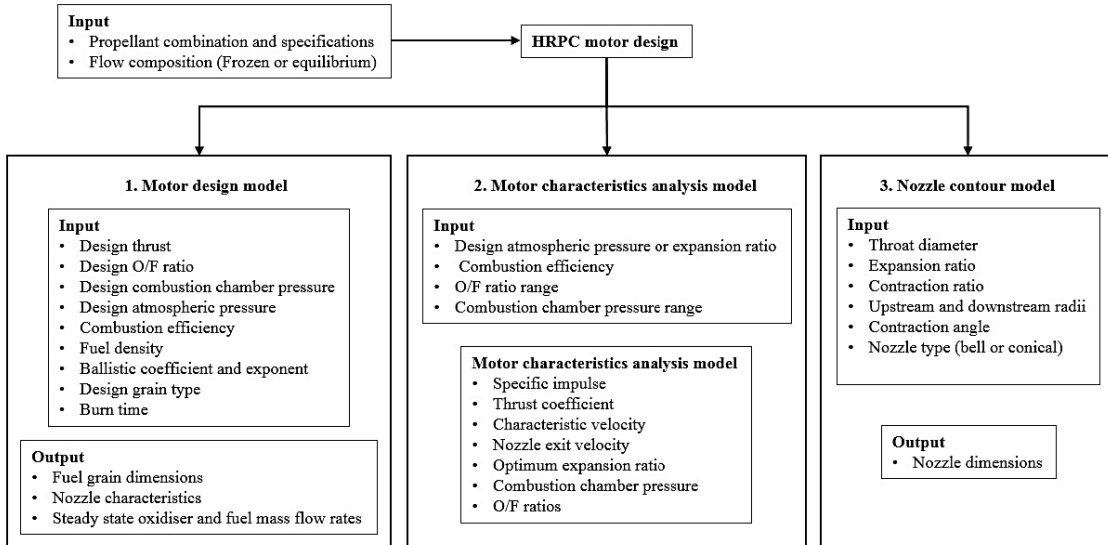


Figure 3-11: HRPC Motor Design Model (Balmogim, 2016).

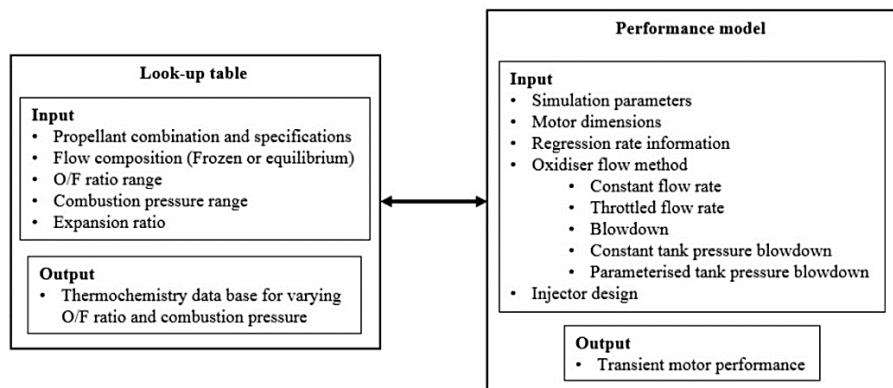


Figure 3-12: HRPC Performance Model (Balmogim, 2016).

3.5.2. 6 DOF Flight Dynamics Simulator

The flight dynamics simulator is an integrated flight performance predictor for atmospheric and near-Earth flight of sub-orbital rockets, and includes 6 DOF rocket flight dynamics, multi-staging, geodetic modelling, uncertainty modelling, aerodynamic performance prediction, and a design optimisation algorithm. It numerically solves for the kinematic and Newtonian equations of

motion using the Runge-Kutta method. The flow structure of the flight dynamics simulator is shown in Figure 3-13.

The tool can model the effects of wind, jet streams, and parachute deployment. It also enables Monte Carlo probability analyses by introducing uncertainties to several parameters and predicting the resultant trajectories and vehicle footprints, which are required by the launch range facility prior to launch. It is able to simulate and display the trajectory of a sub-orbital rocket given the vehicle geometry and mass distribution, transient motor performance (time dependent momentum thrust and nozzle exit pressure), and aerodynamic data.

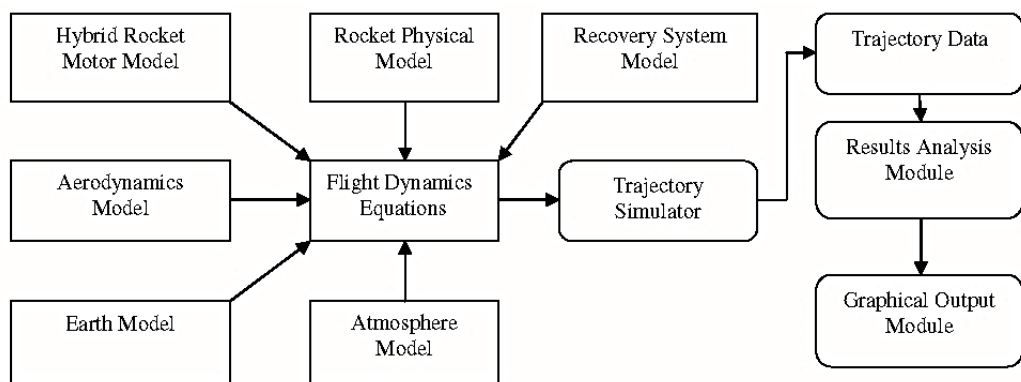


Figure 3-13: Flow structure of the HYROPS flight dynamics simulator (Chowdhury et al., 2011).

3.6. Summary

Design requirements for the P-1B Mk II rocket were derived from the work done on previous Phoenix rockets and from the mission statement applicable to the vehicle. In the following chapter these will be used to arrive at the final propulsion system design. An overview of the HYROPS software tool has also been presented. The three main phases depicted in the project methodology diagram, namely the preliminary system design, motor component design, and testing, correspond to the next four chapters.

4. PRELIMINARY SYSTEM DESIGN

4.1. Introduction

The P-1B Mk II preliminary system design included the necessary steps, trade studies, and design decisions required to specify the final propulsion system of the vehicle to ensure that it achieves its target apogee. This chapter includes a metal additive study and the propulsion system design.

4.2. Metal Additive Study

Metal additives reduce the nominal O/F ratio of a hybrid rocket motor, thereby reducing the required liquid propellant mass for a fixed amount of fuel and resulting in a smaller and lighter vehicle. Both aluminium and magnesium were considered as metal additives in this study, the goal of which was to determine which additive to use and at what concentration, and to investigate the effects on motor and vehicle design and performance.

4.2.1. Thermochemical Analysis

A thermochemical analysis was undertaken for direct comparison of performance metrics between the propellant combinations under identical operational conditions. NASA CEA™ and HRPC Motor Design were used to obtain combustion performance metrics for both aluminium and magnesium additives in paraffin wax with nitrous oxide. Additive concentrations were varied from 0% to 50% (by mass) in 10% increments.

The common input conditions used in the analysis are given in Table 4-1. Combustion efficiency has been shown to decrease with metal additives and thus assumed at a constant 80%, due to lack of empirical efficiency data for various metals and concentrations. Omitted species included AlN (L) with aluminium additive and MgO and MgO (L) with magnesium additive to avoid discontinuities in the results. The magnesium discontinuity solution is discussed further in Appendix B.

Table 4-1: Common input conditions for thermochemical analysis.

| Parameter | Value | Unit |
|-------------------------------------|-------------|------|
| Chamber pressure | 40 | bar |
| O/F ratio range | 1-10 | - |
| Nozzle design pressure | 101325 | Pa |
| Combustion efficiency | 80 | % |
| Inert propellant temperature | 298.15 | K |
| Flow condition | Equilibrium | - |

Results

Figure 4-1 shows the effect of increasing aluminium additive concentration on the characteristic velocity for a sweep of O/F ratios. The optimum O/F ratio for each concentration was taken at the peak of their respective curves. The corresponding performance metrics were then taken at these optimum O/F ratios. With an increase in aluminium concentration, the optimum O/F ratio decreases, with only a slight increase in characteristic velocity. Specific impulse follows a similar trend.

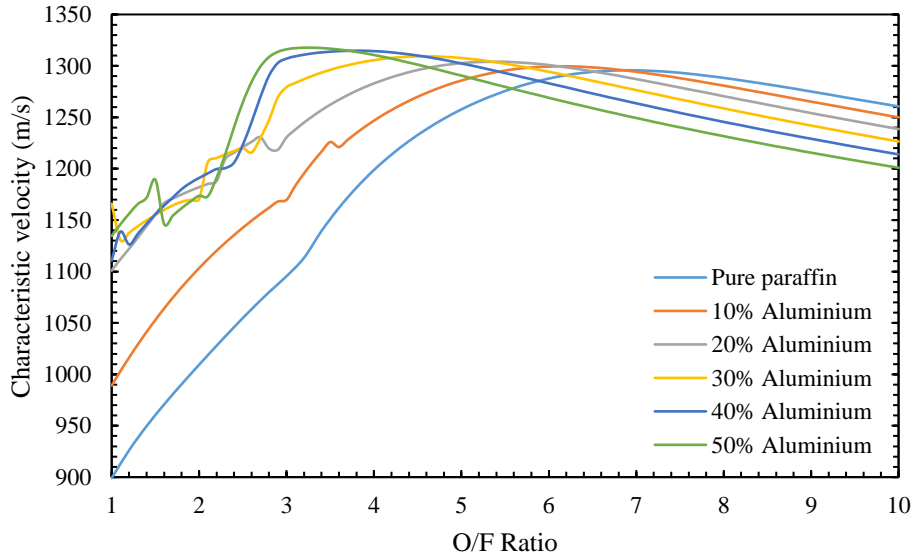


Figure 4-1: Characteristic velocity curves for various aluminium additive concentrations over a range of O/F ratios at 40 bar chamber pressure.

Figure 4-2 gives the performance metrics of aluminium and magnesium additives, varying from 0% to 50% concentration. Tabular data is given in Appendix B. There is a slight increase in characteristic velocity with increasing concentration of aluminium, whereas it remains relatively constant for magnesium. The most prominent effect is the reduction in the optimum O/F ratio for both additives, which follow a similar trend.

Aluminium additive generates better specific impulse performance than magnesium, with up to 3.1% and 1.8% increases respectively. Density specific impulse, important for volume-limited systems such as this case, is defined as the product of the fuel density and the specific impulse. Aluminium outperforms magnesium due to its higher density, with up to 53% improvement compared to 33% for magnesium. A substantial increase in adiabatic flame temperature from 3310 K to 3675 K is noted for aluminium.

Aluminium therefore marginally outperforms magnesium on the critical performance metrics due to its higher energy content and density. However, a constant combustion efficiency was used for

all cases, whereas in reality this depends on concentration and additive type. Magnesium may perform with higher combustion efficiencies, due to its hypothesised ease of ignition, which may bridge the performance gap or even surpass it. Nevertheless, due to lack of experimental data to validate this proposition, and with no regression rate data for magnesium available, the use of magnesium was abandoned in favour of aluminium.

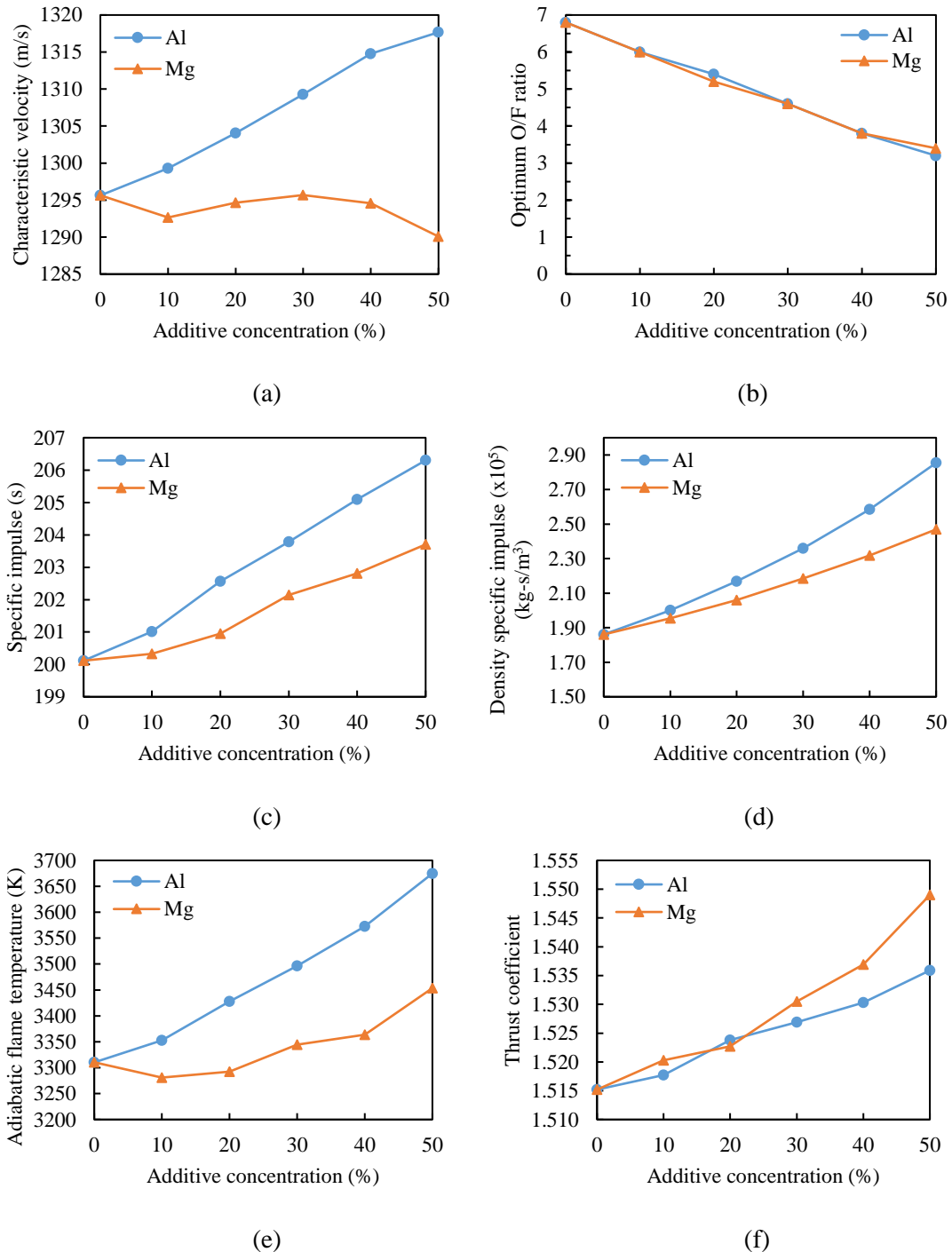


Figure 4-2: Performance metric comparison of aluminium and magnesium additives at various concentrations: (a) characteristic velocity, (b) optimum O/F ratio, (d) specific impulse, (d) density specific impulse, (e) adiabatic flame temperature, and (f) thrust coefficient.

Nozzle Losses

NASA CEA™ was used to quantify the two-phase flow losses and nozzle erosion with aluminium and magnesium additives at various concentrations. The same input conditions given above were used, and data was taken at the optimal O/F ratio for each concentration.

Figure 4-3 (a) compares the molar fraction of condensed phase combustion products (liquid and solid Al_2O_3 and MgO for aluminium and magnesium additive respectively) at the nozzle throat. Molar fractions increase with concentration for both additives, indicating an expected increase in two-phase flow losses and mechanical impingement erosion. Magnesium additive produces comparatively more condensed phase products as concentration increases, however, the analysis assumes complete combustion of the metal particles. Aluminium additive may perform worse in reality due to its expected ignition difficulty.

The condensed phase products for aluminium additive are liquid for all concentrations since the adiabatic flame temperatures at the throat are well above the aluminium oxide melting temperature of 2345 K. For magnesium additive, magnesium oxide transitions from solid to liquid at 30% concentration (3124 K at throat) since its melting temperature is much higher at 3125 K.

Figure 4-3 (b) compares the molar fraction of oxidising species (H_2O , OH , CO_2 , CO , H , H_2 , NO , O , O_2) at the nozzle throat. The molar fractions decrease with increasing concentration, with a greater decrease for magnesium, indicating a decrease in the expected chemical erosion. This is due to the greater consumption of the oxidising products by Al_2O_3 and MgO . A more comprehensive analysis for aluminium additive alone is provided by Balmogim (2016).

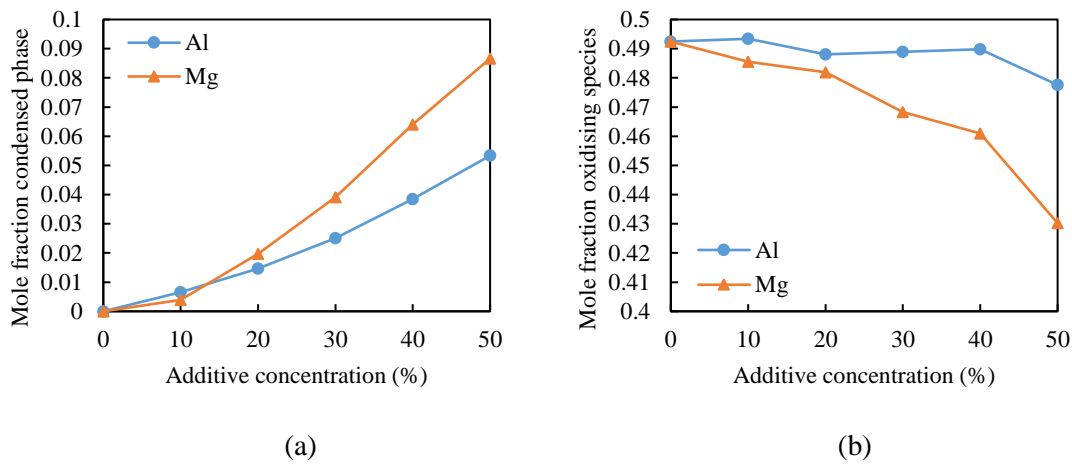


Figure 4-3: (a) Molar fraction of condensed phase species at the nozzle throat and (b) molar fraction of oxidising species at the nozzle throat.

4.2.2. Effect on Motor and Vehicle Performance

Consideration was given to the effect of aluminium concentration on motor and vehicle design, and performance. Figure 4-4 shows the methodology flow chart followed. HRPC was used to generate the motor geometry and transient performance, with the common input design parameters given in Table 4-2. The flight dynamics simulator used the thrust curve and vehicle geometry for each case to simulate the vehicle trajectories.

The P-1B Mk I was used as the reference vehicle for a baseline quantitative comparison. The motor and tank diameters were therefore kept constant between cases, with only their respective lengths allowed to change. The fuel grain length was calculated for each case with a constant fuel port diameter. Nozzle geometry was also calculated for each case and an aluminium tank was used. The variables in the study were the aluminium concentration, the optimum O/F ratio, the regression rate coefficient, the fuel grain density, and the burn time. The burn time was iterated to obtain the fuel grain outer diameter of 147 mm. The mass of oxidiser was calculated by multiplying the fuel mass by the O/F ratio. Each case was allowed to consume all the fuel and only liquid phase thrust was considered.

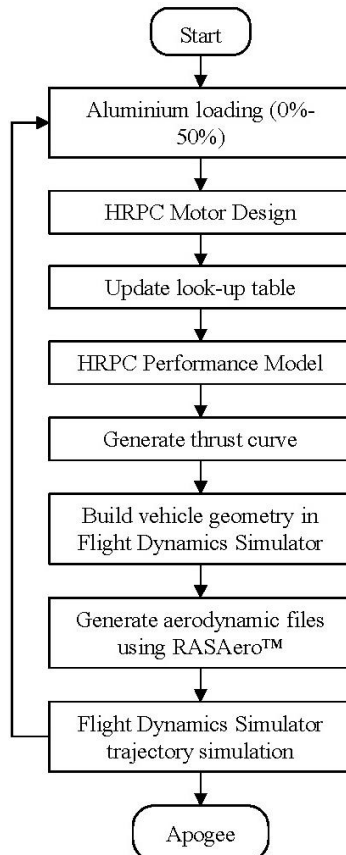


Figure 4-4: Metal additive study methodology considering effects on motor and vehicle performance.

Table 4-2: Common input conditions used in HRPC.

| Parameter | Value | Unit |
|------------------------------------|---------|------|
| HRPC Motor Design | | |
| Nominal thrust | 5000 | N |
| Nominal chamber pressure | 40 | bar |
| Atmospheric design pressure | 1.01325 | bar |
| Combustion efficiency | 80 | % |
| Fuel grain diameter | 0.147 | m |
| Port diameter | 0.06 | m |
| HRPC Performance Model | | |
| Tank pressure | 65 | bar |
| Chamber pressure | 40 | bar |
| Oxidiser tank ullage | 10 | % |
| Coefficient of discharge | 0.8 | - |
| Injector hole diameter | 0.001 | m |
| Feed pipe pressure drop | 1.0 | bar |
| Flight Dynamics Simulator | | |
| Launch angle | 82.5 | ° |
| Wind | None | - |
| Spin | None | - |

There is limited empirical regression rate data available for various aluminium concentrations in paraffin wax with nitrous oxide. The only relevant data found implied a 10% increase in regression rate for 40% aluminium concentration (McCormick et al., 2005). The regression rate coefficient, a , was found for each concentration by linearly interpolating between the values for pure paraffin wax and 40% aluminium concentration, given in Table 4-3. The regression rate exponent, n , was assumed constant at 0.5 which is a common assumption made in literature with paraffin wax and nitrous oxide.

The mixture densities for each aluminium concentration given in Table 4-3 were calculated using Equation 4-1, where x is the mass fraction and the volumes are additive. The densities used for paraffin wax and aluminium were 930 kg/m³ and 2700 kg/m³ respectively.

$$\rho_{mix} = \frac{1}{\left(\frac{x_1}{\rho_1}\right) + \left(\frac{x_2}{\rho_2}\right)} \quad (4-1)$$

Table 4-3: Interpolated regression rate coefficient and theoretical fuel densities for various aluminium additive concentrations.

| Aluminium concentration (%) | Regression rate coefficient, $a (\times 10^{-3})$ | Fuel density (kg/m ³) |
|-----------------------------|---------------------------------------------------|-----------------------------------|
| 0 | 0.1550 | 930.00 |
| 10 | 0.1589 | 995.24 |
| 20 | 0.1628 | 1070.33 |
| 30 | 0.1666 | 1157.68 |
| 40 | 0.1705 | 1260.54 |
| 50 | 0.1744 | 1383.47 |

Results

Table 4-4 gives the effects of aluminium concentration on motor geometry and steady state performance. The fuel grain mass increases significantly due to the increase in mixture density. The fuel mass flow rate increases due to the increase in regression rate and fuel grain length, and thus the burn time decreases. A corresponding decrease in the oxidiser mass flow rate is observed to maintain the decrease in optimum O/F ratio.

Table 4-4: Effect of aluminium concentration on motor geometry and steady state performance.

| Aluminium concentration (%) | O/F ratio | Fuel grain length (m) | Fuel grain mass (kg) | Fuel mass flow rate (kg/s) | Oxidiser mass flow rate (kg/s) | Burn time (s) |
|-----------------------------|-----------|-----------------------|----------------------|----------------------------|--------------------------------|---------------|
| 0 | 6.8 | 0.429 | 5.64 | 0.33 | 2.22 | 17.28 |
| 10 | 6 | 0.438 | 6.17 | 0.36 | 2.17 | 17.02 |
| 20 | 5.4 | 0.437 | 6.62 | 0.39 | 2.12 | 16.83 |
| 30 | 4.6 | 0.456 | 7.47 | 0.45 | 2.05 | 16.72 |
| 40 | 3.8 | 0.484 | 8.64 | 0.52 | 1.97 | 16.69 |
| 50 | 3.2 | 0.501 | 9.81 | 0.59 | 1.88 | 16.67 |

Table 4-5 summarises the effects of aluminium concentration on the vehicle mass and geometry. The total propellant mass decreases with increasing aluminium concentration due to the decrease in oxidiser mass. This results in a decrease in the oxidiser tank mass and length and ultimately the total vehicle mass and length. At 50% aluminium concentration, the vehicle mass and length decrease by 6.9% and 9.2% respectively.

Table 4-5: Effect of aluminium concentration on vehicle mass and geometry.

| Aluminium concentration (%) | Fuel grain mass (kg) | Oxidiser mass (kg) | Propellant mass (kg) | Vehicle mass (kg) | Vehicle length (m) |
|-----------------------------|----------------------|--------------------|----------------------|-------------------|--------------------|
| 0 | 5.642 | 38.368 | 44.011 | 89.941 | 4.983 |
| 10 | 6.165 | 36.990 | 43.155 | 88.392 | 4.888 |
| 20 | 6.617 | 35.730 | 42.347 | 86.857 | 4.790 |
| 30 | 7.467 | 34.350 | 41.818 | 85.695 | 4.704 |
| 40 | 8.641 | 32.835 | 41.476 | 84.731 | 4.618 |
| 50 | 9.806 | 31.379 | 41.185 | 83.761 | 4.524 |

Table 4-6 gives the effect of aluminium loading on vehicle performance, and Figure 4-5 shows the trajectory of each vehicle. The achieved apogee increases with increasing aluminium concentration by as much as 9.3% for 50% aluminium, however, the increase is somewhat limited. The total impulse can be seen to decrease slightly with increasing aluminium concentration which is due to the decreasing burn time. Therefore, the main contributor to the increase in the apogee is the decrease in total propellant mass and vehicle inert mass. Vehicle length also decreases which reduces the drag force experienced. An aluminium concentration of 20% was ultimately selected, which was a compromise between the increased performance and apogee achieved, and the expected decrease in combustion efficiency with aluminium additive.

Table 4-6: Effect of aluminium concentration on vehicle performance.

| Aluminium concentration (%) | Apogee (m) | Burn time (s) | Total impulse (Ns) | Change in vehicle mass | Change in vehicle volume | Change in apogee |
|-----------------------------|------------|---------------|--------------------|------------------------|--------------------------|------------------|
| 0 | 21755 | 19.51 | 75524.00 | - | - | - |
| 10 | 22061 | 19.20 | 74928.79 | -1.72% | -1.91% | +1.40% |
| 20 | 22131 | 18.98 | 74004.81 | -3.43% | -3.87% | +1.73% |
| 30 | 22662 | 18.85 | 73989.31 | -4.72% | -5.60% | +4.17% |
| 40 | 23407 | 18.85 | 74389.86 | -5.79% | -7.32% | +7.59% |
| 50 | 23780 | 18.81 | 74160.57 | -6.87% | -9.21% | +9.31% |

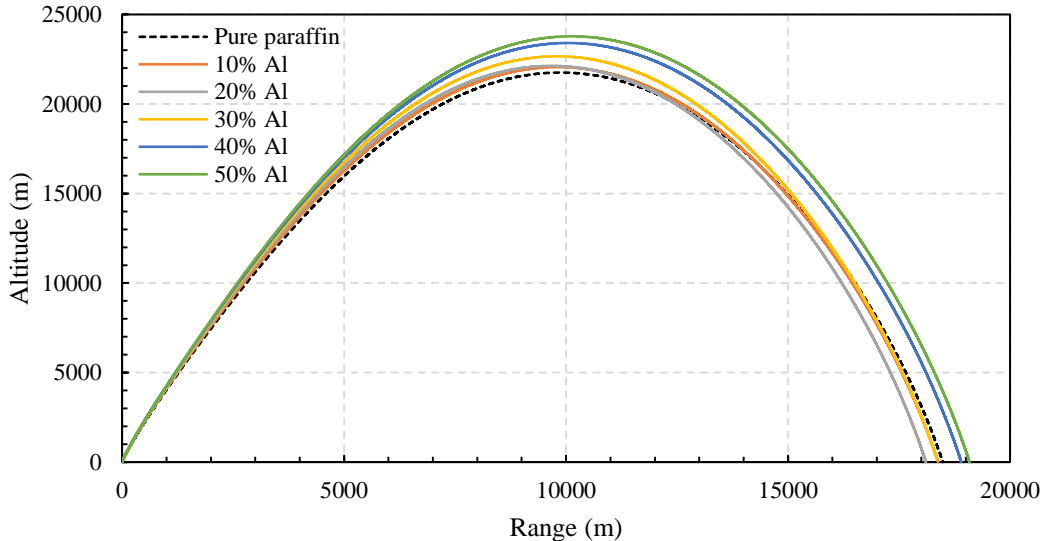


Figure 4-5: Altitude vs. range for various aluminium concentrations (Broughton et al., 2018).

4.3. Propulsion System Design

Having selected the propellant composition, the design of the propulsion system for the P-1B Mk II followed. In the following sections, the design requirements and constraints for the motor, propellant performance, iterative design methodology, and final motor specifications are discussed.

4.3.1. Design Requirements and Constraints

The P-1B Mk II propulsion system is required to propel the vehicle to a 35 km apogee. A propellant combination of nitrous oxide and paraffin wax with aluminium additive at 20% concentration by mass was specified. A conservative combustion efficiency of 85% was assumed based on the data in Table 2-4.

A tank blowdown oxidiser delivery method was chosen to take advantage of the self-pressurising nature of nitrous oxide. Nitrous oxide has a vapour pressure of 56.5 bar at room temperature which is nominally supercharged to 65 bar using helium with a 10% tank ullage. This mitigates cavitation in the feedline and allows a greater chamber pressure. By design, the injector pressure drop must be at least 20% of the chamber pressure chosen throughout the burn.

The primary constraint imposed on the propulsion system was the use of an available aluminium 6061-T6 tube for the combustion chamber. This enabled nozzle modularity between the P-1B Mk I and Mk II. A diametrical constraint of 164 mm was then set on the combustion chamber.

4.3.2. Propellant Performance Analysis

A propellant performance analysis was required prior to propulsion system sizing so as to select the nominal chamber pressure and O/F ratio. HRPC and NASA CEA™ were used to generate motor performance metrics for a range of chamber pressures and O/F ratios. Figure 4-6 shows the characteristic velocity and specific impulse curves for a range of O/F ratios at a 40 bar chamber pressure. The input conditions applied were an 85% combustion efficiency, a bell-shaped nozzle with no losses, and a nozzle design pressure of 1.01325 bar.

There is a negligible difference in the characteristic velocity curves with pressures between 30 bar and 50 bar, however, a significant increase in specific impulse occurs with increasing chamber pressure. A tank pressure of 65 bar limits the maximum chamber pressure to 50 bar considering a minimum required injector pressure drop of 20% and an assumed feedline pressure drop of 5 bar. However, high chamber pressures may result in combustion instabilities, therefore, a nominal chamber pressure of 40 bar was selected for the motor, averaging at about 30 bar throughout the burn. The optimum O/F ratio from the characteristic velocity curve is 5.4 at 1385 m/s.

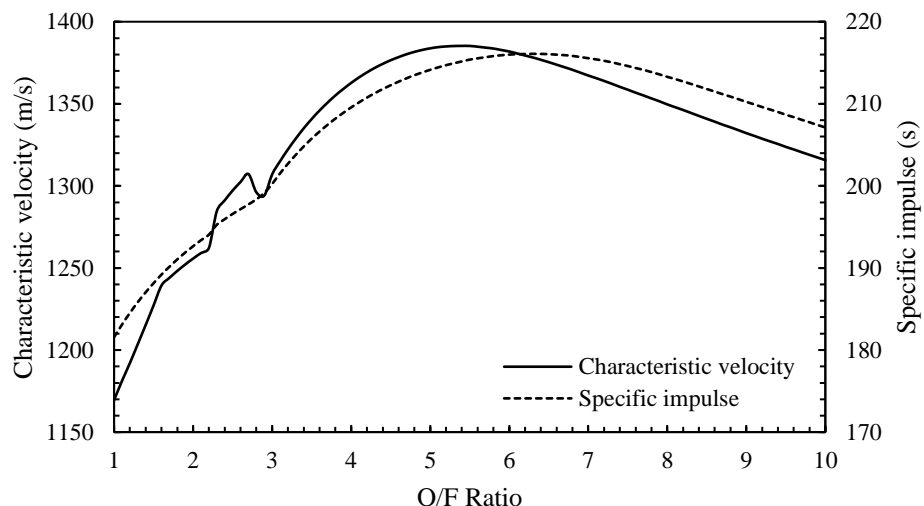


Figure 4-6: Characteristic velocity and specific impulse for various O/F ratios for nitrous oxide/paraffin wax with 20% aluminium additive by mass for 40 bar chamber pressure and 85% combustion efficiency.

4.3.3. PV-3 Motor Design and Methodology

Figure 4-7 provides the design methodology flow chart based on HYROPS used to obtain the final propulsion system design. It consists of two iteration loops, where the motor design parameters and vehicle geometry are iterated to achieve a 35 km apogee with stable flight throughout. Initial motor specifications and vehicle geometry were based off the design

requirements and the P-1B Mk I motor. HYROPS was used extensively following the methodology discussed in Chapter 3.

The primary design variables were the design thrust and the fuel port diameter. The burn time was iterated to obtain the fuel grain outer diameter constraint of 147 mm, allowing for a 3 mm thick thermal liner. The nozzle was preliminarily designed for sea-level operation. The mass of oxidiser was adjusted to ensure a few seconds of gaseous oxidiser burn after the liquid burn to mitigate the risk of a chamber burn-through and due to the uncertainty of the fuel regression rate.

An injector pressure drop of at least 20% of the chamber pressure was maintained and the chamber pressure was kept below the saturation pressure of the oxidiser to encourage the generation two-phase flow, thus isolating the tank pressure from the chamber pressure instabilities. A composite oxidiser tank made from carbon fibre/epoxy and a PVC liner and was used, with an updated specific heat variation given in Appendix C. The trajectory simulations were done at an 85° launch angle with no wind.

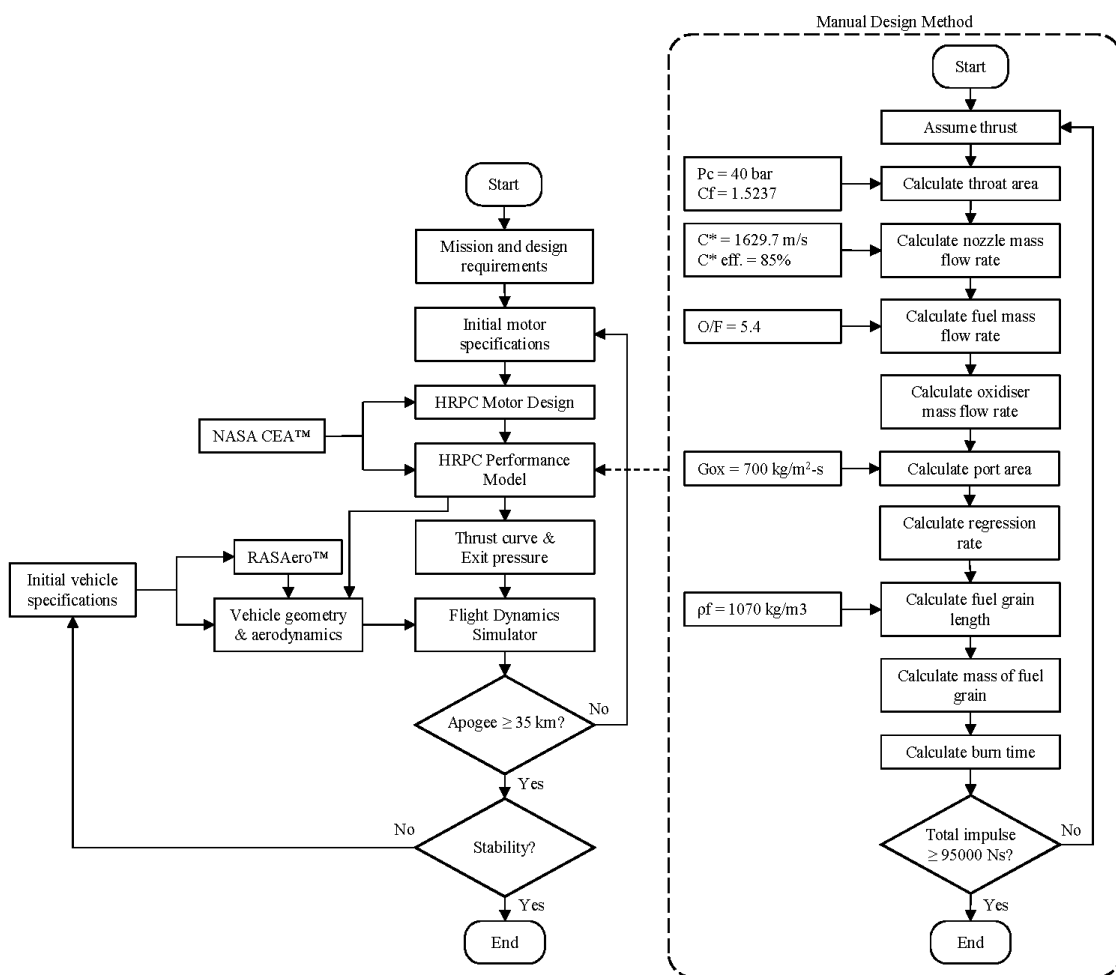


Figure 4-7: Design methodology flow chart based on HYROPS for Phoenix-1B Mk II propulsion system.

Initial iterations revealed that a theoretical steady-state total impulse of 95 000 Ns, was needed to propel a 76 kg vehicle to 35 km apogee. However, the initial motor design had a high initial oxidiser mass flux of more than $1000 \text{ kg/m}^2\text{-s}$. High oxidiser mass fluxes have been shown to cause flame-holding combustion instabilities, as discussed in Chapter 2. Although there is no known theoretical oxidiser mass flux limit for combustion stability, a limit of $700 \text{ kg/m}^2\text{-s}$ was imposed in this study based on recommendations by Zilliac et al. (2012) and Werner et al. (2016), and on previous Phoenix hot-fire tests.

A manual design method, shown in the dotted box in Figure 4-7, was subsequently adopted for the motor, bypassing the HRPC Motor Design step, with the initial oxidiser mass flux as a design input. This determined the minimum fuel port diameter for a given thrust. The thrust was then iterated to obtain the steady-state total impulse requirement of 95 000 Ns. The iterative methodology exhibited a trade-off between thrust and burn time, since as thrust increases the port diameter increases, which reduces the burn time due to fuel grain outer diameter constraint. Therefore, it is postulated that a total impulse upper limit exists with respect to motor diameter based on motor stability.

4.3.4. Final Propulsion System Specifications

The theoretical flight performance and final propulsion system specifications for the P-1B Mk II are given in Table 4-7 and Table 4-8, respectively. The motor has a peak thrust of 7250 N with a liquid burn time of 14.2 s, delivering a transient total and specific impulse of 76 500 Ns and 192 s, respectively. A total propellant mass of 41.05 kg includes 7.05 kg of fuel and 34 kg of oxidiser. The preliminary injector design consists of 1 mm diameter orifices, 78 orifices, and a coefficient of discharge of 0.8. The injector design is described in greater detail in Chapter 5. The transient thrust, chamber, and tank pressure curves are given in Figure 4-8, with the characteristic decrease over time of a blowdown system. Average motor performance is given in Appendix D.

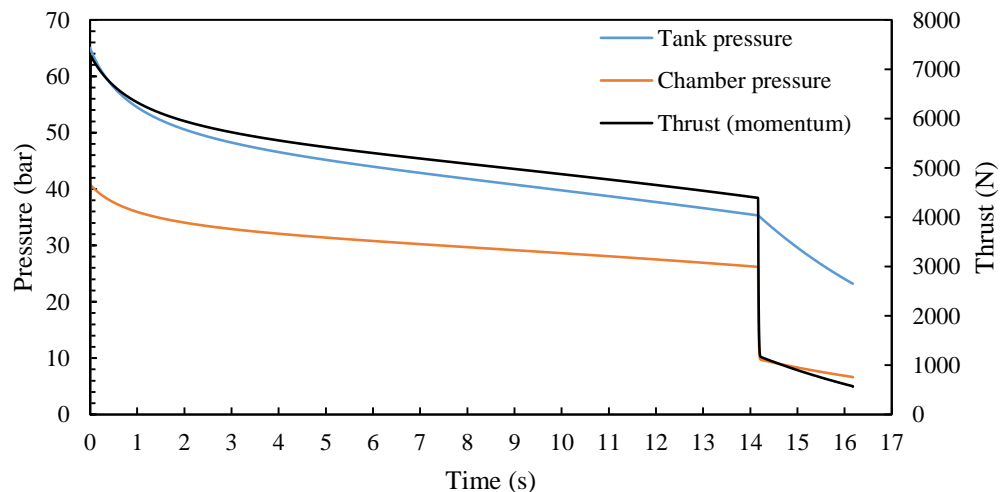


Figure 4-8: PV-3 motor theoretical pressure and thrust curves.

The bell-shaped nozzle has an expansion ratio of 5.93 with the detailed nozzle specifications given in Appendix D. Due to the short burn time, optimising the nozzle expansion ratio with respect to apogee had negligible effect. Figure 4-9 compares the nozzle exit pressure to the atmospheric pressure over the burn time during flight. Due to the characteristic decrease in chamber pressure over time for a blowdown system, the nozzle varies from over-expanded to under-expanded operation throughout the burn.

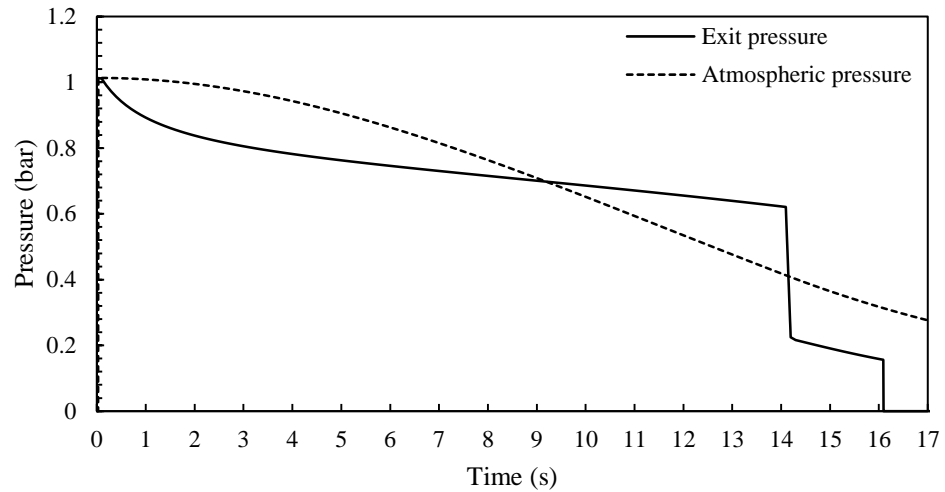


Figure 4-9: Nozzle exit pressure and atmospheric pressure comparison over burn time.

A review of the recommended hybrid motor design and performance constraints was conducted in order to gauge where the PV-3 motor operated. This is provided in Appendix E.

Table 4-7: Phoenix-1B Mk II theoretical flight performance.

| Parameter | Specification | Unit |
|--------------------------------|----------------------------|------|
| Vehicle mass | 76 | kg |
| Vehicle length | 4.9 | m |
| Vehicle diameter | 0.17 (tank), 0.164 (motor) | m |
| Apogee | 35 | km |
| Range | 16 | km |
| Maximum speed | Mach 2.8 | - |
| Maximum acceleration | 8.7 g | - |
| Flight time (ballistic) | 178 | s |

Table 4-8: Phoenix-1B Mk II propulsion system design specifications.

| | Parameter | Specification | Unit |
|------------------------|------------------------------------------------|-----------------------------|----------------------|
| Propellants | Oxidiser | Nitrous oxide | - |
| | Fuel | SASOL 0907 Paraffin wax | - |
| | Fuel additive | Aluminium (20%) | - |
| | Fuel density | 1070.33 | kg/m ³ |
| | Design O/F ratio | 5.4 | - |
| | Oxidiser flow method | Blowdown | - |
| Oxidiser Tank | Supercharge gas | Helium | - |
| | Oxidiser mass | 34 | kg |
| | Supercharge gas mass | 0.011 | kg |
| | Ullage | 10 | % |
| | Oxidiser tank volume | 0.04764 | m ³ |
| | Nominal tank pressure | 65 | bar |
| PV-3 Motor | Peak nominal thrust | 7250 | N |
| | Nominal chamber pressure | 40 | bar |
| | Design combustion efficiency | 85 | % |
| | Fuel grain diameter | 0.147 | m |
| | Port diameter | 0.072 | m |
| | Fuel grain length | 0.51 | m |
| | Initial grain volume | 0.006586 | m ³ |
| | Initial grain mass | 7.049 | kg |
| | Web thickness | 0.0375 | m |
| | Optimum nozzle expansion ratio | 5.9317 | - |
| | Nozzle throat diameter | 0.03892 | m |
| | Nozzle exit diameter | 0.09478 | m |
| | Injector hole diameter* | 0.001 (0.0012) | m |
| | Number of injector holes | 78 | - |
| PV-3 Motor Performance | Initial oxidiser mass flux | 711.8 | kg/m ² -s |
| | Burn time (steady-state) | 13.13 | s |
| | Burn time (transient) | 14.2 (liquid), 16.2 (total) | s |
| | Total impulse (steady-state) | 95 225 | Ns |
| | Total impulse (transient, sea-level) | 76 537 | Ns |
| | Specific impulse (steady-state) | 215.16 | s |
| | Specific impulse (transient, sea-level) | 192 | s |
| | Nominal oxidiser mass flow rate | 2.898 | kg/s |
| | Nominal fuel mass flow rate | 0.537 | kg/s |
| | Total mass flow rate | 3.435 | kg/s |

*Updated to 1.2 mm after cold flow test.

4.4. Summary

The effect of aluminium and magnesium additives at various concentrations on motor and vehicle performance was quantified. Aluminium out-performed magnesium with a higher adiabatic flame temperature. Magnesium additive was found to have greater two-phase flow losses and mechanical erosion than aluminium additive, but with less chemical erosion. Vehicle inert mass and length decreases with increasing aluminium concentration, resulting in an increase in vehicle apogee, up to 9.3% with 50% aluminium concentration. Aluminium additive at 20% concentration by mass was selected for the PV-3 motor as a compromise, which reduces the O/F ratio from 6.8 to 5.4.

The motor diameter constraint posed a challenge in sizing the motor to simultaneously reach the target apogee whilst remaining within the safe oxidiser mass flux limit. A manual design method was employed, resulting in a motor peak thrust of 7250 N with a burn time of 14.2 s, at a peak chamber pressure of 40 bar. It is postulated that a total impulse limit exists with respect to motor diameter based on motor stability. The final propulsion system specifications are used to design the motor components, as described in Chapters 5 and 6. The final Computer Aided Design (CAD) model of the P-1B Mk II is shown in Figure 4-10.

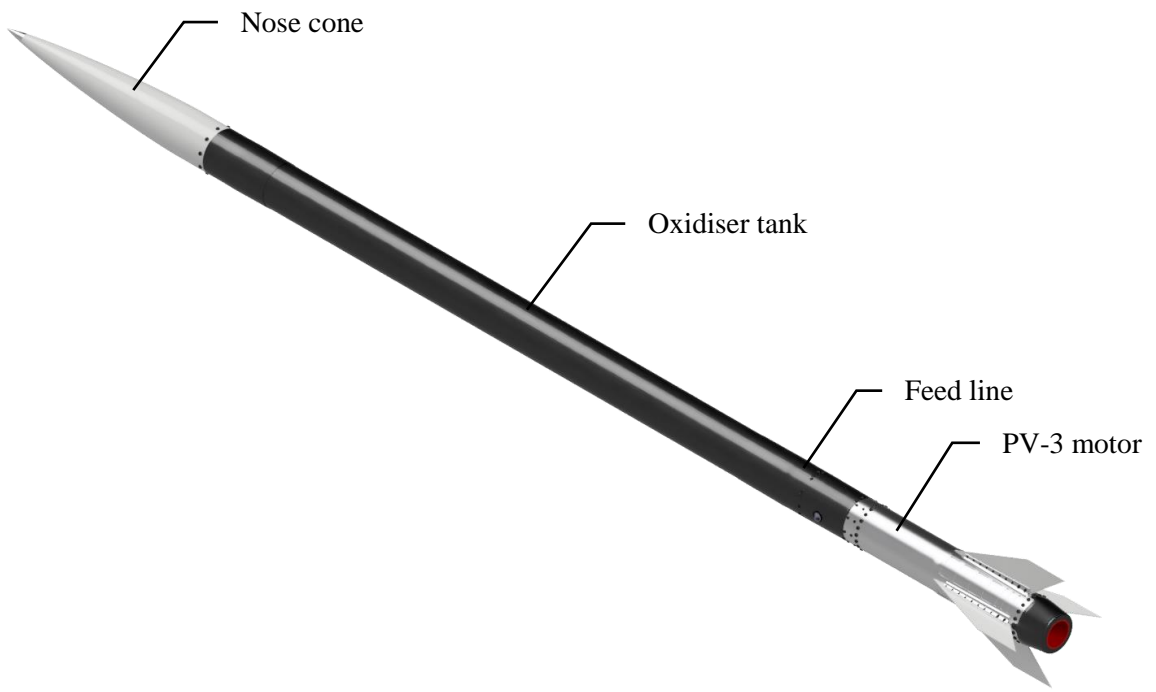


Figure 4-10: CAD model of the Phoenix-1B Mk II.

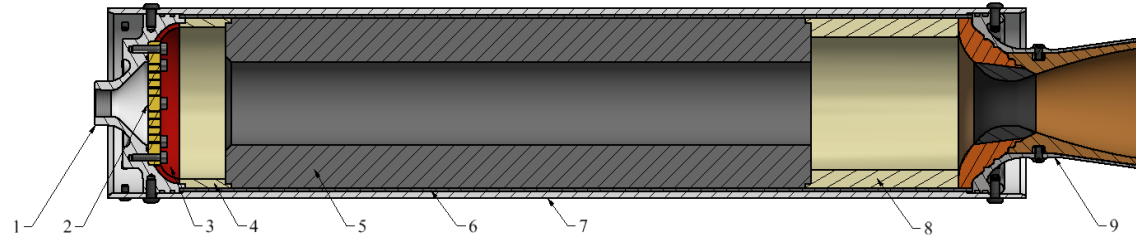
5. PV-3 MOTOR COMPONENT DESIGN

5.1. Introduction

This chapter describes the design and manufacture of the major components of the PV-3 motor, excluding the nozzle. Work focused on the design of the injector as it is critical to achieving the specified motor performance. The fuel grain cartridge development is also described.

5.2. PV-3 Motor Overview

The PV-3 motor cross-section is shown in Figure 5-1. The motor consists of an aluminium combustion chamber casing, an aluminium injector bulkhead, a copper axial injector plate, an ablative-cooled nozzle, a fuel grain cartridge, and a feedline connecting the oxidiser tank to the motor (not shown). Sealing of the combustion chamber to the injector bulkhead and nozzle is achieved with dual Viton O-ring seals. Radial cap screws secure the injector bulkhead and nozzle to the casing. The interstage coupler attaches to the chamber casing, above the injector bulkhead, via a coupling ring with two sets of radial cap screws.



1) Injector bulkhead, 2) Injector plate, 3) Bulkhead insulation, 4) Pre-combustion chamber insert, 5) Fuel grain, 6) Thermal liner, 7) Chamber casing, 8) Post-combustion chamber insert, 9) Nozzle.

Figure 5-1: Cross-section of PV-3 motor.

5.3. Combustion Chamber Casing

The purpose of the combustion chamber casing is to hold the fuel grain cartridge and to secure and seal the injector bulkhead and nozzle. The casing serves as the structural body of the motor, containing the motor components as well as the primary vehicle structure. It must withstand the chamber pressure and transmit the thrust load to the oxidiser tank. An available aluminium 6061-T6 tube was used, of 164 mm outer diameter and 5.5 mm wall thickness, for modularity with the nozzle structure. This was the primary constraint on the propulsion system design and sizing of the vehicle. A composite filament-wound combustion chamber casing was considered but rejected due to cost and time constraints. The material properties for aluminium 6061-T6 are provided in Table 5-1. Aluminium has no clearly identified yield point and thus the yield tensile strength was taken as 0.2% of the proof strength.

Table 5-1: Aluminium 6061-T6 properties (Aerospace Specification Metals, 2018).

| Property | Value | Unit |
|----------------------------------------|-----------------------|-------------------|
| Density | 2700 | kg/m ³ |
| Ultimate tensile strength | 310 | MPa |
| Yield tensile strength | 276 | MPa |
| Ultimate bearing strength | 607 | MPa |
| Yield bearing strength | 386 | MPa |
| Shear strength | 207 | MPa |
| Modulus of elasticity | 68.9 | GPa |
| Shear modulus | 26 | GPa |
| Poisson's ratio | 0.33 | - |
| Coefficient of linear expansion | 23.6×10^{-6} | m/m-K |
| Specific heat capacity | 896 | J/kg-K |
| Thermal conductivity | 167 | W/m-K |
| Melting point | 582-652 | °C |

Loading Conditions

The loading conditions experienced by the combustion chamber casing include internal pressure, acceleration, aerodynamic drag, thrust force, and thermal expansion. These loads peak at different points in time and are different for static testing and flight. The worst case loading occurs at motor start-up during static hot-fire testing, where the peak chamber pressure of 40 bar and thrust of 7250 N are experienced.

A conservative safety factor of 1.5 for the chamber casing and radial bolted joints was deemed adequate, considering the safety factor generally used for unmanned systems is 1.25. The maximum expected operating pressure (MEOP) was chosen as 60 bar to accommodate combustion instabilities.

5.3.1. Pressure Vessel Design

The combustion chamber casing was analysed as a cylindrical pressure vessel to determine if the available tube provided had an adequate safety factor. Both an analytical and numerical analysis was performed to verify the strength of the aluminium tube.

Analytical Design

Standard pressure vessel theory was used to calculate the stresses in the casing wall. The thickness-to-radius ratio is less than 0.1, allowing the use of thin-wall theory which assumes the stress is averaged over the wall thickness. The ideal hoop stress, longitudinal stress, and shear

stress equations are given below. Longitudinal stress is considered as this is an internal pressure vessel with capped ends. Radial stress is neglected as it is insignificant compared to hoop stress.

$$\sigma_{hoop} = \frac{pR}{t} \quad (5-1)$$

$$\sigma_{long} = \frac{pR}{2t} \quad (5-2)$$

$$\tau_{max} = \frac{-\sigma_h}{2} \quad (5-3)$$

In the above, σ_{hoop} is the hoop stress, σ_{long} is the longitudinal stress, τ_{max} is the shear stress, p is the pressure, R is the internal radius, and t is the wall thickness. These equations are only valid away from discontinuities that cause stress concentrations such as the bolted joint holes. The analytical results are summarised in Table 5-2 for both the standard wall thickness of 5.5 mm and for a reduced wall thickness of 3.95 mm, which occurs at the nozzle side of the casing. A minimum wall thickness of 2.5 mm is required for a safety factor of 1.5 at 60 bar MEOP. The safety factors are well above 1.5 for both cases, with the minimum being 2.33. The burst pressure is 198.43 bar and 139.68 bar for both cases respectively.

FEM Analysis

An axisymmetric finite element method (FEM) analysis was performed using Siemens NX™ 11. Figure 5-2 shows the revolved Von-Mises stress result from a 60 bar internal pressure load, and the results are given in Table 5-2. Only the hoop stress was an output since no capped ends were applied. The radial bolt holes cause stress concentrations which are analysed in the next section. The safety factors are in close agreement with the analytical results.

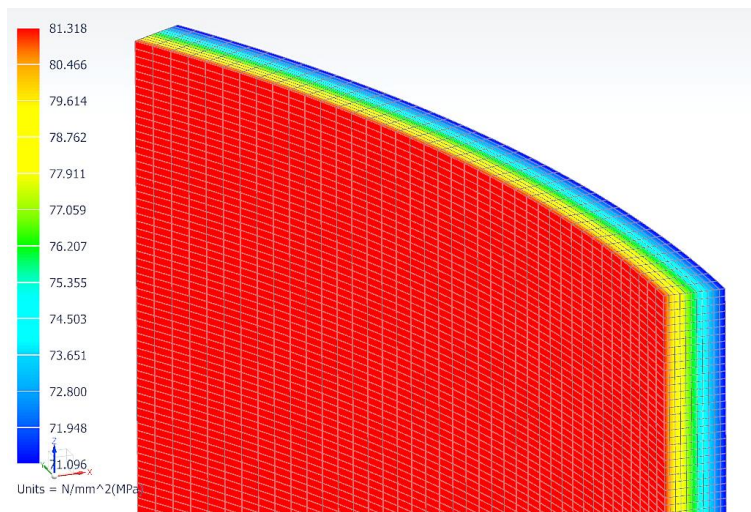


Figure 5-2: Revolved axisymmetric FEM analysis of chamber casing showing Von-Mises stress.

Table 5-2: Analytical and FEM results of chamber casing analysis.

| Parameter | 5.5 mm wall thickness | 3.95 mm wall thickness | Unit |
|------------------------------------------|--------------------------|---------------------------|------|
| Analytical results | | | |
| Hoop stress | 83.46 | 118.56 | MPa |
| Longitudinal stress | 41.73 | 59.28 | MPa |
| Shear stress (max., out-of-plane) | -41.73 | -59.28 | MPa |
| Safety factor (hoop) | 3.31 | 2.33 | - |
| Safety factor (longitudinal) | 6.61 | 4.66 | - |
| Safety factor (shear) | 4.96 | 3.49 | - |
| FEM results | | | |
| Hoop stress (Von-Mises) | 81.32 | | MPa |
| Shear stress | 46.28 | | MPa |
| Displacement | 0.0885 | | mm |
| Safety factor (hoop) | 2.951 | | - |
| Safety factor (shear) | 4.473 | | - |

5.3.2. Bulkhead Retention

Two methods of bulkhead retention were considered for the injector bulkhead and nozzle: the radial bolting and spiral locking ring methods. Welding was avoided due to bulging seen on the P-1A. The spiral locking ring method, desirable for its lack of bolt head protrusions, was abandoned due to testing done by Balmogim (2016) which indicated yielding of the aluminium tube groove. The radial bolting method was therefore chosen which allows for easy assembly and disassembly. The bolted joints for the interstage coupler were also considered.

Analytical Design

The worst case loading on the injector bulkhead and nozzle bolted joints was at a MEOP of 60 bar during hydrostatic pressure testing. In reality the nozzle side will experience less loading since it has a throat opening. The worst case loading experienced by the interstage coupler bolted joints is during static hot-fire testing with a peak thrust of 7250 N expected. The bolted joints are primarily loaded in shear with the major failure modes comprising:

1. Bolt single shear
2. Bearing deformation of bolt hole
3. Shear-out from bolt hole to edge (shear failure)
4. Tear-out between two bolt holes (tensile failure)
5. Compression of casing wall by bolt head from bolt preload

SAE Grade 10.9 button head cap screws were used for the radial bolts, with proof and yield strengths of 830 MPa and 940 MPa respectively. The shear strength was assumed to be 60% of the yield strength. The large difference in strength between the high tensile bolts and the weaker thin aluminium casing resulted in the casing strength being the limiting factor. Twenty M8 cap screws were found to be sufficient to resist all failure modes whilst maintaining a safety factor of 1.5, for the injector bulkhead and nozzle. Ten M6 cap screws were found to be sufficient for the interstage coupler bolted joint. The number, size, and spacing between the bolt holes were chosen to ensure no failure mode was encountered, with the primary failure mode being bolt hole bearing stress. An edge-to-hole ratio and hole-to-hole ratio of at least 2 was maintained to prevent hole shear-out and tear-out.

Table 5-3 summarises the safety factors calculated via analytical bolted joint theory for each failure mode. It should be noted that the casing wall thickness is reduced to 4.1 mm at the injector bulkhead and interstage coupling, and 3.95 mm at the nozzle bolted joints due to inner diameter machining and bolt hole spot-facing.

A bolt preload was also imposed to help keep the bolted joints rigid, thus preventing separation, ensuring sealing, and preventing bolt loosening. It also introduces a frictional force which reduces the bearing stress on the hole and shear stress in the bolt, further strengthening the joint. The bolt preload is however limited by the compressive stresses on the casing wall from the bolt head and by the thread shear in the aluminium bulkhead and interstage coupler. A preload of 6 kN or 9.72 Nm torque for the injector bulkhead and nozzle bolts, and 4.1 kN or 6.67 Nm for the interstage coupler bolts was found to be adequate.

Table 5-3: Safety factors for failure modes present on bolted joints of injector bulkhead, nozzle and interstage coupler.

| Joint failure modes | Injector bulkhead | Nozzle | Interstage coupler |
|---------------------------------|-------------------|-----------|--------------------|
| | (M8 bolt) | (M8 bolt) | (M6 bolt) |
| Bolt shear | 3.74 | 3.74 | 15.64 |
| Hole bearing deformation | 1.64 | 1.58 | 9.37 |
| Hole shear-out | 2.97 | 2.86 | 14.05 |
| Hole tear-out | 3.60 | 3.47 | 79.60 |
| Wall compression | 4.71 | 4.71 | 4.65 |

FEM Analysis

A FEM analysis was performed using Siemens NX™ 11 to verify the analytical design. A three dimensional (3D) cyclic-symmetry assembly of the chamber casing, simplified injector bulkhead,

and interstage coupler with simplified bolts is shown in Figure 5-3. An assembly analysis allows for a more realistic contact between the bolts and the casing holes.

Mesh refinement was applied to the bolt hole regions to capture the bearing stress. Symmetry constraints were applied to the cyclic symmetry planes as well as the bottom of the casing wall. Face contacts were applied between the bolt shanks and bolt holes, bolt heads and casing walls, and between the casing wall, bulkhead, and interstage coupler. Static friction coefficients were applied to all contacts. Face gluing was used to model the contacts between the bolt external thread and the bulkhead internal thread. A 60 bar pressure load was applied to all internal surfaces and a 725 N force load (one-tenth symmetry) was applied to the top of the interstage coupler. A bolt preload of 6 kN each was applied to the M8 bolts.

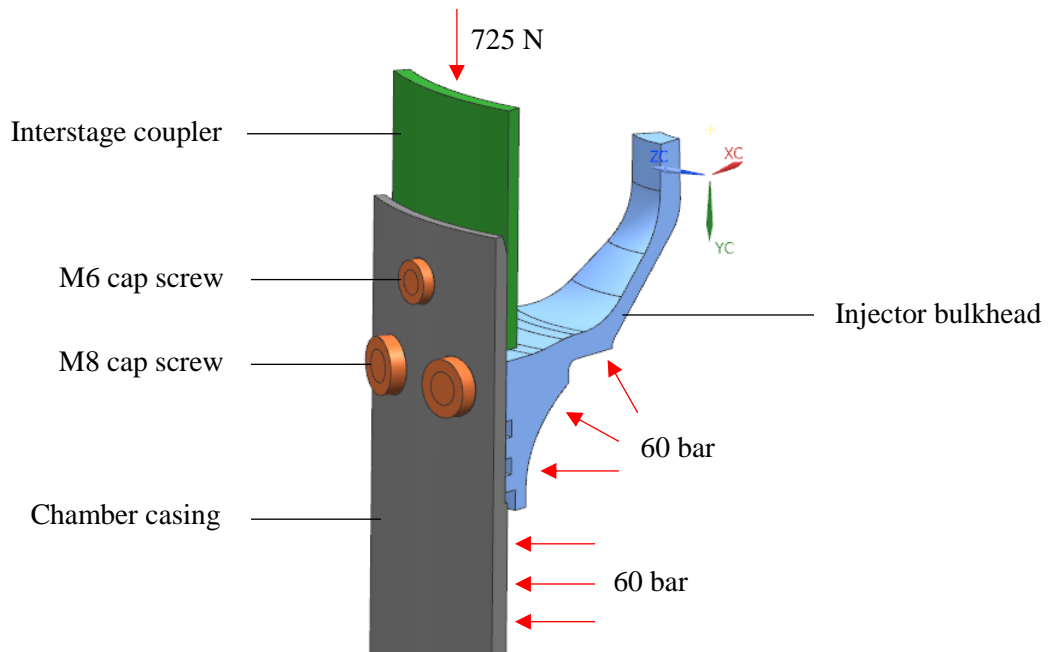


Figure 5-3: 3D cyclic-symmetry assembly of casing, injector bulkhead, interstage coupler, and simplified bolts.

Figure 5-4 (a) and (b) show the Von-Mises stress of the casing wall in the vicinity of the bolt holes with no preload applied, while Figure 5-4 (c) and (d) show the Von-Mises stress with a 6 kN bolt preload. The red zones represent local yielding. The preload can be seen to have reduced the bearing stress at the top of the holes and between the holes, while increasing the compressive stress on the inside wall. The preload strengthens the joint with respect to hole bearing, hole shear-out, and hole tear-out due to the greater friction force generated between the bolt, casing wall, and bulkhead. Both cases provide a safety factor of 1.5 for the casing wall, with the 6 kN preload chosen. A preload is also essential to ensure a concentric seal is obtained since the machined casing ends exhibited ovality.

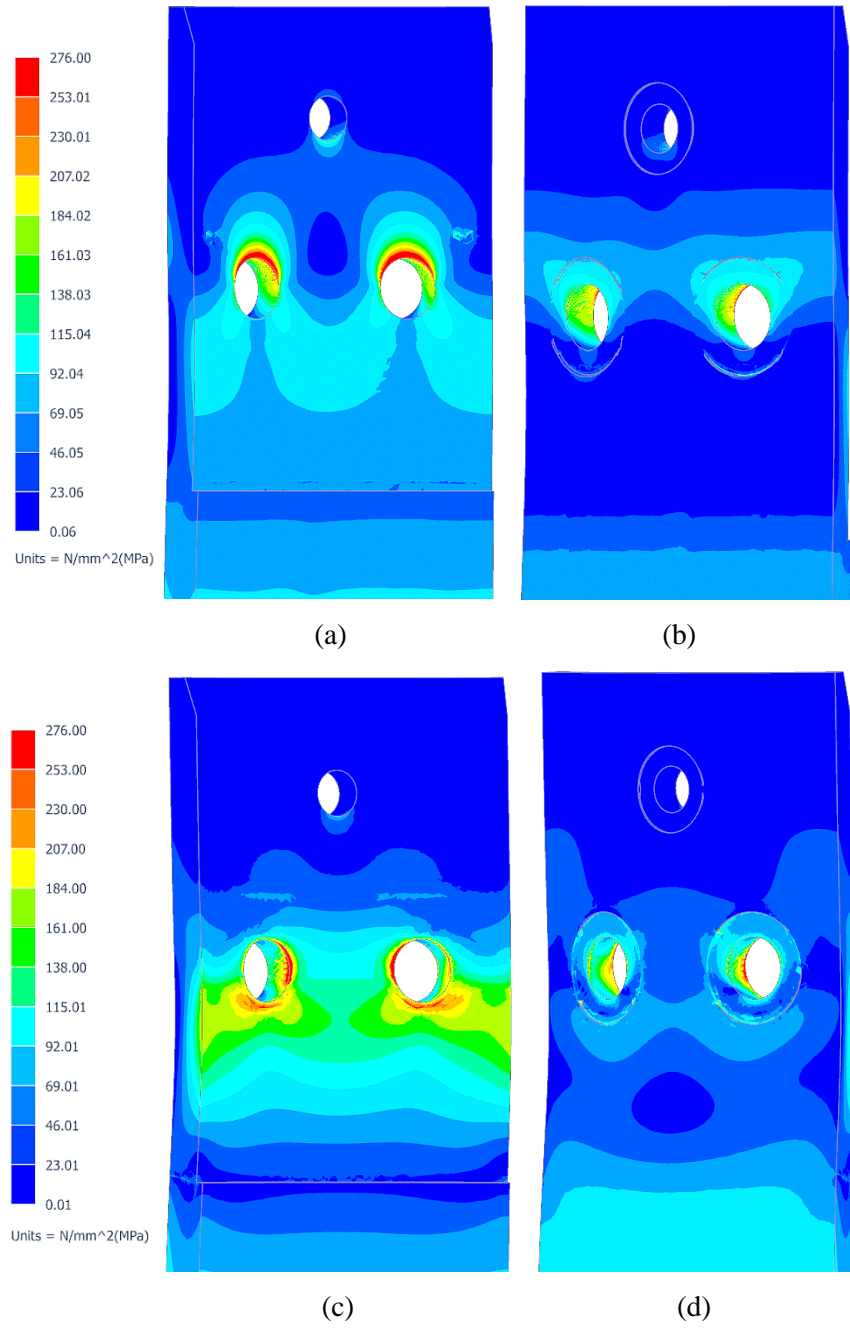


Figure 5-4: Von-Mises stress on casing wall for (a) internal wall (no preload), (b) external wall (no preload), (c) internal wall (6 kN preload), and (d) external wall (6 kN preload) (capped at 276 MPa).

5.3.3. Manufacture and Pressure Testing

The aluminium tube used for the casing exhibited diametrical ovality and slight axial bending, of approximately 0.14° off axis. To ensure a concentric seal with the O-rings, the casing ends were internally machined, but still exhibited 0.4 mm (0.26%) and 0.1 mm (0.06%) of ovality at the injector bulkhead and nozzle sides respectively. Figure 5-5 shows the final combustion chamber casing and assembled PV-3 motor.



(a)



(b)

Figure 5-5: (a) Combustion chamber casing and (b) motor assembly with injector bulkhead and nozzle.

The combustion chamber casing was hydrostatically pressure tested with water to verify its structural integrity and to ensure there were no leaks at the O-ring seals. Figure 5-6 shows the assembled combustion chamber with the injector bulkhead and blank bulkhead on the nozzle side. It was pressure tested to 60 bar and held for 1 minute with no leaks observed.



Figure 5-6: Hydrostatic pressure test setup of combustion chamber with bulkheads attached.

5.4. Injector Bulkhead Assembly

The injector bulkhead assembly consists of the injector bulkhead and the injector plate. These components were designed simultaneously since they are structurally coupled.

5.4.1. Bulkhead Design

The purpose of the injector bulkhead is to seal the fore end of the combustion chamber, secure the injector plate, and provide a manifold for the oxidiser from the feedline to the injector plate. A pressure tap is also required through the bulkhead to obtain the chamber pressure. The injector plate is fastened and axially sealed to the bulkhead with a Viton O-ring.

Material Selection

The materials considered for the bulkhead were aluminium and stainless steel. Aluminium alloy 7075-T6 was chosen due to its superior strength-to-weight ratio compared to other aluminium alloys and stainless steels. It has excellent machinability, cannot be welded, and is susceptible to localised corrosion, therefore anodising is recommended. Table 5-4 gives the material and mechanical properties for aluminium 7075-T6 as well as strength values taken from the material test certificate, given in Appendix F. Hardness testing was performed to verify the heat treatment consistency in the billet, given in Appendix F.

Table 5-4: Aluminium 7075-T6 properties (Aerospace Specification Metals, 2018), specifications in parenthesis from material test certificate (Metal and Tool Trade, 2015).

| Property | Specification | Unit |
|------------------------------------------------------|-----------------------|-------------------|
| Density | 2810 | kg/m ³ |
| Ultimate tensile strength | 572 (564.24) | MPa |
| Yield tensile strength | 503 (478.32) | MPa |
| Shear strength | 331 (296.55*) | MPa |
| Modulus of elasticity | 71.7 | GPa |
| Shear modulus | 26.9 | GPa |
| Hardness | 53.5 (50) | HRA |
| Poisson's ratio | 0.33 | - |
| Coefficient of linear expansion (20 – 300 °C) | 25.2×10^{-6} | m/m-K |
| Specific heat capacity | 960 | J/kg-°C |
| Thermal conductivity (25 °C) | 130 | W/m-K |
| Melting point | 477-635 | °C |

*Calculated as 62% of yield strength from test certificate.

Analytical Design

The bulkhead design was initially analysed as a pressure vessel head. A 2:1 ellipsoidal head shape was selected as this is a good compromise between head length, head thickness and stress distribution. For a 2:1 ellipsoidal head, the minimum thickness required is calculated as follows (Megyesy, 2001):

$$t = \frac{pD}{2SE - 0.2p} \quad (5-4)$$

where p is the design pressure, D is the inside diameter, S is the yield tensile strength (taken as 478 MPa) and E is the joint efficiency (taken as 1). A minimum thickness of 1.3 mm was calculated for a MEOP of 60 bar, a safety factor of 1.5, and an inside diameter of 139 mm. The minimum bulkhead thickness was increased to 5 mm for manufacturability. With this thickness a maximum allowable working pressure of 341 bar was found with a maximum stress of 84 MPa.

Figure 5-7 shows the injector bulkhead isometric CAD model and cross-section. The injector plate was recessed into the bulkhead to promote a smooth recirculation zone in the pre-combustion chamber and to remove stagnant flow areas. The bulkhead features twenty M8 threaded holes, two O-ring sealing grooves on its outer diameter, a $\frac{3}{4}$ " National Pipe Thread (NPT) hole in the centre to accommodate the feedline fitting, and a $\frac{1}{4}$ " NPT hole to accommodate the pressure sensor fitting.

There are eight threaded holes in the bosses to accommodate M6 cap screws for injector plate retention. An axial O-ring groove seals the bulkhead manifold from the combustion chamber. Ribs were added between the M6 vertical hole bosses with four M10 holes for the bulkhead assembly tool. The bulkhead features a 45° diffuser which forms the manifold for the oxidiser to spread out to the injector plate orifices.

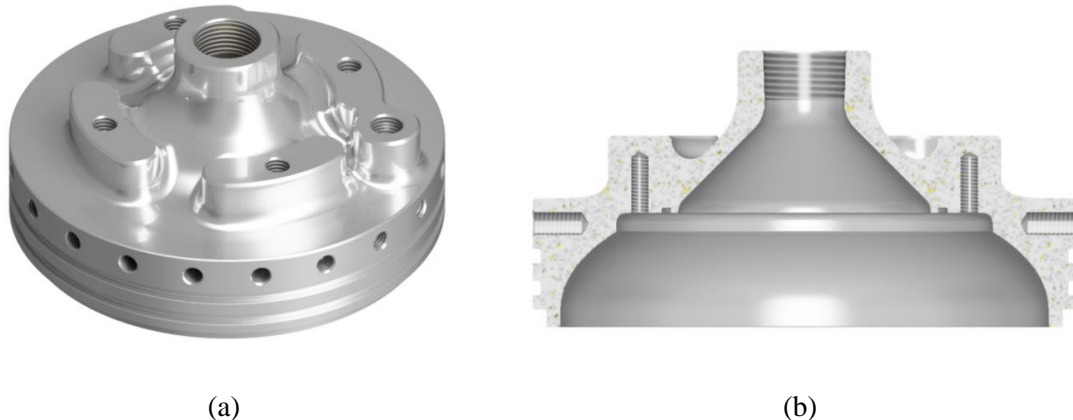


Figure 5-7: Injector bulkhead CAD model (a) isometric and (b) cross-section.

FEM Analysis

A FEM analysis was performed to verify the strength of the injector bulkhead design. A simplified complete model was imported into Siemens NX™ 11. Mesh refinement was applied to the bolt holes, O-ring groove, and fillets of the bosses. The bolt holes were split to allow a cylindrical constraint to be applied to the bottom half of the holes, and a cylindrical constraint was applied to the outer circumferential surface to model the presence of the casing. Three load conditions were analysed: pressure testing with 60 bar pressure applied to the internal surface, cold-flow testing with 65 bar pressure applied to the top half of the internal surface, and hot-fire testing with 65 bar pressure on the top half and 60 bar MEOP to the bottom half of the surface.

Figure 5-8 shows the Von-Mises stress distribution on the injector bulkhead for the hot-fire loading condition, capped at the yield strength of aluminium 7075-T6. The peak stress seen at the end of the radial bolt holes is due to the rigid cylindrical constraints. The bulkhead is not significantly stressed with a minimum safety factor of 2.78 for the hot-fire loading condition. Peak stresses of 147 MPa and 172 MPa are experienced on the top boss fillet and bottom injector mounting fillet respectively. It should be noted that with the preloaded injector bolts, the stresses on these two zones will decrease.

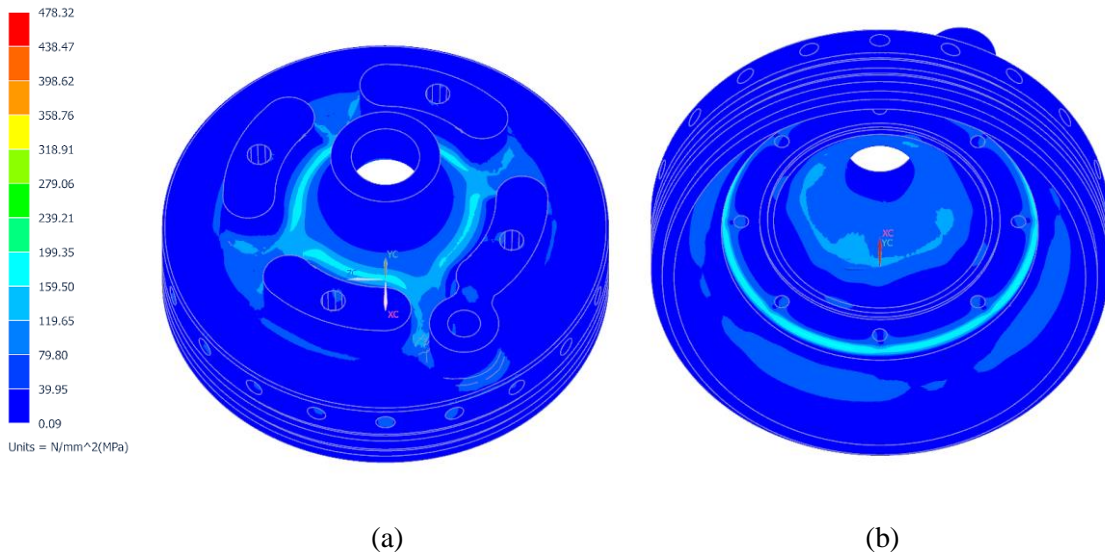


Figure 5-8: Von-Mises stress of the injector bulkhead (a) top view and (b) bottom view (capped at 478.32 MPa).

5.4.2. Injector Plate Design

The structural design of the injector plate and its retention method was undertaken in conjunction with the design of the injector bulkhead due to their proximity and transfer of stress between parts. The injector configuration, geometry and orifice sizing and distribution are discussed in section

5.6. An axial flow injector plate was chosen for the injector type with a preliminary orifice diameter of 1 mm.

Material Selection

Copper was selected for the injector plate material for its high thermal conductivity compared to other candidates such as brass, aluminium or stainless steel. This reduces the probability of hot-spots occurring over the plate. Table 5-5 gives the properties of copper CDA110 ETP (Electrolytic Tough Pitch) in the half-hard condition (H02) obtained as a flat hot-rolled plate.

Table 5-5: Copper CDA 110 (ETP) H02 properties (Non-Ferrous Metals, 2018), specifications in parenthesis from material test certificate (Non-Ferrous Metals, 2017).

| Property | Specification | Unit |
|-------------------------------------------------------|-----------------------|-------------------|
| Density | 8910 | kg/m ³ |
| Ultimate tensile strength | 290 (258) | MPa |
| Yield tensile strength | 248 (255) | MPa |
| Shear strength | 180 | MPa |
| Modulus of elasticity | 117 | GPa |
| Shear modulus | 44.13 | GPa |
| Poisson's ratio | 0.33 | - |
| Hardness Rockwell A | 31 | HRA |
| Coefficient of thermal expansion (20 - 100 °C) | 16.9×10^{-6} | m/m-K |
| Specific heat capacity (20 °C) | 393.5 | J/kg-K |
| Thermal conductivity (20 °C) | 391.1 | W/m-K |
| Melting point | 1083 | °C |

Analytical Design

The injector plate was treated as a flat circular pressure vessel head for the initial analytical design. The worst case loading condition is during a cold-flow test when 65 bar pressure is applied to the top of the plate with a pressure drop to atmosphere. A plate thickness of about 8.2 mm was obtained using the following equation (Moss, 2004):

$$t = D \sqrt{\frac{0.3p}{SE}} \quad (5-5)$$

In the above, D is the inside diameter, p is the internal pressure, S is the yield strength of the material and E is the joint efficiency. The bolt pitch circle diameter (PCD) of 93.8 mm was used for the internal diameter and a joint efficiency of 1 was used. The peak bending stress at the centre of the plate was calculated as follows (Moss, 2004):

$$\sigma_b = \pm \frac{3(3 + \nu)}{8} \left(\frac{pD^2}{4t^2} \right) \quad (5-6)$$

where ν is the poisons ratio of copper, p is the internal pressure, D is the inside diameter, and t is the head thickness. An 11 mm thick plate was finally selected based on the FEM analysis resulting in a bending stress of 147.6 MPa at the centre of the plate and a safety factor of 1.73.

Injector Plate Retention

Axial cap screws in threaded holes were chosen for injector plate retention method for simplicity, reliability, and easy disassembly. The failure modes present in this joint design are screw failure in tension and thread stripping of the aluminium threaded holes. It is desirable to have the screw fail in tension before thread stripping occurs. A safety factor of 1.25 was deemed acceptable in this case due to the reliability of the expected loading.

Table 5-6 gives the injector applied loads and joint safety factors. Eight grade 10.9 M6 screws were specified with each screw experiencing a maximum axial force of 13.47 kN at a 10 kN preload (60% of proof strength). The screw axial load and clamping force were calculated taking into account the relative stiffness between the screw and clamping member. A 60% preload was selected to reduce the shear stress on the aluminium threads in the threaded holes to prevent thread stripping. A preload was also required to generate a clamping force such that the plate does not separate from the bulkhead, maintaining the O-ring seal. The clamping force of 9.7 kN per screw is more than double the applied load of 3.78 kN.

The female aluminium thread in the bulkhead is weaker than the screw thread, therefore the required thread engagement length was calculated using Equation 5- 7:

$$L_{min} = \frac{0.7454(D - 0.9382P)^2 \sigma_{yb}}{0.34875\pi(D - 0.54127P)\sigma_{yn}} \quad (5-7)$$

where L_{min} is the minimum thread engagement length, D is the screw nominal diameter, P is the thread pitch, σ_{yb} is the yield strength of the bolt, and σ_{yn} is the yield strength of the nut material. Assuming the shear strength as 62% of the yield strength (Fernando, 2001), a minimum engagement length of 6.3 mm was found. The load is however not evenly distributed between the threads, so Heli-Coil™ thread inserts were utilised. These balance out the difference in bolt tensile strength and aluminium yield strength, and ensure that the screw fails prior to thread shear.

The tensile strength of the Heli-Coil™ insert assembly was found using the M6 screw graph, given in Appendix G (Stanley, 2018). The 2-diameter length insert was chosen for a shear strength of 296.55 MPa and a screw ultimate tensile strength of 1040 MPa, resulting in an assembly tensile strength of 51 kN and a safety factor of 3.78.

Table 5-6: Injector plate joint design per screw.

| Parameter | Value | Unit |
|-----------------------------------------------|-------|------|
| Applied load | 3.78 | kN |
| Screw preload | 10 | kN |
| Screw axial load | 13.47 | kN |
| Clamping force | 9.7 | kN |
| Max. bolt load (yield) | 18.9 | kN |
| Thread pull-out force (2-Diam. insert) | 51 | kN |
| Screw safety factor (on yield) | 1.40 | - |
| Thread safety factor | 3.78 | - |

Figure 5-9 shows an isometric sectioned CAD model of the injector bulkhead assembly and Figure 5-10 shows the final injector plate CAD model. A 4 mm thick layer of Room Temperature Vulcanising (RTV) silicone was applied to the internal surface of the bulkhead to counter radiative heating.

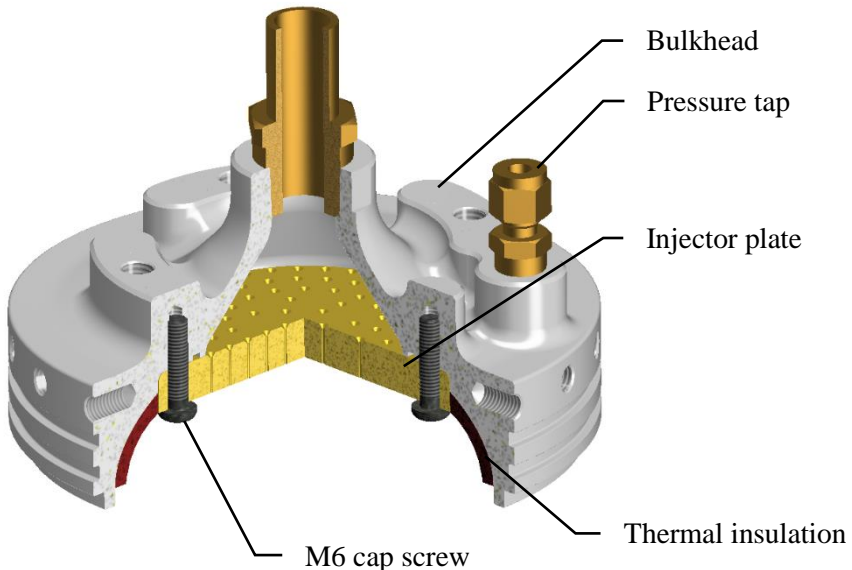


Figure 5-9: Sectioned view of injector bulkhead assembly.

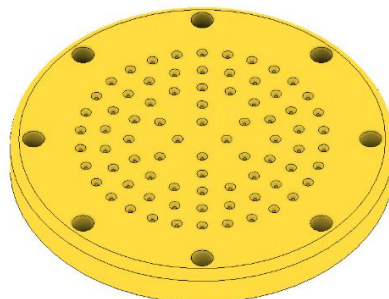


Figure 5-10: Injector plate.

Assembly FEM Analysis

An assembly FEM analysis was performed with the injector plate fastened to the bulkhead. A one-eighth cyclic-symmetry model was used, shown in Figure 5-11, which represents geometric, loading, and constraint symmetry with respect to the injector plate, but not the bulkhead radial holes. The radial bolt hole constraints were found to have a negligible effect on the stresses on the injector plate.

Two loading conditions were considered: for cold-flow, a pressure of 65 bar was applied to the top of the injector plate and bulkhead and 1.0325 bar at the bottom of the plate and bulkhead, and the hot-fire condition has the addition of a 40 bar pressure load to the bottom the injector plate and bulkhead.

The radial threaded holes had a cylindrical constraint (radial only) applied to the bottom half of the hole and only for the length of the engaged thread. A cylindrical constraint (radial only) was applied to the outside diameter of the bulkhead to represent the casing internal wall. Surface-to-surface contact was set up between the plate and the bulkhead with static friction modelled. The plate was constrained to the bulkhead with the use of one dimensional (1D) bolted joints that consist of CBAR elements to represent the bolt shank and rigid body (RBE2) spider elements to model the bolt head and thread engagement in the tapped hole. The use of the 1D bolted joint model is applicable in this case since there is no shear or bearing stress and it is more computationally efficient. A bolt preload was applied to the CBAR element.

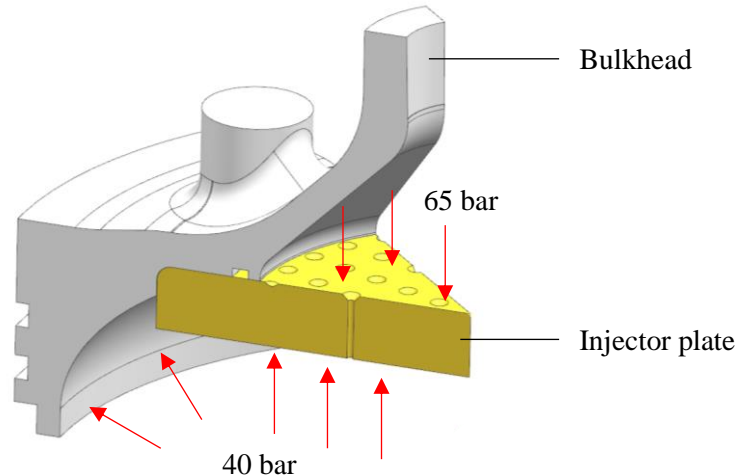


Figure 5-11: Assembly model of injector plate and injector bulkhead.

Figure 5-12 gives the displacement results for both loading conditions which show how the assembly reacts, and Figure 5-13 shows the Von-Mises stress distribution on the injector plate. The peak stress of concern is at the top and bottom of the centre of the plate caused by bending stress.

Table 5-7 summarises the results of the FEM analysis. For a 10 kN bolt preload, the peak stress is 126 MPa and 27 MPa at the centre of the injector plate for the cold flow and hot-fire conditions respectively, corresponding to a minimum safety factor of 2.02. The plate loading is worse in the cold-flow condition due to the higher pressure drop. The bulkhead loading is greater in the hot-fire condition, with a higher stress of 265 MPa at the inside fillet compared to the single part FEA, due to contact with the plate. However, the stress at the fillet on the top of the bulkhead decreased which could be attributed to the presence of the preloaded 1D bolts.

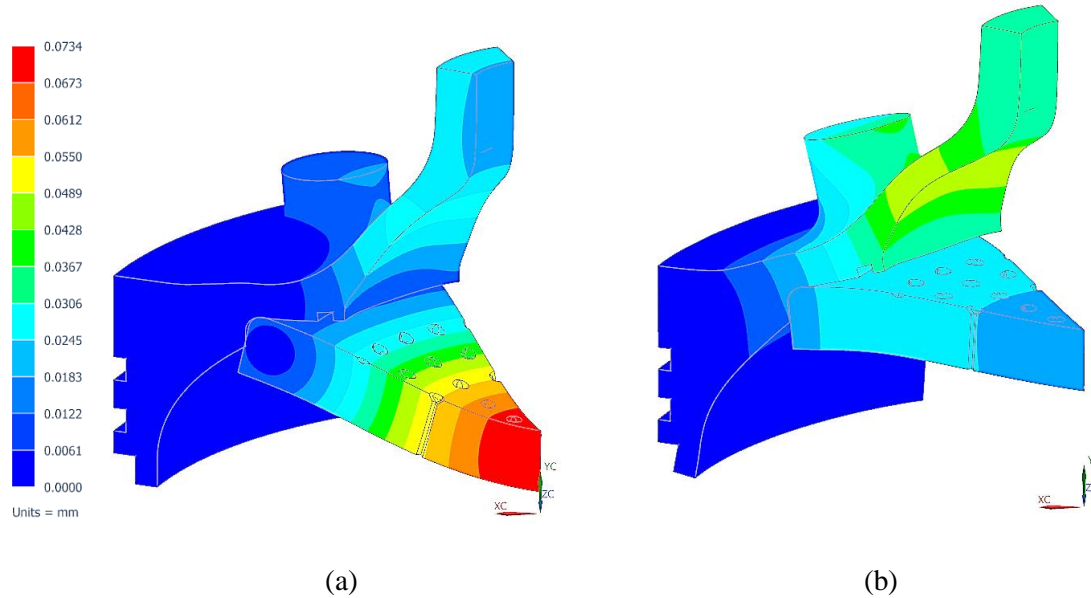


Figure 5-12: Displacement (10% of model) of injector bulkhead assembly FEA for (a) cold-flow condition and (b) hot-fire condition, with a 60% preload.

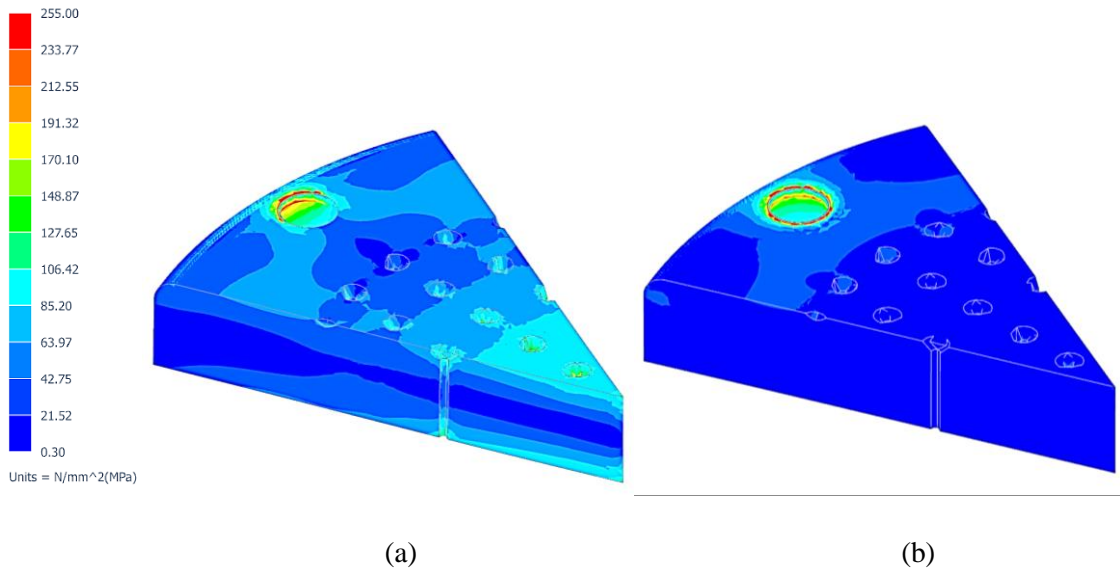


Figure 5-13: Von-Mises stress (capped at yield stress) of injector plate for (a) cold-flow condition and (b) hot-fire condition, with a 60% preload.

Table 5-7: Results of the injector bulkhead assembly FEA with a 60% preload.

| Parameters | Cold flow | Hot-fire | Unit |
|-------------------------|-----------|----------|------|
| Injector plate | | | |
| Von-Mises Stress | 126.08 | 27.33 | MPa |
| Displacement | 0.0734 | 0.027 | mm |
| Safety factor | 2.02 | 9.33 | - |
| Bulkhead | | | |
| Von-Mises Stress | 265.70 | 146.93 | MPa |
| Displacement | 0.0258 | 0.0465 | mm |
| Safety factor | 1.80 | 3.25 | - |

Preload Study

A study was performed on the 1D bolt joint in order to determine the preload. Excessive preload can crush the aluminium bulkhead or the copper plate and risk thread stripping, while insufficient preload can put the injector plate under excessive bending stress. Table 5-8 shows the effect of the preload on the stress and displacement of the injector plate. For both conditions, the stress at the centre of the plate can be seen to decrease with an increase in preload. All preloads provide an adequate safety factor with the 60% preload selected, corresponding to a 10 kN force or 12 Nm torque.

Table 5-8: Results from the preload study.

| Preload | Von-Mises stress (MPa) | | Displacement (mm) | | Safety factor | |
|----------------------|------------------------|----------|-------------------|----------|---------------|----------|
| | Cold-flow | Hot-fire | Cold-flow | Hot-fire | Cold-flow | Hot-fire |
| 0% (0 N) | 179.50 | 51.56 | 0.1260 | 0.0197 | 1.42 | 4.95 |
| 40% (6673 N) | 143.74 | 29.29 | 0.0897 | 0.0244 | 1.77 | 8.71 |
| 50% (8342 N) | 134.27 | 27.80 | 0.0810 | 0.0258 | 1.90 | 9.17 |
| 60% (10010 N) | 126.08 | 27.33 | 0.0734 | 0.0270 | 2.02 | 9.33 |
| 70% (11678 N) | 119.57 | 27.34 | 0.0670 | 0.0281 | 2.13 | 9.33 |
| 80% (13346 N) | 115.81 | 27.88 | 0.0634 | 0.0291 | 2.20 | 9.15 |

5.4.3. Manufacture and Pressure Testing

Figure 5-14 (a) and (b) show the final injector bulkhead assembled with the brass oxidiser ball valve and the copper injector plate. The injector plate orifices were wire-cut using an Electrical Discharge Machining (EDM) process.

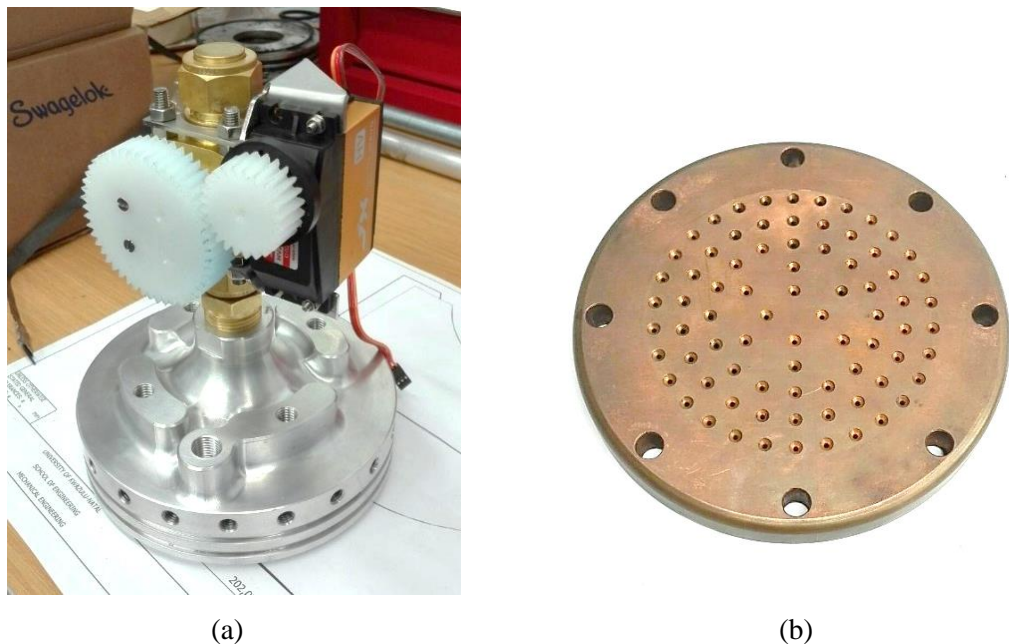


Figure 5-14: (a) Injector bulkhead assembly and (b) Injector plate.

The injector bulkhead assembly was hydrostatically pressure tested to verify the structural integrity of the copper injector plate and the preloaded cap screw joints. A blank injector plate with no orifices was made for this purpose. Figure 5-15 (a) and (b) show the assembled bulkhead and blank injector plate which was pressure tested to 70 bar and held with no leaks or failure.

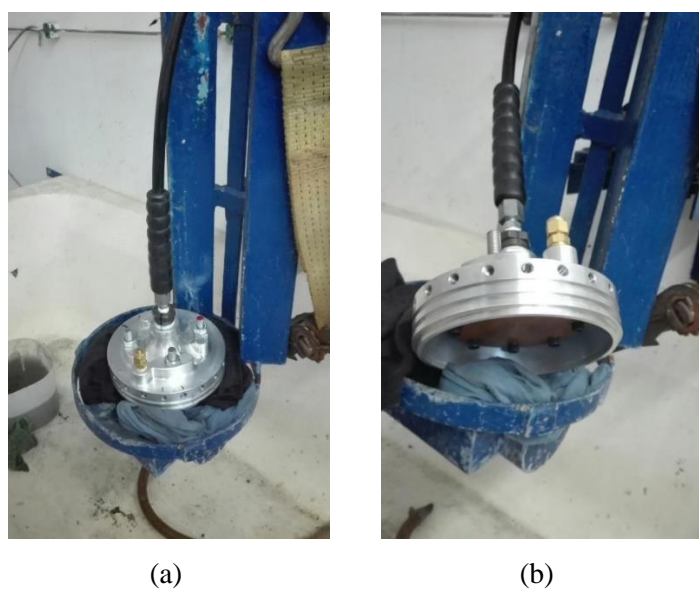


Figure 5-15: Hydrostatic pressure test setup of (a) injector bulkhead and (b) injector bulkhead.

5.5. Feed System Design

The feed system consists of the tubing, fittings, instrumentation, and an oxidiser valve which connects the oxidiser tank to the combustion chamber. It is used for filling and monitoring the oxidiser tank and allowing the oxidiser to flow to the injector plate. Only the oxidiser valve and its actuation were designed in this work, with the rest designed by Williams (2018).

5.5.1. Oxidiser Valve and Feedline Sizing

A feedline and oxidiser valve diameter of $\frac{3}{4}$ " was selected, this being limited by the combustion chamber diameter constraint. With a nominal oxidiser mass flow rate of 2.898 kg/s in a $\frac{3}{4}$ " feedline, a relatively high flow velocity of 21.75 m/s is obtained. A high flow velocity results in higher than desired frictional losses in the feedline and increases the risk of nitrous oxide decomposition as local heating may result from increased frictional heating, adiabatic compression, and particle impingement. The P-1A operated with an initial pipe flow velocity of 27 m/s which suggests that nitrous oxide may have a higher flow velocity limit than LOX at 12.3 m/s at 65 bar (European Industrial Gases Association, 2012). Since a blowdown system is being used, the flow velocity rapidly decreases.

It has been observed that the potential for decomposition is more closely coupled to the quenching characteristics of the system, namely the temperature, pressure, and pipe size, than the initial decomposition energy (Gas Industries Association, 2014). Figure 5-16 shows the decomposition propagation threshold of nitrous oxide for various pipe sizes. Smaller pipe diameters have a larger internal surface area-to-volume ratio and thus lose more heat per unit volume to the pipe wall. Therefore, smaller pipe diameters have higher decomposition propagation thresholds. Although the $\frac{3}{4}$ " pipe size is not shown, the operating point is close to its interpolated propagation threshold, and is therefore considered acceptable.

Precautions were taken to mitigate the risk of decomposition by following a strict cleaning procedure, opening the ball valve slowly to reduce adiabatic compression, and minimising dead volumes in the feed line.

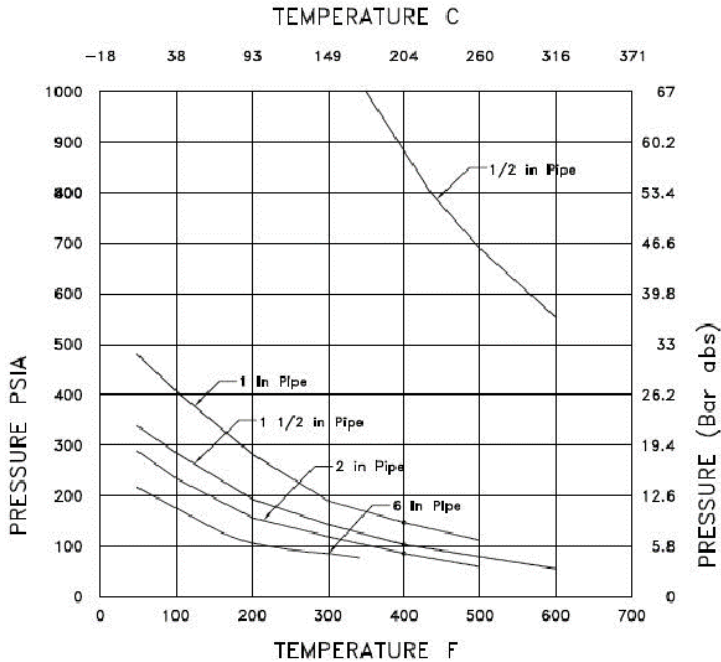


Figure 5-16: Propagation threshold for nitrous oxide in various pipe sizes (Gas Industries Association, 2014).

5.5.2. Feedline Losses

Table 5-9 gives the calculated theoretical pressure drops for a $\frac{3}{4}$ " feedline at both the start-up and average motor conditions. A total feedline pressure drop of 2 bar at start-up flow conditions results in a theoretical pressure at the injector plate of about 63 bar. Therefore, for a 40 bar nominal chamber pressure, an initial injector pressure drop of about 23 bar is required.

Table 5-9: Feedline pressure drop for a $\frac{3}{4}$ " feedline at start-up and average flow conditions.

| Type | Pressure drop (bar) | |
|-------------------------------------|---------------------|---------|
| | Start-up | Average |
| Major losses | 0.2085 | 0.0874 |
| Minor losses | 1.7945 | 0.7986 |
| Dynamic pressure | 0.0029 | 0.0016 |
| Total feedline pressure drop | 2.0030 | 0.8876 |

5.5.3. Oxidiser Valve Actuation

The oxidiser valve comprises a Swagelok $\frac{3}{4}$ " three piece brass ball valve with an opening torque of 6.6 Nm at 68.9 bar (Swagelok, 2016). A JXTM PDI-HV2060MG 180° digital servo motor with a 2:1 reduction gear set was used, to provide a stall torque of 12.2 Nm. This also slows down the opening of the valve to mitigate the risk of adiabatic compression heating. An ArduinoTM Pro

Micro was used as the microcontroller with the servo powered by a 7.4 V power supply. The Arduino™ board receives open and close commands from two 5V logic signals from the National Instruments™ CompactRIO™ into rising edge interrupt pins. The control schematic is given in Appendix H.

Figure 5-17 shows a CAD model of the feedline, ball valve, servo motor, and reduction gear set assembly. The gears were manufactured from nylon and the servo motor bracket was designed, laser cut, and bent from 2 mm thick stainless steel. The pressure transducers for tank and chamber pressures are WIKA™ A-10's (100 bar) and a K-type thermocouple is used for the tank temperature.

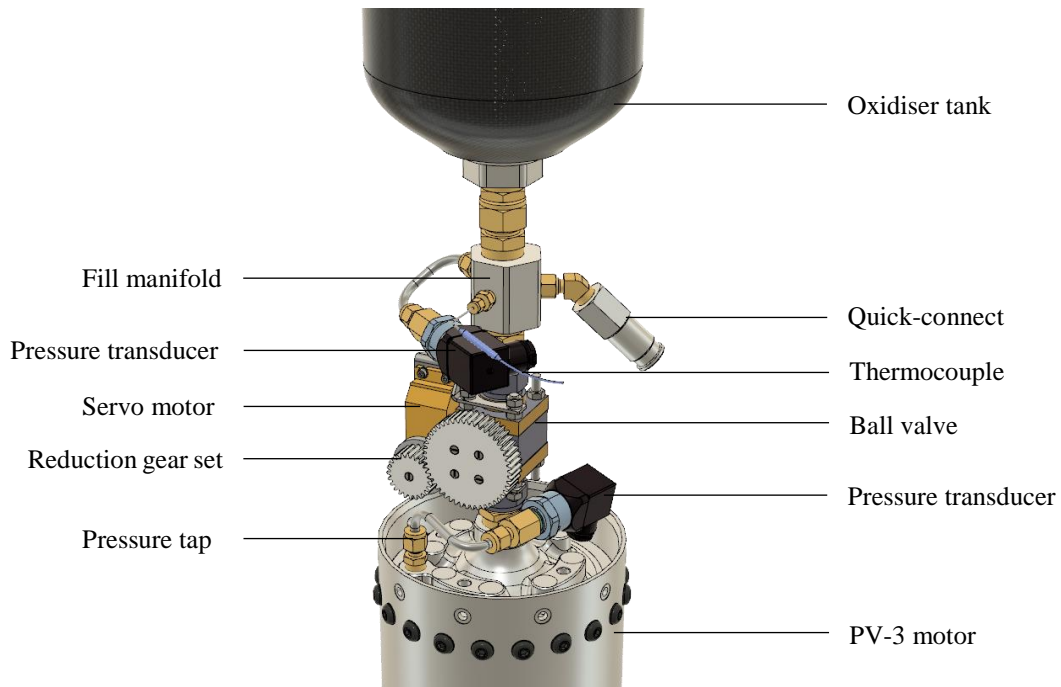


Figure 5-17: Feedline and ball valve actuation mechanism assembly.

5.6. Injector Design

The purpose of the injector is to atomise and distribute the oxidiser into the combustion chamber, while delivering the specified oxidiser mass flow rate to achieve the nominal O/F ratio and thrust. It is a critical component in a hybrid motor as it can significantly affect the overall behaviour including the regression rate, uniformity, combustion efficiency, and stability.

5.6.1. Injector Configuration

Hybrid rocket motors generally use three types of injector configurations: axial, impinging, and swirl. Axial or showerhead injectors deliver the oxidiser in axial, non-impinging streams emerging normal to the injector face. They are simple, cost effective and easily manufactured but

typically provide non-uniform regression rates along the fuel grain, and they rely on turbulence and diffusion to achieve mixing. Impinging or conical injectors deliver the oxidiser at an off-axis angle with the intention of providing a uniform regression rate. However, they are known to produce combustion instabilities (Waxman et al., 2010). Swirl injectors add a rotation to the oxidiser flow with the aim of increasing the regression rate and combustion efficiency but may flood the pre-combustion chamber and extinguish the flame.

Figure 5-18 shows a comparison between the effects of the axial and impinging injectors. Axial injectors produce a hot-gas recirculation zone in the pre-combustion chamber whereas impinging injectors produce a diminished or non-existent hot-gas recirculation zone. The recirculating gas helps to pre-heat the oxidiser entering the boundary layer diffusion flame which stabilises combustion (Sutton and Biblarz, 2001). This is evident in the transient pressure graphs shown from hot-fire tests done with an axial and impinging injector by Waxman et al. (2010). An axial injector configuration was chosen for use on the PV-3 motor.

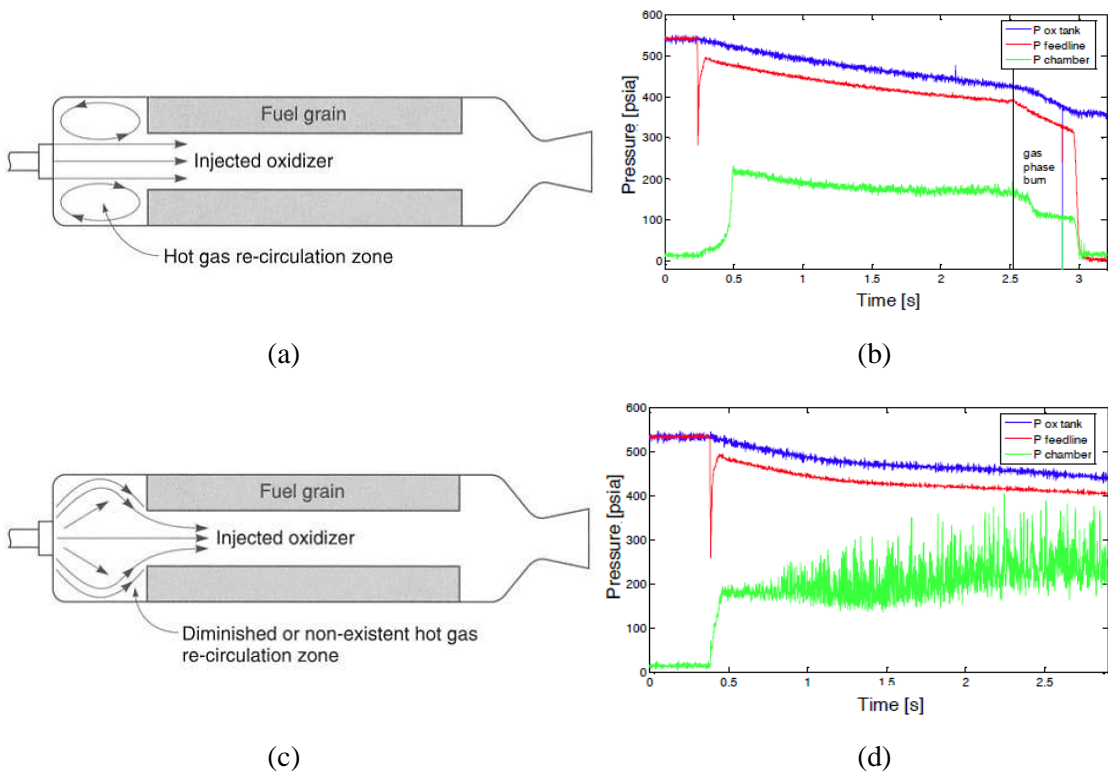


Figure 5-18: (a) Axial injector (Sutton and Biblarz, 2001), (b) pressure trace from hot-fire with axial injector (Waxman et al., 2010), (c) impinging injector (Sutton and Biblarz, 2001), and (d) pressure trace from hot-fire with impinging injector (Waxman et al., 2010).

5.6.2. Hydraulic Characteristics and Injector Geometry

The selection of an axial injector simplifies the geometric variables to be determined, which include the orifice diameter, orifice length, number of orifices, and the orifice pattern. The orifice

diameter and length, and their associated hydraulic characteristics, affect the overall behaviour of the injector, while the number of orifices determines the delivered oxidiser mass flow rate. The characteristics dependent on orifice diameter are atomisation and cavitation while the orifice length affects the probability of hydraulic flip.

Atomisation

Liquid propellant injectors generally operate by either the mechanical breakup or flash atomisation of a liquid jet. Mechanical breakup occurs due to aerodynamic and viscous effects which form a droplet spray from an unstable, turbulent jet. The jet velocity and orifice diameter are the dominating factors affecting liquid jet break up. Flash atomisation occurs when the liquid jet becomes metastable in a superheated state caused by a sudden pressure drop across the injector. The jet breaks up in a more violent manner due to rapid bubble growth resulting in finer droplet sprays (Waxman et al., 2012). The atomisation of a fluid through an orifice can be described by three non-dimensional numbers, namely, the Reynolds, Weber and Ohnesorge numbers:

$$Re = \frac{\rho v D}{\mu} \quad (5-8)$$

$$We = \frac{\rho v^2 D}{\sigma} \quad (5-9)$$

$$Oh = \frac{\mu}{\sqrt{\rho \sigma D}} = \frac{\sqrt{We}}{Re} \quad (5-10)$$

In the above, ρ is the fluid density, v is the fluid velocity, D is the orifice diameter, μ is the dynamic viscosity of the fluid, and σ is the surface tension. The Reynolds number is the ratio of the inertial to viscous forces. Turbulent flow is desirable to enhance the mixing process so a Reynolds number greater than 2300 is required.

The Weber number compares the inertial and surface forces between the liquid and gaseous phase. A Weber number greater than 50 is required to create small droplets (Gamper and Hink, 2013), while Weber numbers greater than 10 000 are typical for nitrous oxide injectors due to high velocity and low surface tension (Waxman et al., 2012).

The Ohnesorge number, a ratio of Weber and Reynolds numbers, compares the influence of the viscosity to droplet formation forces. It incorporates all the main liquid properties. An adequate Reynolds and Ohnesorge number combination on the graph in Figure 5-19 is required for atomisation to occur. High jet velocities are therefore desirable to achieve fine atomisation. When in the atomisation regime, two-phase flow can also occur due to cavitation of the liquid oxidiser at high velocities.

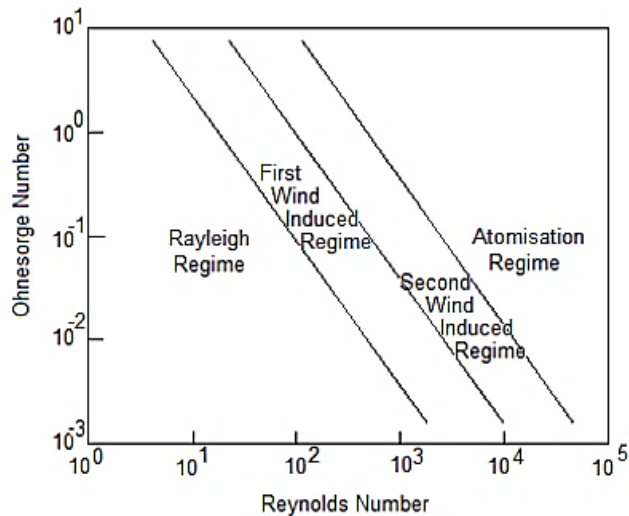


Figure 5-19: Atomisation regimes dependent on Reynolds and Ohnesorge numbers (Van Romunde, 2011).

Cavitation

Cavitation occurs in a liquid when the static pressure drops below the liquids vapour pressure, causing it to cavitate and flash from liquid to vapour. A high liquid velocity increases the dynamic pressure drop, which decreases the local static pressure. Cavitation in injector orifices is beneficial as it increases turbulence, improves oxidiser atomisation, reduces breakup length of the liquid jet, and thus reduces the subsequent vaporisation time. The phenomenon can be characterised by a dimensionless cavitation number:

$$Ca = \frac{p_{inj} - p_v}{\frac{1}{2} \rho v^2} \quad (5-11)$$

where p_{inj} is the injection pressure and p_v is the fluid vapour pressure. Critical cavitation exists when incipient cavitation occurs. A decrease in the cavitation number below the critical number will increase the amount of vapour bubbles. The thermodynamic properties of the fluid also have a significant effect on the degree of cavitation.

An initial orifice diameter of 1 mm was chosen since it was successfully used on the PV-2 motor. Table 5-10 gives the non-dimensional atomisation and cavitation numbers for the injector. The thermodynamic and transport properties of nitrous oxide were taken at 15 °C and 65 bar from REFPROP™. A liquid jet velocity of 56 m/s was found at a nominal mass flow rate of 2.898 kg/s. The Reynolds, Weber, and Ohnesorge numbers are well above the recommended ranges for atomisation to occur, with cavitation and flash atomisation expected to be prevalent. The orifice diameter was revised to 1.2 mm after cold flow testing.

Table 5-10: Non-dimensional atomisation and cavitation numbers for the PV-3 motor injector with a 1 mm orifice diameter at nominal flow conditions.

| Non-dimensional number | Value | Recommended range |
|------------------------|---------|-------------------|
| Re | 630214 | > 2300 |
| We | 1029337 | > 10 000 |
| Oh | 0.00161 | > 0.0001 at Re |
| Ca | 1.36 | - |

Pressure Drop

A pressure drop of at least 15% to 20% of the chamber pressure is required to minimise feed system coupled instabilities. With a nominal chamber pressure of 40 bar, the initial pressure drop across the injector is in the region of 20 to 25 bar, with the average pressure drop over the burn at about 12.2 bar. Figure 5-20 shows the transient injector pressure drop, reaching a minimum of 31% at the end of the burn.

Experimental work performed by Waxman (2014) showed that when the chamber pressure falls below 80% of the oxidiser vapour pressure, a maximum critical flow regime is reached due to the presence of two-phase flow. The orifice is effectively choked in this condition which makes the orifice mass flow rate insensitive to the chamber pressure. This hydrodynamically isolates the feed system from the chamber pressure and thus prevents the occurrence of feed system coupled instabilities. Figure 5-20 shows that the chamber pressure remains below 80% of the vapour pressure for the duration of the PV-3 motor burn, but only for an initial tank temperature of 20 °C. Therefore, an initial oxidiser temperature of at least 20 °C, corresponding to a vapour pressure of 50.5 bar, should be ensured at the start of a test.

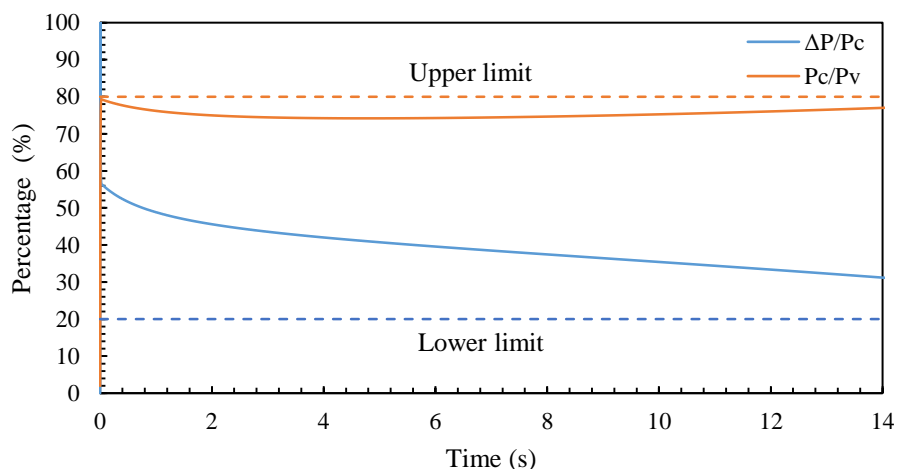


Figure 5-20: Theoretical transient injector pressure drop ($\Delta P/P_c$) and chamber pressure compared to oxidiser vapour pressure (P_c/P_v).

Orifice L/D Ratio

The orifice L/D ratio must be large enough to prevent hydraulic flip in the orifices. This occurs when the flow at the orifice exit detaches from the orifice wall, causing reverse flow and reducing the coefficient of discharge by at least 20%. It is predominantly a function of orifice L/D ratio and chamber pressure, with orifice diameter having a minor effect (Chew, 1973). High L/D ratios produce more unstable jets leading to an earlier liquid jet breakup and thus faster atomisation (Nyantekyi-kwakye et al., 2011). However, the coefficient of discharge decreases with increasing L/D ratio due to the higher frictional pressure drop.

For L/D ratios greater than 4, no hydraulic flip has been shown to occur, regardless of pressure drop (Chew, 1973). With an 11 mm thick injector plate and a 1 mm orifice, an L/D ratio of 11 results. This was subsequently revised to 9.17 after the cold flow test, but remains acceptable.

Orifice Inlet Geometry and Pattern

Chamfered or rounded orifice inlets increase the critical mass flow rate by 20%, with negligible difference found between the two (Waxman, 2014). Therefore, chamfered inlets were specified with a typical discharge coefficient of 0.8 for a 1 mm diameter orifice with a chamfered inlet.

A uniform distribution of atomised oxidiser is crucial to achieving homogenous combustion in the boundary layer flame zone in the fuel grain port. Figure 5-21 shows the final injector plate orifice pattern and spatial distribution, consisting of five equally spaced concentric rings with a total of 78 orifices. Space was left in the second ring of orifices and in the centre to allow for more orifices to be added if needed.

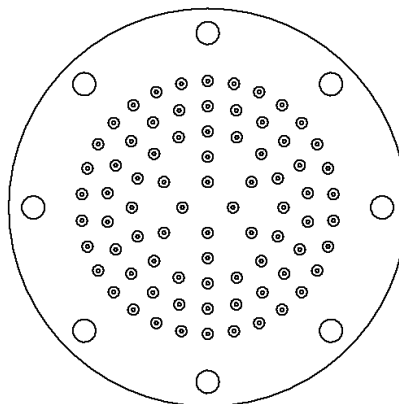


Figure 5-21: Injector plate orifice pattern.

5.6.3. Mass Flow Rate Modelling

Several analytical mass flow rate models with varying complexity were used in this study to determine the number of orifices required to deliver the nominal oxidiser mass flow rate. To start, the compressible mass flow rate through an orifice can be found using Equation 5-12:

$$\dot{m}_{com} = Y C_d N_{inj} A_{inj} \sqrt{2\rho(p_1 - p_2)} \quad (5-12)$$

where C_d is the coefficient of discharge, N_{inj} is the number of orifices, A_{inj} is the cross-sectional area of the orifice, ρ is the upstream fluid density, and $p_1 - p_2$ is the pressure drop across the injector. This is the incompressible flow equation modified with a compressibility correction factor, Y , since nitrous oxide has a high vapour pressure. Nitrous oxide has a compressibility factor of 0.12 for saturated liquid and 0.57 for saturated vapour at room temperature and two-phase flow develops in the injector orifices. A Y value of about 0.99 occurs at nominal operating conditions (Waxman et al., 2013).

The effect of compressibility on the mass flow rate is overshadowed by the effect of two-phase flow. Assuming nitrous oxide expands isothermally through the orifice and at the nominal operating conditions, there will be a phase change from liquid to vapour as it passes through the metastable region. The operating pressures in the feed system are also very close to the vapour pressure of nitrous oxide causing the local static pressure in the orifice to drop below the vapour pressure. Thus, cavitation and flash vaporisation can occur in the orifices, introducing two-phase flow. Figure 5-22 shows the injector pressure history for low and high vapour pressure propellants. If the bulk static pressure drops below the vapour pressure, vapour formation will occur which limits the mass flow rate.

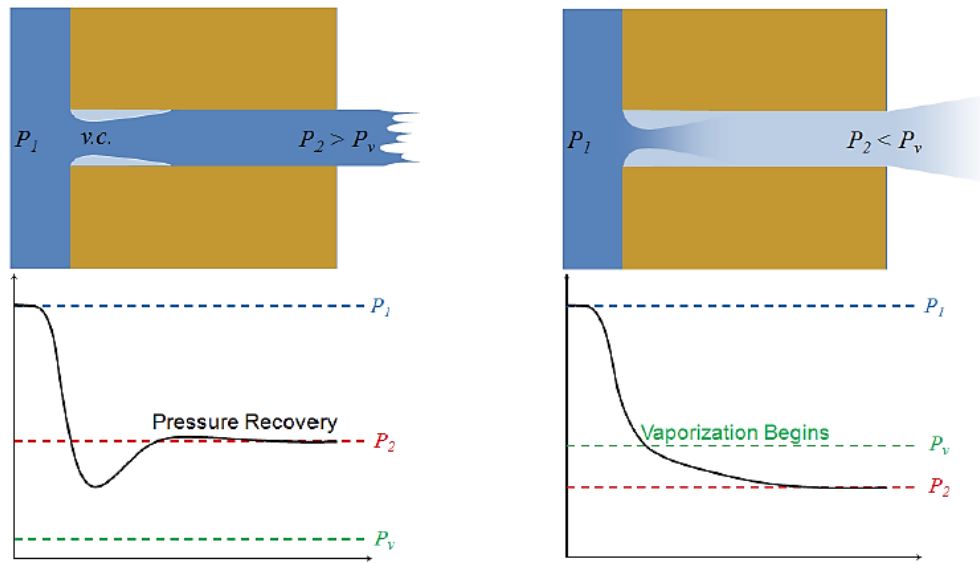


Figure 5-22: Injector pressure history for (a) low vapour pressure propellant and (b) high vapour pressure propellant (Waxman et al., 2013).

The Homogenous Equilibrium Model (HEM), given in Equation 5-13, can be used to predict the effect of two-phase flow. It assumes isentropic flow through the injector, no velocity difference between the phases, and that the liquid and vapour phases are in thermal equilibrium.

$$\dot{m}_{HEM} = C_d N_{inj} A_{inj} \rho_2 \sqrt{2(h_1 - h_2)} \quad (5-13)$$

where ρ_2 is the downstream fluid density and $h_1 - h_2$ is the change in specific enthalpy across the injector. The HEM does not consider non-equilibrium effects and thus represents the lower limit for the critical mass flow rate. A model was therefore developed that combines the incompressible model and the HEM, known as the Non-Homogenous Non-Equilibrium Model (NHNE). This uses a weighting for each model, called the non-equilibrium parameter, κ , defined as the ratio of the bubble growth time, τ_b , to the residence time of the fluid, τ_r :

$$\tau_b = \sqrt{\frac{3}{2} \frac{\rho_l}{p_{v1} - p_2}} \quad (5-14)$$

$$\tau_r = L \sqrt{\frac{\rho_l}{2(p_1 - p_2)}} \quad (5-15)$$

$$\kappa = \frac{\tau_b}{\tau_r} = \sqrt{\frac{p_1 - p_2}{p_{v1} - p_2}} \quad (5-16)$$

$$\dot{m}_{NHNE} = C_d N_{inj} A_{inj} \left(\left(1 - \frac{1}{1 + \kappa}\right) \dot{m}_{incom} + \left(\frac{1}{1 + \kappa}\right) \dot{m}_{HEM} \right) \quad (5-17)$$

Here, ρ_l is the fluid density, p_{v1} is the upstream vapour pressure, and L is the orifice length. When $\tau_b \gg \tau_r$, very little vapour formation will occur and the incompressible model is sufficiently accurate. When $\tau_b \ll \tau_r$, two-phase flow is present, and the flow rate approaches the critical value found by the HEM.

Table 5-11 gives the thermodynamic and transport properties of nitrous oxide for both upstream and downstream state points. These properties were taken at the specified state point 1 (upstream) of 15 °C and 63 bar where nitrous oxide is subcooled. The values at state point 2 (downstream) are taken at 40 bar with the same entropy. The results from each model are summarised in Table 5-13.

Table 5-11: Properties of nitrous oxide used for mass flow rate models for upstream and downstream state points. Properties obtained from REFPROP™.

| Property | Upstream (1) | Downstream (2) | Unit |
|-------------|--------------|----------------|--------|
| Pressure | 63 | 40 | bar |
| Temperature | 15 | 10 | °C |
| Density | 844.61 | 711.43 | kg/m³ |
| Enthalpy | 197650 | 194890 | J/kg |
| Entropy | 816.27 | 816.27 | J/kg-K |

5.6.4. Axisymmetric Orifice CFD Analysis

A numerical approach was adopted to validate the analytical oxidiser mass flow rate results. Work performed by Invigorito et al. (2016) showed that a numerical analysis can reasonably predict the critical mass flow rate and pressures drop within 10% of the experimental results of Waxman (2014). An axisymmetric CFD analysis was performed on a single injector orifice using Star-CCM+™.

Computational Domain and Boundary Conditions

The axisymmetric computational domain is shown in Figure 5-23 (a). A two dimensional (2D) polygonal mesh was used that was refined in the orifice inlet and at the outlet of the orifice to capture the high gradients of pressure and velocity. A pressure inlet of 63 bar and a pressure outlet of 40 bar was applied to represent the nominal starting condition, with a 2 bar pressure drop expected in the feedline.

Multiphase Solver

The Volume of Fluid (VOF) multiphase model was used with a K-Epsilon turbulence model and Realizable two-layer all y^+ wall treatment. Liquid nitrous oxide was initially specified in the area upstream of the orifice and air downstream of the orifice. The flow is assumed to be incompressible and thus the segregated flow solver was used. An implicit unsteady time model was employed with a time step of 8×10^{-8} s to obtain a reasonable convective Courant number. The simulation was run for approximately 1 ms to reach steady-state cavitation. The thermodynamic and transport properties of nitrous oxide were obtained from REFPROP™ and are given in Table 5-12.

Table 5-12: Properties of liquid and gaseous nitrous oxide at equilibrium. Properties taken from REFPROP™.

| Property | N ₂ O (L) | N ₂ O (G) | Unit |
|----------------------|-------------------------|-------------------------|-------------------|
| Temperature | 15 | 15 | °C |
| Density | 820.71 | 134.2 | kg/m ³ |
| Saturation pressure | 45.037 | - | bar |
| Dynamic viscosity | 7.0223×10^{-5} | 1.6773×10^{-5} | Pa-s |
| Heat of formation | -188610.0 | 188610.0 | J/kg |
| Specific heat | 2812.4 | 2484.5 | J/kg-K |
| Thermal conductivity | 0.090078 | 0.025735 | W/m-K |

Results

The computational model was first verified using the same computational domain and boundary conditions as Invigorito et al. (2016). Figure 5-23 (b) indicates the volume fraction of gaseous nitrous oxide, showing that cavitation occurs on the walls of the orifice and immediately aft of the orifice. The orifice is in the choked regime where it has reached its critical mass flow rate.

The velocity of oxidiser in orifice reaches approximately 66 m/s resulting in the static pressure dropping to the vapour pressure. A mass flow rate of 0.03566 kg/s was found for a pressure drop of 23 bar. For a total mass flow rate of 2.898 kg/s, 81 orifices are required. With the nominal mass flow rate applied to the inlet, a pressure drop of 23.15 bar was found across the orifice, which is close to the expected 23 bar.

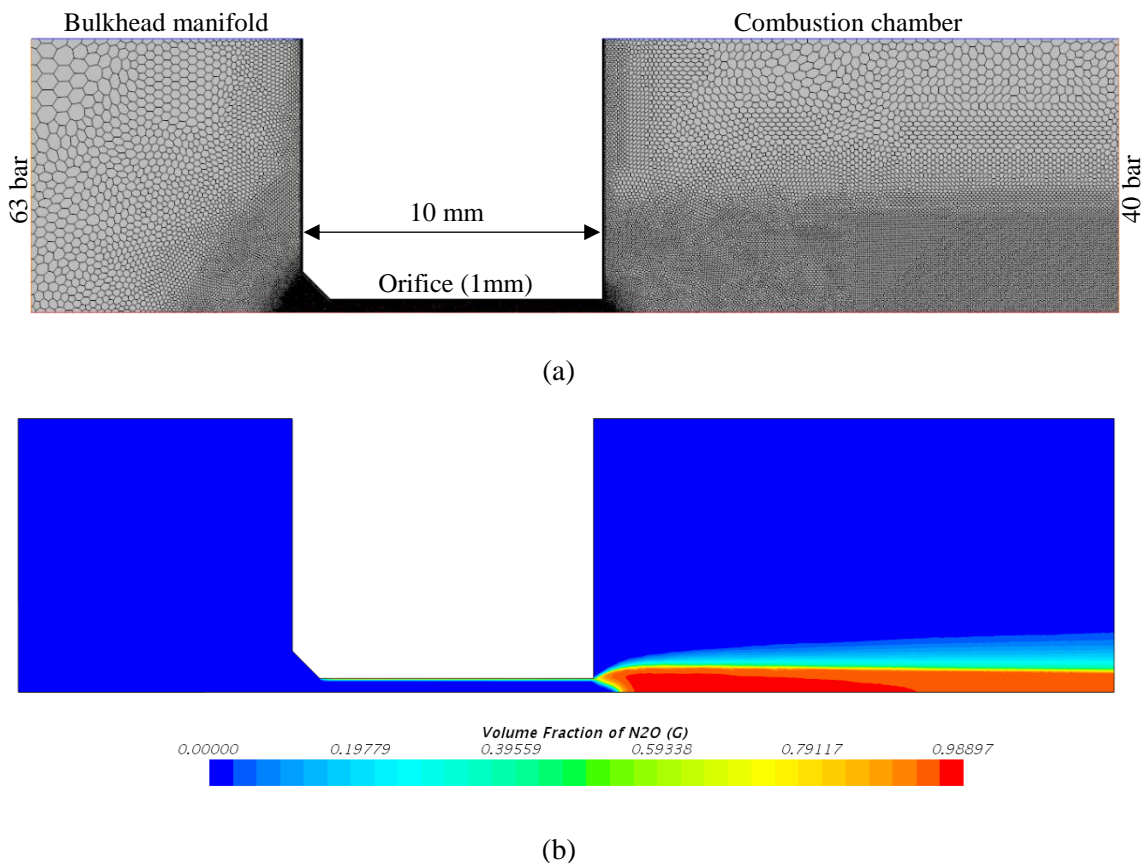


Figure 5-23: (a) Meshed computational domain and (b) nitrous oxide vapour volume fraction.

5.6.5. 3D Injector CFD Analysis

A 3D CFD analysis of the injector was performed to gain a qualitative understanding of the oxidiser flow characteristics in the bulkhead diffuser, injector orifices, and in the pre-combustion chamber. The pattern of orifices and consequently the distribution and homogeneity of the atomised oxidiser were considered to ensure uniform combustion and increase combustion

efficiency. Combustion and fuel regression were not considered as only the oxidiser flow characteristics were of interest.

Computational Domain and Boundary Conditions

A quarter-symmetry model of the internal volume of the motor from the beginning of the bulkhead fitting to half-way down the fuel grain port was used as the computational domain, shown in Figure 5-24 (a). The post-combustion chamber and nozzle were excluded from the analysis since combustion was not being modelled. A 78 orifice injector was used for the simulation. A polyhedral mesh of about 1300000 cells was used with mesh refinement applied to the orifices, shown in Figure 5-24 (b).

A pressure inlet of 65 bar and a pressure outlet of 40 bar were applied to represent the nominal starting condition. The pressure inlet was set at 65 bar in this case since the dynamic pressure drop reduces the static pressure to the required starting 63 bar at the injector.

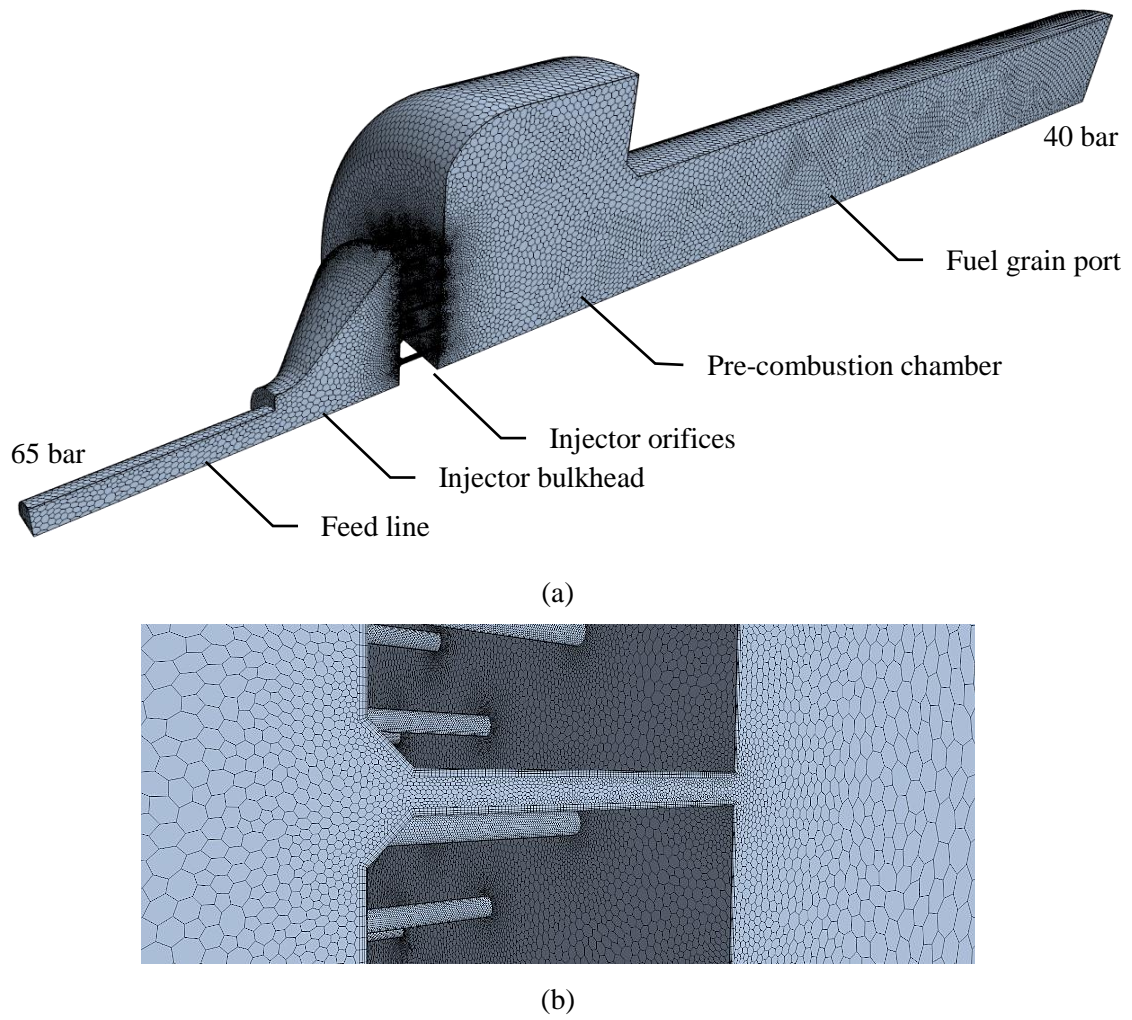


Figure 5-24: (a) Quarter-symmetry computational domain of 3D injector CFD analysis, (b) polyhedral mesh close-up on orifice.

Multiphase Solver

The same multiphase solver setup used in the axisymmetric CFD analysis was used. Liquid nitrous oxide was specified in the area upstream of the orifices and air downstream of the orifice and in the combustion chamber. An implicit unsteady time model with a time step of 8×10^{-7} s was used to obtain a reasonable convective Courant number. The simulation was run for approximately 8 ms to reach convergence with respect to mass flow rate and to obtain quasi-steady flow structures in the areas of interest. The same thermodynamic and transport properties of nitrous oxide were used as in Table 5-12. The boundary layer thickness was calculated from flat plate theory and the number of prism layers was chosen to ensure the wall y^+ was below 300 in the areas of interest.

Results

The total mass flow rate was found to be 2.78 kg/s for a 78 orifice injector. A mass flow rate per orifice of 0.03565 kg/s corresponds to 82 orifices required to reach the nominal mass flow rate of 2.898 kg/s. The lower mass flow rate compared to the axisymmetric CFD is likely caused by the lower pressure drop across the injector due to the higher pressure drop caused by the bulkhead diffuser and the asymmetric mass flow rate in the orifices.

Figure 5-25 (a) shows the volume fraction of nitrous oxide vapour indicating cavitation occurring in each orifice. Nitrous oxide vapour can be seen flowing into to the fuel grain port. Figure 5-25 (b) and (c) show the velocity vector field and static pressure distributions. The incoming oxidiser can be seen to impact the plate with complete flow separation in the feedline and thus no expansion in the diffuser region. This is a concern as adiabatic compression of the oxidiser may occur at the impact point, where the flow reaches stagnation pressure and almost zero velocity. Eddy structures are formed due to the flow of oxidiser spreading out to the rest of the orifices along the plate, seen in Figure 5-26. An uneven radial distribution of oxidiser thus occurs with less oxidiser reaching the outer orifices than the centre orifices. A steeper angle diffuser would be beneficial to remove the volume present for eddies to form and would make the injector bulkhead shorter.

The pre-combustion chamber forms a large recirculating eddy flow structure. It is also sufficiently long to allow the oxidiser to cavitate and vaporise before entering the fuel grain port. The orifice pattern provides sufficient oxidiser distribution into the initial port diameter. Figure 5-27 shows the velocity streamlines, providing a qualitative analysis of the flow structures generated.

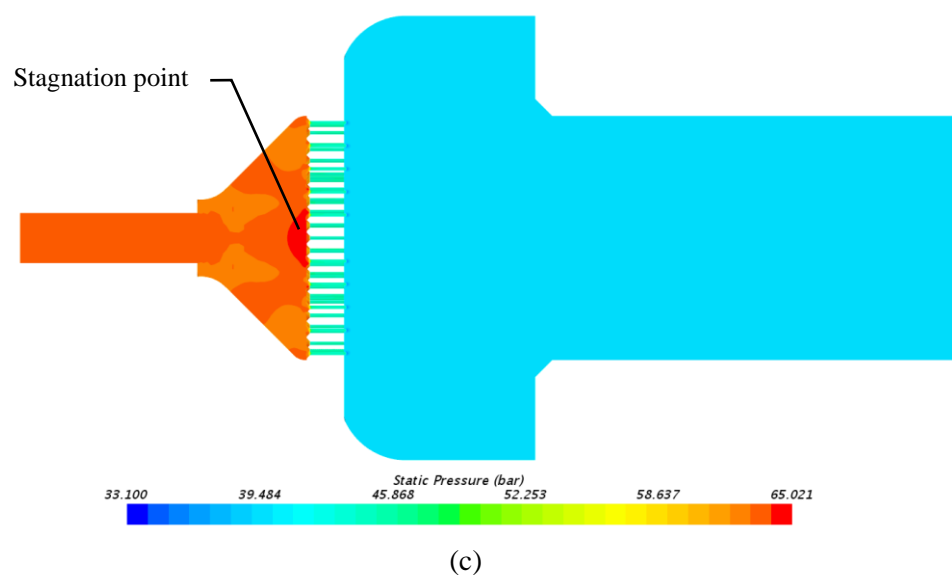
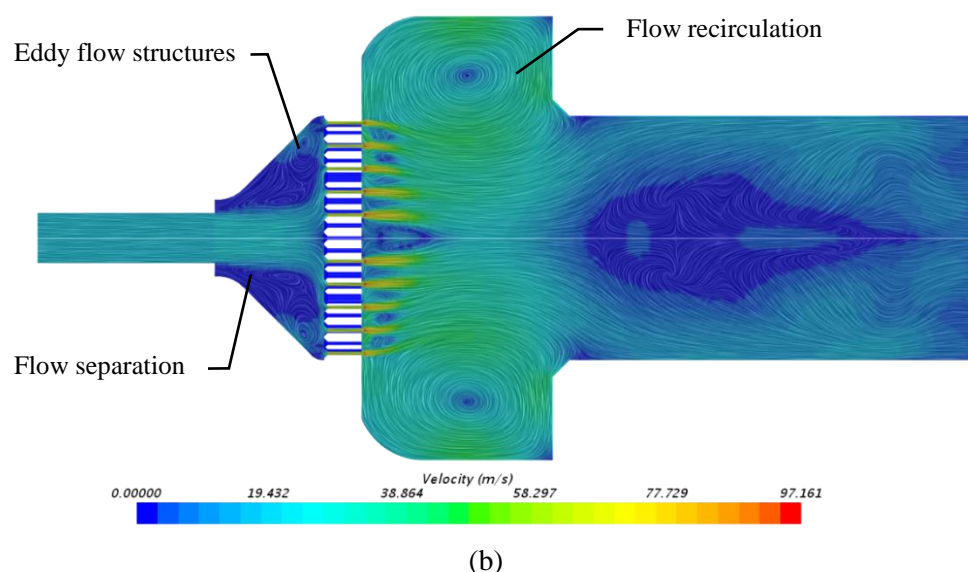
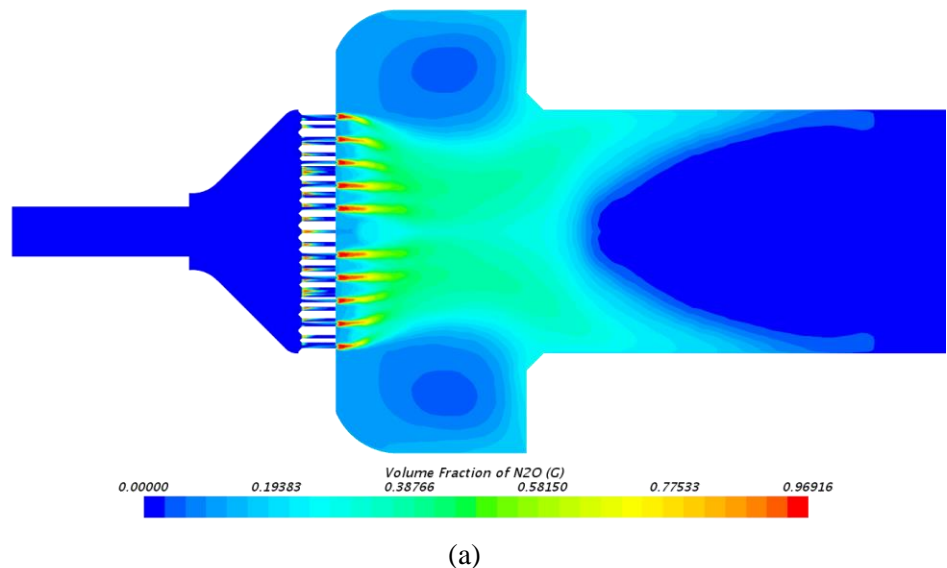


Figure 5-25: (a) Volume fraction of nitrous oxide vapour, (b) velocity vector field, and (c) static pressure distribution.

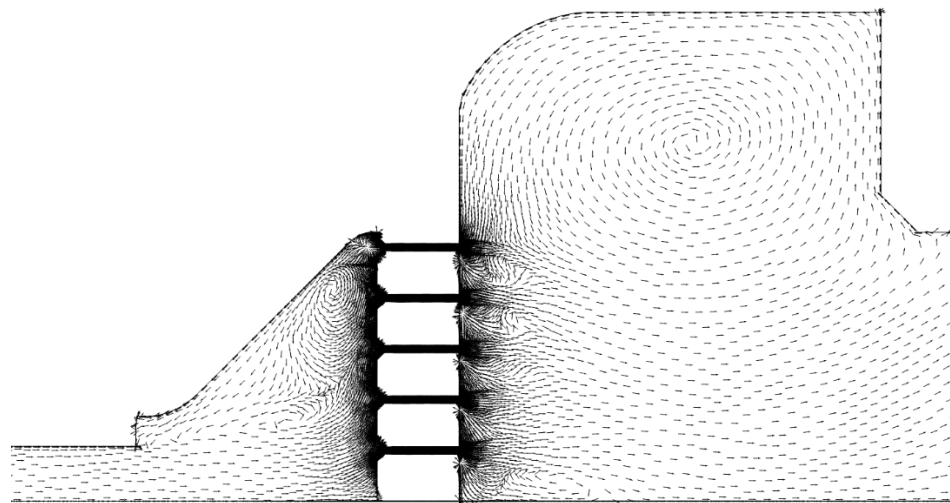


Figure 5-26: Vector field distribution in injector manifold and chamber.

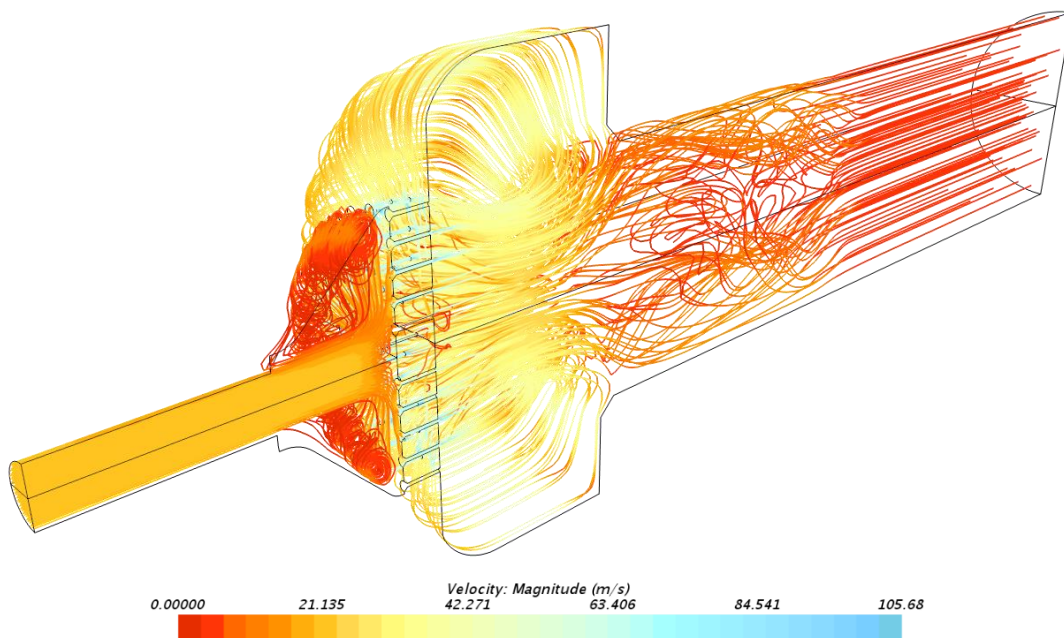


Figure 5-27: Velocity streamlines of nitrous oxide flow through injector.

5.6.6. Final Injector Design

Table 5-13 summarises the orifice mass flow rates and number of orifices required from the various analytical and numerical modelling methods applied in this study. The compressible liquid model is believed to be inaccurate for high vapour pressure propellants due to the presence of two-phase flow and produces the least number of orifices. The HEM tends to under predict the mass flow rate and produces the most number of orifices. The NHNE model finds a balance between the compressible liquid model and the HEM, evident in the prediction of 78 orifices. Due to the uncertainty of the coefficient of discharge for nitrous oxide, all the above models will include some error. For this reason, the injector was designed with 78 orifices of 1 mm diameter,

but with space available to increase the orifice size or add additional orifices if needed. This was a conservative approach since the motor operates close to the oxidiser mass flux limit.

The cold flow test however indicated that the mass flow rate was much lower than expected and the orifice diameters were subsequently revised to 1.2 mm in order to increase the mass flow rate. The injector design revision is discussed in Chapter 7.

Table 5-13: Mass flow rate per orifice (1 mm diameter) and number of orifices required for both analytical and numerical modelling techniques.

| Method | Mass flow rate/orifice (kg/s) | Orifices required |
|---------------------------------------------|-------------------------------|-------------------|
| Compressible liquid model | 0.03877 | 75 |
| Homogenous Equilibrium Model | 0.03321 | 87 |
| Non-homogenous Non-equilibrium model | 0.03726 | 78 |
| Axisymmetric orifice CFD | 0.03566 | 81 |
| 3D injector CFD | 0.03565 | 82 |

5.7. Fuel Grain Cartridge

The fuel grain cartridge consists of the aluminised paraffin wax fuel grain flanked by polyethylene pre- and post-combustion chamber inserts and encased in a glass/cotton/phenolic thermal liner.

5.7.1. Fuel Grain

The PV-3 motor fuel grain was specified to contain 20% aluminium additive by mass. Aluminium powder (Supramex 2021) with an average particle size of 45 micrometres was used. Mixing paraffin with aluminium powder produces an opaque grey coloured fuel grain, shown in Figure 5-28 (a). It is essential to have an opaque fuel grain, with at least a minimum level of absorptivity, to prevent radiative heating from the flame into the fuel grain. This can result in sloughing and break away of the fuel grain towards the end of the burn causing combustion instabilities. Laboratory-scale hot-fire tests performed by Maharaj (2018) suggested that fuel grains with aluminium additive do not exhibit sloughing, therefore no pigmentation additive was added to the PV-3 fuel grain.

An existing fuel grain casting apparatus was modified for the PV-3 motor fuel grains. It consists of a casing and a mandrel with a piston that is actuated by a spring-loaded mechanism to compress the wax during solidification. The fuel grain was cast in two halves that were bonded together with RTV silicone prior to thermal liner application, as shown in Figure 5-28 (b).

5.7.2. Thermal Insulation

The fuel grain is wrapped in a 3 mm thick glass/cotton/phenolic thermal liner that reduces the heat transmitted to the aluminium combustion chamber and provides mechanical strength to the fuel grain cartridge. A hand lay-up of glass fibre, cotton and phenolic resin was applied, shown in Figure 5-28 (c). This was allowed to cure for 24 hours and then post-cured for a few hours at 40 °C. The fuel grain cartridge outer diameter was then machined, seen in Figure 5-28 (d), to ensure a tight fit with the combustion chamber and prevent expansion and cracking during combustion.

The pre- and post-combustion chambers each have a polyethylene insert to reduce the heat flux transmitted to the chamber casing in these areas. The 8 mm thick pre-combustion chamber insert is not directly exposed to the combustion flame with minimal melting expected. The post-combustion chamber insert is however directly exposed to the combustion flame and thus has double the thickness at 16 mm.

During assembly of the motor, the pre-combustion chamber insert mates with the injector bulkhead with a convoluted pressure leak path, that allows the chamber pressure to leak to the external side of the fuel grain cartridge. The post-combustion chamber insert is bonded to the nozzle with RTV silicone to prevent a chamber-burn through. The final fuel grain cartridge is shown in Figure 5-28 (e).



(a)



(b)



(c)



(d)



(e)

Figure 5-28: (a) Fuel grain half, (b) fuel grain assembly, (c) wrapped fuel grain, (d) post-cured fuel grain being machined, and (e) final fuel grain cartridge.

5.8. Summary

Each of the PV-3 motor components has been successfully designed and manufactured. The combustion chamber casing and injector bulkhead assembly have both been successfully pressure tested. The injector design attempted to consider the two-phase flow nature of nitrous oxide, resulting in 78, 1 mm diameter orifices, which were subsequently revised to 1.2 mm diameter. A fuel grain was successfully cast with no cracks, voids, or powder settling and manufactured. The nozzle design verification follows.

6. NOZZLE DESIGN

6.1. Introduction

The PV-3 nozzle design was adapted from the PV-2 version for reasons of modularity and cost. Balmogim (2016) performed a detailed design analysis the PV-2 ablatively-cooled nozzle to withstand thermal loading with the use of 40% aluminium. The PV-3 motor uses 20% aluminium additive, and therefore has a lower adiabatic flame temperature and thus lower thermal loading. However, with an increased design thrust and different propellant composition, the internal aerodynamic contour, throat diameter, and expansion ratio changed. Given a predefined outer nozzle structure, the insulation thickness at the throat and divergent section were reduced. Although the thermal loading on the PV-3 nozzle is lower versus that of the PV-2 motor, the decrease in insulation thickness required that a thermal-structural analysis be carried out for verification.

6.2. Nozzle Design Considerations

The purpose of a rocket nozzle is to control the expansion of the combustion exhaust gases to convert thermal energy to kinetic energy as efficiently as possible. The design of hybrid rocket nozzles is similar to solid rocket nozzles, with considerations given below.

6.2.1. Design and Construction

Figure 6-1 shows a typical external nozzle configuration. Generally, hybrid rocket nozzles are ablatively cooled like their solid rocket counterparts. The general construction consists of a metal or composite shell designed to carry structural loads and a composite liner to provide the internal aerodynamic contour, and to ablate so as to prevent heat build-up. The thickness should be designed to maintain the liner-to-shell adhesive bond line below the temperature that would degrade the adhesive structural properties. Nozzle components rely on their heat absorbing capacity and slow heat transfer to withstand stresses enacted by thermal gradients (Sutton and Biblarz, 2001).

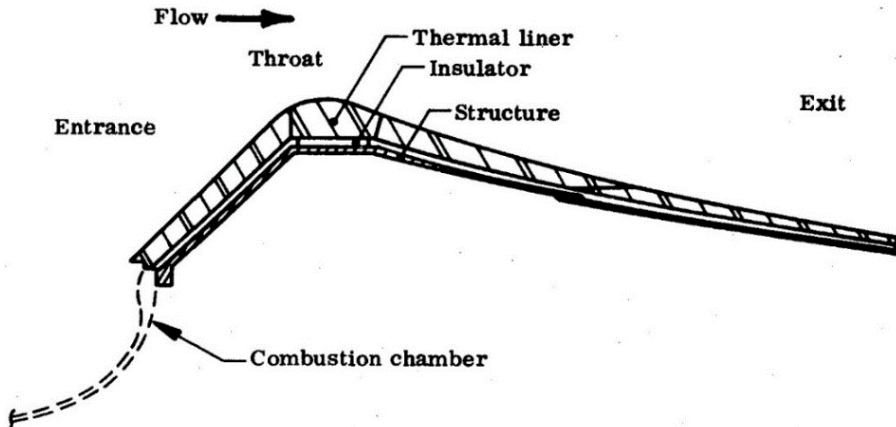


Figure 6-1: Typical external nozzle configuration (NASA, 1975).

6.2.2. Ablation

Ablative materials used in nozzles are typically a composite material made from carbon, silica, or glass fibres impregnated with phenolic or epoxy resin. These cool and protect the nozzle from the high exhaust gas temperature by decomposing into a char material and pyrolysis gases in progressive layers. The pyrolysis gases form a boundary layer over the char which carries heat away. The char material maintains the geometry but is a weaker material which can be removed by particle impingement.

6.2.3. Multiphase Flow and Nozzle Erosion

With the addition of aluminium powder into the fuel grain, the exhaust gas will contain unreacted agglomerated liquid droplets or solid particles of either aluminium or aluminium oxide. These droplets or particles are accelerated by the exhaust gas and give up heat during expansion in the nozzle. Particles in the exhaust gas result in two-phase flow losses as they pass through the nozzle and can cause losses up to 5% (Sutton and Biblarz, 2001).

Nozzle erosion is caused by the interaction between the high temperature, high velocity gas flow, the chemically aggressive species in the gas, and mechanical abrasion by particles (Sutton and Biblarz, 2001). This erodes the nozzle internal surface which decreases motor performance over time. The different types of nozzle erosion include mechanical erosion, chemical erosion, vaporisation, melting, and charring.

Mechanical erosion is most prevalent in the converging section of nozzles due to particle impingement. The erosion can become acceptable if the turn-back angle and thus the inflection/inlet angles are reduced (Sutton and Biblarz, 2001). Minimal erosion is present on the throat and divergent sections due to droplet trajectories moving away from the surface in those sections (Thakre et al., 2013). There can be impingement of the particles against the divergent section of the nozzle if the nozzle is incorrectly designed. Chemical erosion, caused by aggressive

oxidising species in the exhaust gas, is most severe in the throat region since this experiences the greatest heat flux (Thakre and Yang, 2008).

Slagging is the deposition of exhaust products on the nozzle internal contour, which also needs to be considered in nozzle design. With an aluminised fuel grain, slagging and subsequent accumulation of agglomerated aluminium droplets on the convergent section is expected which can alter the aerodynamic contour, increase heat transfer and cause thrust oscillations as slag is expelled periodically (NASA, 1975).

6.3. Design Methodology

A recommended nozzle design methodology is given in Figure 6-2. Nozzle design is an iterative process that considers weight, performance, and cost. The initial design is developed in a logical process starting at the internal surface and working outwards. The internal contour is defined in the aerodynamic design; throat inserts, thermal liners and insulators are configured in the thermal design; structural shells are configured to support the thermal components and sustain predicted loads in the structural design phase. Since this is only a verification analysis, no iteration loops were followed.

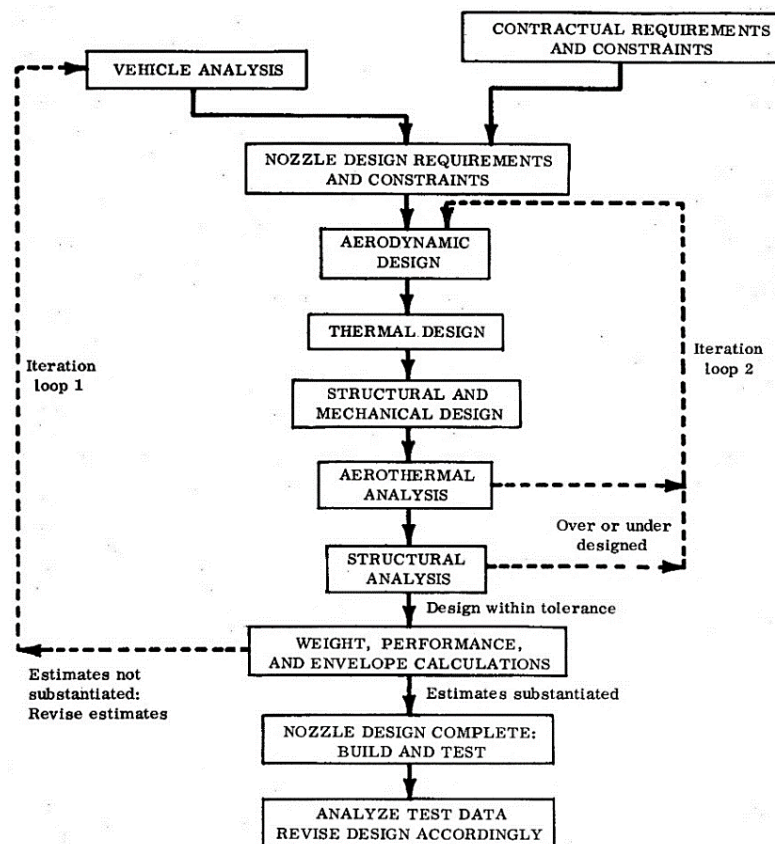


Figure 6-2: Nozzle design flow chart (NASA, 1975).

6.4. Design Requirements and Constraints

The nozzle geometry and characteristics were obtained from the HRPC Motor Design model, and are given in Appendix D. These specifications were used to obtain the aerodynamic contour design and nozzle loading conditions to be used in the numerical verification analysis. The PV-2 nozzle was used as the baseline design with the same external structure used for modularity but with a revised internal aerodynamic contour and expansion ratio. The same configuration and materials used on the PV-2 nozzle were specified, with silica/phenolic insulation and a graphite throat. Figure 6-3 gives the adiabatic flame temperature over the burn time for the PV-3 motor, obtained from the HRPC Performance Model.

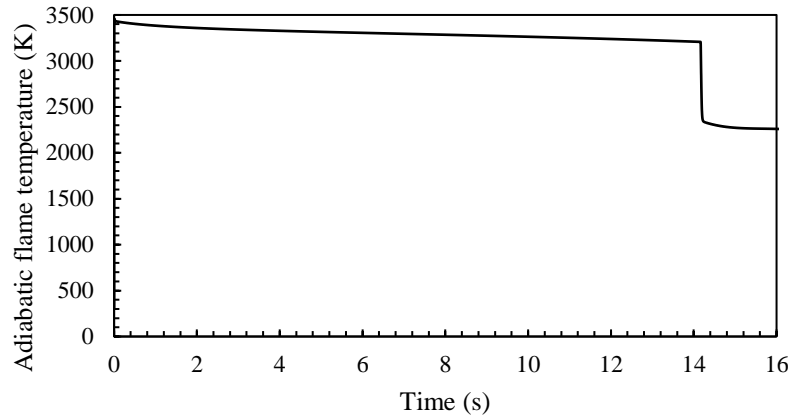


Figure 6-3: Adiabatic flame temperature over burn time of PV-3 motor.

6.5. Aerodynamic Contour Design

The aerodynamic contour design consists of defining the nozzle internal contour surface exposed to the exhaust gases in order to convert thermal to kinetic energy efficiently. The nozzle contour was generated using the HRPC Nozzle Contour model (Geneviève, 2013). The model utilises the approximate optimisation approach, developed by Rao (1958), to determine the bell-shaped diverging section. The nozzle contour can be seen in Figure 6-4 and the nozzle specifications are summarised in Appendix D. The sizing of each nozzle section is discussed below.

6.5.1. Converging Section

The converging section geometry is not critical to performance since subsonic flow in this region can be easily turned with low pressure drop. The inlet half-angle is typically between 1° to 75° , with 45° being most common (NASA, 1975). An angle of 47.5° was chosen to reduce the length of the nozzle to fit in the existing nozzle structure.

6.5.2. Throat Section

The throat contour is not critical to performance and any radius or curve is acceptable (Sutton and Biblarz, 2001). The recommended values of 1.5 and 0.382 were used for the upstream and downstream arc radius ratios respectively. A finite cylindrical throat length was used to aid in nozzle alignment, machining, and erosion mitigation. The throat cylindrical length was set as half of the throat radius, as this has been shown to reduce throat erosion rate significantly (NASA, 1975).

6.5.3. Diverging Section

Bell-shaped nozzles are shaped to minimise flow losses and thus improve specific impulse. Particle impingement in a nozzle can be minimised by using an inlet angle of 20° to 26° and a turn-back angle of 10° to 15° (Sutton and Biblarz, 2001). Turn-back angles greater than 12° have been shown to have a significant effect on performance (NASA, 1975). A 100% bell-shaped nozzle length was chosen which results in a nozzle correction factor of 0.983, found from Figure I-1 in Appendix I. The nozzle inlet and outlet parabola angles were 20.51° and 8.1° , respectively, with an expansion ratio of 5.9317.

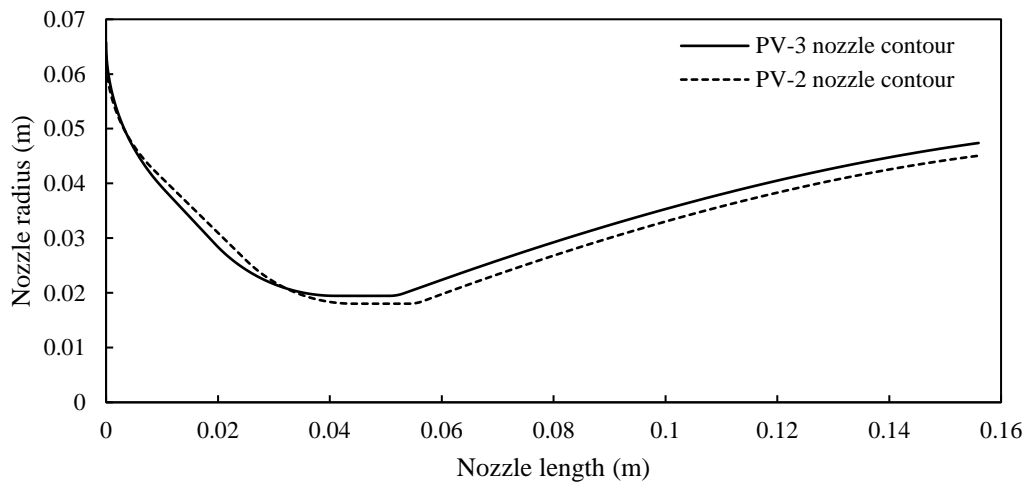


Figure 6-4: Nozzle contour comparison between PV-2 and PV-3 nozzles.

6.6. Nozzle Loading

The nozzle experiences both thermal and structural loading. Nozzles with a smooth continuous contour and a convergent half-angle less than 45° are usually adequately analysed with one-dimensional isentropic flow theory to obtain the inviscid flow properties (NASA, 1975).

6.6.1. Thermal Loading

The heat transfer between the exhaust gases and the nozzle wall must first be defined in order to determine the thermal response of the nozzle materials. The total heat transfer includes the effects of convection, radiation, and particle impingement heating, but in the supersonic flow regime, convective heat transfer dominates. However, due to the use of an aluminised fuel grain, and thus the presence of aluminium agglomerates and aluminium oxide particles, the radiation effect will be more prominent, particularly in the subsonic flow regime. Particle impingement heating is also prevalent only in the subsonic flow regime. Radiation and particle impingement heating are excluded from the analysis

The heat flux transferred across the viscous boundary layer is found with the forced convection heat transfer equation:

$$\dot{q} = h_g(T_{aw} - T_{wg}) \quad (6-1)$$

where \dot{q} is the heat flux transferred across the stagnant gas layer per unit surface area, h_g is the gas-side heat transfer coefficient, and T_{aw} and T_{wg} are the adiabatic wall and hot gas-side wall temperatures respectively. The adiabatic wall temperature is obtained from:

$$T_{aw} = T_0 \left[\frac{1 + r \left(\frac{\gamma - 1}{2} \right) M_x^2}{1 + \left(\frac{\gamma - 1}{2} \right) M_x^2} \right] \quad (6-2)$$

where T_0 is the stagnation temperature, r is the ratio of frictional temperature increase to the increase caused by adiabatic compression, and M_x is the Mach number at any axial location. The gas-side convective heat transfer coefficient was found using the simplified Bartz equation (Bartz, 1957):

$$h_g = \left[\frac{0.026}{D_t^{0.2}} \left(\frac{\mu^{0.2} C_p}{Pr^{0.6}} \right)_0 \left(\frac{P_0 g}{C^*} \right) \left(\frac{D_t}{R} \right)^{0.1} \right] \left(\frac{A_t}{A_x} \right)^{0.9} \sigma \quad (6-3)$$

where D_t is the throat diameter, μ is the dynamic viscosity, C_p is the specific heat capacity, Pr is the Prandtl number, c^* is the characteristic velocity, R is the radius of curvature of the nozzle throat, A_x is the cross sectional area, and σ is the correction factor for property variation across the boundary layer. Note that the value in the square brackets is constant through the nozzle and only the area ratio and correction factor need to be evaluated at each station. It is clear that the smaller the throat diameter, the larger the heat flux, thus the maximum heat flux occurs at the throat. The correction factor is evaluated in terms of T_{wg} , T_0 and M_x :

$$\sigma = \left[\frac{1}{2} \frac{T_{wg}}{T_0} \left(1 + \frac{\gamma - 1}{2} M_x^2 \right) + \frac{1}{2} \right]^{-0.68} \left[1 + \frac{\gamma - 1}{2} M_x^2 \right]^{-0.12} \quad (6-4)$$

The area ratio relationship and isentropic flow equations are also required for evaluation of the Bartz equation, given as follows:

$$\frac{A_x}{A^*} = \frac{1}{M_x} \sqrt{\left[\frac{2}{\gamma + 1} \left(1 + \frac{\gamma - 1}{2} M_x^2 \right) \right]^{\frac{\gamma+1}{\gamma-1}}} \quad (6-5)$$

$$T_x = T_0 \left(1 + \frac{\gamma - 1}{2} M_x^2 \right)^{-1} \quad (6-6)$$

6.6.2. Structural Loading

The structural loading experienced by the nozzle is primarily due to the pressure distribution along the nozzle internal contour. This can be found using the isentropic flow equation:

$$\frac{P_0}{P_x} = \left[1 + \frac{\gamma - 1}{2} M_x^2 \right]^{\frac{\gamma}{\gamma-1}} \quad (6-7)$$

6.6.3. Spatial and Temporal Modelling

The spatial and temporal variations of the convective heat transfer coefficient, pressure, and temperature were calculated using a MATLAB™ program developed by Balmogim (2016) for the design of the PV-2 nozzle. The code requires the discretised nozzle contour as an input, obtained via CAD software. The time, O/F ratio, chamber pressure, chamber temperature, specific heat ratio, and characteristic velocity are obtained from the HRPC Performance Model results. The program uses NASA CEA™ to obtain the transport properties such as the gas viscosity, Prandtl number and specific heat. It computes the Bartz equation and the isentropic flow equations at each station along the nozzle contour to obtain a spatial variation. The specific heat is assumed to be constant through the nozzle but not over time.

The spatial variations are computed at each time-step to obtain the temporal variation. The program outputs a file for each specified time-step which can then be imported into a FEM analysis software. Figure 6-5 and Figure 6-6 show the spatial variation of convective heat transfer coefficient, temperature, and pressure at an instantaneous 40 bar chamber pressure (start-up). The methodology and code used to obtain these results are given in detail by Balmogim (2016).

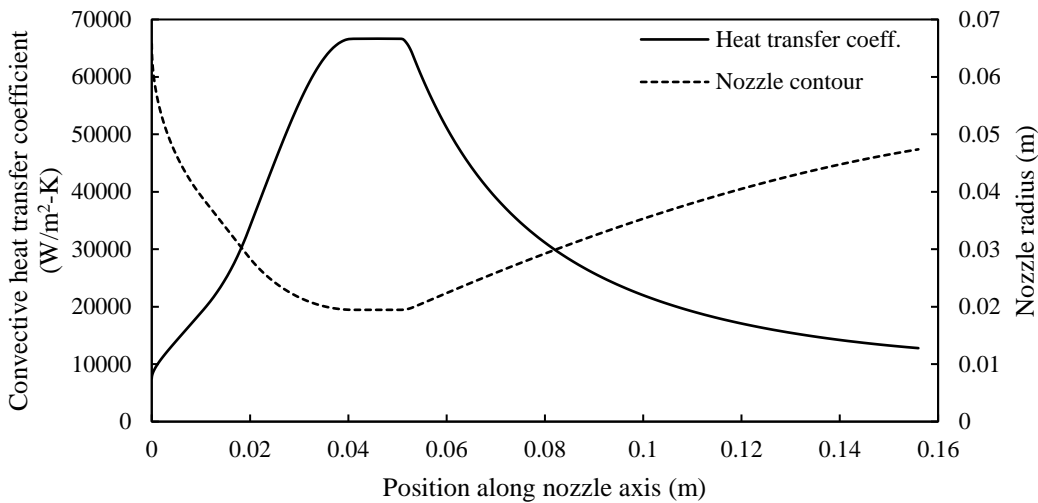


Figure 6-5: Convective heat transfer coefficient spatial variation and nozzle contour for 20% aluminised fuel grain at instantaneous 40 bar chamber pressure.

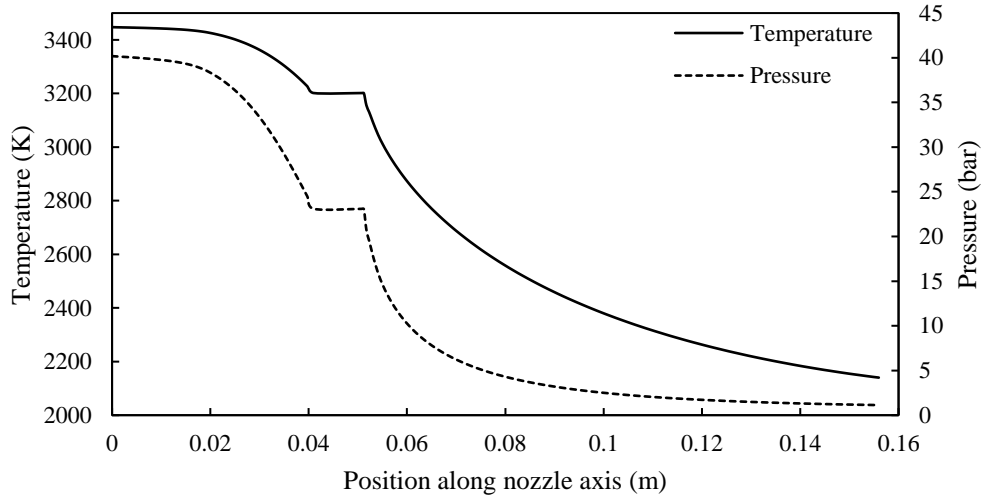


Figure 6-6: Temperature and pressure spatial variation for 20% aluminised fuel grain at instantaneous 40 bar chamber pressure.

6.7. Thermal and Structural Design

The thermal and structural design consists of the geometry development and material specification. The purpose of the thermal insulation is to maintain the nozzle aerodynamic contour and to limit the temperature on the nozzle structure. The thermal components include the throat insert and thermal insulators. The structural design must adequately support the insulators and withstand the nozzle loading.

Figure 6-7 shows the cross-section of the final PV-3 nozzle design. It includes a graphite throat insert, silica/phenolic fore and aft insulation sections, an EN19T alloy steel nozzle structure, and an EN19T alloy steel retaining ring. The retaining ring keeps the aft insulation in place and is

secured to the nozzle structure with ten M6 cap screws. Two Viton O-rings form the pressure seal.

A 0.2 mm gap between the nozzle components allows for thermal expansion and sealing with RTV silicone. Dimples are present between the insulation and structure to increase the bond area and gas leak path length. They also aid in assembly and form a mechanical lock during operation (Balmogim, 2016). The throat insert has a 7° half-angle taper so that it locks into place after ignition from the combustion chamber pressure. This also forms the pressure seal between the components. The material properties used for each nozzle component are described below.

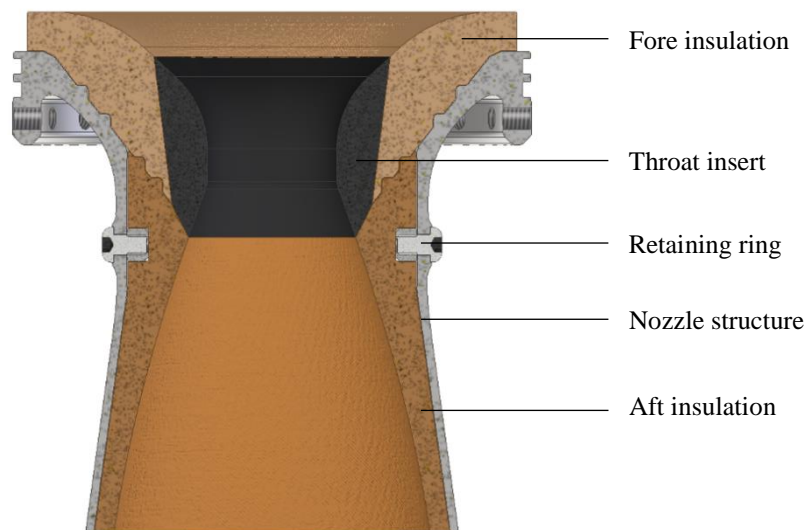


Figure 6-7: PV-3 nozzle cross-section.

6.7.1. Throat Insert

Nozzles generally have a throat insert with a low erosion rate material to reduce the loss in expansion ratio during operation. The throat is exposed to the greatest heat transfer and thus thermal stress in the nozzle. Polycrystalline graphite was used as the throat insert material, with the properties of ATJ graphite given in Table 6-1. Non-linear temperature dependent thermal properties are given Appendix J. Graphite has mild orthotropy but was assumed as isotropic to simplify the analysis. It has a relatively low strength, is brittle, and prone to cracking from thermal shock, but its strength increases with temperature. Graphite has a high thermal conductivity and thus a layer of insulation is required behind the insert to reduce thermal diffusion, shown in Figure 6-7. Its high thermal expansion coefficient also requires consideration. The 0.2 mm gap filled with RTV silicone allows movement in the radial direction whereas the insert can expand forward for allowance in the axial direction.

Table 6-1: Properties of ATJ graphite (GRAFTech, 2009).

| Property | Value | Unit |
|--------------------------------------------------|--------------------|-------------------|
| Density | 1760 | kg/m ³ |
| Tensile strength | 26 | MPa |
| Compressive strength | 66 | MPa |
| Flexural strength | 31 | MPa |
| Modulus of Elasticity | 9.7 | GPA |
| Poisson's ratio | 0.13 | - |
| Thermal conductivity (25 °C) | 116 | W/m-K |
| Specific heat (25 °C) | 710 | J/kg-K |
| Thermal expansion coefficient (to 100 °C) | 3x10 ⁻⁶ | 1/K |

6.7.2. Fore and Aft Insulation

The insulation is split into fore and aft pieces, for ease of nozzle assembly. Silica/phenolic was chosen as the insulation material since it is somewhat less expensive than other materials with a low thermal diffusivity.

The thickness of insulators is typically determined by estimating the erosion depth, adding a safety factor, adding estimated char thickness, and adding thickness of insulation to drop the temperature at the structure interface. The erosion rate for silica/phenolic at the motor operating conditions can be scaled from measured data using the method provided by Bartz (1957):

$$\dot{e} = \dot{e}_m \times \left(\frac{p_c}{p_{c,m}} \right)^{0.8} \left(\frac{D_{t,m}}{D_t} \right)^{0.2} \quad (6-8)$$

where \dot{e}_m is the measured erosion rate, p_c and D_t are the chamber pressure and throat diameter of the motor being designed, and $p_{c,m}$ and $D_{t,m}$ are the chamber pressure and throat diameter of the motor from which the measured rate was obtained. The measured erosion rate of silica/phenolic was averaged from experimental results obtained from Pavli (1968). An average measured erosion rate of 0.0648 mm/s was found for a motor operating at a 6.9 bar chamber pressure and with a throat diameter of 12.7 mm. Scaling it to the PV-3 motor operating conditions of 40 bar and a throat diameter of 38.92 mm, an erosion rate of 0.211 mm/s resulted. For a 14 s burn time, a maximum erosion depth of 3 mm is therefore expected. This will be most dominant in the throat region, where the graphite insert is located. The minimum insulation thickness on the nozzle is 6 mm at the exit plane, which is a conservative design.

By recommendation of the nozzle manufacturer, the fore insulation section was compression moulded and the aft insulation section tape-wrapped. A tape-wrapped item forms an orthotropic

material with three mutually perpendicular directions. However, the silica/phenolic material properties were assumed as isotropic due to lack of orthotropic material data. The material properties used here are shown in Table 6-2. Non-linear properties with respect to temperature for silica/phenolic were not available.

Table 6-2: Material properties for tape-wrapped and compression moulded Silica/phenolic (Park Electrochemical Corp, 2018).

| Property | Tape-wrapped | Compression moulded | Unit |
|--------------------------------------|----------------------|----------------------------|-------------------|
| Density | 1700 | 1700 | kg/m ³ |
| Tensile strength | 89.6 | 62 | MPa |
| Tensile modulus | 16.5 | 26.2 | GPa |
| Compressive strength | 165 | 276 | MPa |
| Compressive modulus | 16.5 | 13.8 | GPa |
| Flexural strength | 159 | 110 | MPa |
| Flexural modulus | 17.2 | 21 | GPa |
| Poisson's ratio | 0.3 | 0.3 | - |
| Thermal conductivity (149 °C) | 0.38 | 0.31 | W/m-K |
| Specific heat capacity | 1000 | 960 | J/kg-K |
| Thermal expansion coefficient | 4.5×10^{-6} | 4.5×10^{-6} | 1/K |

6.7.3. Nozzle Structure

The nozzle structure supports the thermal components, withstands the applied loading, and transfers the loading to the combustion chamber casing. It must withstand the pressure distribution loading and thermal loading due to conduction of heat from the insulation material that expands during the burn and applies additional hoop stress. EN19T (AISI 4140) alloy steel was selected for the nozzle structure with its material properties given in Table 6-3. The thermal conductivity and specific heat capacity with respect to temperature are given in Appendix J.

Table 6-3: EN19T alloy steel material properties (Macsteel, 2018; Voestalpine High Performance Metals (Australia), 2018).

| Property | Value | Unit |
|-----------------------------------------------------|-------|-------------------|
| Density | 7850 | kg/m ³ |
| Ultimate tensile strength | 820 | MPa |
| Yield tensile strength | 680 | MPa |
| Modulus of Elasticity | 210 | GPa |
| Poisson's ratio | 0.29 | - |
| Thermal conductivity (25 °C) | 42 | W/m-K |
| Specific heat (25 °C) | 460 | J/kg-K |
| Thermal expansion coefficient (up to 100 °C) | 11.1 | 1/K |

6.8. Axisymmetric Thermal Analysis

A 2D axisymmetric thermal FEM analysis was initially performed to verify that the insulation thickness for the updated nozzle geometry was sufficient without major design changes. The analysis did not take ablation into account where material and heat are removed, or the charring of the silica/phenolic and graphite which changes the material properties of the virgin material. Nozzle erosion and radiative heating were also not considered.

6.8.1. Solver

The Simcentre Thermal/Flow solver of Siemens NX™ 11 was utilised to conduct the axisymmetric thermal analysis. The solution is transient due to varying thermal loading with time.

6.8.2. Model and Mesh

A simplified geometry was used for the axisymmetric analysis, seen in Figure 6-8. Gaps were disregarded and all holes and bolts were removed to give a perfect revolved geometry. Linear CQUAD4 axisymmetric elements were used. The mesh was refined to an element size of 0.3 mm for the throat insert and 0.5 mm for the thermal liner and chamber casing wall. A total of 45602 nodes and 43715 elements were generated, with 99.9% of the elements passing the element quality check.

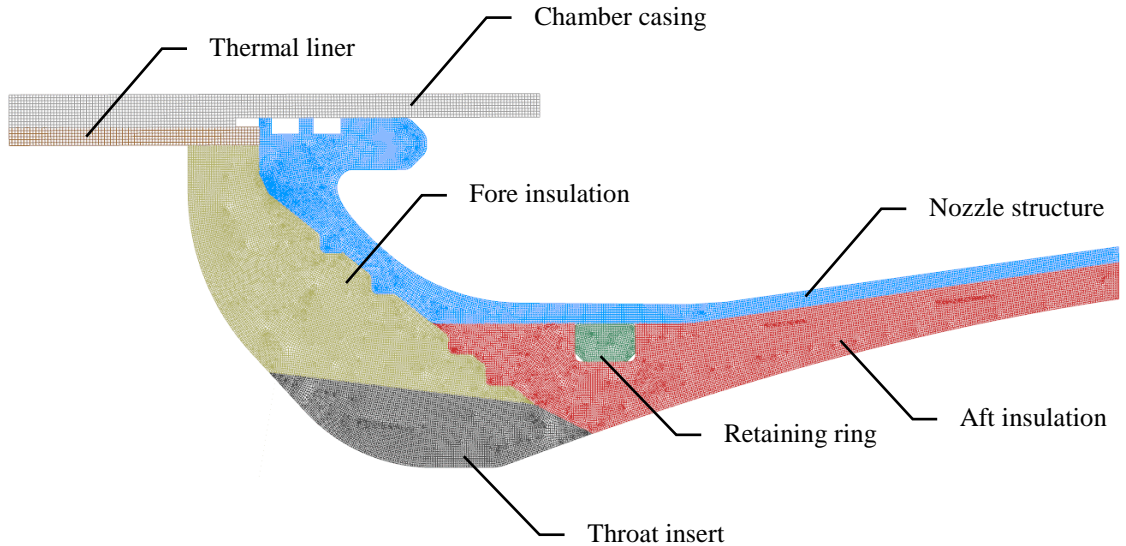


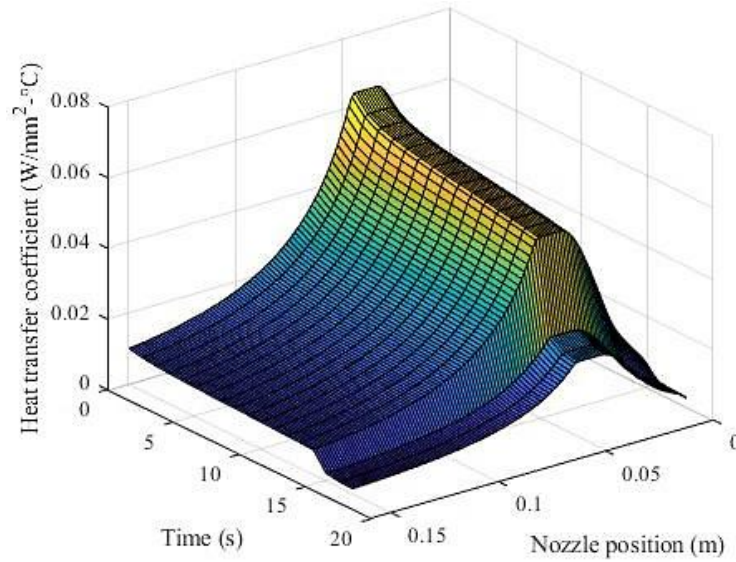
Figure 6-8: Mesh of axisymmetric nozzle model.

6.8.3. Constraints and Loading Conditions

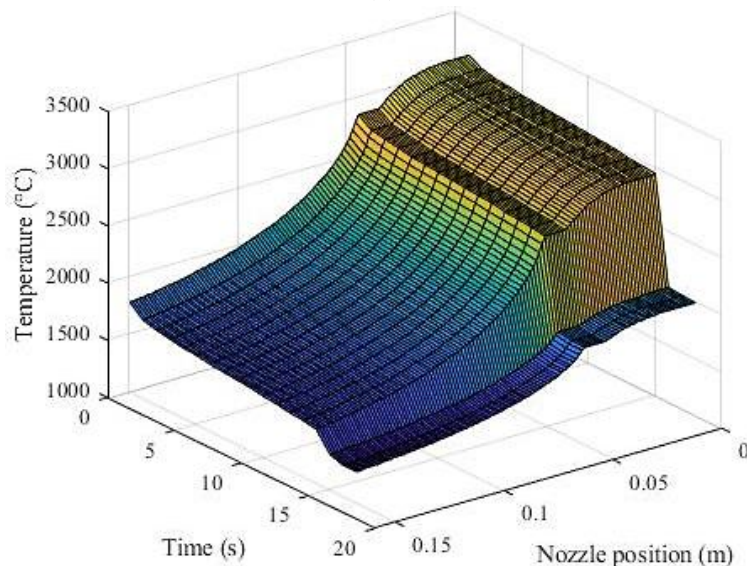
Advanced thermal coupling was applied to all contacts between parts with the ‘perfect’ contact type used to ensure large conductance’s between meshes. An initial temperature of 22 °C was applied uniformly to the mesh. A convection constraint was applied to the external nozzle geometry with a convection coefficient of 5 W/m²-K and an ambient temperature of 21 °C to represent stagnant air free convection.

A convection constraint was applied to the internal nozzle contour to represent the gas flow thermal loading. The spatial and temporal heat transfer coefficients and temperatures were imported into tables with time and length (nozzle x-coordinate) as the independent variables and heat transfer coefficient and temperature as the dependent variables respectively, depicted in Figure 6-9.

A soak-through analysis was also run for a total time of 250 s to capture the transient conduction of heat after the burn. Free convection was assumed to exist on the internal nozzle contour after the end of the 18 s burn.



(a)



(b)

Figure 6-9: Temporal-spatial graphs of (a) heat transfer coefficient and (b) temperature for 20% aluminium concentration imported into Siemens NX™ 11.

6.8.4. Results

Figure 6-10 (a) shows the temperature distribution of the nozzle after 18 s. The peak temperatures of each nozzle component during and after the burn time are summarised in Table 6-4. The maximum temperature of the graphite is reached 9 s into the burn at 2906 °C, which is well below the melting temperature of graphite at about 3930 °C. The higher thermal conductivity of graphite, about 300 times higher than that of silica/phenolic, is evident as the entire throat insert heats up rapidly.

There is sufficient insulation thickness behind the graphite insert to keep the nozzle structure temperature at acceptable levels.

At the end of the 18 s burn, the nozzle structure reaches only 35 °C at the exit plane, indicating that the insulation thickness is more than sufficient. The soak-through analysis indicates that the nozzle structure peaks at 211 °C shown Figure 6-11, which is acceptable, and suggests that the structure is likely reusable. The peak temperatures are acceptable for all the nozzle components, indicating an adequate thermal design and no requirements for change.

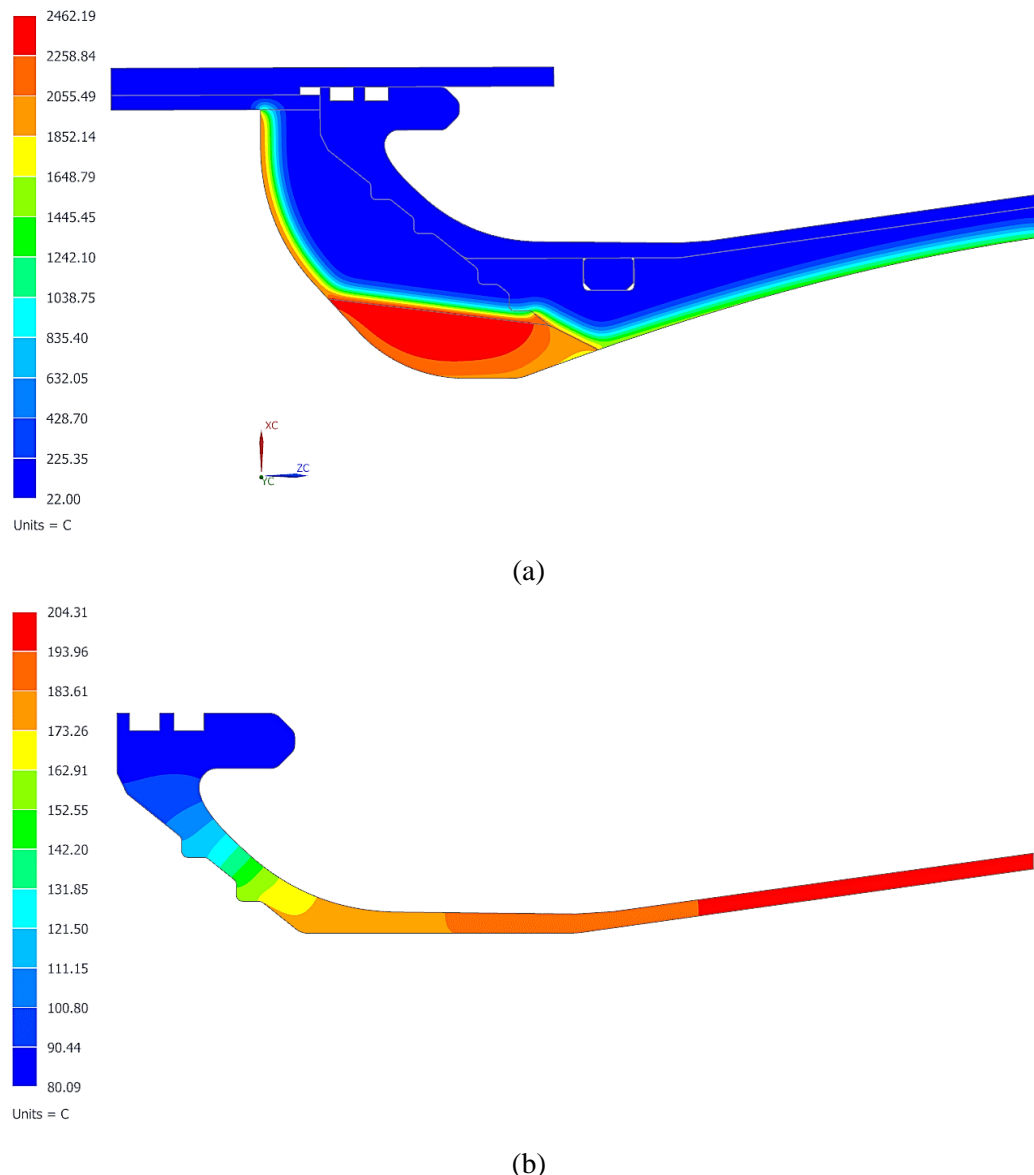


Figure 6-10: (a) Temperature distribution of nozzle after 18 s and (b) temperature response of the nozzle structure after 250 s.

Table 6-4: Peak temperatures of nozzle components from axisymmetric thermal FEA for burn time and soak-through analyses.

| Component | Peak temperature (°C) [time (s)] | |
|-------------------------|----------------------------------|--------------------|
| | 18 s burn | 250 s soak-through |
| Throat insert | 2906 [9 s] | - |
| Fore insulation | 3092 [1 s] | - |
| Aft Insulation | 2274 [15 s] | - |
| Thermal liner | 1455 [15 s] | - |
| Nozzle structure | 35 [18 s] | 211 [160 s] |
| Retaining ring | 22.1 [18 s] | 195 [250 s] |
| Chamber casing | 29.5 [18 s] | 83 [250 s] |

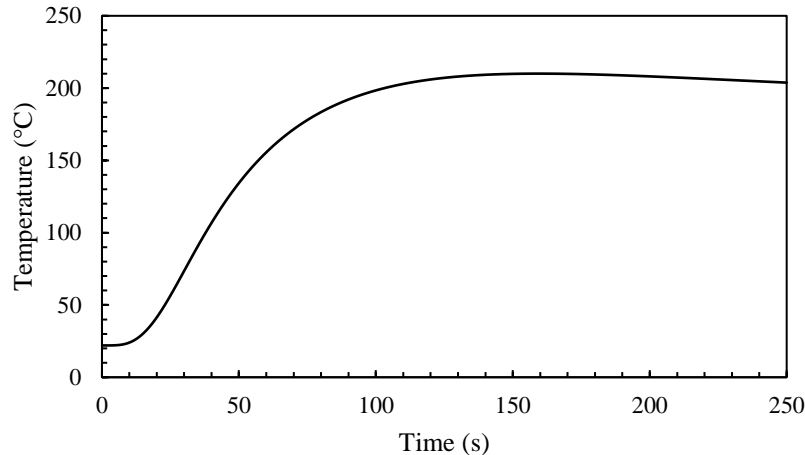


Figure 6-11: Soak-through temperature response of the nozzle structure at the exit plane.

6.9. 3D Thermal-Structural Analysis

A cyclic-symmetric 3D, one-way coupled thermal-structural FEM analysis was performed to verify that the nozzle structure could withstand the stress resulting from thermal and pressure loading. The high temperatures of the thermal insulation components and consequently their thermal expansion will cause additional hoop stress on the structural components during and after the burn. A coupled thermal-structural analysis was therefore done to consider the effect of thermal expansion of the insulation material.

6.9.1. Solver

The Simcentre Multiphysics solver environment of Siemens NX™ 11 was utilised which can perform both one-way and two-way coupled thermal-structural analyses. One-way coupling couples the thermal solution to the structural solution to include the effects of the thermal results

in the structural analysis. A one-way coupled analysis was chosen as no significant deformation was expected. The methodology employed for the analysis is shown in Figure 6-12. First a transient thermal analysis was performed to obtain the temporal temperature distribution. The mapping solution maps the temperature distribution results on to the mesh of the structural solution. The transient structural analysis uses the NX Nastran™ Multi-step Nonlinear (SOL 401) solution type, however, it is still performed as a static linear analysis per time step. The same assumptions and simplifications used in the axisymmetric analysis were employed.

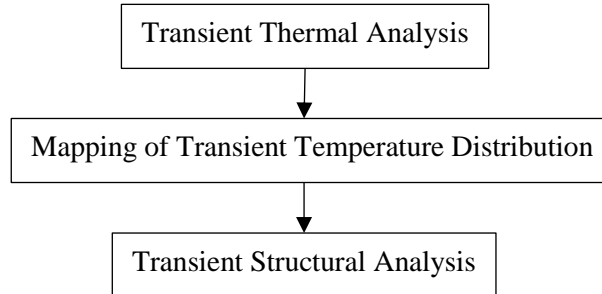


Figure 6-12: One-way coupled thermal-structural FEM analysis methodology.

6.9.2. Model and Mesh

A 36° cyclic-symmetric section of the nozzle model was used to reduce solution time, shown in Figure 6-13. All gaps in the insulation were removed and simplified bolt geometry was used. For the thermal solution, linear hexahedron elements were used to mesh the insulation components and linear tetrahedrons for the structural components. A 1 mm mesh was applied to all components with the throat using 0.75 mm. A total of 323196 nodes and 557788 elements were generated. The structural solution used parabolic hexahedrons and parabolic tetrahedrons for the insulation and structural components respectively, with a courser mesh.

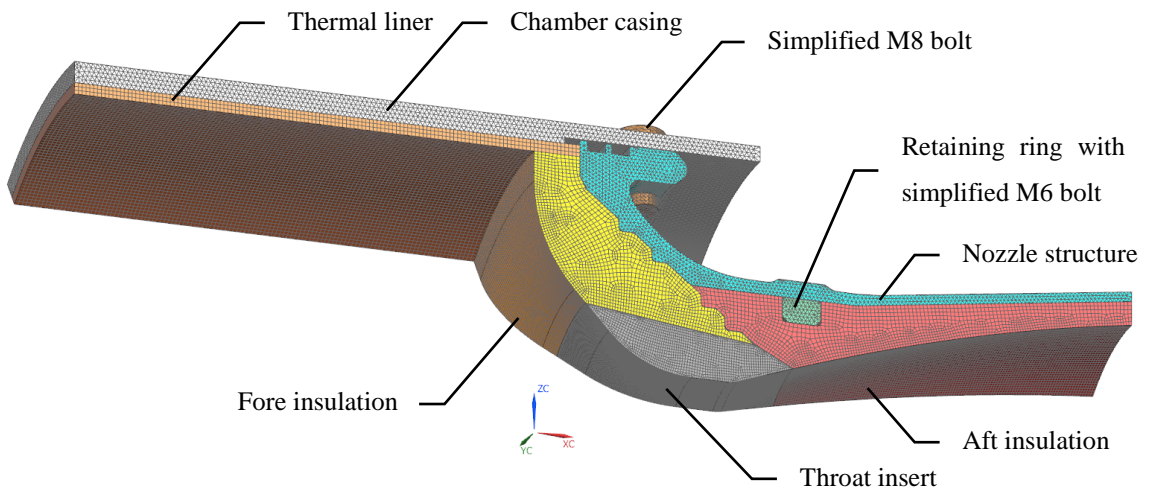


Figure 6-13: Cyclic-symmetric model thermal solution mesh for the thermal-structural analysis.

6.9.3. Constraints and Loading Conditions

For the thermal solution, surface-to-surface gluing was applied between all parts with a perfect thermal contact applied. The same temperatures set in the axisymmetric analysis were used.

A convection constraint was applied to the internal nozzle contour to represent the internal thermal load. The same spatial and temporal heat transfer coefficients and temperature data used in the axisymmetric analysis were imported into tables and used in the convection constraint on the internal surface. For the structural solution, all the nozzle parts were face glued together and a face contact was applied to the cap screws and chamber casing contacts. Symmetry constraints were applied to the symmetry planes and at the top of the thermal liner and chamber casing. The spatial and temporal pressure loading data were applied to the internal surface.

6.9.4. Results

Figure 6-14 (a) shows the temperature distribution in the nozzle after 15 s. The results are similar to the axisymmetric analysis, indicating sufficient insulation thickness. The Von-Mises stress and displacement response of the nozzle after 15 s is shown in Figure 6-14 (b) and (c). The nozzle structure, shown in Figure 6-15, is the only item of interest for structural verification, since the insulation items and nozzle configuration were verified experimentally with the PV-2 motor hot-fire test. The peak stress experienced by the nozzle structure, excluding bolt hole stress concentration, is 373 MPa at 15 s (liquid burn-out) on the nozzle exit plane. This corresponds to a minimum safety factor of 1.82, which is deemed acceptable.

The transient stress and displacement response are given in Figure 6-16, which shows that the stress increases over time until liquid burn-out. This indicates that the peak stress is directly caused by the thermal expansion of the aft insulation section, with stress hot-spots arising over the whole structure from thermal expansion of the other insulation parts. Minimal stress is caused by the pressure loading, indicating the importance of performing a coupled thermal-structural analysis.

The chamber casing also experiences additional hoop stress due to the thermal expansion of the fore insulation section, dropping the safety factor down to 1.4. This analysis indicates that the nozzle structure design is adequate for use with no alteration needed.

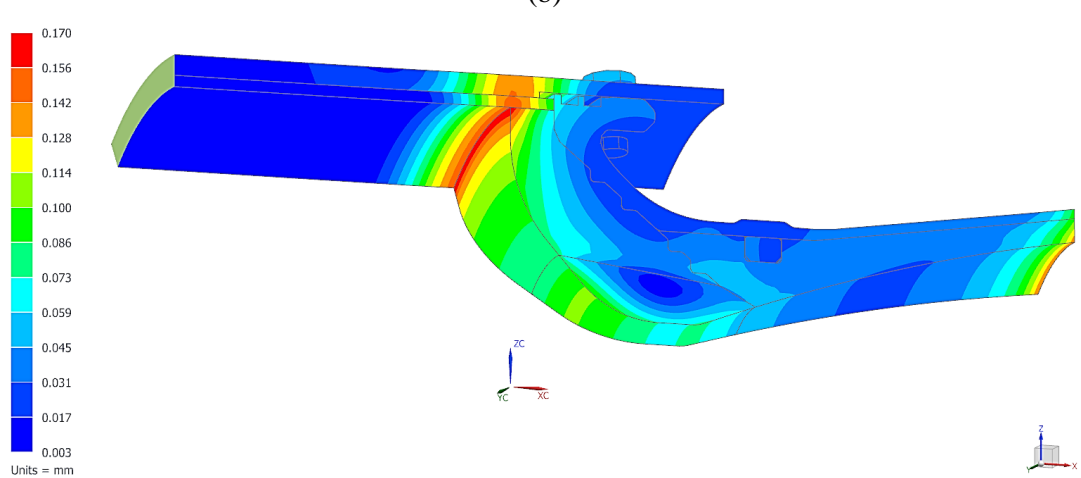
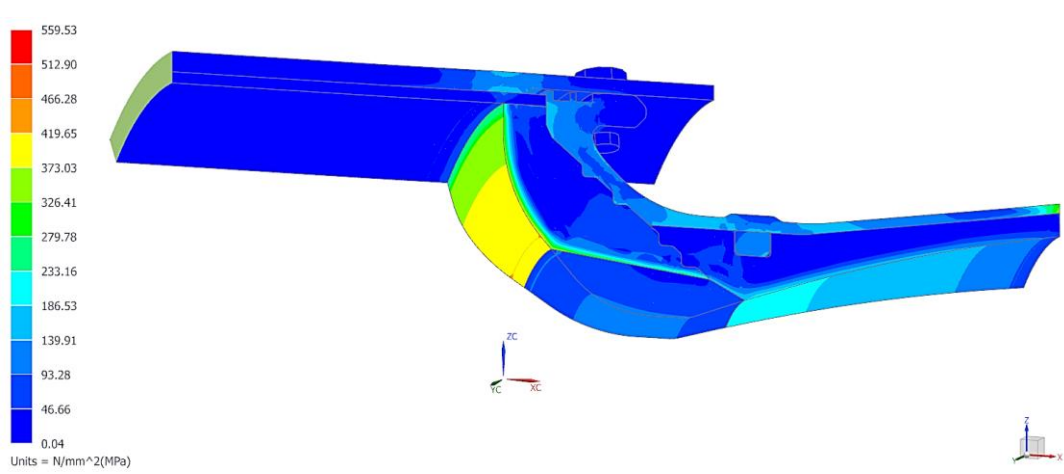
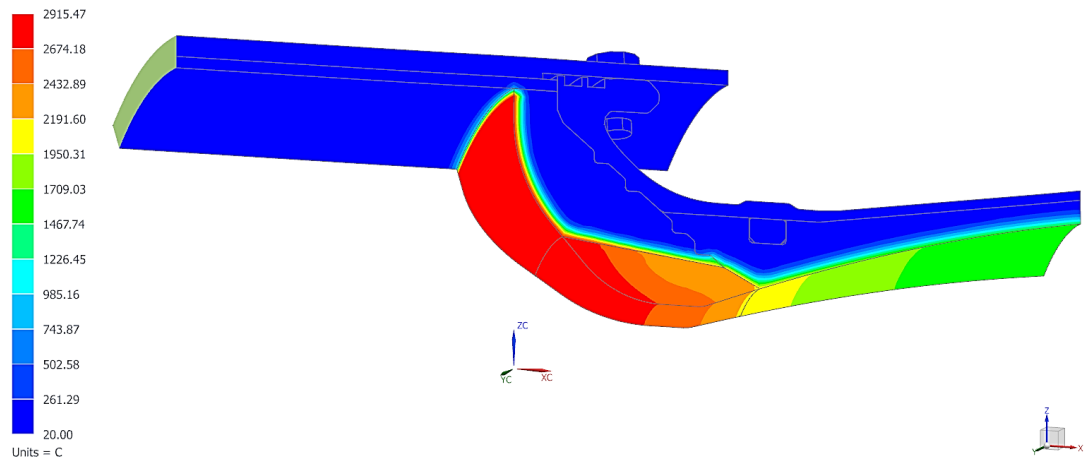


Figure 6-14: (a) Temperature distribution, (b) Von-Mises stress distribution, and (c) displacement of the cyclic-symmetric nozzle after 15 s.

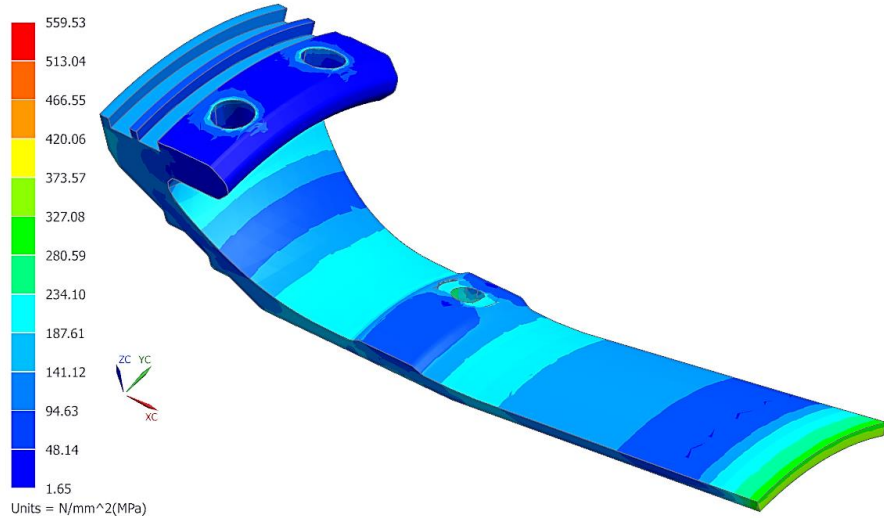


Figure 6-15: Von-Mises stress of nozzle structure after 15 s.

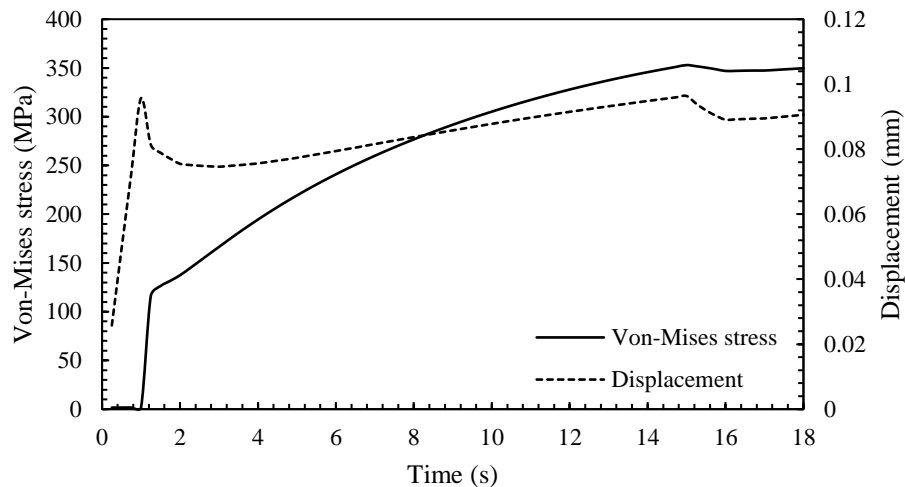


Figure 6-16: Transient (a) Von-Mises stress and (b) displacement response on a point on the nozzle exit plane.

6.10. Nozzle Manufacture

The PV-3 nozzle insulation manufacture and final assembly were undertaken for UKZN by Rheinmetall Denel Munition. Figure 6-17 (a) and (b) show the compression moulded and tape wrapped billets for the fore and aft insulation sections respectively. The compression moulded billet was made from a mixture of $\frac{1}{2}'' \times \frac{1}{2}''$ chopped squares of pre-impregnated silica/phenolic fabric and “rubber” phenolic which was formed under pressure and temperature in a proprietary sequence. The tape wrapped billet was made from $\frac{1}{2}''$ tape cut at 45° from pre-impregnated silica/phenolic fabric and sewed together. The tape was wrapped over a mandrel at a 60° angle to the axis and was post-cured in an autoclave. Both billets were then machined along with the graphite throat insert, and bonded together with a two-part RTV silicone. Figure 6-17 (c) and (d)

show the final assembled nozzle which was painted with a polyurethane enamel to prevent moisture absorption during storage.

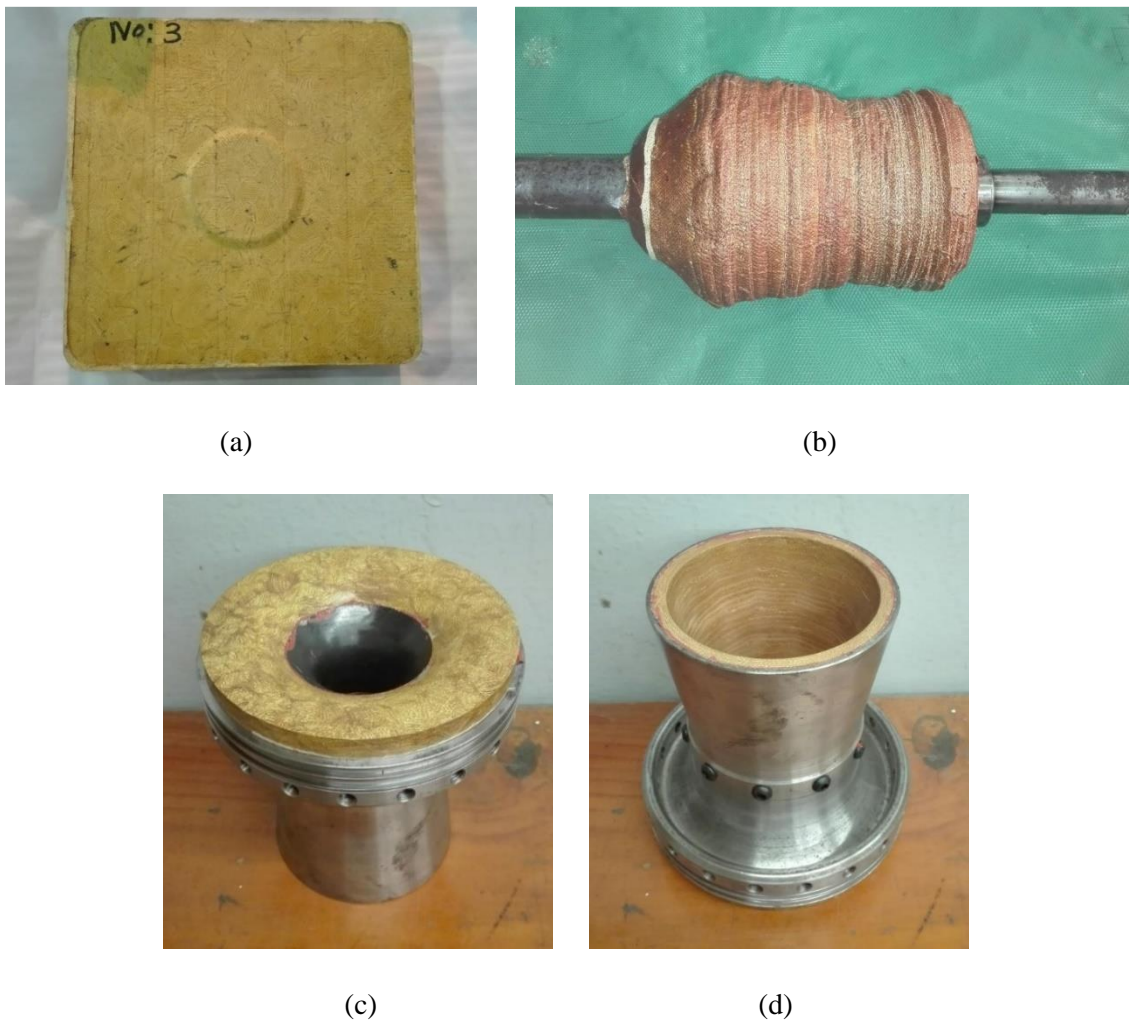


Figure 6-17: (a) Compression moulded silica/phenolic, (b) tape-wrapped silica/phenolic, (c) final nozzle top view, and (d) final nozzle bottom view.

6.11. Summary

The PV-2 motor nozzle was updated for use on the PV-3 motor with a revised aerodynamic contour and expansion ratio. The thermal loading associated with 20% aluminium additive was obtained and the nozzle design was verified with a thermal-structural analysis, with no changes required. The testing chapter follows which focuses on experimentally verifying the motor performance.

7. STATIC TESTING

7.1. Introduction

This chapter describes the static testing phase of the PV-3 motor with the goal of verifying the performance and testing the associated Ground Support Equipment (GSE). Static testing was performed on the Mobile Rocket Launch Platform (MRLP), positioned on a sports field at the Howard College campus of UKZN. The static motor testing phase included igniter testing, a cold flow test, and a hot-fire test.

7.2. Mobile Rocket Launch Platform

The MRLP can be used for both static testing of flight-weight motors and for launching of sounding rockets. It consists of a trailer base structure with four stabilising arms and a gantry that can be adjusted to an angle between 60° and 90° . The gantry is extended to 7 m in length for the launch configuration. It consists of all the necessary GSE required for filling the oxidiser tank and firing the motor. A Tank Inverting System (TIS) is used for loading and inverting the nitrous oxide supply tanks on the MRLP. Each tank is supported by a load cell to measure the mass of nitrous oxide used.

The Propellant Feed System (PFS) consists of a pneumatic pump that feeds nitrous oxide from the supply tanks to the oxidiser tank via a quick-connect on the fill station. A vent station is situated at the top of the gantry with a servo motor actuated ball valve connected to the top of the oxidiser tank via another quick-connect. This valve is used for venting nitrous oxide vapour in the oxidiser tank ullage to atmosphere, thereby dropping oxidiser tank pressure and creating a larger pressure difference between the oxidiser tank and the pneumatic pump, to speed up the oxidiser filling process.

A National Instruments™ CompactRIO™ is used for control of the PFS and data acquisition from the load cells, pressure transducers, and thermocouples. The CompactRIO™ is operated remotely using a LabVIEW™ program on a laptop. Figure 7-1 shows a CAD model of the MRLP in the static test configuration. The oxidiser tank is mounted to a thrust frame on the gantry via a load cell which measures the oxidiser mass loaded during filling and thrust during the hot-fire test. Three support brackets secure the oxidiser tank and motor to the gantry to allow for axial movement.

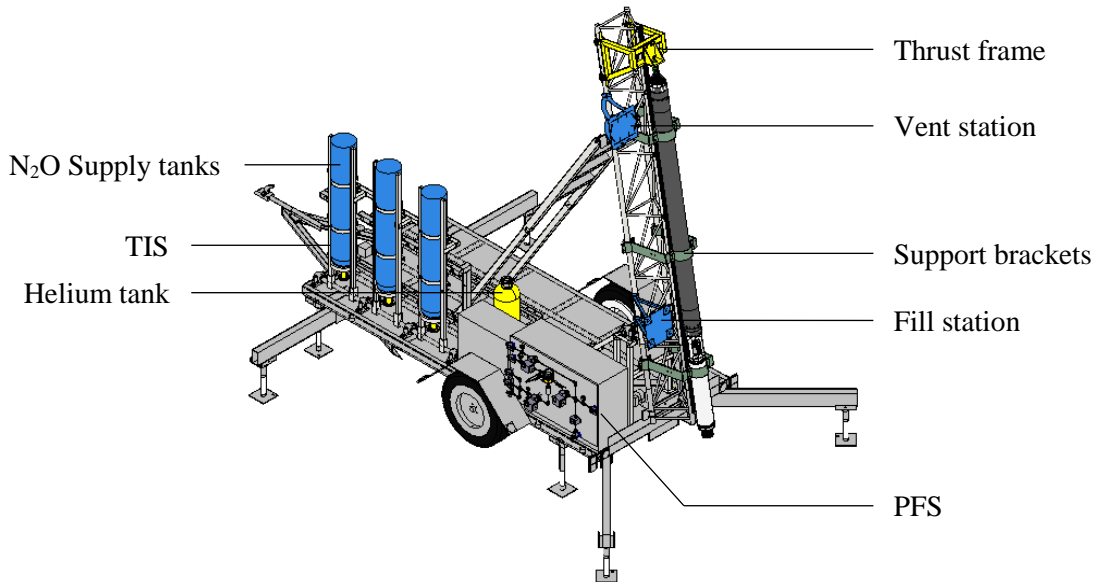


Figure 7-1: Mobile Rocket Launch Platform in static test configuration.

7.3. Igniter Test

Each PV-3 motor igniter consists of a 19 mm internal diameter cardboard tube, 30 mm long, that is filled with a compacted mixture of potassium nitrate and castor sugar. Ignition is achieved with a thin gauge nichrome wire connected to a 12 V battery. Figure 7-2 is a still image from igniter test 2 which had a successful burn of 8 s. Three of these igniters are bonded into the motor's pre-combustion chamber during assembly for hot-fire testing and provide at least a 6 s burn time during which paraffin wax fuel is vaporised to initiate combustion.



Figure 7-2: Still image of igniter test 2.

7.4. Cold Flow Test

A cold flow test of the P-1B Mk II propulsion system was undertaken to characterise the injector atomisation and oxidiser mass flow rate, to leak-test the oxidiser tank and feedlines using nitrous

oxide, to practice the oxidiser tank filling process, and to verify the operation of the PFS, LabVIEW™ program and data acquisition.

7.4.1. Test Setup

The test was performed on the MRLP in the static test configuration at a gantry angle of 75°, as seen in Figure 7-3. The motor casing and nozzle were removed for the cold flow test to observe the oxidiser atomisation, with just the oxidiser tank, feedline, injector bulkhead, and injector plate assembled to the MRLP.

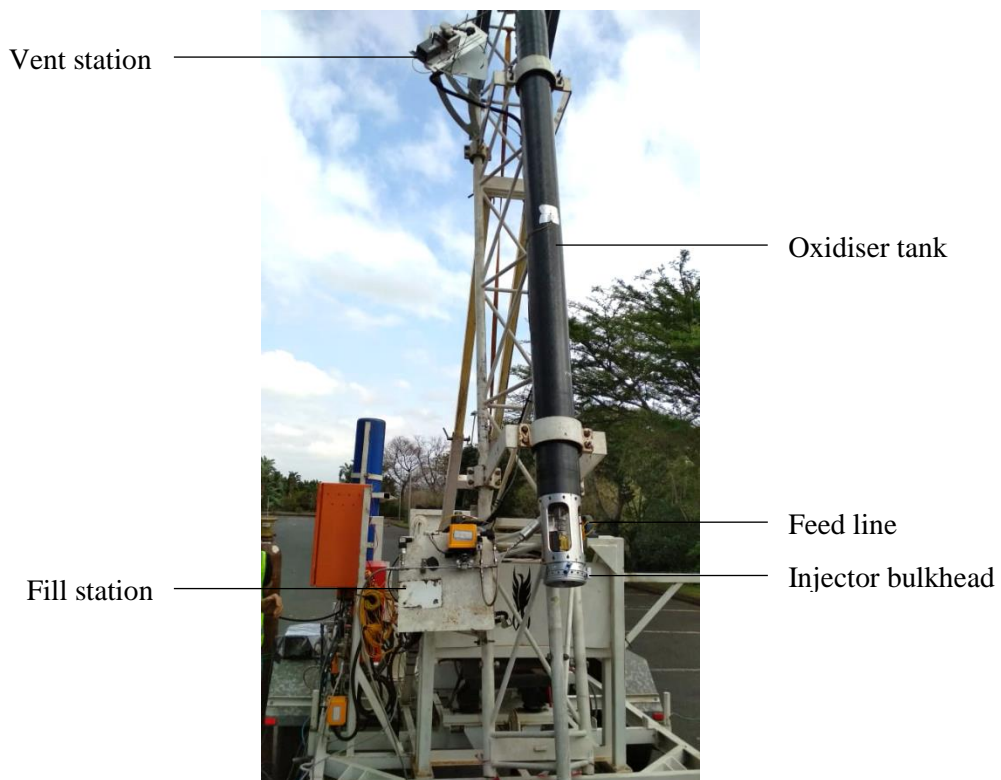


Figure 7-3: Cold flow test setup with propulsion system on the MRLP.

7.4.2. Results and Discussion

The filling process and blowdown test proceeded without incident or leaks. Figure 7-4 shows the injector plume after 1 s, indicating good atomisation. Figure 7-5 includes the pressures and mass traces during the filling process. The oscillating pressures during the filling phase are due to venting of the oxidiser tank. The warming phase allows the vapour pressure to increase in the oxidiser tank, but this was cut short due to time constraints and only reached a pressure of 41.2 bar. The supercharging phase increased the tank pressure to the nominal 65 bar pressure with helium.

The mass of nitrous oxide loaded into the oxidiser tank was determined from two sources: the thrust load cell at the top of the oxidiser tank and two load cells under the nitrous oxide supply

tanks. Both methods introduced error in the measurement, with the thrust load cell affected by the mass of water condensation, friction with the support brackets and flexible hose expansion, and the supply tank load cells affected by mass lost during venting and feedline dumping. It is noticeable that both the mass traces in Figure 7-5 decrease with time during the warming and filling phases. This is attributed to load cell drift with changing temperatures and possibly due to mechanical coupling between the tanks and the GSE.



Figure 7-4: Injector plume after 1 s.

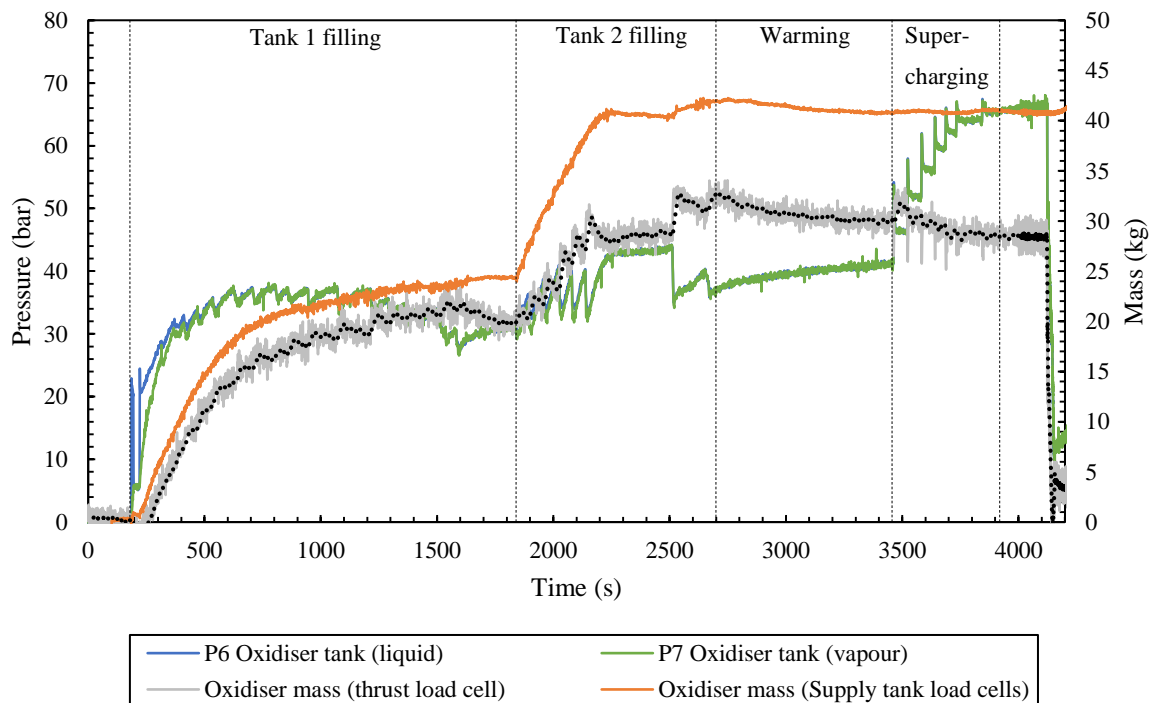


Figure 7-5: Cold flow test pressure and mass traces during filling process.

Figure 7-6 shows the liquid and vapour pressure traces during the blowdown test. The dip in pressure at the start is attributed to the lower than desired initial oxidiser vapour pressure and the filling of the feedline volume between the ball valve and injector plate.

Table 7-1 gives the experimental results from the cold flow test for the liquid feed time only. The liquid oxidiser was expelled from the tank in 22.65 s which was longer than expected, indicating an inadequate oxidiser mass flow rate. The average oxidiser mass flow rate of 1.437 kg/s was found by dividing the mass of liquid oxidiser loaded by the liquid feed time. A liquid oxidiser mass of 32.54 kg was loaded into the oxidiser tank, taken at the point at the end of the filling phase, excluding the gaseous oxidiser mass. Figure 7-7 shows an infrared image of the oxidiser tank after the filling process confirming that the tank was slightly under-loaded, indicating an ullage of approximately 15%.

A lower than expected average coefficient of discharge of 0.282 was found using the incompressible flow equation. This coefficient includes the losses in feedline from the oxidiser tank to the injector plate exit, since only the tank and ambient pressures are known. The lower coefficient is attributed to higher than expected losses in the feedline due to oxidiser cavitation and two-phase flow. A higher injector pressure drop is experienced in the cold flow test since the back pressure is ambient pressure. While this increases the driving force across the injector, the coefficient of discharge decreases due to the presence of two-phase flow, thus limiting the mass flow rate to a critical value.

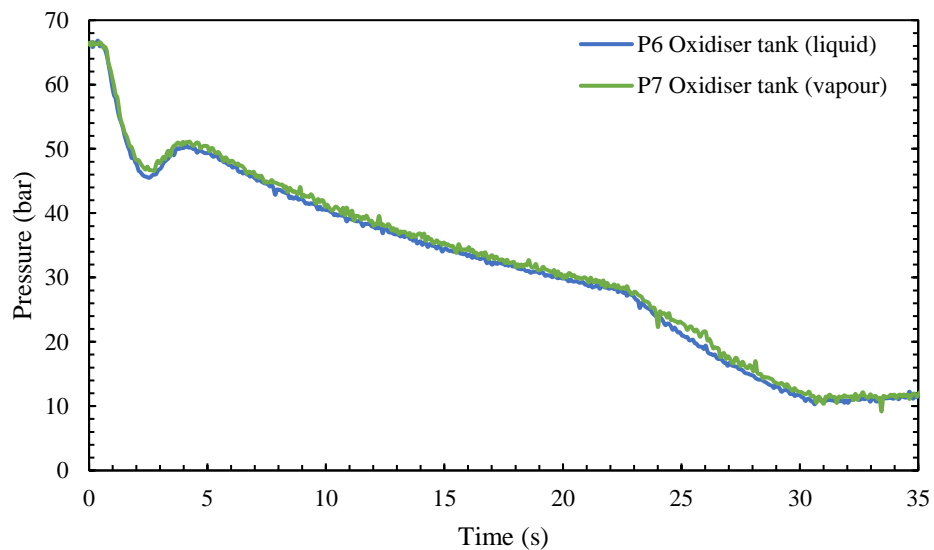


Figure 7-6: Cold flow test pressure traces.

Table 7-1: Cold flow test results for liquid feed time only.

| Result | Test | Unit |
|-----------------------------------------|-------|------|
| Time | 22.65 | s |
| Liquid oxidiser | 32.54 | kg |
| Average tank pressure | 39.33 | bar |
| Average injector pressure drop | 39.33 | bar |
| Average oxidiser mass flow rate | 1.437 | kg/s |
| Average coefficient of discharge | 0.282 | - |

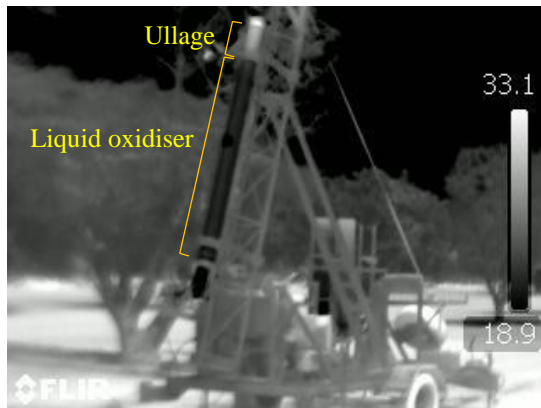


Figure 7-7: Infrared camera image of oxidiser tank after filling process.

7.4.3. Injector Plate Revision

The lower than expected oxidiser mass flow rate necessitated a redesign of the injector plate. To this end, an average coefficient of discharge was found empirically from the P-1A, P-1B Mk I, and laboratory-scale motor hot-fire tests at UKZN. This yielded an average value of 0.414, which also includes the feedline losses.

Using an average nitrous oxide density of 880 kg/m^3 , an average pressure drop of 13.22 bar, and a required average oxidiser mass flow rate of 2.1826 kg/s (liquid only from HRPC), a required injector area of $1.923 \times 10^{-4} \text{ m}^2$ was found, which is an increase of 78% over the original design area. With the original orifice diameter of 1 mm, a total of 139 orifices would be required, but this was not possible with the existing injector plate. Therefore, the orifice diameter was increased to 1.2 mm while keeping the original number of 78 orifices, resulting in a conservative area increase of 44%. The conservative approach is warranted due to uncertainty in the coefficient of discharge of the PV-3 motor under hot-fire test conditions and the possibility of the initial oxidiser mass flux breaching the upper limit. The orifice L/D ratio drops to 9.17, which is acceptable.

7.5. Hot-fire Test

A hot-fire test of the P-1B Mk II propulsion system was performed on the 4 October 2018, after the injector plate area had been updated. The objectives of the test were to verify the motor performance, test the igniters, test the motor ignition sequence, and to verify the structural integrity of the vehicle under the thrust load.

7.5.1. Test Setup

The P-1B Mk II assembled in the static test configuration is shown in Figure 7-8. The hot-fire test was performed at a gantry angle of 75° , shown in Figure 7-9. The test was conducted on a sports field at UKZN for safety. Thermocouples were attached to the motor's bulkhead, combustion chamber, and nozzle to obtain soak-through temperatures and thereby verify that the components could be reused for launch. An oxidiser mass of 25 kg was loaded into the tank. This corresponded to an estimated 10 s burn time and was intended to leave some fuel unburnt for the purpose of measuring the regression rate. This was to validate the regression rate coefficient assumption made during the design phase and to obtain motor performance metrics.



(a)



(b)

Figure 7-8: (a) P-1B Mk II assembled in static test configuration and (b) feedline assembly.

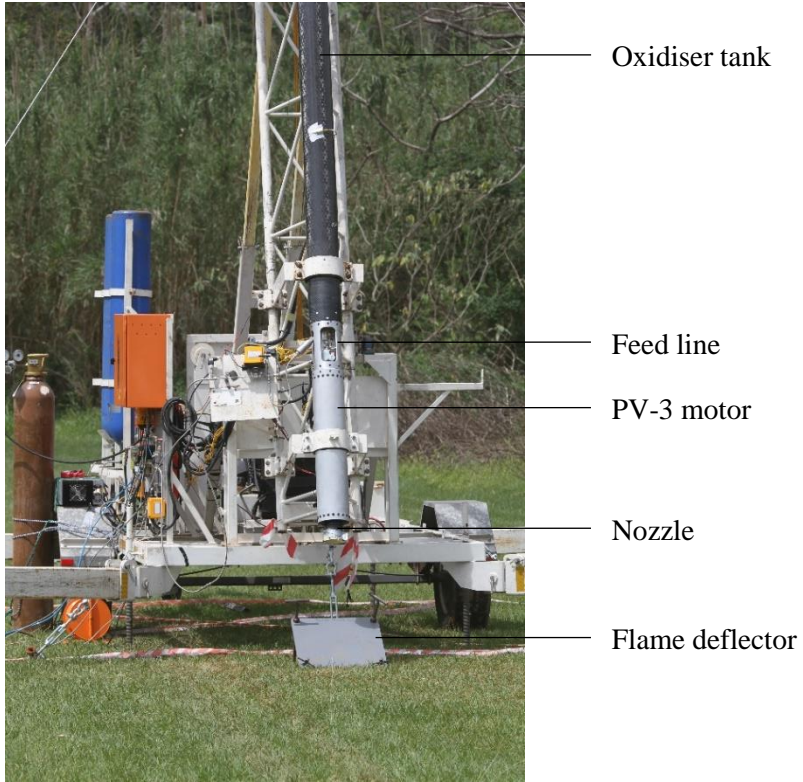


Figure 7-9: Hot-fire test setup with propulsion system on the MRLP.

7.5.2. Results and Discussion

The PV-3 motor ignited successfully and burned for 10.85 s during the liquid oxidiser blowdown phase. However, for safety reasons, the test was allowed to run to 20 s until the oxidiser ball valve was closed. This resulted in a longer than expected gas burn after the liquid oxidiser had been depleted which consumed all the remaining fuel. The regression rate, and thus fuel mass flow rate, could therefore not be measured and had to be assumed, introducing a degree of uncertainty into the calculated performance metrics.

The key hot-fire test results are given in Table 7-2 for the liquid burn only, with comparison to nominal design metrics from HRPC. The averaged quantities were calculated over the time period when the chamber pressure was greater than 50% of the mean chamber pressure. The average oxidiser mass flow rate was found by dividing the mass of liquid oxidiser loaded by the liquid burn time. A mass of 22.75 kg of liquid nitrous oxide was loaded into the oxidiser tank during filling and an ullage volume of 40% was determined from an infrared camera deployed during the test.

Most of the performance metrics are under the nominal design values by a few percent. A total impulse of 53.4 kNs was achieved for the liquid burn only which is about 29% lower than the nominal value, due to the lower oxidiser mass loaded and thus lower burn time. For the whole

burn, a total impulse of 63.3 kNs was achieved, which is 17% below nominal. The oxidiser mass flow rate is an average of 3.93% below nominal with an average coefficient of discharge of 0.457.

The cold flow and hot-fire tests suggest that the analytical and numerical methods used to predict the oxidiser mass flow rate in the injector design section are inadequate and that experimental testing is necessary to obtain an acceptable injector design in hybrid rockets.

Table 7-2: PV-3 motor hot-fire test results for liquid burn only. Nominal design values for liquid burn only given for comparison.

| Result | Unit | Test | Design | Difference (%) |
|----------------------------------------|----------------------|---------|--------|----------------|
| Burn time | s | 10.85 | 14.17 | -23.4 |
| Peak thrust | N | 7366 | 7250 | 1.6 |
| Average thrust | N | 4920 | 5279 | -6.8 |
| Average tank pressure | bar | 43.04 | 43.89 | -1.9 |
| Average chamber pressure | bar | 27.82 | 30.66 | -9.3 |
| Average injector pressure drop | bar | 15.22 | 13.22 | 15.1 |
| Average oxidiser mass flow rate | kg/s | 2.097* | 2.183 | -3.4 |
| Total impulse | Ns | 53374 | 74809 | -28.7 |
| Average specific impulse | s | 196.5* | 202.9 | -3.2 |
| Average oxidiser mass flux | kg/m ² -s | 268.69* | 254.47 | 5.6 |
| Average O/F ratio | - | 4.6* | 4.68 | -1.8 |

*Based off assumed regression rate.

Table 7-3 gives the averaged performance efficiencies from the hot-fire test for the liquid burn phase. The theoretical values were found using NASA CEA™ with the nominal motor operating conditions. The experimental combustion efficiency is lower than the design value of 85%, although this may be due to the uncertainty of the fuel and oxidiser mass flow rates.

Table 7-3: Hot-fire test averaged efficiencies for liquid burn only.

| Result | Efficiency (%) |
|--------------------------------------|----------------|
| Combustion efficiency | 79.4* |
| Specific impulse efficiency | 77.6* |
| Thrust coefficient efficiency | 97.6 |

*Based off assumed regression rate.

Figure 7-10 shows the tank pressure, chamber pressure, and thrust traces. The thrust trace is highly unstable with an average roughness of 12.6%, peaking up to 51.2%, during the liquid burn. Roughness is defined as the absolute percentage difference between the measurement and the mean smoothed curve. The chamber pressure trace is more stable with an average pressure roughness of 4.3%. The sampling rate was inadvertently set at about 10 samples per second which

resulted in low frequency data resolution and the inability to generate a frequency spectrogram to investigate the type of instabilities experienced.

There is an observable coupling between the chamber pressure and the thrust traces at times but the thrust trace is highly variable suggesting there is another source for the irregularity. Possible causes for the instabilities could be DC pressure shift caused by the change in fuel grain geometry over time. The thrust load cell connecting the top of the oxidiser tank to the thrust frame could have been affected by the support brackets cradling the tank or the flexible hoses on the quick-connects. The gantry to which the thrust frame is attached may have oscillated since it is situated at the end of the gantry, creating a large moment arm to the gantry pivot point.

Figure 7-11 compares the smoothed experimental traces to the nominal design traces obtained from HRPC. The chamber pressure and thrust traces are an average of 9.3% and 6.8% below the simulated traces respectively. Figure 7-12 shows still images from the hot-fire test and the test aftermath. The test was performed on the MRLP at 75° and the nozzle being near to the ground, thus most of the plume could not be observed and was obscured by smoke for most of the burn.

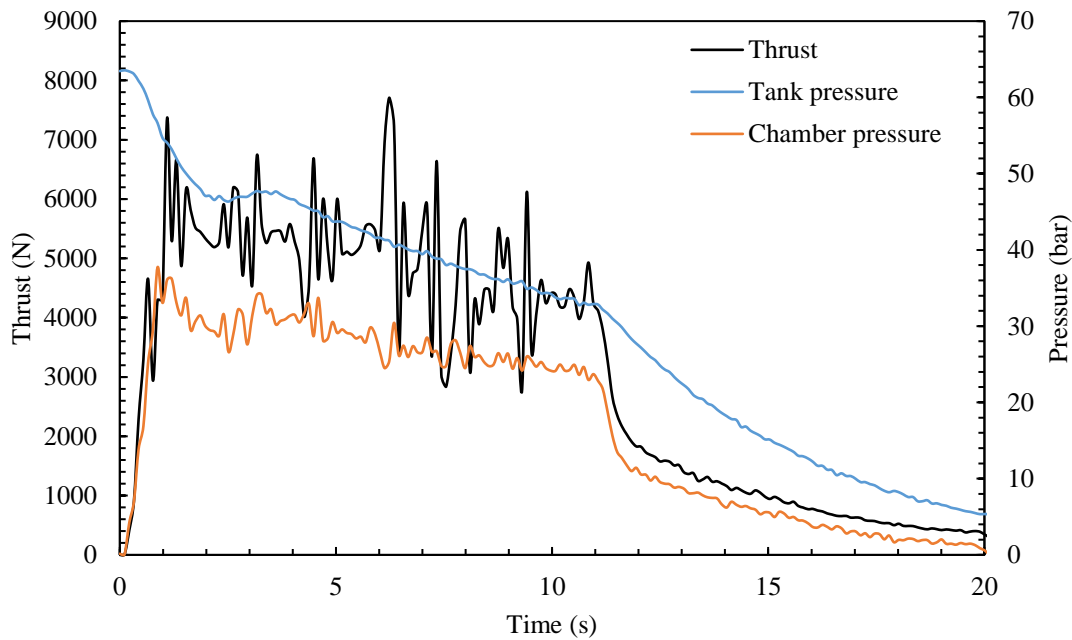


Figure 7-10: Thrust and pressure traces from the hot-fire test.

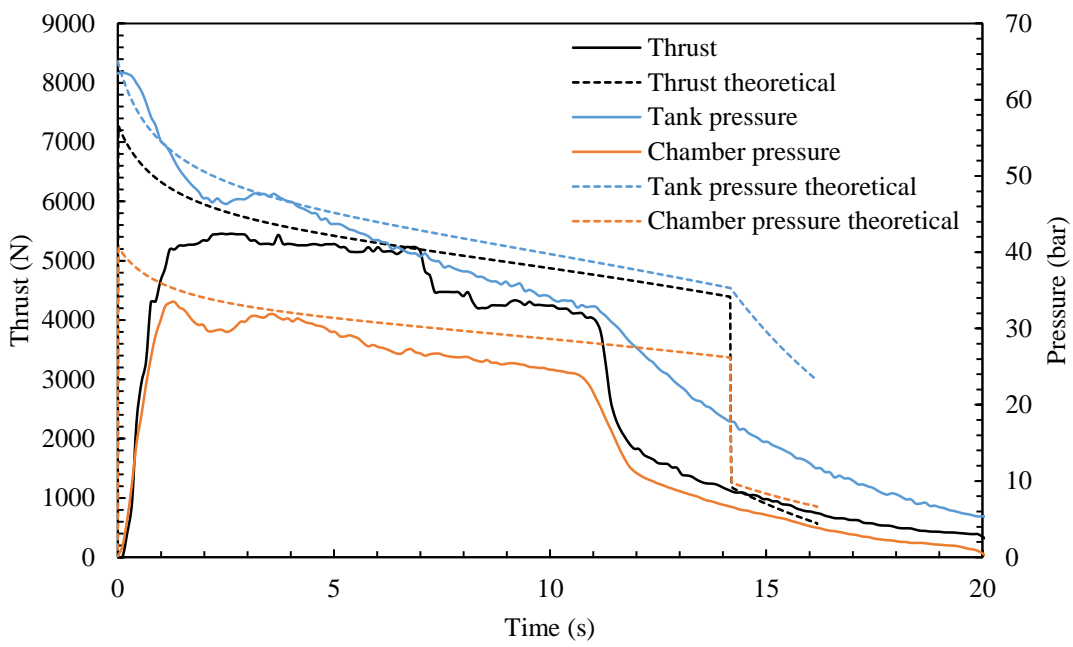


Figure 7-11: Comparison of hot-fire test results to nominal simulated results from HRPC (thrust and chamber pressure traces smoothed).



(a)



(b)



(c)

Figure 7-12: Hot-fire test (a) still image 1, (b) still image 2, and (c) MRLP after hot-fire test.

During the hot-fire test, data was recorded after the burn for up to 200 s to obtain the soak-through temperatures. The injector bulkhead drops to -12 °C at the end of the burn, caused by the flow of nitrous oxide, and rises up to a maximum of 65 °C due to conduction. The pre- and post-combustion chambers reach maxima of 74 °C and 59 °C, respectively, indicating that all the motor components are likely reusable.

Figure 7-13 gives a comparison between the nozzle soak-through temperature plot and the axisymmetric thermal FEA soak-through plot, taken at the same point on the external nozzle structure. The simulated curve follows a similar trend to the experimental curve. The nozzle structure peaks at 173 °C after 185 s of soak-through while the simulated curve peaks at 201 °C after 220 s. This discrepancy is likely due to the lower burn time of the hot-fire test at 10.85 s compared to 14.2 s of the thermal FEA. The thermal FEA also assumes perfect conduction at interfaces and does not take into account the ablation of the silica/phenolic insulation and subsequent charring. Nevertheless, the thermal FEA can be seen to predict the transient trend and maximum temperature fairly well, adding confidence to the thermal analysis.

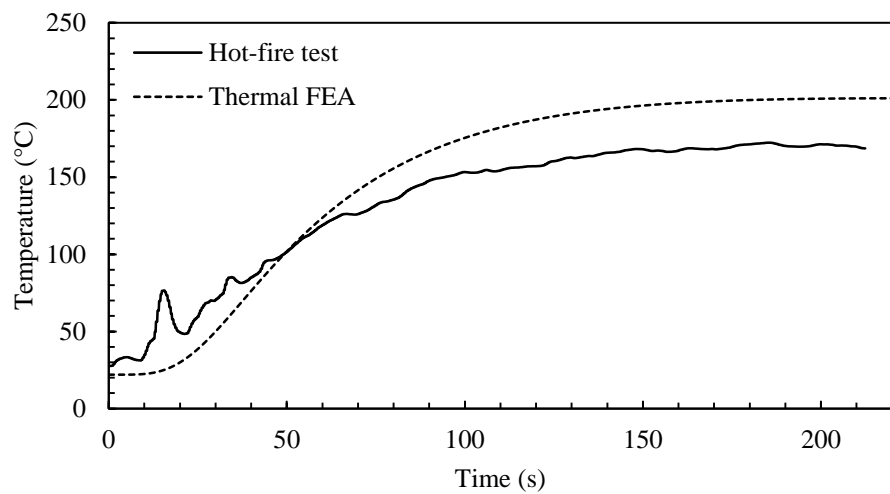


Figure 7-13: Hot-fire test and thermal FEA soak-through nozzle temperatures.

7.5.3. Post-inspection

Figure 7-14 shows images of the nozzle, injector, and thermal liner after disassembly. The nozzle performed well with no visible structural yielding or cracking. The nozzle converging section has a thin layer of slag probably consisting of aluminium, aluminium oxide, exhaust products, and ablation products. The diverging section is clean of any slag and there is minimal erosion throughout the nozzle.

Inspection of the injector plate and bulkhead after disassembly indicated no damage and the part will be re-used for launch. The thermal liner is significantly charred but still intact, with no fuel remaining.



(a)



(b)



(c)



(d)



(e)

Figure 7-14: (a) Nozzle Converging section, (b) nozzle throat, (c) nozzle diverging section, (d) injector plate, and (e) thermal liner.

7.6. Summary

The cold flow test showed that good oxidiser atomisation was achieved, however the mass flow rate was inadequate due to the lower than expected coefficient of discharge. The injector was subsequently revised by increasing the orifice diameter to 1.2 mm, providing a conservative 44% increase in flow area. The analytical and numerical mass flow rate modelling techniques therefore under-predict the required injector area. The hot-fire test confirmed the need for the injector revision, with close to nominal motor performance. The average thrust and chamber pressures were below nominal by 6.8% and 9.3%, respectively. All the fuel was consumed, preventing a regression rate measurement. Relatively low combustion and specific impulse efficiencies of 79.4% and 77.6%, respectively, were achieved. The motor components, particularly the nozzle, all performed well. The motor was deemed qualified for flight and will be integrated with the P-1B Mk II vehicle for launch.

8. CONCLUSION AND RECOMMENDATIONS

8.1. Overview

The development of a sounding rocket service for the African continent is the primary goal of the Phoenix Hybrid Sounding Rocket Programme (HSRP). The service plans to provide access to the upper atmosphere for scientific instruments and rocket sub-system testing. Three sub-orbital rockets have been developed to date, all powered by hybrid propulsion systems, with the third rocket the focus of this study.

The Phoenix-1B Mk II builds upon the foundation of the Mk I vehicle, with the primary mission of improving the apogee from 16 km to 35 km. The aim of this research was to design, manufacture, and test a hybrid rocket motor to propel the vehicle to the target apogee. Methods explored to achieve this included improving motor performance and vehicle propellant mass fraction. The use of energetic metal additives in the fuel was a key enabler of improved motor and vehicle performance, since improving the total impulse delivered was limited by the motor calibre constraint. The vehicle inert mass was reduced with the development of a composite oxidiser tank and airframe dealt with in a parallel project.

8.2. Conclusions

Each of the research objectives given in Chapter 1 is concluded as follows:

Objective 1: Investigate the effects and feasibility of energetic metal additives on motor design and performance.

The effects of aluminium and magnesium additive on motor performance in paraffin wax fuel with nitrous oxide were quantified. A thermochemical analysis found that the optimum O/F ratio decreases with increasing additive concentration for both additives, effectively halving the O/F ratio at 50% concentration. A substantial improvement in density specific impulse with only a marginal improvement in specific impulse was found. Aluminium out-performs magnesium in both performance metrics, however with a comparatively significant increase in flame temperature, increasing from 3310 K to 3675 K at 50% concentration.

Two-phase flow losses and greater nozzle erosion is expected with the introduction of metal additives into the fuel. Magnesium additive was expected to exhibit greater two-phase flow losses and mechanical erosion, whilst aluminium was expected to result in greater chemical erosion. The ejection of condensed metal particles or droplets also reduces the combustion efficiency.

Magnesium was considered as an alternate candidate additive for its relative ease of ignition and potentially better combustion efficiency than aluminium additive. However, only aluminium was

considered due to lack of magnesium regression rate data. Aluminium additive at 20% concentration was selected for the PV-3 motor, decreasing the O/F ratio from 6.8 to 5.4. From a vehicle design perspective, aluminium provided a limited apogee increase of 1.7% with 20% aluminium concentration, versus a baseline vehicle. This was primarily due to the 3.43% decrease in vehicle inert mass and thus an improvement in the propellant mass fraction.

Objective 2: Specify the Phoenix-1B Mk II propulsion system design to meet the apogee requirement of 35 km.

A feasible propulsion system design was obtained in an iterative manner using the HYROPS software tool with the P-1B Mk I vehicle as a foundation. The motor utilises a propellant combination of nitrous oxide and paraffin wax with aluminium additive at 20% by mass. Nominal tank and chamber pressures of 65 bar and 40 bar, respectively, were chosen, and the motor operates via a blowdown feed system. A theoretical steady-state total impulse of 95 000 Ns, or average of 76 537 Ns, was found to propel a 76 kg vehicle with a motor calibre of 164 mm to an apogee of 35 km.

It was a challenge to obtain an adequate system design with the motor diameter constraint whilst remaining in the oxidiser mass flux stability limit. The initial oxidiser mass flux was set as a design input at 700 kg/m²-s, which determined the minimum port diameter for a given thrust. A nominal peak thrust of 7250 N and a burn time of 14.2 s were found to provide the total impulse requirement. An initial oxidiser mass flow rate of 2.9 kg/s was specified at a nominal O/F ratio of 5.4. The nozzle is designed for sea-level with an expansion ratio of 5.93.

A suggested total impulse limit exists with respect to motor calibre based on motor stability and the diametrical constraint. Thrust is limited by the oxidiser mass flux in the fuel grain port due to flame-holding instabilities and the burn time is limited by the motor diameter constraint and port diameter.

Objective 3: Design and manufacture the PV-3 hybrid rocket motor.

Standard pressure vessel theory and numerical methods were used to design the combustion chamber using available aluminium tubing. The aluminium injector bulkhead and copper injector plate were analysed in a coupled manner due to their close interaction. An 11 mm thick injector plate was a structural requirement. The combustion chamber and injector bulkhead assembly were both pressure tested to 60 bar MEOP.

The designs of the injector and nozzle are critical to achieving the required motor performance. An axial injector was selected with 78 orifices of 1 mm diameter, which was later revised to 1.2 mm. A final L/D ratio of 9.17 resulted, which is sufficient to prevent hydraulic flip in the orifices. Analytical equations and numerical CFD analyses were used to predict the mass flow rate through

the injector, considering the two-phase nature of nitrous oxide. For a nominal mass flow rate of 2.9 kg/s, a range of 75 to 87 orifices was found. The CFD analyses verified that the oxidiser cavitates in the orifices, flashing from liquid to vapour, and forming an isolating element. The pre-combustion chamber was sized to allow the injected oxidiser to fully vaporise before entering the fuel port. Sufficient flow recirculation was achieved in the pre-combustion chamber to pre-heat the oxidiser and stabilise combustion.

The nozzle design was adapted from the PV-2 motor nozzle with an updated aerodynamic contour, throat diameter, and expansion ratio due to the different propellant composition and increased thrust. The nozzle is ablatively-cooled and consists of silica/phenolic insulation, a graphite throat insert, and an EN19T alloy steel structure. The temporal and spatial heat transfer coefficient and temperature was found using the Bartz equation. A thermal-structural FEM analysis confirmed that the nozzle design is satisfactory and was found to predict the temperature response fairly well.

Objective 4: Static test the PV-3 hybrid rocket motor to validate performance.

In a cold flow test of the motor, good oxidiser atomisation was achieved but with an inadequate oxidiser mass flow rate. The losses in feed line were higher than predicted resulting in a low coefficient of discharge of 0.282. The injector design was subsequently revised using an empirically derived coefficient of discharge based on data from previous Phoenix hot-fire tests. The injector flow area was increased by 44% by increasing the orifice diameter to 1.2 mm. The analytical and numerical techniques for predicting the oxidiser mass flow rate therefore under-predict the required injector flow area.

The motor was successfully hot-fire tested but slightly under-performed with an average thrust and chamber pressure of 4920 N and 27.9 bar, respectively. These are below nominal by 6.8% and 9.3%, respectively. The total impulse was lower than required due to under-loading of the oxidiser. Combustion and specific impulse efficiencies of 79.4% and 77.6%, respectively, were achieved. A coefficient of discharge of 0.457 was recorded. The motor was deemed qualified for flight and the P-1B Mk II vehicle is now in preparation for launch

8.3. Discussion of Problems

Various assumptions and simplifications were necessary during this study. A constant combustion efficiency was used in the thermochemical analysis for both aluminium and magnesium and for all additive concentrations. In reality, combustion efficiencies differ between additive types and sizes, and are expected to decrease with increasing additive concentrations. There is limited regression rate data available for magnesium and therefore quantifying its effect on motor and vehicle design compared to aluminium was not possible.

The regression rate for aluminium additive was linearly interpolated between data available for pure paraffin and at 40% aluminium additive. This was an assumption made due to lack of empirical data at various additive concentrations.

The motor diameter constraint imposed by availability of aluminium tubing limited the achievable apogee due to a total impulse limit. This resulted in motor operation undesirably close to the maximum recommended oxidiser mass flux limit.

Orthotropic and temperature dependent mechanical and thermal properties were not available for silica/phenolic in the nozzle verification FEM analysis. It was therefore assumed isotropic with room temperature properties. Ablation, charring, and erosion were also not considered, resulting in inaccurate results.

All the fuel was consumed during the hot-fire test preventing the measurement of the regression rate. Consequently, the fuel mass flow rate was estimated to obtain the motor performance metrics, introducing uncertainty in the results. The test setup with the motor coupled to the tank was not ideal as the same load cell was used for the oxidiser mass and thrust measurements. The source of combustion instabilities was inconclusive due to a low data sampling rate.

Despite these shortcomings, the PV-3 hybrid rocket motor was successfully designed and tested, and is capable of providing the total impulse required by the Phoenix-1B Mk II to achieve its flight performance target.

8.4. Recommendations and Future Work

A comprehensive laboratory-scale test series is recommended to fully characterise motor performance with aluminium fuel additives. A good prediction of the combustion efficiency and fuel regression rate is essential for designing a hybrid motor.

The motor diameter constraint made the propulsion system design difficult and resulted in motor operation close to the oxidiser mass flux upper limit. Allowing flexibility of the motor diameter would simplify the propulsion system design and ensure stable motor operation.

Decoupling the motor and oxidiser tank is recommended for hot-fire testing to obtain accurate oxidiser mass and thrust measurements. A high sampling rate for data logging is recommended to investigate the type of combustion instabilities experienced.

Injector design should rather use average motor conditions with a blowdown system for determining the injector flow area. Multiple cold-flow tests are also recommended to fully characterise the injector before hot-fire testing.

Future work includes preparing the Phoenix-1B Mk II vehicle for launch in early 2019. The aerodynamic components including the nose cone, fins, fin can, and boat tail remain to be manufactured and integrated. An avionics module is under development and will be assembled and tested prior to launch. A flight termination system is to be incorporated for shutting down the motor during flight. Monte Carlo trajectory foot prints for various launch cases will also be generated to ensure the safe launch of the vehicle at Denel Overberg Test Range.

REFERENCES

- Aerospace Specification Metals, 2018. *Aluminum 6061-T6* [Online]. Available at: <http://asm.matweb.com/search/SpecificMaterial.asp?bassnum=ma6061t6>. [Accessed: 19 January 2018].
- Aerospace Specification Metals, 2018. *Aluminum 7075-T6* [Online]. Available at: <http://asm.matweb.com/search/SpecificMaterial.asp?bassnum=MA7075T6>. [Accessed: 25 January 2018].
- Altman, D. and Holzman, A., 2007. Overview and History of Hybrid Rocket Propulsion. In: Kuo, K. K. and Chiaverini, M. J. (eds.). *Fundamentals of Hybrid Rocket Combustion and Propulsion*. Reston, VA: American Institute of Aeronautics and Astronautics, 1–36.
- Arves, J., Gnau, M., Kearney, D., and Joiner, K., 2003. Hybrid Sounding Rocket (HYSR) Program. *39th AIAA/ASME/SAE/ASEE Joint Propulsion Conference and Exhibit*. Reston, VA.
- Balmogim, U., 2016. *Design and Development of the Phoenix-1B Hybrid Rocket*. MSc.Eng. Thesis, University of KwaZulu-Natal, Durban, South Africa.
- Balmogim, U., Brooks, M. J., Pitot De Beaujardiere, J., Veale, K., Geneviève, B., and Roberts, L. W., 2015. Preliminary Design of the Phoenix-1B Hybrid Rocket. *51st AIAA/SAE/ASEE Joint Propulsion Conference*. Orlando, FL.
- Bartz, D., 1957. A simple equation for rapid estimation of rocket nozzle convective heat transfer coefficients. *Journal of Jet Propulsion, Technical notes*, 27 (1), 49–53.
- Brooks, M. J., Pitot De Beaujardiere, J., Chowdhury, S. M., Geneviève, B., and Roberts, L. W., 2010. Introduction to the University of KwaZulu-Natal Hybrid Sounding Rocket Program. *46th AIAA/ASME/SAE/ASEE Joint Propulsion Conference & Exhibit*. Nashville, TN.
- Broughton, K. M., Williams, D. R., Brooks, M. J., and Pitot de la Beaujardiere, J., 2018. Development of the Phoenix-1B Mk II 35 km Apogee Hybrid Rocket. *54th AIAA/SAE/ASEE Joint Propulsion Conference & Exhibit*. Cincinnati, OH.
- Cantwell, B., Karabeyoglu, A., and Altman, D., 2010. Recent Advances in Hybrid Propulsion. *International Journal of Energetic Materials and Chemical Propulsion*, 4 (4), 305–326.
- Chandler, A., 2012. *An Investigation of Liquefying Hybrid Rocket Fuels With Applications To Solar System Exploration*. Ph.D Thesis, Stanford University, Stanford, CA.
- Chew, T. J., 1973. *Hydraulic Flip Behavior In Typical Liquid Rocket Operating Regimes*. Air

- Force Rocket Propulsion Laboratory, Edwards Air Force Base, CA.
- Chowdhury, S. M., 2012. *Design and Performance Simulation of a Hybrid Sounding Rocket*. MSc.Eng. Thesis, University of KwaZulu-Natal, Durban, South Africa.
- Chowdhury, S. M., Pitot De Beaujardiere, J., Brooks, M. J., and Roberts, L. W., 2011. An Integrated Six Degree-of-freedom Trajectory Simulator for Hybrid Sounding Rockets. *49th AIAA Aerospace Sciences Meeting Including the New Horizons Forum and Aerospace Exposition*. Orlando, FL.
- Delft University of Technology, 2018. *Delft Aerospace Rocket Engineering* [Online]. Available at: <https://dare.tudelft.nl/>. [Accessed: 28 November 2018].
- Doran, E., Lohner, K., Dyer, J., Dunn, Z., Wooley, E., Decker, V., and Zilliac, G., 2007. Nitrous Oxide Hybrid Rocket Motor Fuel Regression Rate Characterization. *Journal of Propulsion and Power*, 21 (4), 1–3.
- Dyer, J., Doran, E., Dunn, Z., Lohner, K., Zilliac, G., Cantwell, B., and Karabeyoglu, A., 2007. Design and Development of a 100 km Nitrous Oxide/Paraffin Hybrid Rocket Vehicle. *43rd AIAA/ASME/SAE/ASEE Joint Propulsion Conference and Exhibit*. Cincinnati, OH.
- eFunda, 2017. Alloy Steel AISI 4140 [Online]. Available at: http://www.efunda.com/materials/alloys/alloy_steeels/show_alloy.cfm?ID=AISI_4140&show_prop=all&Page_Title=AISI 4140. [Accessed: 19 December 2017].
- European Industrial Gases Association, 2012. *Oxygen Pipeline and Piping Systems* [Online]. Available at: <https://www.eiga.eu/index.php?eID=dumpFile&t=f&f=2464&token=445f73d8905379110b9c1795d62fd76aac05ac3d>. [Accessed: 15 November 2018].
- Fernando, S., 2001. *Ajax Fasteners Innovations, Minimum Thread Engagement*. Braeside, Australia.
- Franz, B., Schultz, R., Sasarita, S., Murphrey, D., and Mason, D., 2013. *Hybrid Rocket Motor (HRM) Test Stand: An Investigation of the Effects of Additives*. Senior Design Final Report, University of Arizona, Tucson, AZ.
- Gamper, E. and Hink, R., 2013. Design and test of nitrous oxide injectors for a hybrid rocket engine. *Deutscher Luft- und Raumfahrtkongress 2013*. Stuttgart, Germany.
- Gas Industries Association, 2014. *Safe Practices for Storage and Handling of Nitrous Oxide* [Online]. Available at: http://www.gasassociation.in/gia-docs/GIA_018_14_Safe_Practices_for_Storage_and_Handling_of_Nitrous_Oxide.pdf. [Accessed: 15 November 2018].

- Geneviève, B., 2013. *Development of a Hybrid Sounding Rocket Motor*. MSc.Eng. Thesis, University of KwaZulu-Natal, Durban, South Africa.
- Geneviève, B., Pitot De Beaujardiere, J., Brooks, M. J., Chowdhury, S. M., Veale, K., Leverone, F., Balmogim, U., and Mawbey, R., 2015. Flight test of the Phoenix-1A Hybrid Rocket. *51st AIAA/SAE/ASEE Joint Propulsion Conference*. Orlando, FL.
- Gilmour Space Technologies, 2018. *Low cost launches for small payloads - suborbital and orbital* [Online]. Available at: <https://www.gspacetech.com/>. [Accessed: 28 November 2018].
- Gordon, S., 1971. Calculation of Theoretical Equilibrium Nozzle Throat Conditions When Velocity of Sound is Discontinuous. *AIAA Journal*, 9 (1), 179–182.
- Gordon, S. and McBride, B., 1994. *NASA Chemical Equilibrium with Applications*. Cleveland, OH: NASA Lewis Research Centre.
- GRAFTech, 2009. *ATJ Graphite* [Online]. Available at: https://nstx.pppl.gov/DragNDrop/Working_Groups/PFCR/materials/20090908_Grade-ATJ-Isomolded-Graphite.pdf. [Accessed: 15 November 2018].
- Greiner, B. and Frederick Jr, R., 1993. Hybrid rocket instability. *AIAA/SAE/ASME/ASEE 29th Joint Propulsion Conference and Exhibit*. Monterey, CA.
- Grosse, M., 2009. Effect of a Diaphragm on Performance and Fuel Regression of a Laboratory Scale Hybrid Rocket Motor Using Nitrous Oxide and Paraffin. *45th AIAA/ASME/SAE/ASEE Joint Propulsion Conference & Exhibit*. Denver, CO.
- Haines, J., 2000. *Graphite / Carbon-Carbon Composite Target R & D* [Online]. Available at: https://www.cap.bnl.gov/mumu/collab/001215/Graphite_RandD.PDF. [Accessed: 15 November 2018].
- Himran, S., Suwono, A., and Mansoori, G. A., 1994. Characterization of Alkanes and Paraffin Waxes for Application as Phase Change Energy Storage Medium. *Energy Sources*, 16 (1), 117–128.
- Ho, C. Y., Powell, R. W., and Liley, P. E., 1968. *Thermal Conductivity of Selected Materials Part 2*. US Department of Commerce, National Bureau of Standards.
- Humble, R., Henry, G., and Larson, W., 1995. *Space Propulsion Analysis and Design*. New York: McGraw-Hill.
- Invigorito, M., Elia, G., and Panelli, M., 2016. An improved approach for hybrid rocket injection system design. *International Journal of Mechanical, Aerospace, Industrial, Mechatronic and Manufacturing Engineering*, 10 (4), 686–696.

- Kalogiannakis, G., Van Hemelrijck, D., and Van Assche, G., 2004. Measurements of thermal properties of carbon/epoxy and glass/epoxy using modulated temperature differential scanning calorimetry. *Journal of Composite Materials*, 38 (2), 163–175.
- Karabeyoglu, A., 2012. *Lecture 8: Hybrid Rocket Propulsion Fundamentals* [Online]. Available at: http://www.spg-corp.com/docs/Stanford_AA284a_Lecture8.pdf. [Accessed: 15 November 2018].
- Karabeyoglu, A., 2012. *Lecture 10: hybrid rocket propulsion design issues* [Online]. Available at: http://www.spg-corp.com/docs/Stanford_AA284a_Lecture10.pdf. [Accessed: 15 November 2018].
- Karabeyoglu, A. and Arkun, U., 2014. Evaluation of Fuel Additives for Hybrid Rockets and SFRJ Systems. *50th AIAA/ASME/SAE/ASEE Joint Propulsion Conference*. Cleveland, OH.
- Karabeyoglu, A., Cantwell, B., and Stevens, J., 2005. Evaluation of the Homologous Series of Normal Alkanes as Hybrid Rocket Fuels. *41st AIAA/ASME/SAE/ASEE Joint Propulsion Conference & Exhibit*. Reston, VA.
- Karabeyoglu, A., Dyer, J., Stevens, J., and Cantwell, B., 2008. Modeling of N₂O Decomposition Events. *44th AIAA/ASME/SAE/ASEE Joint Propulsion Conference & Exhibit*. Hartford, CT.
- Karabeyoglu, A., Stevens, J., and Cantwell, B., 2007. Investigation of Feed System Coupled Low Frequency Combustion Instabilities in Hybrid Rockets. *AIAA/ASME/SAE/ASEE Joint Propulsion Conference & Exhibit*. Cincinnati, OH.
- Karabeyoglu, A., Zilliac, G., Cantwell, B., De Zilwa, S., and Castellucci, P., 2003. Scale-up Tests of High Regression Rate Liquefying Hybrid Rocket Fuels. *41st Aerospace Sciences Meeting and Exhibit*. Reston, VA.
- Karabeyoglu, M. a., Altman, D., and Cantwell, B. J., 2002. Combustion of Liquefying Hybrid Propellants: Part 1, General Theory. *Journal of Propulsion and Power*, 18 (3), 610–620.
- Karabeyoglu, M., Cantwell, B., and Altman, D., 2001. Development and testing of paraffin-based hybrid rocket fuels. *37th Joint Propulsion Conference and Exhibit*. Salt Lake City, UT.
- Karp, A., Nakazono, B., Vaughan, D., Story, G., Oglesby, B., and Prince, A., 2018. Update on Technology Development Plan for a Low Temperature Hybrid Mars Ascent Vehicle Concept. *2018 Joint Propulsion Conference*. Cincinnati, OH.
- Leverone, F. K., 2013. *Performance Modelling and Simulation of a 100 km Hybrid Sounding Rocket*. MSc.Eng. Thesis, University of KwaZulu-Natal, Durban, South Africa.
- Lips, H. R., 1977. Experimental Investigation on Hybrid Rocket Engines Using Highly

- Aluminized Fuels. *Journal of Spacecraft*, 14 (9), 539.
- Lohner, K., Dyer, J., Doran, E., Dunn, Z., and Zilliac, G., 2006. Fuel Regression Rate Characterization Using a Laboratory Scale Nitrous Oxide Hybrid Propulsion System. *42nd AIAA/ASME/SAE/ASEE Joint Propulsion Conference & Exhibit*. Sacramento, CA.
- Macsteel, 2018. *709M40* [Online]. Available at: <https://macsteel.co.za/product/bs970-part-1-1983-709m40-en19-en19t/>. [Accessed: 5 November 2018].
- Maharaj, C. S., 2018. *Performance Characterisation of Metal Additives in Paraffin Wax Hybrid Rocket Fuel Grains*. MSc.Eng. Thesis, University of KwaZulu-Natal, Durban, South Africa.
- Marconi, E. M., 2004. *What is a Sounding Rocket?* [Online]. Available at: https://www.nasa.gov/missions/research/f_sounding.html. [Accessed: 15 February 2017].
- Marxman, G. A., Wooldridge, C. E., and Muzzy, R. J., 1963. Fundamentals of Hybrid Boundary Layer Combustion. *AIAA Heterogeneous Combustion Conference*. Palm Beach, FL.
- Marxman, G. and Gilbert, M., 1963. Turbulent boundary layer combustion in the hybrid rocket. *Ninth Symposium (International) on Combustion*.
- McCormick, A., Hultgren, E., Lichtman, M., Smith, J., Snead, R., and Azimi, S., 2005. Design, Optimization, and Launch of a 3" Diameter N₂O/Aluminized Paraffin Rocket. *41st AIAA/ASME/SAE/ASEE Joint Propulsion Conference & Exhibit*. Tucson, AZ.
- Megyesy, E., 2001. *Pressure Vessel Handbook*. 12th ed. Tulsa: Pressure Vessel Publishing, Inc.
- Metal and Tool Trade, 2015. *Certificate of Quality 7075-T6*. Johannesburg, South Africa.
- Moss, D., 2004. *Pressure Vessel Design Manual*. 3rd ed. Burlington: Gulf Professional Publishing.
- NASA, 1975. *Space Vehicle Design Criteria - Solid Rocket Motor Nozzles*. Cleveland: National Aeronautics and Space Administration.
- Non-Ferrous Metals, 2017. *Test Certificate - Copper plate (hot rolled)*. Durban, South Africa.
- Non-Ferrous Metals, 2018. *CDA110 (Electrolytic Tough Pitch)* [Online]. Available at: <http://nonferrousmetalworks.co.za/wp/cda110-electrolytic-tough-pitch/>. [Accessed: 15 November 2018].
- Nyanterkyi-kwakye, B., Birouk, M., and Popplewell, N., 2011. Effect of Cavitation and Hydraulic Flip on a Liquid Jet's Breakup in Subsonic Crossflow. *Proceedings of Combustion Institute – Canadian Section, Spring Technical Meeting*. Winnipeg, Manitoba, Canada.

Park Electrochemical Corp, 2018. *F-554 Phenolic Prepregs* [Online]. Available at: https://parkelectro.com/wp-content/uploads/2017/05/F-554-M_a4.pdf. [Accessed: 8 November 2018].

Pastrone, D., 2012. Approaches to low fuel regression rate in hybrid rocket engines. *International Journal of Aerospace Engineering*, 2012, 1–12.

Pavli, A., 1968. *Experimental evaluation of several advanced ablative materials as nozzle sections of a storable propellant rocket engine*. Cleveland: NASA, Lewis Research Centre.

Rao, G. V. R., 1958. Exhaust nozzle contour for optimum thrust. *Jet Propulsion Journal*, 28, 377–382.

Risha, G. A., Evans, B. J., Boyer, E., and Kuo, K. K., 2007. Metals, Energetic Additives, and Special Binders Used in Solid Fuels for Hybrid Rockets. In: Chiaverini, M. J. and Kuo, K. (eds.). *Fundamentals of Hybrid Rocket Combustion and Propulsion*. 413–456.

Rocket Crafters, 2018. *Intrepid Launcher Family* [Online]. Available at: <http://rocketcrafters.space/>. [Accessed: 28 November 2018].

Van Romunde, R. Z., 2011. *Factors affecting the development of sprays produced by multihole injectors for direct-injection engine applications*. Ph.D Thesis, University College London, London.

Seibert, G., 2007. *The history of sounding rockets and their contribution to European space research*. European Space Agency, (Special Publication) ESA SP. Noordwijk, Netherlands.

Stanley, 2018. *HELI-COIL Tensile strength of threaded insert assembly, Metric Series, Technical Bulletin PP-15*.

Sutton, G. and Biblarz, O., 2001. *Rocket Propulsion Elements*. 7th ed. New York: Wiley.

Swagelok, 2016. *Actuated Ball Valve Selection Guide* [Online]. Available at: <https://www.swagelok.com/downloads/webcatalogs/EN/MS-02-136.PDF>. [Accessed: 15 November 2018].

Thakre, P., Rawat, R., Clayton, R., and Yang, V., 2013. Mechanical Erosion of Graphite Nozzle in Solid-Propellant Rocket Motor. *Journal of Propulsion and Power*, 29 (3).

Thakre, P. and Yang, V., 2008. Chemical Erosion of Carbon – Carbon / Graphite Nozzles in Solid-Propellant Rocket Motors. *Journal of Propulsion and Power*, 24 (4).

University of Stuttgart, 2018. *Hybrid Engine Development - HyEnD* [Online]. Available at: <http://www.hybrid-engine-development.de/>. [Accessed: 28 November 2018].

Velthuysen, T., 2018. *Closed loop throttle control of a hybrid rocket motor*. MSc.Eng. Thesis, University of KwaZulu-Natal, Durban, South Africa (Submitted).

Virgin Galactic, 2018. *Virgin Galactic* [Online]. Available at: <https://www.virgingalactic.com/>. [Accessed: 28 November 2018].

Voestalpine High Performance Metals (Australia), 2018. *4140 High tensile* [Online]. Available at:

http://www.voestalpine.com/highperformancemetals/australia/app/uploads/sites/72/2018/03/4140_-update.pdf. [Accessed: 5 November 2018].

Waxman, B. S., 2014. *An Investigation of Injectors for Use with High Vapor Pressure Propellants with Applications to Hybrid Rockets*. Ph.D Thesis, Stanford University, Stanford, CA.

Waxman, B. S., Cantwell, B. J., and Ames, N., 2012. Effects of Injector Design and Impingement Techniques on the Atomization of Self-Pressurizing Oxidizers. *48th AIAA/ASME/SAE/ASEE Joint Propulsion Conference & Exhibit*. Atlanta, GA.

Waxman, B. S., Zimmerman, J. E., Cantwell, B. J., and Zilliac, G. G., 2013. Mass flow rate characterisation of injectors for use with self-pressurising oxidisers in hybrid rockets. *49th AIAA/ASME/SAE/ASEE Joint Propulsion Conference*. San Hose, CA.

Waxman, S., Beckwith, R., Tybor, F., Zimmerman, J., and Stoll, A., 2010. Paraffin and Nitrous Oxide Hybrid Rocket as a Mars Ascent Vehicle Demonstrator. *AIAA SPACE 2010 Conference & Exposition*. Anaheim, CA.

Werner, T. R., Knop, T., Wink, J., Ehlen, J., Huijsman, R., Powell, S., Florea, R., Wieling, W., Cervone, A., and Zandbergen, B., 2016. Development and performance of the 10 kN hybrid rocket motor for the stratos II sounding rocket. *Space Propulsion Conference*. Rome.

Williams, D. R., 2018. *Development of a composite oxidiser tank for the Phoenix-1B Mk II hybrid rocket*. MSc.Eng. Thesis, University of KwaZulu-Natal, Durban, South Africa (in preparation).

Zilliac, G. G., Waxman, B. S., Doran, E., Dyer, J., Karabeyoglu, M. A., and Cantwell, B. J., 2012. Peregrine Hybrid Rocket Motor Ground Test Results. *48th AIAA/ASME/SAE/ASEE Joint Propulsion Conference & Exhibit*. Atlanta, GA.

Zilliac, G. and Karabeyoglu, M., 2006. Hybrid Rocket Fuel Regression Rate Data and Modeling. *42nd AIAA/ASME/SAE/ASEE Joint Propulsion Conference & Exhibit*. Sacramento, CA.

Appendix A: P-1A and P-1B Mk I Design Specifications and Performance

Table A-1: Design specifications of the P-1A and P-1B Mk I rockets.

| | Parameter | Specification | | Unit |
|--------------------------------|-------------------------------------|---------------|---------------|----------------|
| | | P-1A | P-1B Mk I | |
| Propellants | Oxidiser | Nitrous oxide | Nitrous oxide | - |
| | Fuel | Paraffin wax | Paraffin wax | - |
| | Design O/F ratio | 6 | 6.8 | - |
| | Oxidiser flow method | Blowdown | Blowdown | - |
| Oxidiser Tank | Supercharge gas | Helium | Helium | - |
| | Oxidiser mass | 30 | 30 | kg |
| | Ullage | 10 | 10 | % |
| | Oxidiser tank volume | 0.043 | 0.041 | m ³ |
| | Nominal tank pressure | 65 | 65 | bar |
| | Tank length | 1.6 | 2.28 | m |
| | Tank diameter | 0.2 | 0.164 | m |
| Motor | Nominal thrust | 4250 | 5000 | N |
| | Nominal chamber pressure | 40 | 40 | bar |
| | Design combustion efficiency | 95 | 90 | % |
| | Fuel grain diameter | 0.156 | 0.148 | m |
| | Port diameter | 0.05 | 0.06 | m |
| | Fuel grain length | 0.4 | 0.404 | m |
| | Initial fuel mass | 6.4 | 5.4 | kg |
| | Nozzle expansion ratio | 5.99 | 6.38 | - |
| | Nozzle throat diameter | 0.0298 | 0.032 | m |
| | Nozzle exit diameter | 0.0731 | 0.083 | m |
| | Injector hole diameter | 0.002 | 0.001 | m |
| | Number of injector holes | 17 | 60 | - |
| Steady State Motor Performance | Chamber diameter | 0.18 | 0.164 | m |
| | Chamber length | 0.66 | 0.67 | m |
| | Oxidiser mass flow rate | 1.36 | 1.974 | kg/s |
| | Fuel mass flow rate | 0.24 | 0.29 | kg/s |
| | Total mass flow rate | 1.6 | 2.264 | kg/s |
| | Burn time | 20 | 18 | s |
| | Total impulse | 75000 | 69000 | Ns |
| | Vacuum specific impulse | 243 | 252 | s |
| | Design combustion efficiency | 95 | 90 | % |

Table A-2: Theoretical flight performance of the P-1A and P-1B Mk I rockets.

| Parameter | Specification | | Unit |
|------------------------------|----------------------|-------------|------------------|
| | P-1A | P-1B | |
| Design apogee | 15 | 17.2 | km |
| Maximum speed | 571 | 661 | m/s |
| Maximum acceleration | 32.8 | 58.6 | m/s ² |
| Ballistic flight time | 126 | 132 | s |
| Lift-off vehicle mass | 90 | 70 | kg |
| Vehicle length | 4.55 | 4.224 | m |

Appendix B: Metal Additive Study

Magnesium Discontinuity Solution

A problem was encountered when selecting the optimal O/F ratio using magnesium additive in the fuel using NASA CEA™. The characteristic velocity abruptly drops at a specific O/F ratio depending on additive concentration, such as in Figure B-1 at 40% magnesium concentration. The abrupt drop is due to an abrupt change in the slope of temperature with pressure at the melting point of magnesium oxide (MgO). This occurs due to the simultaneous presence of two condensed phases of the same species in the vicinity of the throat. This causes a discontinuity in the velocity of sound when there is a transition from one condensed phase to two condensed phases of that species during expansion. When this occurs in the vicinity of the throat, the usual procedure for determining the throat conditions provide inaccurate results.

Gordon (1971) incorporated a special technique to obtain the throat conditions into NASA CEA™ which locates the pressure ratio at which the solid phase just begins (Gordon, 1971). The resulting graph of characteristic velocity versus O/F ratio however has two local maximums. It was therefore decided to omit the solid and liquid phases of magnesium oxide, which solved the problem seen in Figure B-1. The optimum O/F ratio was taken from the peak of this curve rather, although there is a slight decrease in characteristic velocity due to the removal. Figure B-2 further justifies this choice as the removal of the phases results in an increase in combustion temperature with increasing magnesium concentration, which is expected.

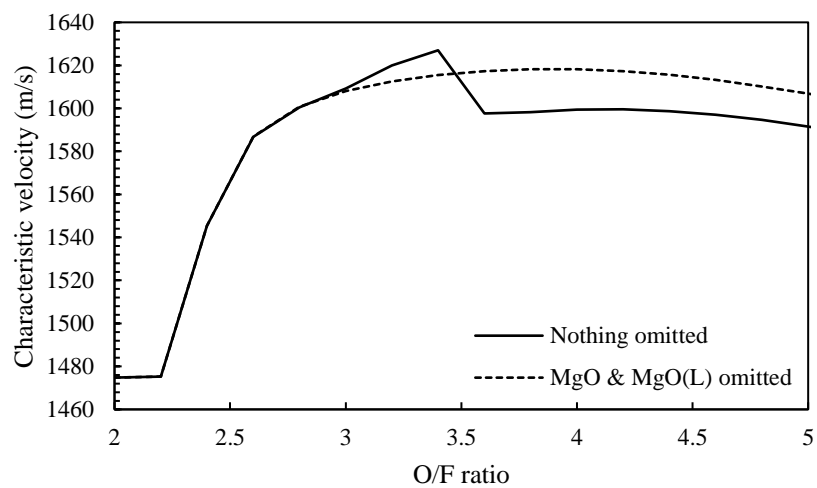


Figure B-1: Characteristic velocity for various O/F ratios for 40% magnesium concentration at 40 bar chamber pressure, with and without MgO and MgO (L) omitted in NASA CEA™.

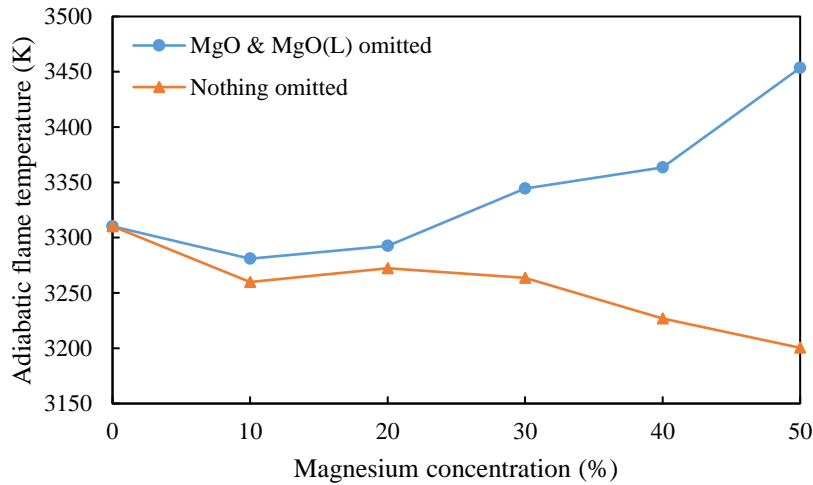


Figure B-2: Combustion temperature for various magnesium additive concentrations at 40 bar chamber pressure with and without MgO and MgO (L) omitted in NASA CEA™.

Effects of Aluminium and Magnesium Additive Concentration on Motor Performance

Table B-1: Effect of aluminium additive concentration on motor performance.

| Aluminium (%) | Peak C* (m/s) | Opt. O/F | I _{sp} (s) | I _v (kg·s/m ³) (x10 ⁵) | Flame temp. (K) |
|---------------|---------------|----------|---------------------|-----------------------------------------------------------|-----------------|
| 0 | 1295.63 | 6.8 | 200.10 | 1.86 | 3310.3 |
| 10 | 1299.30 | 6 | 201.01 | 2.00 | 3352.7 |
| 20 | 1304.06 | 5.4 | 202.56 | 2.17 | 3428 |
| 30 | 1309.28 | 4.6 | 203.78 | 2.36 | 3496.4 |
| 40 | 1314.76 | 3.8 | 205.09 | 2.59 | 3572.4 |
| 50 | 1317.67 | 3.2 | 206.30 | 2.85 | 3674.7 |

Table B-2: Effect of magnesium additive concentration on motor performance.

| Magnesium (%) | Peak C* (m/s) | Opt. O/F | I _{sp} (s) | I _v (kg·s/m ³) (x10 ⁵) | Flame temp. (K) |
|---------------|---------------|----------|---------------------|-----------------------------------------------------------|-----------------|
| 0 | 1295.63 | 6.8 | 200.10 | 1.86 | 3310.3 |
| 10 | 1292.64 | 6 | 200.33 | 1.95 | 3281.0 |
| 20 | 1294.64 | 5.2 | 200.95 | 2.06 | 3292.6 |
| 30 | 1295.68 | 4.6 | 202.14 | 2.19 | 3344.3 |
| 40 | 1294.56 | 3.8 | 202.81 | 2.32 | 3363.5 |
| 50 | 1290.08 | 3.4 | 203.70 | 2.47 | 3453.5 |

Effects of Aluminium and Magnesium Additive Concentration on Two-phase Losses and Nozzle Erosion

Table B-3: Condensed phase species and oxidising species molar fractions for aluminium additive.

| Aluminium (%) | Condensed phase mole fraction | | | Oxidising species mole fraction | | |
|---------------|-------------------------------|---------|---------|---------------------------------|---------|---------|
| | Chamber | Throat | Exit | Chamber | Throat | Exit |
| 0 | 0 | 0 | 0 | 0.49881 | 0.49244 | 0.48174 |
| 10 | 0.00616 | 0.00655 | 0.00693 | 0.49902 | 0.4934 | 0.48334 |
| 20 | 0.01400 | 0.01463 | 0.01536 | 0.49366 | 0.48809 | 0.47627 |
| 30 | 0.02398 | 0.02507 | 0.02638 | 0.49363 | 0.48897 | 0.47758 |
| 40 | 0.03645 | 0.03850 | 0.04115 | 0.49285 | 0.48985 | 0.47955 |
| 50 | 0.04931 | 0.05335 | 0.06010 | 0.47846 | 0.47758 | 0.46816 |

Table B-4: Condensed phase species and oxidising species molar fractions for magnesium additive.

| Magnesium (%) | Condensed phase mole fraction | | | Oxidising species mole fraction | | |
|---------------|-------------------------------|---------|---------|---------------------------------|---------|---------|
| | Chamber | Throat | Exit | Chamber | Throat | Exit |
| 0 | 0 | 0 | 0 | 0.49881 | 0.49244 | 0.48174 |
| 10 | 0 | 0.00391 | 0.01525 | 0.48959 | 0.48555 | 0.47928 |
| 20 | 0.01271 | 0.01970 | 0.03410 | 0.48375 | 0.48187 | 0.47624 |
| 30 | 0.03042 | 0.03916 | 0.05674 | 0.47034 | 0.46827 | 0.46259 |
| 40 | 0.05430 | 0.06399 | 0.08693 | 0.46232 | 0.46093 | 0.45634 |
| 50 | 0.07627 | 0.08662 | 0.11920 | 0.43164 | 0.43020 | 0.42491 |

Appendix C: Composite Oxidiser Tank Specific Heat Variation

HRPC Performance Model requires the variation in specific heat with temperature for the tank material. Since a composite tank was being used in this case, the constants in the specific heat function in HRPC were updated for carbon fibre/epoxy, neglecting the effect of the PVC liner, with the function given by Equation C-1.

$$C_{P,T} = G_1 + G_2 T_T \quad (\text{C-1})$$

where $G_1 = 804.3$ and $G_2 = 3.692$ for carbon fibre/epoxy in the pre-glass transition stage (Kalogiannakis et al., 2004) and T_T is the temperature of the oxidiser tank in °C. Figure C-1 compares the specific heat capacity as a function of temperature for aluminium and carbon/fibre epoxy.

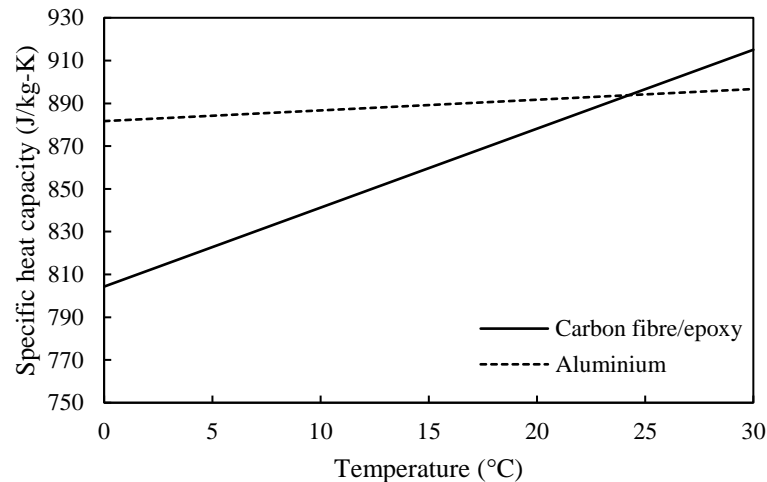


Figure C-1: Specific heat capacity as a function of temperature for aluminium and carbon fibre/epoxy in the pre-glass transition stage.

Appendix D: PV-3 Motor Specifications and Theoretical Performance

Table D-1: PV-3 steady-state motor design specifications.

| Parameter | Specification | Unit |
|---------------------------------------|---------------|-------------------|
| Design Peak Thrust | 7250 | N |
| Design O/F Ratio | 5.4 | - |
| Design Chamber Pressure | 4000000 | Pa |
| Design Atmospheric Pressure | 101325 | Pa |
| Combustion Efficiency | 85 | % |
| Burn Time | 13.13 | s |
| 1st Critical Pressure Ratio | 0.994125 | - |
| 2nd Critical Pressure Ratio | 0.226927 | - |
| 3rd Critical Pressure Ratio | 0.02533 | - |
| Characteristic Velocity | 1629.74 | m/s |
| Thrust Coefficient | 1.5237 | - |
| Optimum Nozzle Expansion Ratio | 5.9317 | - |
| Nozzle Throat Area | 0.00119 | m ² |
| Nozzle Exit Area | 0.007056 | m ² |
| Nozzle Throat Diameter | 0.038917 | m |
| Nozzle Exit Diameter | 0.094784 | m |
| Total Oxidiser Mass Flow Rate | 2.898 | kg/s |
| Total Fuel Mass Flow Rate | 0.537 | kg/s |
| Total Mass Flow Rate | 3.435 | kg/s |
| Nozzle Mass Flow Rate | 3.435 | kg/s |
| Grain Length | 0.5105 | m |
| Grain Diameter | 0.147 | m |
| Initial Grain Volume | 0.006586 | m ³ |
| Initial Grain Mass | 7.049 | kg |
| Fuel Density | 1070.33 | kg/m ³ |
| Burnt Web Thickness | 0.0375 | m |
| Total Web Thickness | 0.0375 | m |
| Number of Ports | 1 | - |
| Initial Port Diameter | 0.072 | m |
| Final Port Diameter | 0.147 | m |

Table D-2: PV-3 average motor performance.

| Parameter | Specification | Unit |
|---------------------------------------|---------------|----------------------|
| Oxidiser Mass Flow Rate | 1.978 | kg/s |
| Fuel Mass Flow Rate | 0.436 | kg/s |
| Total Mass Flow Rate | 2.414 | kg/s |
| Nozzle Mass Flow Rate | 2.413 | kg/s |
| Oxidiser Mass Flux Per Port | 226.99 | kg/m ² -s |
| Fuel Regression Rate | 0.002318 | m/s |
| Chamber Oxidiser-to-Fuel Ratio | 4.388 | - |
| Chamber Pressure | 2787554 | Pa |
| Nozzle Exit Pressure | 67483.01 | Pa |
| Nozzle Exit Velocity | 2405.86 | m/s |
| Nozzle Exhaust Velocity | 1883.10 | m/s |
| Characteristic Velocity | 1364.78 | m/s |
| Thrust Coefficient | 1.37498 | - |
| Thrust | 4731.53 | N |
| Vacuum Thrust | 5446.48 | N |
| Momentum Thrust | 4970.41 | N |
| Specific Impulse | 191.96 | s |
| Vacuum Specific Impulse | 228.32 | s |
| Total Impulse | 76537.28 | Ns |

Table D-3: PV-3 nozzle design specifications.

| Parameter | Specification | Unit |
|--------------------------------------------------------|--------------------|------|
| Nozzle throat diameter | 0.038917 | m |
| Nozzle expansion ratio | 5.9317 | - |
| Nozzle contraction ratio | 10.65 | - |
| Nozzle contraction angle | 47.5 | ° |
| Ratio of upstream to throat radius | 1.5 | - |
| Ratio of downstream to throat radius | 0.382 | - |
| Nozzle Type | Bell-Shaped Nozzle | - |
| Nozzle parabola inlet angle | 20.51 | ° |
| Nozzle parabola exit angle | 8.1 | ° |
| Nozzle fractional length | 1 | - |
| Nozzle half cone angle | 15 | ° |
| Chamber radius | 0.063502 | m |
| Nozzle throat radius | 0.019459 | m |
| Nozzle exit radius | 0.047392 | m |
| Nozzle upstream radius | 0.029188 | m |
| Nozzle downstream radius | 0.007433 | m |
| Nozzle length from inlet to throat plane | 0.053202 | m |
| Length from contraction angle position to throat plane | 0.021520 | m |
| Radius of contraction angle position to throat plane | 0.028928 | m |
| Nozzle total length from throat to exit plane | 0.105227 | m |
| Nozzle parabolic bell length | 0.102622 | m |

Appendix E: Recommended Motor Design and Performance Constraints

A review of motor design constraints and recommended performance limits was conducted in order to gauge where the PV-3 motor operated. Table E-1 gives the constraint, constraint type, its recommended range, and the PV-3 motor value.

Table E-1: Motor design and performance constraints.

| Constraint | Constraint type | Limits | PV-3 Motor | Reference |
|------------------------------------------------|----------------------|-----------------------------------------------------|----------------------------|--------------------------------------------------------------------|
| Chamber-to-throat area ratio* | Performance | $A_c/A_t \geq 4$ | 3.48 | (Sutton and Biblarz, 2001) |
| Characteristic length** | Performance | $0.8 \leq L^* \leq 3.0$ | 3.8 m | (Sutton and Biblarz, 2001) |
| Port-to-fuel grain diameter ratio | Stress | $2 \leq D_{gr}/D_p \leq 3$ | 2.04 | (Chandler, 2012) |
| Grain length-to-diameter ratio | Performance | $10 \leq L_{gr}/D_p \leq 15$ | 7.1 | (Chandler, 2012) |
| Initial oxidiser mass flux | Safety & stability | $G_o \leq 650 - 700 \text{ kg/m}^2\text{-s}$ | 711.8 kg/m ² -s | (Humble et al., 1995; Zilliac et al., 2012) |
| Injector pressure drop | Stability | $\Delta p_{inj}/p_c \geq 15 - 20\%$ min. | 31% min. | (Humble et al., 1995) |
| Chamber pressure-to-saturation pressure | Stability | $p_c < p_{sat.}$ | True | (Waxman et al., 2013) |
| Pipe velocity*** | Safety & performance | $7 \text{ m/s} \leq v_{pipe} \leq 12.3 \text{ m/s}$ | 21.75 m/s | (Humble et al., 1995; European Industrial Gases Association, 2012) |
| Feedline pipe size | Safety | $D_{pipe} \leq \frac{3}{4}''$ | $\frac{3}{4}''$ tube | (Gas Industries Association, 2014) |

*Chamber diameter being the initial port diameter for single-port hybrid motors, **Ratio of the chamber volume to the throat area, ***Based off of oxygen pipe system (7 m/s for impinging sites and 12.3 m/s for non-impinging sites at 65 bar).

The PV-3 motor chamber area-to-throat area is below the recommended value at 3.48, due to the oxidiser mass flux limit imposed. However, the port diameter increases and the oxidiser mass flow rate decreases during the burn and thus the ratio will increase beyond the recommended ratio. Ratios smaller than 4 have specific impulse losses (Sutton and Biblarz, 2001).

The chamber characteristic length is a useful measure of required combustion residence time. The PV-3 motor has an L^* of 3.8, slightly higher than the recommended range, however this value is dependent on propellant combination and is not used in chamber design today (Sutton and Biblarz, 2001).

The recommended ratio of the fuel grain port diameter to the outside diameter is based on the stress distribution on the fuel grain from pressure loading. Figure E-1 shows the stress distribution for a paraffin-based fuel grain at 34.5 bar chamber pressure, where b is the radius of the fuel grain and a is the radius of the port. The material approaches the failure boundary as the ratio of b/a increases.

Chandler (2012) recommends the fuel grain length-to-diameter ratio be between 10 and 15 based on boundary layer combustion process for higher combustion efficiency. The rate of growth of the boundary layers in the fuel grain port governs the propellant mixing process which affects the combustion efficiency. A fuel grain length too short or too long will result in incomplete combustion due to either the oxidiser flowing through without reacting or the premature merging of the boundary layers. The complex turbulent boundary layer and changing port diameter makes this a challenging design problem.

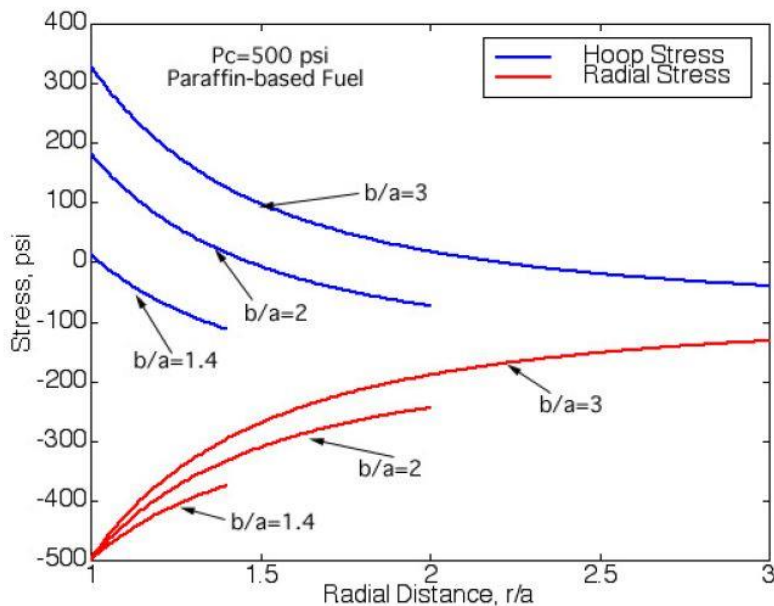


Figure E-1: Fuel grain stress distribution due to pressure loading for a 34.5 bar chamber pressure paraffin-based fuel grain (Karabeyoglu, 2012).

Appendix F: Injector Bulkhead Aluminium 7075-T6

CERTIFICATE OF QUALITY

| Ship to | Metal and Tool Trade (pty) Ltd. | | | | | | | | | | |
|------------------------|---------------------------------------|--------------------|--------|---------|-----------|---------|--------|------------|--------------|--------|--|
| Order No. | OPOR0016*1 OPOR0016*2 | | | | | | | | | | |
| Material | D7075-T6 | | | | | | | | | | |
| Quantity | 16 PCS (2702.30 KG) 3 PCS (506.68 KG) | | | | | | | | | | |
| Lot No. | OTW2715072106 OTW2715072107 | | | | | | | | | | |
| Specification | :Customer required | | | | | | | | | | |
| No | Items | Measurement | Unit | | | | | | | | |
| 1 | Dimension | Ø160x3000L | mm | | | | | | | | |
| 2 | Tensile Strength | >540 | MPa | | | | | | | | |
| 3 | Yield Strength | >470 | MPa | | | | | | | | |
| 4 | Elongation | >5 | % | | | | | | | | |
| 5 | Hardness | >80 | HRB | | | | | | | | |
| 6 | Chemical composition | OK | | | | | | | | | |
| Si | Fe | Cu | Mn | Mg | Cr | Zn | Ti | Others Max | Others Total | AL rem | |
| 0.40 | 0.50 | 1.2-2.0 | 0.30 | 2.1-2.9 | 0.18-0.28 | 5.1-6.1 | 0.20 | 0.05 | 0.15 | | |
| Quality checked | | | | | | | | | | | |
| No | Items | Measurement result | Unit | | | | | | | | |
| 1 | Dimension | Ø160.33x3001L | mm | | | | | | | | |
| 2 | Tensile Strength | 564.24 | MPa | | | | | | | | |
| 3 | Yield Strength | 478.32 | MPa | | | | | | | | |
| 4 | Elongation | 15.57 | % | | | | | | | | |
| 5 | Hardness | 81.2 | HRB | | | | | | | | |
| 6 | Chemical composition | OK | | | | | | | | | |
| Si | Fe | Cu | Mn | Mg | Cr | Zn | Ti | Others Max | Others Total | AL | |
| 0.0838 | 0.1255 | 1.5120 | 0.0372 | 2.4690 | 0.2272 | 5.5400 | 0.0286 | 0.05 | 0.15 | 89.9 | |

Date AUG. 25, 2015 Date AUG. 25, 2015

Figure F-1: Aluminium 7075-T6 material test certificate (Metal and Tool Trade, 2015).

Since a large diameter (160 mm) billet of aluminium 7075-T6 was used, Rockwell Hardness A tests were performed over the cross-section of the billet to check for sufficient heat treatment depth, shown in Figure F-2. It shows consistent hardness over the cross-section, indicating sufficient heat treatment depth with an average hardness of 52 HRA.

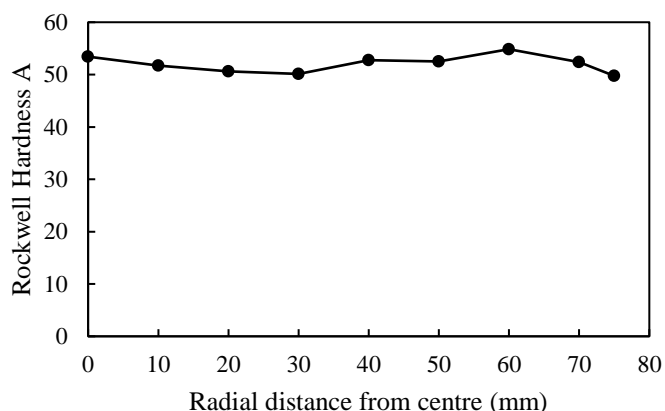


Figure F-2: Rockwell Hardness A (HRA) over the cross-section of the aluminium 7075-T6 billet (average from two tests).

Appendix G: Heli-Coil™ Chart

Tensile Strength of Heli-Coil Assembly vs. Shear Strength of Parent Material
for M6x1 Size

(*) Bolt Material Ultimate Tensile Strength

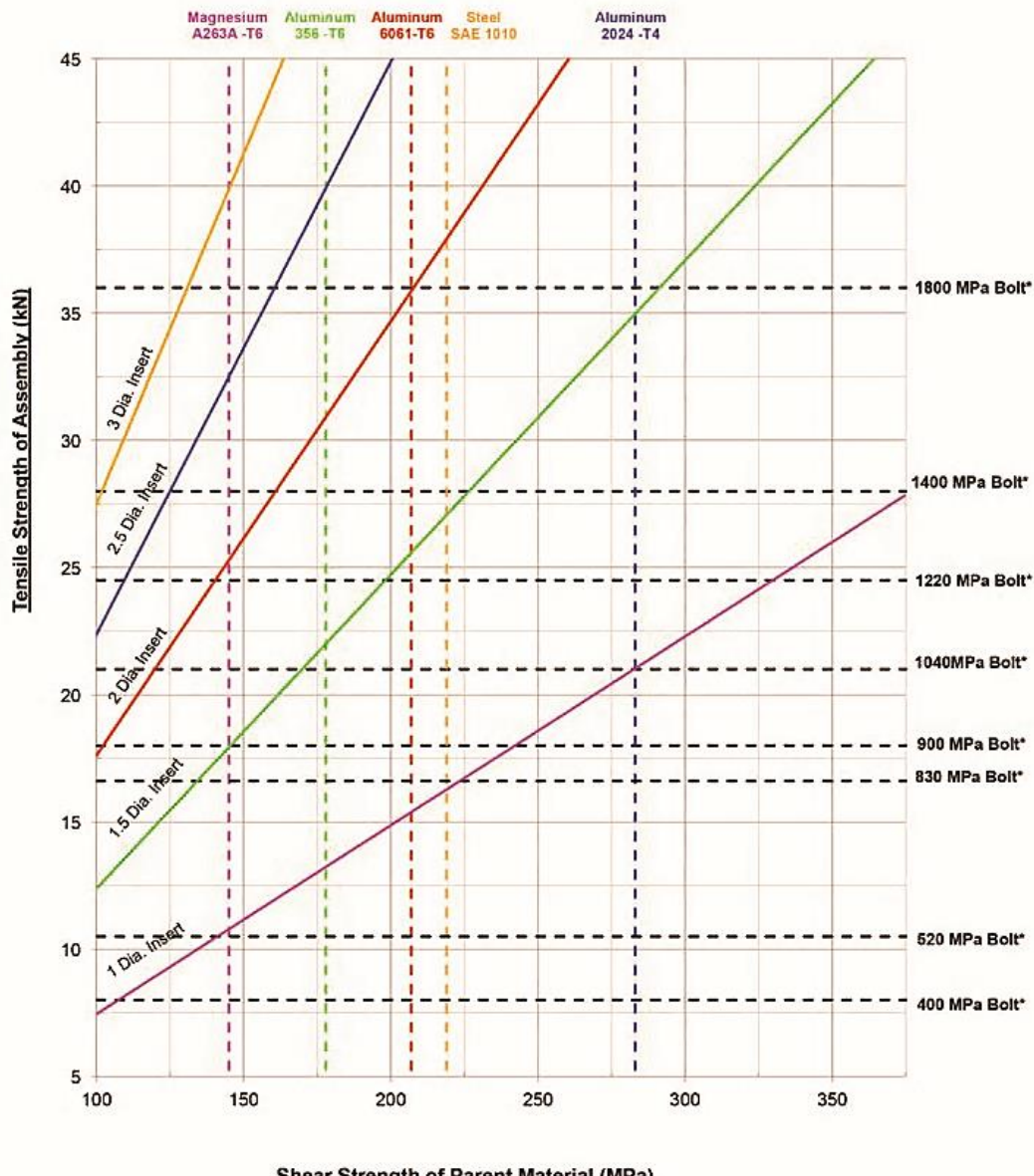


Figure G-1: Heli-Coil™ chart of tensile strength versus shear strength of parent material
(Stanley, 2018).

Appendix H: Oxidiser Valve Control Schematic

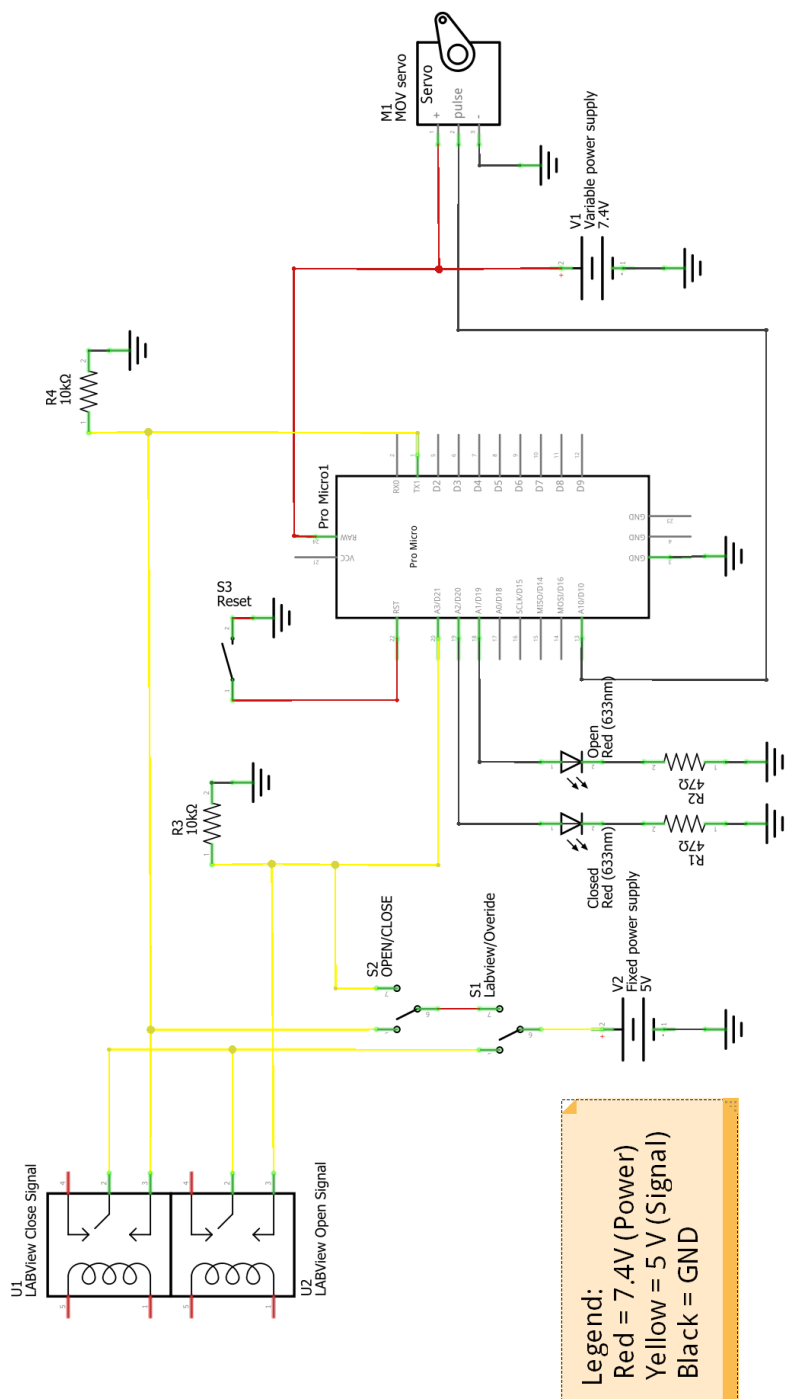


Figure H-1: Oxidiser valve control schematic.

Appendix I: Nozzle Design Charts

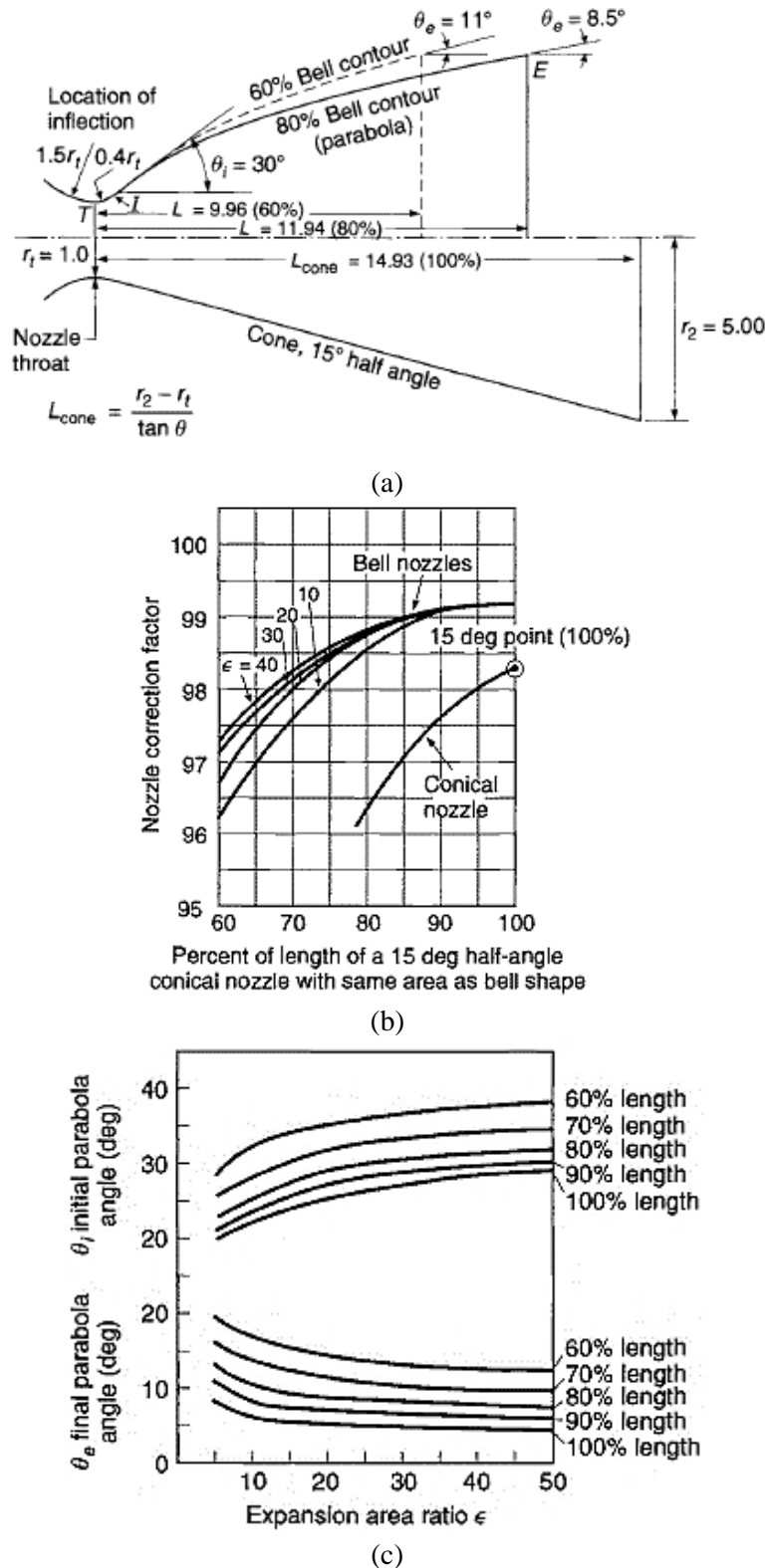


Figure I-1: (a) Nozzle geometric nomenclature for different nozzle types at an area ratio of 25, (b) nozzle losses in terms of a correction factor for conical and bell-shaped nozzles, and (c) nozzle initial and final parabola angles as functions of the nozzle percent length and expansion ratio (Sutton and Biblarz, 2001).

Appendix J: Nozzle Material Properties

Table J-1: Thermal conductivity of ATJ graphite (taken as the average between the perpendicular and parallel directions) (Ho et al., 1968).

| Temperature (K) | Thermal conductivity (W/m-K) |
|-----------------|------------------------------|
| 273 | 116 |
| 400 | 104 |
| 600 | 83 |
| 800 | 67 |
| 1000 | 57 |
| 1400 | 43 |
| 1800 | 37 |
| 2000 | 35 |
| 2400 | 33 |
| 2800 | 30 |

Table J-2: Specific heat capacity of ATJ graphite (Haines, 2000).

| Temperature (K) | Specific heat (J/kg-K) |
|-----------------|------------------------|
| 273 | 710 |
| 500 | 1100 |
| 750 | 1450 |
| 1000 | 1700 |
| 1500 | 1900 |
| 2000 | 2050 |
| 2500 | 2100 |

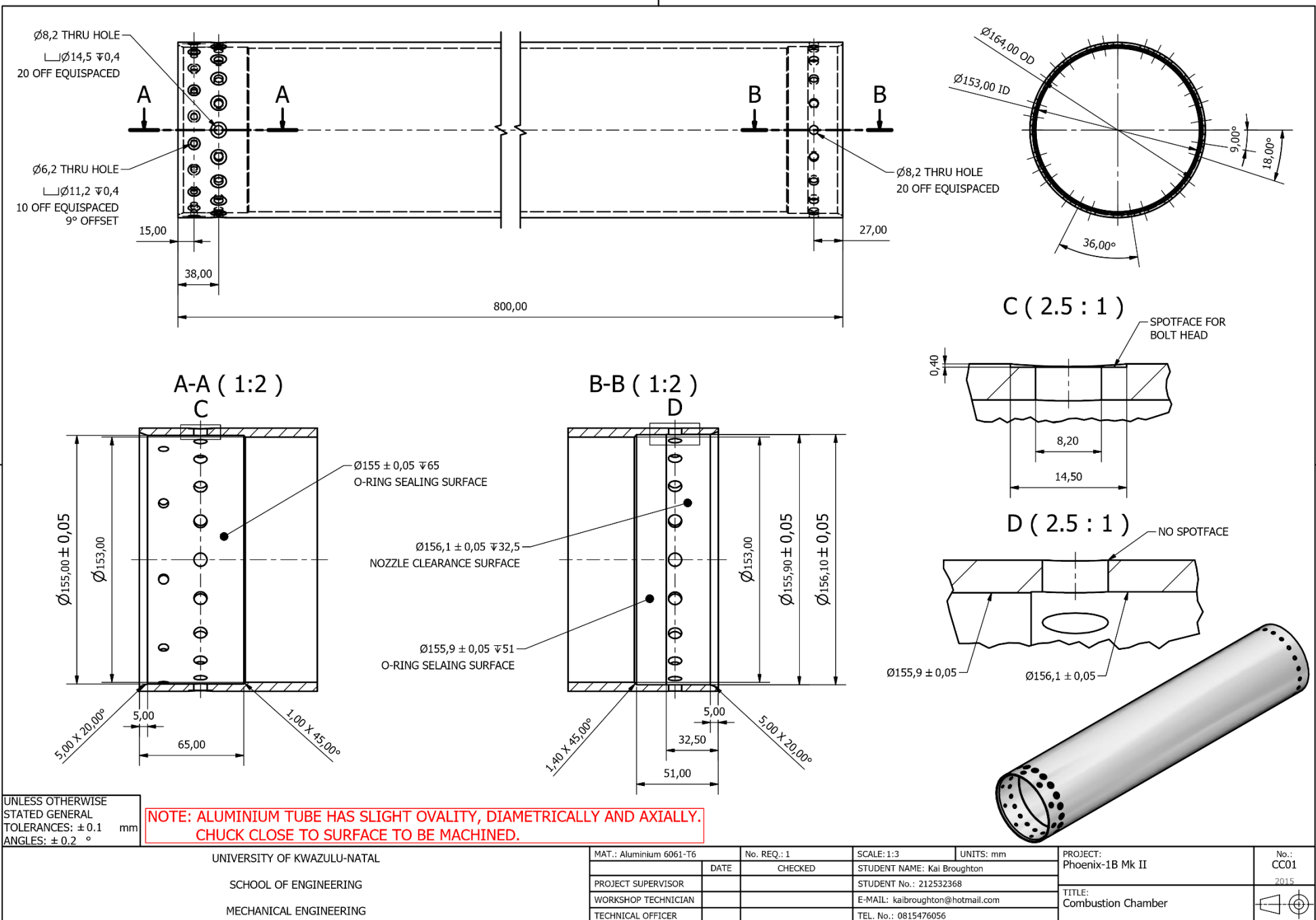
Table J-3: Thermal conductivity of EN19T alloy steel (eFunda, 2017).

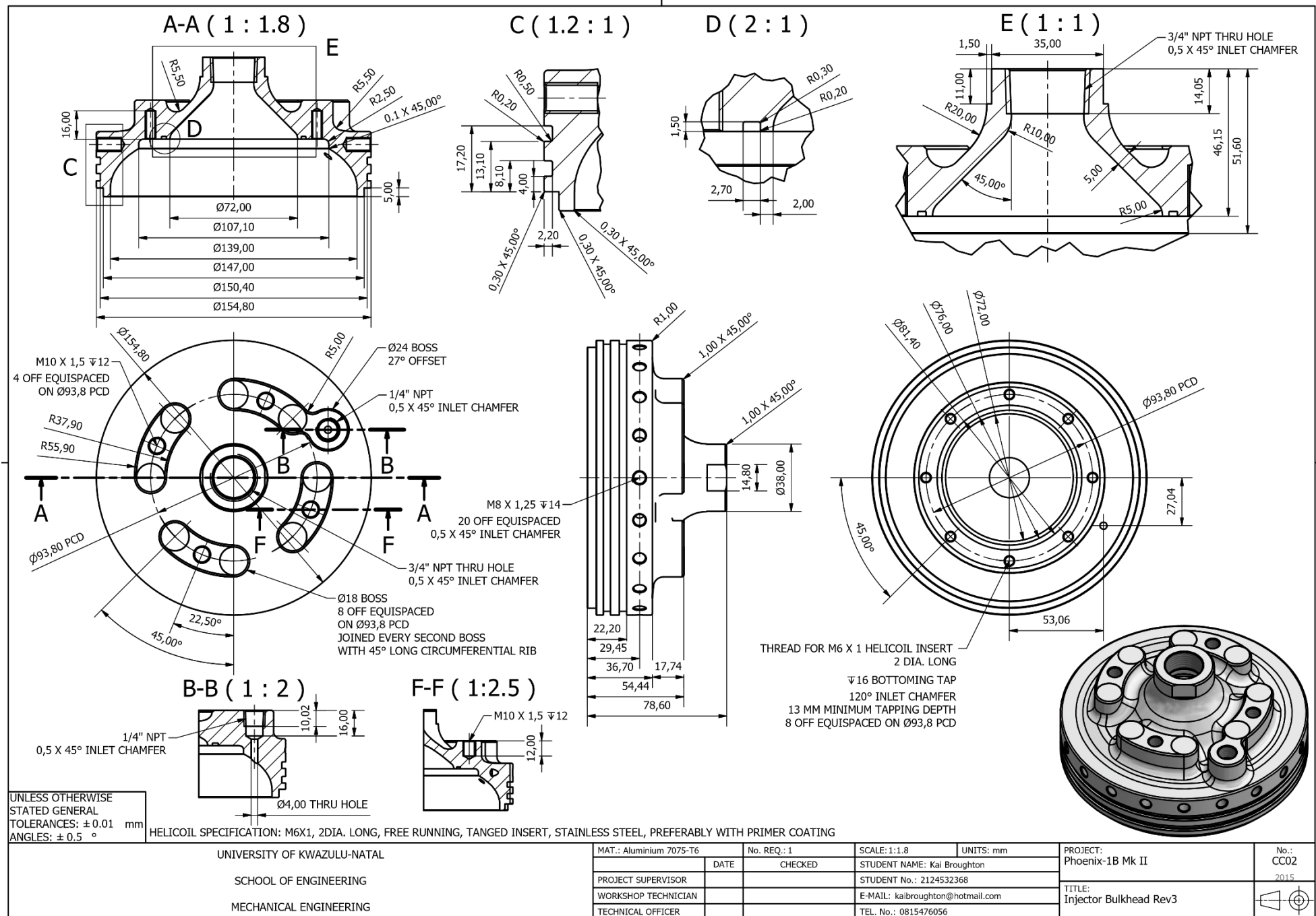
| Temperature (°C) | Thermal conductivity (W/m-K) |
|------------------|------------------------------|
| 100 | 42.6 |
| 200 | 42.2 |
| 400 | 37.7 |
| 600 | 33 |

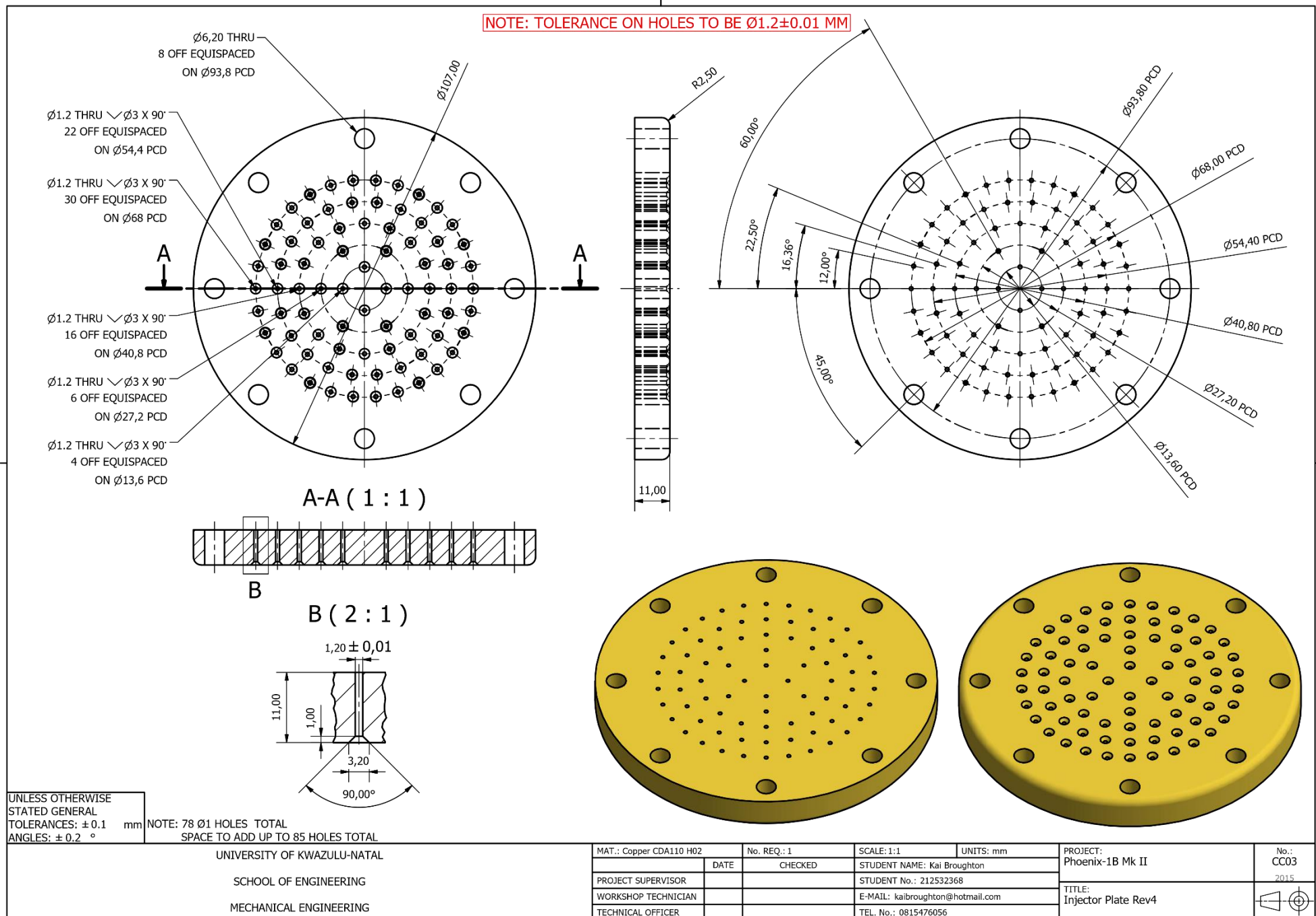
Table J-4: Specific heat capacity of EN19T alloy steel (eFunda, 2017).

| Temperature (°C) | Specific heat (J/kg-K) |
|------------------|------------------------|
| 150 - 200 | 473 |
| 350 - 400 | 519 |
| 550 - 600 | 561 |

Appendix K: Manufacturing Drawings





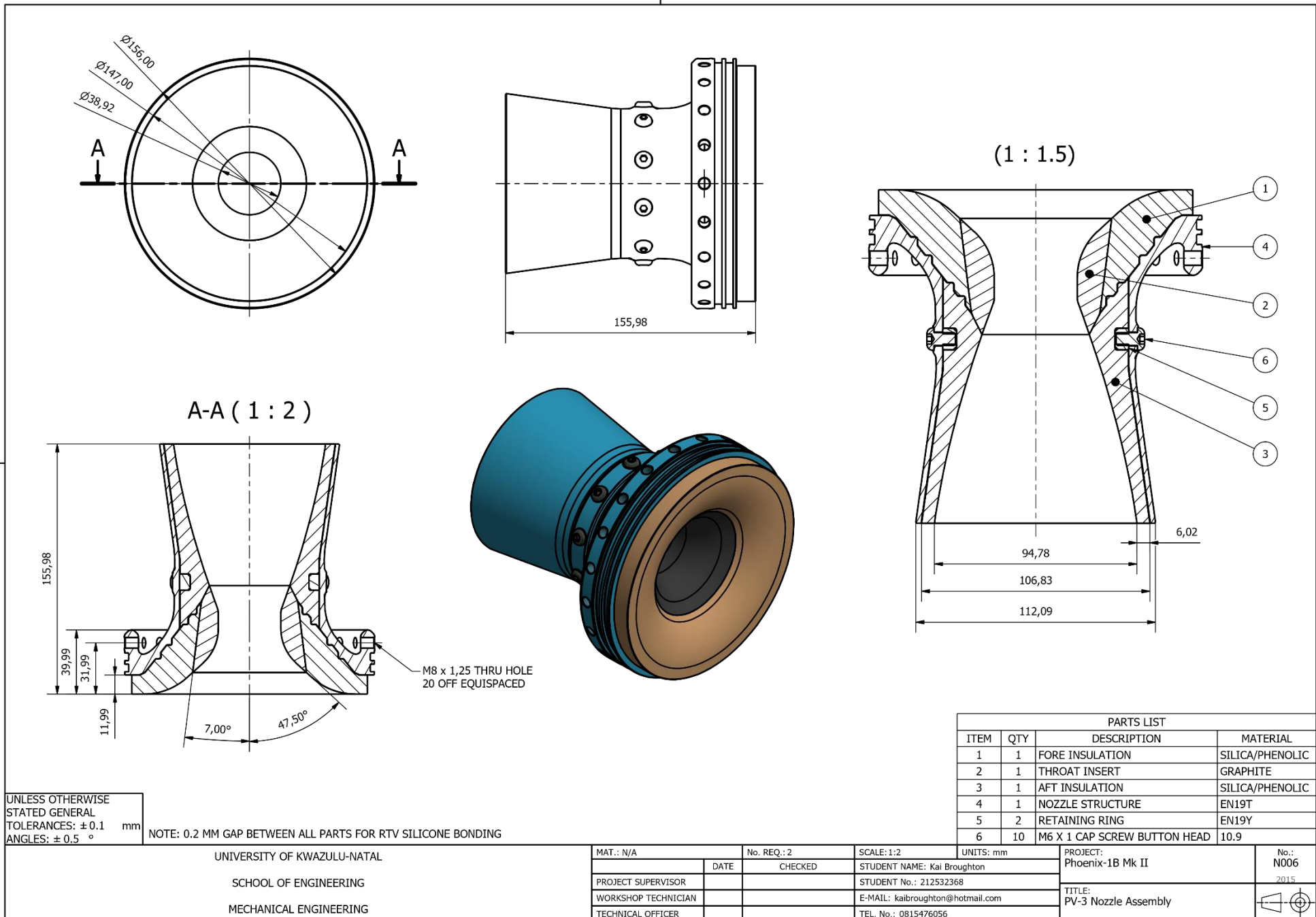


UNLESS OTHERWISE
STATED GENERAL
TOLERANCES: ± 0.1 mm
ANGLES: $\pm 0.2^\circ$

NOTE: 78 Ø1 HOLES TOTAL
SPACE TO ADD UP TO 85 HOLES TOTAL

UNIVERSITY OF KWAZULU-NATAL
SCHOOL OF ENGINEERING
MECHANICAL ENGINEERING

| MAT.: Copper CDA110 H02 | No. REQ.: 1 | SCALE: 1:1 | UNITS: mm | PROJECT: Phoenix-1B Mk II | No.: CC03 |
|-------------------------|-------------|------------|-----------------------------------|----------------------------|-----------|
| | DATE | CHECKED | STUDENT NAME: Kai Broughton | | 2015 |
| PROJECT SUPERVISOR | | | STUDENT No.: 212532368 | | |
| WORKSHOP TECHNICIAN | | | E-MAIL: kai.broughton@hotmail.com | TITLE: Injector Plate Rev4 | |
| TECHNICAL OFFICER | | | TEL. No.: 0815476056 | | |



UNIVERSITY OF KWAZULU-NATAL

SCHOOL OF ENGINEERING

MECHANICAL ENGINEERING

Appendix L: Videos

Videos are provided on attached CD disk:

Video L-1: 3D injector CFD transient flow animation

Video L-2: Nozzle thermal-structural FEM analysis transient temperature response

Video L-3: PV-3 motor igniter test

Video L-4: PV-3 motor cold flow test

Video L-5: PV-3 motor hot-fire test